Down Under – Aspects of Microbial Fuel Cell's sewer implementation

Von der Fakultät für Lebenswissenschaften

der Technischen Universität Carolo-Wilhelmina zu Braunschweig

zur Erlangung des Grades

eines Doktors der Naturwissenschaften

(Dr. rer. nat.)

genehmigte

D i s s e r t a t i o n

von Jonas Maximilian Sven Andrich
aus Paderborn

1. Referent: Professor Dr. Uwe Schröder
2. Referent: apl. Professor Dr. Rainer Krull
eingereicht am: 26.06.2017
mündliche Prüfung (Disputation) am: 27.10.2017

Druckjahr 2017

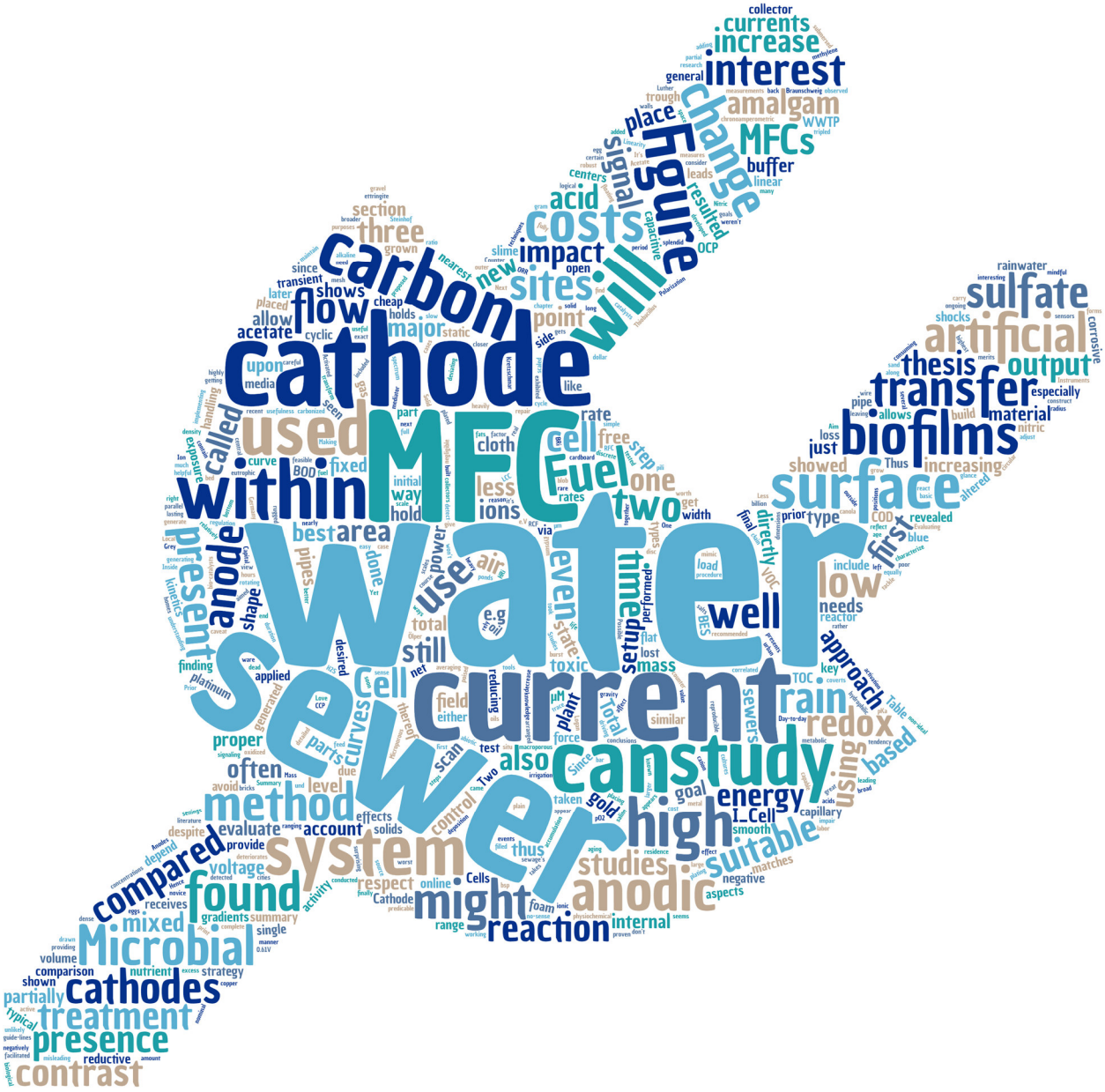

Thesis word-cloud

www.wortwolken.com

Table of contents

Danksagung

Wo fängt man an sich zu bedanken, wenn im Verlauf eines so umfangreichen Vorhabens wie dem einer Promotion so viele Menschen positiven Einfluss genommen haben? Es ist unmöglich den Beitrag derer die an meiner Seite standen vergleichend zu bewerten und aufzuwiegen.

Fange ich an bei meinem Betreuer Prof. Dr. Uwe Schröder, der mir überhaupt erst ermöglichte mich in dieser grandiosen, vielfältigen und freundlichen Arbeitsgruppe als entdeckender und kreativer Wissenschaftler in diesem vielseitigen Forschungsvorhaben zu entfalten. Danke Uwe, danke Dir für die Freiheit und diese Möglichkeit. Dank gilt demjenigen, der meine wissenschaftliche Karrie am längsten begleitete, Professor André Fleißner, der mir vor fast 10 Jahren schon erste eigene Schritte in der Forschung ermöglichte. Ich danke Herrn Professor Dr. Krull für sein Zweitreferat und für sein langjährig gehegtes und gepflegtes Austauschprogramm, durch das ich meinen Horizont in einer wunderbaren Zeit im kanadischen Waterloo erweitern durfte.

Meinen lieben Kollegen Sebastian, Waldi, Diane, Hilke und Christiane danke ich für die gemeinsame Zeit, ihren Zuspruch, ihre Motivation, ihren Humor, die viele Ratschläge und natürlich ihr Korrektorat. Die kritischen Kollegen waren sicherlich gleichsam auch die besten Lehrer – Keith und Igor danke ich für die Diskussion meiner Vorhaben und Ideen. Meinen Schülern Pratik Kumar und David Schmiede danke ich, denn durch sie durfte ich beständig selbst weiter lernen. Ich danke Frau Dr. Bente Thamsen für ihre Berechnungen.

Ich danke dem ganzen Braunschweiger Abwasserbetrieb, ohne dessen unermüdlichen Einsatz wir niemals so unbeschwert den Wasserhahn aufdrehen könnten und durch den ich mich für die Mikrobiellen Brennstoffzellen überhaupt erst in das Gebiet der Entsorgungsinfrastruktur vorwagen konnte. Ich danke insbesondere Frau Fiebig, Herrn Walter und Herrn Lampe.

Ich danke meinen Freunden André, Daniel, Leonie, Luna, Niko, Lutz, Therese und so vielen mehr, all meinen liebgewonnenen Mitbewohner aus meiner wahnsinnigen Gaußstraße 16, die weiter leben wird, meinem Foodsharing Team, das mit mir gemeinsam viele Tonnen Lebensmittel rettete, meinen Gewichthebern und meinem Verein mit dem ich gemeinsam stärker werden durfte.

Was hat mich maßgeblich beeinflusst? Ich bin dankbar für die bedachten Ratschläge meines Mentors Dr. Gehder, die mir als Licht in weiter Ferne den Weg wiesen. Ich danke für den Zugewinn an Ruhe und Kraft, durch meinen Trainer Maik Nill.

Danke Mutter, nur dadurch, dass Du mich hast sein lassen, konnte ich das werden was ich bin.

Widmung

Denen die mit dem wenigen, das ihnen gegeben war, alles tun, um dort hinzugelangen, wo sie all denen geben können die nichts haben und denen die Neues schaffen, wo nichts war, um allen mehr zu bieten.

Dir Vater, widme ich diese Arbeit, denn Du wusstest und wolltest, dass ich einmal Wissenschaftler werden würde – hier bin ich und ich bin noch viel mehr geworden. Ich wünschte, Du könntest noch einen kurzen Moment sehen was aus mir trotz oder gerade wegen Deiner Abwesenheit geworden ist. Ruhe Dich in Frieden von Deinem kurzen rastlosen und uns alle verzehrenden Leben aus.

Mir, denn es war meine Prüfung, mich in Beständigkeit zu üben, kommend aus einer Welt, in der die Konstante darin lag, dass ungewiss war was morgen sein würde.

Zusammenfassung

Mikrobielle Brennstoffzellen (MFCs), erlauben es aus dem Abfallstoff Abwasser Energie zurückzugewinnen, während dieses gleichzeitig aufbereitet wird. Ein hochinteressantes Anwendungsfeld stellt dabei das Abwasserkanalsystem mit seinen Millionen Kilometern Länge dar. Die vorliegende Arbeit widmet sich daher den Aspekten einer integrativen Implementation in diese Umgebung.

Zuerst wurde das Abwasserkanalsystem als mögliches Anwendungsfeld für die MFC bewertet. Dazu wurden die physiochemischen Anforderungen einer MFC als Bewertungskriterien für die Standorte herangezogen und genutzt, um einen Teil der Braunschweiger Abwasserinfrastruktur zu evaluieren. Damit wurde die Eignung eines stadtauswärts liegenden Kanalabschnittes abgeschätzt und ein generelles Vorgehen für zukünftige Studien aufgezeigt.

Neben dem Standort beeinflussen die einzelnen Komponenten einer MFC maßgeblich, ob und mit welcher Leistung diese zum Einsatz kommen kann. Verschiedene kohlenstoffartige Kathodenmaterialien wurden hinsichtlich ihrer Reduktionsrate, ihrer Leitfähigkeit und der Änderung der Katalysefähigkeit durch Säurebehandlung verglichen. Es wurde dabei deutlich, dass die Methoden typischer Performance-Studien für die Materialien und deren angestrebten Einsatzgebiet angepasst werden müssen, um genauere Leistungsvorhersagen treffen zu können.

Nach der Untersuchung der Komponenten, stellte sich die Frage wie Sauerstoffkathoden im anaeroben Kanal eingebracht werden könnten. Außerhalb des Elektrolyten platzierte poröse Luft-Kathoden blieben durch ihre Kapillarkräfte Elektrolyt getränkt und erlaubten so einen verbesserten Massentransfer. Im cm-Maßstab konnten Interphaseneffekte die Ströme aller Materialien verbessern. Es zeigten sich jedoch auch Nachteile, wie ein erhöhter Gesamtwiederstand oder die Blockade durch ahesierenden Öle.

Der vorletzte Teil widmet sich der Kontrolle kanalschädigender biogener Sulfid-Emission und dessen Toxizität für elektroaktive Organismen. Die Balance zwischen Emission und Rückoxidation konnte vergleichend für elektroaktive Organismen und eine speziell entwickelte artifizielle Sielhaut untersucht werden.

Zu guter Letzt wurde eine elektroanalytische Methode zur Online Sulfid-Bestimmung an die komplexe Probenmatrix des artifiziellen Abwassers adaptiert. Zusätzlich wurde die Herstellung und der Alterungsprozesse der dazu nötigen Gold-Amalgam-Mikroelektrode untersucht, um Hinweise für den Bau und die Verwendung geben zu können.

Summary

Microbial Fuel Cells (MFCs) represent an exciting technology that allows the recovery of energy from waste water while simultaneously cleaning it. There is still a long way to go to implement the fundamental research of this microbially catalyzed transformation from chemical to electrical energy. The sewage system, with its million-kilometer-length is a highly interesting field of application. The present work is therefore devoted to aspects of integrative implementation in this environment.

Firstly, the wastewater infrastructure was evaluated as a possible field application of the MFC. For this purpose, the physiochemical requirements of an MFC were used as the assessment criteria for the sites and to evaluate a part of the City of Braunschweig's waste water infrastructure. The suitability of an outlying channel section was thus identified and a general procedure for future studies was developed.

In addition to the location, the individual components of an MFC have a decisive influence on its performance. The cathodes can be particularly problematic. Thus, various carbonaceous materials were compared for their reduction rate, their conductivity and their change due to nitric acid treatment. It became clear that the typical methods for performance studies of materials and their intended area of application had to be adapted to make more precise performance predictions.

After investigating the components, the question arose as to how oxygen cathodes could be placed in the anaerobic channel. Porous air cathodes protruding from the electrolyte remained soaked in electrolyte due to their capillary forces, thus allowing an improved rate of mass transfer. On the scale of cm, these interphase effects could improve the currents of all materials. However, disadvantages such as increased overall resistance or the adhesion of electrode blocking oils have also been found.

The penultimate section of this thesis is devoted to the control of sewer-damaging biogenic sulfide emissions and their toxicity towards electroactive organisms. The balance between emission and re-oxidation could be shown for electroactive organisms and a specially developed artificial sewer slime.

Finally, an electroanalytical method for online sulfide determination was adapted to the complex sample matrix of the artificial sewage. In addition, the production and aging processes of the gold-amalgam microelectrode necessary for this purpose were investigated to provide advice on construction and usage.

List of abbreviations

Abbreviation	Term
AC	activated carbon
AWW	artificial waste water
BES	bioelectrochemical system
BOD	Biological oxygen demand
CA	chronoamperometry
CCP	closed circuit potential
CE	counter electrode
COD	chemical oxygen demand
CV	cyclic voltammetry or cyclic voltammogram
EAB	electroactive biofilm
GDL	gas diffusion layer
LCC	layered corrugated carbon
MFC	Microbial Fuel Cell
OCP	open circuit potential
ORR	oxygen reduction reaction
PBS	phosphate buffered saline
RCF	reticulated carbon foam
RE	reference electrode
SWV	square wave voltammetry
TOC	total organic carbon
VOC	volatile organic compound
WE	working electrode

1. Introduction and theory

1.1. Aim and structure of the thesis

Microorganisms have an extensive and surprising variety of capabilities - they even produce electricity within the setup of a Microbial Fuel Cell (MFC). A possible feedstock for this biological energy source is waste water. It is an abundant resource present in millions of kilometers of sewer pipes. Thus, the fusion of Microbial Fuel Cells and the sewer system could hold tremendous potential for urban energy recovery. Yet, its implementation within the waste water infrastructure remains unrealized. Therefore, the goal of this thesis was to investigate a way how this could be done. An integrative approach was followed. It aimed to combine electricity generation, waste water cleaning and infrastructure protection at the same time. For this purpose, three aspects were focused on:

1. Deployment sites within the municipal sewer infrastructure were identified and evaluated.
2. MFC's major bottleneck is the cathode. It was targeted by comparing renewable carbonaceous materials, by improving the required analytics and by a spatial positioning strategy to reduce mass transfer.
3. Sulfide emission-control trough electroactive biofilms was examined to tackle sewer corrosion. In addition, a method for electroanalytical online sulfide determination was adapted.

1.2. Microbial Fuel Cells – electricity generated by microbes

Bioelectrochemical systems (BES) make use of bio-catalysts to accelerate redox reactions and electron-transfer. A special type of BES is the Microbial Fuel Cell. Inside the MFC, microorganisms convert chemical energy into electricity by using the anode as a final electron acceptor for their respiratory chain. This process is called anodic respiration [1].

MFC-Setup

Figure 1 shows a typical MFC which reminds of a classical galvanic element with anode and cathode placed within two separated compartments. The voltage between anode and cathode is derived from the different redox potentials present in the anode and cathode chamber. When the electrodes are connected by a conductive wire (Figure 1, R), electrons might flow from

anode to cathode until both compartments reach equilibrium. A higher potential difference allows higher possible current.

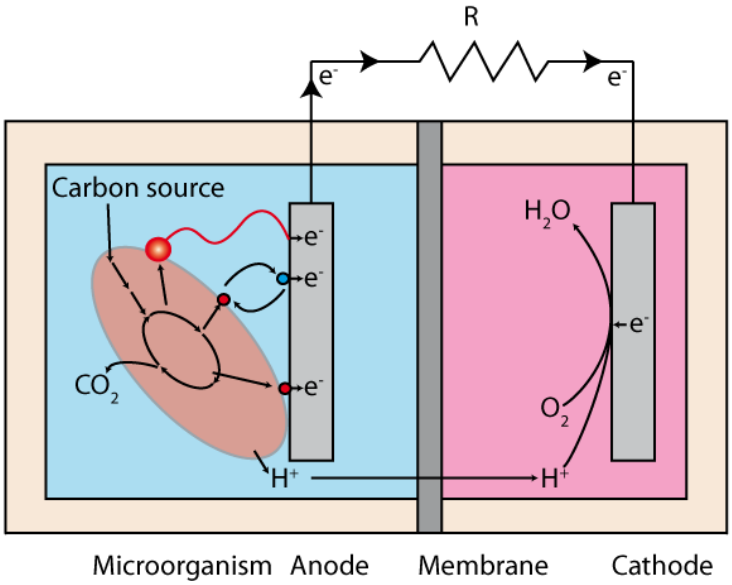

Figure 1: Schematic setup of a Microbial Fuel Cell adapted from Logan et al. [2]. It illustrates the general setup, the three microbial electron transfer mechanisms on the anode side (Microorganisms not scaled, left) and the oxygen reduction reaction at the cathode (right). The MFC electrodes are connected via a resistor (R) to allow current flow.

In most laboratory MFCs, anolyte and catholyte are separated by a semipermeable cation exchange membrane (e.g. Nafion) which reaches two goals: Firstly, it allows the flow of ions, and thus charge neutrality during current flow. Secondly, it prevents diffusion of substrates or oxygen from one compartment into another and therefore reduces electrochemical cross-reactions and mixed potentials [3]. Both aspects sustain a high cell voltage and defined reaction conditions in the respective compartments. Despite its cost and its increase of internal resistance its benefits often predominate [4].

Electrodes, potential and current

The potential between two connected electrodes is called closed circuit potential (CCP), and in contrast, if not being connected, open circuit potential (OCP). The OCP is a good estimate of the possible thermodynamic difference between the two half-reactions. As soon as the electrodes are connected, a current might flow, which is illustrated above (Figure 1). This current causes the electrode potentials to change as illustrated in the polarization curve below (Figure 2). How the electrode potential will deviate from its respective standard half-reaction potential is of great interest for performance evaluation and expressed as the overpotential η, an important denotation for electrode studies.

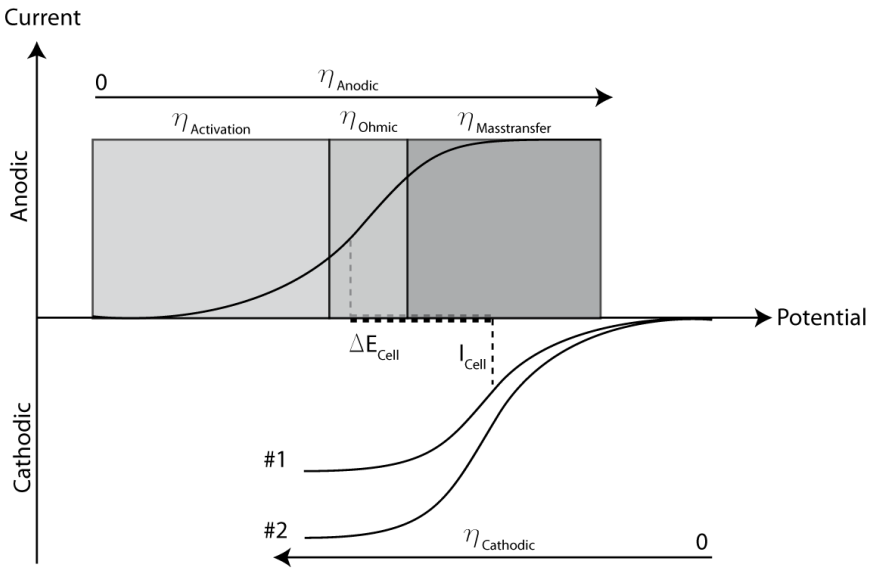

Figure 2: Illustration of polarization curves and estimate of cell potential ΔE_{Cell} at an arbitrary current I_{Cell}. Grey areas represent how the activation, ohmic resistance and mass transfer contribute to the total anodic overpotential η_{Anodic}. The $\eta_{Cathodic}$-current behavior is shown at the bottom. The change from #1 to #2 illustrates the impact of increasing electrode surface area on cathode performance.

At low overpotentials the electrochemical reaction is limited by electrode kinetics. At higher overpotentials the electrochemical reaction scales linear with increasing potentials proportional to the ohmic resistance of the system. Lastly, at highest overpotentials the mass transfer of the electrochemical species becomes limiting and the current increases less steep. Mass transfer limitations are avoided by continuous supply of electrochemical reactant. As it will be seen later, this is a challenge for the application of oxygen reducing cathodes in oxygen poor environments. Therefore, parts of this study were dedicated to avoiding transfer limitations at cathodes intended for sewer application.

Both electrodes can be analyzed separately by using a potentiostat controlled setup. The polarization curves allow to estimate the overall cell potential ΔE_{Cell} at a given current I_{Cell} and therefore the power output (P = I x E) of the cell. The MFC-engineer can use this information to adjust the operational parameters and dimensions accordingly for proper upscaling. This can be done e.g. by increasing the cathode surface area which leads to a higher cell potential at the same I_{Cell} (Figure 2, #1 to #2) and a subsequent higher power output.

Anodes with electroactive biofilm

The distinct feature of MFCs is the use of biocatalysts at the anode surface. Anodic biofilms contain diverse mixed cultures capable to consume and oxidize a broad spectrum of substrates found in waste water [5–8]. The driving force is the microbial need for a final electron acceptor

in the absence of oxygen. Figure 1 illustrates how microorganisms transfer their electrons either directly, via an mediator substance or via an electroactive pili [9,10]. The most significant contributor to electron transfer of these biofilms is *Geobacter sulfurreducens* [11]. It is an acetate consuming gram-negative bacterium. Acetate can be either added directly as feed to the anodic compartment or generated in situ by other fermentative species present within the biofilm. Several other metabolic pathways could be found in an MFC biofilm as for example hydrogenotrophic methanogenesis, dissimilatory sulfate reduction and many others [7].

Anodic biofilms grow naturally during MFC operation, but more selectively and dense during potentiostat-controlled enrichment [12]. Anodic biofilms are partially resistant to oxygen [13] and their active redox centers can be determined by cyclic voltammetry [14]. Their performance depends on environmental factors such as Temperature [15] and pH [16]. Highest and most stable performance is achieved by secondary anodic biofilms whose inoculum is taken from a previous round of enrichment [17].

Cathodes for oxygen reduction

Oxygen reducing cathodes are used most commonly, because oxygen is abundant, free and it holds a high redox potential. The preferred 4-electron reduction reaction has a standard potential of 1.032 V vs. Ag/AgCl [18], which can be still 0.61V vs. Ag/AgCl (pH 7; pO_2 = 0.2 bar) under MFC operation [2]. The 4-e^--reaction proceeds in three steps: Firstly, oxygen absorbs to the electrode surface, secondly, it receives electrons and thirdly, it receives protons to react to water. The downsides of oxygen are its low solubility in water and its hindered reaction kinetics. Both factors contribute significantly to the overpotentials required to achieve adequate current flow.

A variety of potential materials can be used for the oxygen reduction reaction (ORR) [19] but all of them will provide significant overpotentials, even platinum which is considered as the best possible reduction catalyst [20]. A major goal is to find sustainable and cheap noble-metal-free cathode catalysts which are suitable for the application within the MFC-environment. Some possible materials and modifications thereof will be examined and compared within this study.

Electrolyte – required for fuel cell function while mimicking waste water

Solid, liquid or dissolved chemical compounds, which are dissociated to ions are called an electrolyte [21]. In the presence of an electric field a force is applied to the ions, resulting in their migration. The wandering ions represent the movement of charge, and thus an electric current trough the electrolyte. An ionic conductor can change its composition upon charge transport, whereas an electric conductor does not. This has important implications for the design of an

MFC, because it can result in changing resistance, the formation of chemical gradients or especially the change in pH [22]. Besides its function as a highly saline conductor, the laboratory based MFC-electrolyte is intended to imitate its potential feedstock, such as waste water, which requires suitable nutrients and supplements for the growth of anode respiring bacteria. This is done by adding vitamins, minerals, carbon sources and buffer compounds. These supplements allow microbes to prosper and prevent substantial pH changes during operation, but also represent electrochemical complexity, which might impact analytical methods. A phosphate buffered acetate media is used in most experiments of this study. Additionally, an advanced carbonate buffered media reflecting waste water even better by being supplemented with a variety of carbon sources was used during some of the experiments.

Implementation of MFCs

Scale-up requires that the benefits outweigh the costs. Those associated with MFCs comprise capital and operational costs. Capital costs are fixed and include one-time purchases such as plants or new equipment. Operational costs include variable and fixed positions, whereas the fixed costs remain the same at any level of productivity, but variable costs depend on the output of production. The major benefits of the MFC are waste water cleaning, energy generation and possibly the increased longevity of less-corroding sewers. The costs will be associated with construction, material, labor and maintenance.

Recent upscaling attempts focused on present laboratory setups without engaging implementation strategies for existing infrastructures. Accordingly, the derived suggestions do mostly target known factors impacting MFC-performance, such as catalyst activity, accessible electrode surface area or nutrient influx [23] [24] [25]. If the environment of the sewer infrastructure is considered, unknown inherent challenges will arise. What might they be like?

1.3. The sewer – the way of the waste

For the most of us the enormous merit of the waste water infrastructure remains invisible just because it functions so well and because for most of us it disappears behind the walls of our homes. The extensive net of the waste water infrastructure spans underneath the cities.

How does the net look like? There is no general blue print, since local factors determine its shape [26] but there are repetitive patterns. Within a branched network the sewage is collected at a central point and then discharged to the closest waste water treatment plant (WWTP). Greater municipal networks don’t have just one single collection point but several independent networks each with their own. Often, a pumping station elevates the waste water of these

collection points prior to a free-falling pipe. The composition and amounts of waste water influx will depend on the respective drainage area and its composition will change while approaching the WWTP.

There are two types of drainage system [26]: The first one combines wastewater with rain water which is called the mixed water system. Its pipes require larger cross sections to carry additional rain water and upon overrun, the diluted waste water is discharged into the nearest receiving water. The second system carries waste water and rain water in two separate pipe systems. Here the rainwater drainage leads directly to the nearest receiving water. It is called separate system. Mixed systems construction-costs and space requirements are lower compared to separate systems, but their potential pollution of the receiving water is higher.

Local factors determine not only the shape of the sewer network but also the geometry of the sewer [26]. It should have beneficial hydraulic properties while handling the incoming channel flow. It is influenced by the possible maximum sewer height, the static load and the maximum construction costs. Figure 3 shows three typical geometries, but practically any other shape is possible as well.

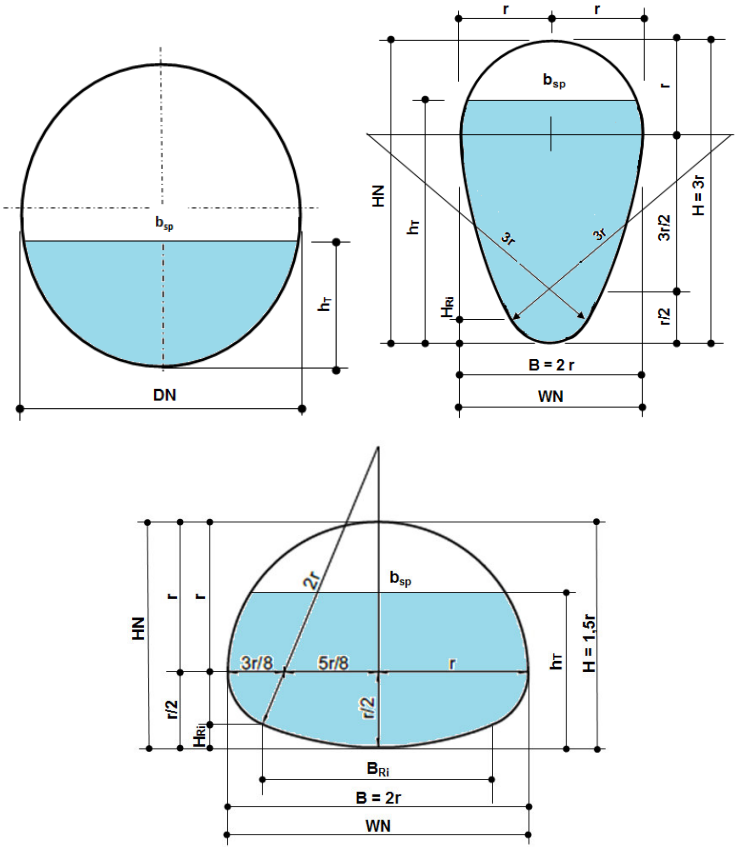

Figure 3: Typical sewer geometries: Round, egg shaped and taper-cross section sewer profile. Courtesy of the German professional association of concrete and reinforced concrete pipes (Fachvereinigung Betonrohre und Stahlbetonrohre e.V.). DN and WN represent the nominal diameter. HN is the sewer height whereas h_T represents the water level height. b_{sp} represents the water level width. H_{Ri} and B_{Ri} represent the hydraulic height and width, respectively and they are used for hydraulic calculations. r is the radius of the circular parts of the illustrated geometries.

Knowledge about sewer construction reaches back to the ancient roman and Greek Empire. In Germany, sewers with large geometries have been built from bricks since 1843 and from site-mixed concrete starting from 1875 [27] whereas in contrast, smaller diameters have been made mostly from stone ware. Reinforced concrete has been used only in the modern age. The sewer infrastructure is laid-out and build to persist with low maintenance and high resistance to stress.

Despite its sophisticated design and the rugged materials in use, the longevity of sewers can be shortened. The material is stressed constantly: physically, statically and chemically [27]. The physical stress derives mostly from bed load, namely sand, gravel and pebble. Hence, the wearing increases with the water velocity. The static stress originates from exterior forces such as pressure, displacement and movement. The chemical stress results from corrosive, toxic and even explosive substances, mostly from acids, salts and sulfide. Table 1 specifies the complex aqueous mixture of organic and inorganic compounds of waste water.

Table 1: Example for waste water composition [28,29].

Compound	Concentration [mg/L]
Solids	300 - 1200
Dissolved total	250 - 850
Suspended solids	100 - 350
Settable solids	5 -20
Biological oxygen demand (BOD)	110 - 400
Total organic carbon (TOC)	80 - 290
Chemical oxygen demand (COD)	250 - 1000
Total nitrogen	20 - 85
Organic nitrogen	8 - 35
Ammonia	12 - 50
Phosphate	4 - 15
Organic phosphate	1 - 5
Chloride	20 - 50
Sulfate	20 - 50
Grease	50 - 150
Volatile organic compounds (VOC)	100 - 400

Especially the biogenic sulfide production from sulfate and its induced sewer corrosion represents a global challenge. Sulfide forms when organic matter degrades under anaerobic conditions. It is a toxic gas with the unpleasant smell of rotten eggs. It has a pKa value of 6.98 at 25°C and is well soluble in water. Therefore, under acidic conditions it is mostly present as H_2S gas and under basic conditions it is mostly present as HS^- Ion. Its chemistry is complex and reviewed extensively elsewhere [30–35].

Prior to sewer corrosion, it volatilizes, condenses at the sewer crown and gets oxidized to sulfuric acid by *Thiobacillus* sp. Then, sulfuric acid deteriorates the alkaline concrete and coverts it to ettringite and gypsum whose higher volume causes its surface to burst open. Counter measures, maintenance and repair costs are worth more than a billion dollar [36,37]. An interesting approach would be the regulation of biogenic sulfide emission by control of dissimilatory sulfate reduction in the first place.

2. Materials and methods

This section presents the tools and materials commonly used throughout this thesis. The distinct application parameters to generate results can be found in the respective results section.

2.1. Instruments and electrodes

Table 2: List of instruments and electrodes.

Equipment	Name	Manufacturer
Atomic emission spectroscopy	Vista-MPX	Varian
Confocal laser scanning microscope	TCS SPE	Leica
Electrode	SenTix 41	Xylem
Electrode	CellOx 325	Xylem
Electrode	TetraCon® 325	Xylem
Electrode	GE105	Greisinger
Contact angle determination	OCE 15EC	Dataphysics
Handheld meter	Multi 340i	Xylem
Handheld meter	GPRT 1400 AN	Greisinger
Motorized actuator	ENCODER MIKE™ actuator	Oriel
Motorized actuator controller	ENCODER MIKE™ Controller 18011	Oriel
Multimeter	2701 Digital	Keithley
Multipoint surface area and pore size analyzer	Gemini V	Micromeritics
Peristaltic pump	MCP Process	Ismatec
Photometer	USB200+	Ocean Optics
Photometer light source	DH-2000	Ocean Optics
Potentiostat	SP 200	Biologics
Potentiostat	VMP3	Biologics
Potentiostat	MPG2	Biologics
Tube furnace	MTF 1200	Carbolite

2.2. Chemicals and solutions

2.2.1. Chemicals

All chemicals were analytical grade ≥98% if not otherwise stated (Table 3).

Table 3: List of chemicals.

Chemical	Supplier	Chemical	Supplier
(-)-Riboflavin	Sigma-Aldrich	$MnSO_4 \cdot 1H_2O$	Sigma-Aldrich
4-Aminobenzoic acid	Fluka	N,N-Dimethyl-p-phenylenediamine	Sigma-Aldrich
$AlK(SO_4)_2 \cdot 12H_2O$	Sigma-Aldrich	Na_2CO_3	Sigma-Aldrich
Biotin	Carl Roth GmbH	Na_2HPO_4	Sigma-Aldrich
$CaCl_2$	Sigma-Aldrich	$Na_2HPO_4 \cdot 2H_2O$	Sigma-Aldrich
$CoCl_2 \cdot 6H_2O$	Sigma-Aldrich	$Na_2MoO_4 \cdot 2H_2O$	Sigma-Aldrich
$CuSO_4$	Carl Roth GmbH	$Na_2S \cdot 9H2O$	Carl Roth GmbH
$CuSO_4 \cdot 5H_2O$	Fluka	NaCl	Carl Roth GmbH
Cysteine	SAFC	NaH_2PO_4	Carl Roth GmbH
D-Glucose	Carl Roth GmbH	$NaH_2PO_4 \cdot 1H_2O$	Carl Roth GmbH
DL-Calcium pantothenate	Fluka	$NaH_2PO_4 \cdot 2H_2O$	Sigma-Aldrich
DL-Lactate (60%)	Sigma-Aldrich	$NaHCO_3$	Carl Roth GmbH
D-Ribose	Carl Roth GmbH	NaOH	Sigma-Aldrich
$FeCl_3 \cdot 6H_2O$	Carl Roth GmbH	NH_4Cl	Sigma-Aldrich
$FeSO_4 \cdot 7H_2O$	Sigma-Aldrich	Niacin	Sigma-Aldrich
Folic acid	Sigma-Aldrich	Nitrilotriacetic acid	Sigma-Aldrich
Glycin	Carl Roth GmbH	Potassiumhydrogenphthalate	Carl Roth GmbH
H_3BO_3	Sigma-Aldrich	Pyridoxinhydrochloride	Sigma-Aldrich
HCl (≥37%)	Sigma-Aldrich	Sodium acetate	Sigma-Aldrich
$Hg(NO_3)_2$	Acros Organics	Thiaminhydrochloride	Sigma-Aldrich
HNO_3 (65%)	VWR	Vitamin B12	Sigma-Aldrich
KCl	Carl Roth GmbH	Zinc acetate	Fluka
KOH	Grüssing	$ZnSO_4$	Sigma-Aldrich
Lipoic acid	Sigma-Aldrich	$ZnSO_4 \cdot 7H_2O$	Sigma-Aldrich
$MgSO_4 \cdot 7H_2O$	Sigma-Aldrich		

2.2.2. Solutions

Phosphate buffer

Phosphate buffer was used for acetate based artificial wastewater of type one and for most electrochemical reduction studies. Whenever this thesis mentions phosphate buffer it refers to the following recipe (Table 4).

Table 4: Composition of 50 mM pH 7 phosphate buffer.

Compound	Concentration [g/L]
$NaH_2PO_4 \cdot 1H_2O$	2.69
or	
$NaH_2PO_4 \cdot 2H_2O$	3.04
Na_2HPO_4	4.33
or	
$Na_2HPO_4 \cdot 2H_2O$	5.43
NH4Cl	0.31
KCl	0.13

Carbonate buffer

Carbonate buffer was used for artificial wastewater of type two (AWW 2). Whenever this thesis mentions carbonate buffer it refers to the following recipe (Table 5).

Table 5: Carbonate buffer composition.

Compound	Concentration [g/L]
Potassiumhydrogenphthalate	0.1361
NH_4Cl	0.3100
KCl	0.1300
$NaHCO_3$	0.8393
Na_2CO_3	0.0011
NaH_2PO_4	0.1551

Vitamin and trace element solution

Vitamin and trace-element solution were required for microbial growth in artificial waste water and kept in stock at 4°C.

Table 6: Trace-element and vitamin solution used for artificial waste water [38].

Trace-element solution		Vitamin solution	
Compound	**Concentration [g/L]**	**Compound**	**Concentration [mg/L]**
Nitrilotriacetic acid	1.5	Biotin	2.0
$MgSO_4 \cdot 7H_2O$	3.0	Folic acid	2.0
$MnSO_4 \cdot 1H_2O$ or	0.45	Pyridoxinhydrochloride	10
$MnSO_4 \cdot 2H_2O$	0.5	Thiaminhydrochloride	5.0
NaCl	1.0	Riboflavin	5.0
$FeSO_4 \cdot 7H_2O$	0.1	Niacin	5.0
$CoCl_2$ or	0.1	DL-Calcium pantothenate	5.0
$CoCl_2 \cdot 6H_2O$	0.183	Vitamin B12	0.1
$CaCl_2$ or	0.075	4-Aminobenzoic acid	5.0
$CaCl_2 \cdot 2\ H_2O$	0.1	Lipoic acid	5.0
$ZnSO_4$ or	0.1		
$ZnSO_4 \cdot 7H_2O$	0.178		
$CuSO_4$ or	0.0064		
$CuSO_4 \cdot 5H_2O$	0.01		
$AlK(SO_4)_2$ or	0.01		
$AlK(SO_4)_2 \cdot 12H_2O$	0.0184		
H_3BO_3	0.01		
$Na_2MoO_4 \cdot 2H_2O$	0.01		

For a stock of 1 L, firstly, nitrilotriacetic acid is dissolved in 750 mL deionized water and then brought to pH 6.5 by adding KOH.

Artificial waste water

Two types of artificial waste water have been used. Artificial waste water type one (AWW 1) consisted of 50 mM phosphate buffer supplemented with 10 mM acetate as sole carbon source. Its total atomic sulfur content was 212 µM. On the opposite, artificial waste water of the second type (AWW 2) was based on carbonate buffer and more diverse with regards to its carbon sources. It was supplemented with 2.5 mM sodium acetate, 0.42 mM glucose, 0.5 mM D-ribose, 3.33 mM glycine and 2 mM cysteine. Its total atomic sulfur content was >2000 µM. Both types of AWW were supplemented with 12.5 ml/L vitamin and 12.5 ml/L trace element solution.

2.3. Materials

Many of the materials were used either for preparing electrodes, creating electrode materials or building reactors (Table 7).

Table 7: List of materials used in this study.

Material	Supplier
Activated carbon Zorflex FM10	Chemviron Carbon
Activated carbon Zorflex FM100	Chemviron Carbon
Banana jack, 2 mm	Stäubli Multi-Contact
Carbon felt 43201	Alfa Aesar
Copper mesh, 800 µm mesh width, 250 µm Ø	GKD
Copper wire 1000 and 500 µm Ø	Chempur
Epoxy resin + hardener GL 1	R&G GmbH
Epoxy resin + hardener GL 2	R&G GmbH
Gold wire 100 µm Ø	Chempur
Graphite rods and sheets	CB Graphite
Laboratory connector 2 mm	Stäubli Multi-Contact
Lacquer, one compound, blue	Brilliant
Layered Corrugated Carboard	-
Leit-C conductive carbon cement	Neubauer Chemikalien
MetaDi polishing fluid	Bühler
Micro-mesh polishing cloth	Micro-Surface Finishing
Monocrystalline diamond particles	Bühler
Patch clamp glass cappilaries	WPI
Platinum wire, 500 µm Ø	Chempur
Pomelo	Supermarket
PTFE tube, 2 mm ID and 4 mm OD	Bola
Sandpaper	Hornbach
Shrinking tube	HellermannTyton
Stainless-steel V2A 500 µM Ø	Chempur/Goodfellow
Transition piece for tubing	neoLab
Tygon® LFL tubing ID 2.79 mm	Ismatec

2.4. Electrode fabrication and modification

2.4.1. Standardized cathode backbones

A universal cathode backbone was used for cathode material performance studies. It was made from a graphite block of 1 cm x 1 cm x 0.5 cm and endued with a drilled pocket to pressure connect a 0.5 mm diameter stainless steel wire (Goodfellow Cambridge Limited, England). The backbone was painted with one component lacquer (Brilliant, Germany) and dried over night to become insulated. A round area of 0.5 cm diameter was smoothed with emery to provide a spot for mounting the desired electrode materials with approximately 50 µL Leit-C conductive

carbon cement (Leit-C, Neubauer Chemikalien). The stainless-steel wire was insulated using shrinking tubes.

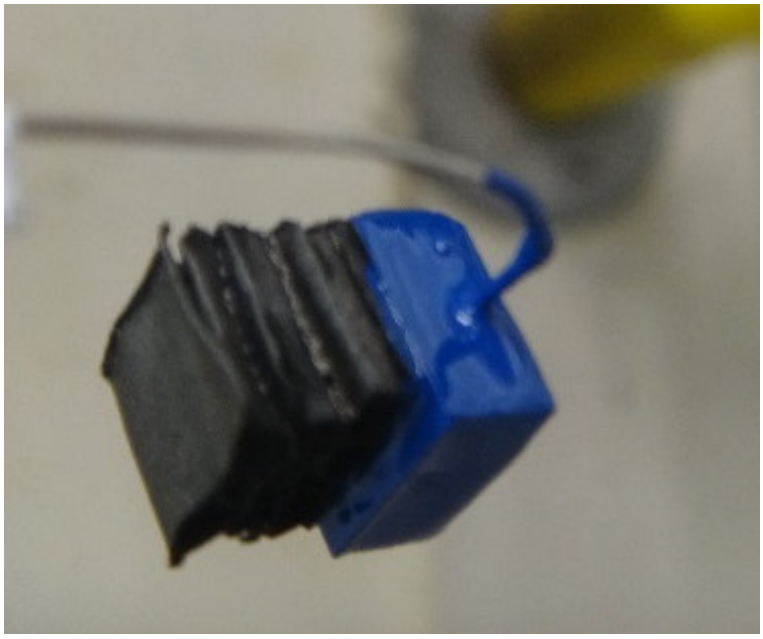

Figure 4: Electrode backbone mounted with layered corrugated carbon, yet without insulated stainless steel current collector.

2.4.2. Carbonization

The Carbolite MTF CF 12/38 furnace was used to carbonize materials in nitrogen gas atmosphere. A quartz crystal tube was inserted into the oven with samples placed on a porcelain carrier. The tube was adjusted in the oven to position the samples in the region of homogeneous heat distribution. The tube was purged with nitrogen for half an hour before heating and during the carbonization procedure. Heat was increased to 800 °C with a ramp of 5°C/s and held for 2 hours. Nitrogen was further sparged until the temperature dropped below 100 °C. After cooling the samples were taken out, visually examined, weighted and stored.

2.4.3. Nitric acid treatment

Electrode materials were placed 40 minutes in boiling concentrated nitric acid (65%) and neutralized afterwards in deionized water. This was done under reflux under the fume hood while precautions were taken as nitrogen oxides formed.

2.5. Material characterization methods

2.5.1. Electrode resistance by four-wire measurement

Ohmic resistance of electrodes was measured by four-wire sensing with a Keithley digital multimeter. When measuring resistances below 100 Ω, four-wire sensing was preferred as it eliminates errors originating the contacting resistance. Two probes were connected to the current collector of the electrode and the other two probes were attached to the electrode material with light pressure. The probes were applied three times at random spots at each respective accessible electrode surface to calculate the average resistance. Five sides were measured for three-dimensional materials and only one side was measured for two-dimensional materials (Figure 5).

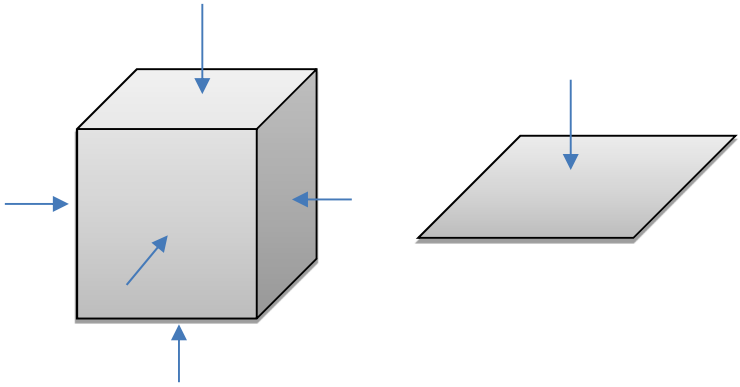

Figure 5: Application sides of the four-wire probe at three- and two-dimensional electrode materials.

2.5.2. Confocal laser scanning microscopy

Three-dimensional electrode images were taken by the Leica TCS SPE confocal laser scanning microscope equipped with the HC PL FLUOTAR 50x/0.80 DRY objective at 500x magnification. A blue laser (480 nm) was used at low intensity (5–15%) to scan the sample with a gain of 400 and zero percent offset at 400 Hz. After the laser light was reflected by the sample, it passed the RT 30/70 beam splitter. The final image of each stack was averaged of three frames taken at a resolution of 1024 x 1024 pixels reflecting a 220 µm x 220 µm sample area. Thus, a pixel represented 215 nm x 215 nm. The pinhole was set to 0.5 airy units. The z-stack slice height was less than 1 µm.

2.5.3. Electrode surface area determination by Brunauer, Emmett and Teller

Isotherms and multipoint surface areas were estimated by the method of Brunauer, Emmett, Teller (BET) [39] using a Micromeritics Gemini V 2380. Electrode materials were prepared and measured in the sample tubes type 236-61703-00 with 0.95 cm outer diameter and 15.5 cm length resulting in a sample capacity of 2 cm^3. Samples were degassed (water removal) using the VacPrep 061 at 110 °C for 60 minutes under continuous nitrogen flow. Sample preparation and unit operation were performed according to the manual.

The evacuation took place at 1333.2 mBar/min for the duration of 10 minutes. Free space and the environmental pressure p_0 were determined by the device. The equilibrium time was set to 5 s. A molecular cross section of 0.1620 nm^2 was assumed for nitrogen gas. The dewars for sample tube submersion were filled with liquid nitrogen.

The absorbed amount of nitrogen at six equidistant points between 0.05 to 0.3 p/p° was used to determine the multipoint BET surface. Adsorptive and desorptive isotherms were determined by increasing pressure from 0.25 and 0.99 p/p° decreasing backwards respectively. Isotherms were evaluated according to the UPAC [40] and BET was estimated as previously described [41,42]. The steep increase of adsorbed species at low relative pressure represents the nitrogen-monolayer formation. The presence of mesopores is indicated by a hysteresis and the absence of a horizontal absorption plateau at increase of relative pressure beyond monolayer formation. The wider the pore size distribution, the less defined the pore condensation step. Thus, a broad hysteresis indicated a wider pore size distribution within the material. The mean BET and standard deviation of a sample type was calculated from at least three independent samples. Sample tubes were cleaned and dried after use as described in the manual.

2.5.4. Contact angle measurements

The contact angle was digitally estimated from photographs of 9 µl droplets on the sample surface. The time between photographs and droplet deposition were kept constant to reduce the impact of evaporation. Measurements were performed with shades closed to avoid disturbing reflections. For each material five droplets were estimated resulting in a total of ten contact angles (Figure 6). Porous materials were considered as very hydrophilic if the droplets were completely absorbed. Drops were generated with the OCE 15EC (DataPhysics, Germany) and analyzed with the SCA 20 software package.

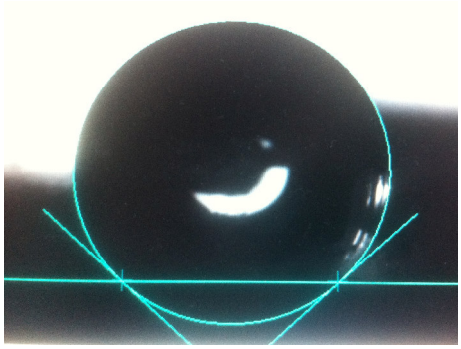

Figure 6: Graphical contact angle determination from digital images of a 9 µL drop using the SC 20 DataPhysics software package.

2.5.5. X-ray photoelectron spectroscopy

X-ray photoelectron spectroscopy (XPS) was used to determine the atomic composition of fresh and used solid state amalgam electrodes. Photoelectrons are knocked out from the sample by the high energy X-rays. They have characteristic kinetic energies that directly identify each element and chemical bond present in the sample surface [43]. The measurements were carried out on the XPS system PHI Versa Probe II (Physical Electronics, Inc., Minneapolis, USA) in high vacuum at 10^{-6} Pa. The exciting line radiation was generated by a monochromatized Al Kα X-ray source with a line width of 0.26 eV. The survey spectra ranged from 0 eV up to 1400 eV and its resolution was below 0.5 eV. X-ray spots were aimed either at the gold amalgam electrode surface or aside onto the epoxy/glass surrounding and their diameter was chosen between 50 µm and 100 µm. For analysis of the atom ratios in the sample, the photoelectron peak areas were calculated after Shirley background correction. The peak fitting was performed using MultiPak Software (Ulvac-Phi, Inc., Minneapolis, USA). The measurements and calculations were performed by Mr. Leander Loewenthal at the HAWK University of Applied Sciences and Arts in Göttingen.

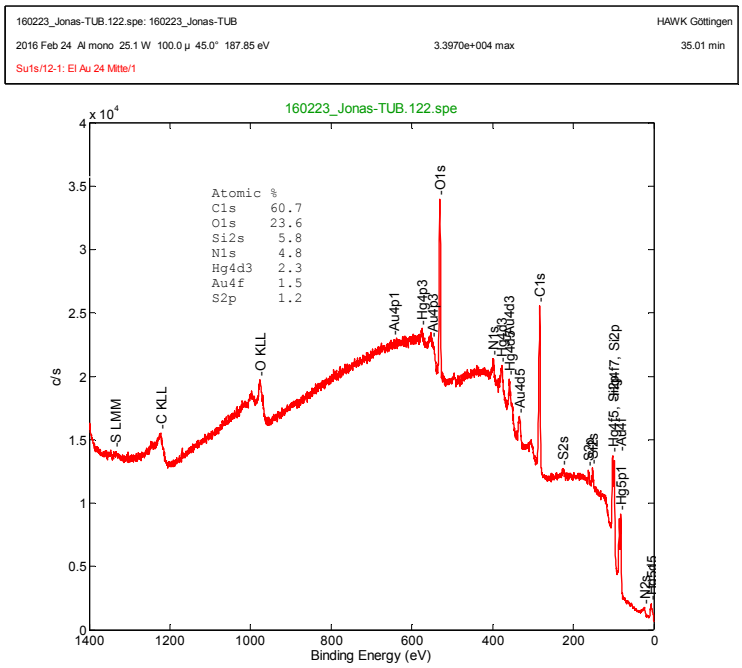

Figure 7: Example report of the XPS spectra with calculated atomic % of the 100 µm Ø gold amalgam region of JMSA_EL_AuHg_24.

2.6. Electrochemical Methods

Electrochemical methods, especially types of voltammetry, were the major tool of investigation during this study. The current-potential-curves where compared amongst different cathode materials, to estimate their performance for MFC-applications and constantly positive poised graphite electrodes allowed enrichment of anode respiring electroactive organisms. The negative polarization of a polished gold surface allowed to deposition of mercury from a mercury nitrate solution. The constant positive polarization of the derived amalgam electrode allowed to specifically enrich analytes of interest and the controlled shift from a positive to a negative potential allowed the controlled stripping and detection of those respective analytes. A potential sweep performed on electroactive biofilms before and after sulfide exposure served the qualitative assessment of the redox processes. An alternating voltage method was used to determine the electrolyte resistance of the system.

All these powerful electrochemical techniques required the precise control of the potential of the electrode of interest, whether it was for analytical or manufacturing purposes. This was realized by a three-electrode setup, consisting of a working electrode whose electrochemical processes are of interest (WE), a counter electrode (CE), a reference electrode (RE) and

potentiostat. The potentiostat controls the electrical current between the working electrode and the counter electrode with respect to the reference electrode.

The reference electrode used throughout during this study was based on the second order silver/silver-chloride system (from here on referenced to as vs. Ag/AgCl) with a potential of +197 mV vs. NHE using saturated KCl (Meinsberger, Germany) [21]. It is connected to the potentiostat via a high ohmic input resistance, to avoid any current flow through the reference electrode.

The potentiostat controls the potential by inducing a current between the WE and the CE. The potentiostat constantly compares the potential between the RE and the WE to a desired set-value and adjusts the induced current accordingly. The CE material was chosen to be chemically inert not to interfere with the reaction of interest at the WE.

The current flow between WE and CE causes a voltage drop according to Ohms law. This so called iR-Drop leads to an actual WE potential that deviates from the desired set point, and thus misleading results. Its value is the electrolyte resistance between RE and WE multiplied with the current. At currents of several mA, a few ohms of electrolyte resistance can cause a deviation of several mV, and therefore, the electrochemical setup needs careful consideration, to reduce these respective deviations. This was done by reducing the distance between the WE and RE and by using to the EC-Lab inbuild IR-drop compensation.

2.6.1. Chronoamperometry

For chronoamperometry (CA) a constant potential E_i is applied to the WE while the respective current flow is recorded. It was performed in a three-electrode setup and was used for three different purposes:

1) The enrichment of anode respiring bacteria at +200 mV vs. Ag/AgCl,
2) detection of EAB's sulfide shock response and
3) the measurement of cathodic currents at −200 mV vs. Ag/AgCl under mass transport limitations (Figure 8)
    a. for comparison of electrode materials and
    b. for comparison of capillary effects while varying spatial electrode position with respect to the electrolyte.

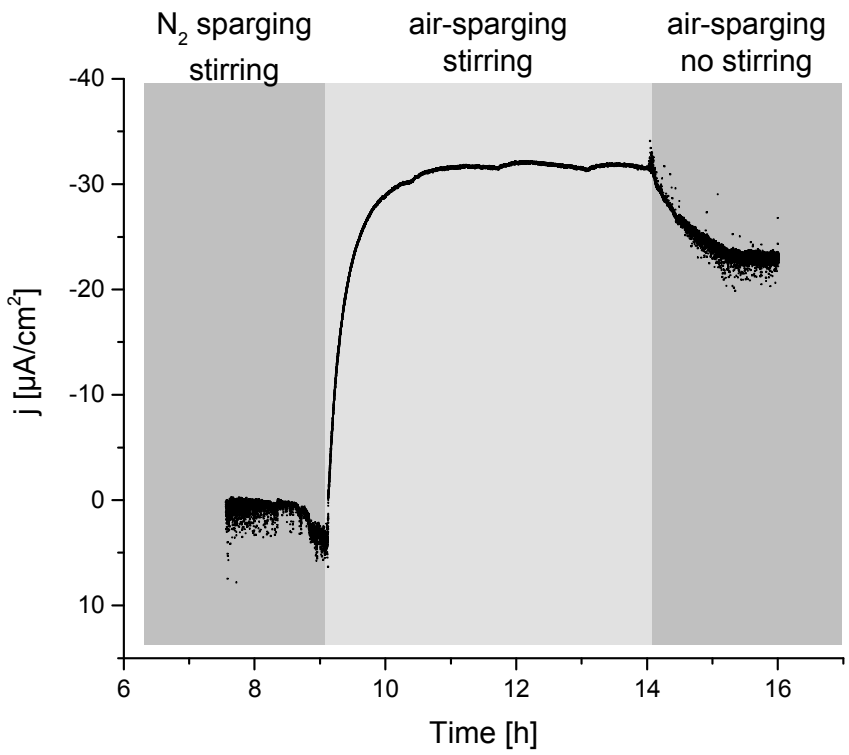

Figure 8: Cathodic current of negatively poised platinum electrode (-200 mV vs. Ag/AgCl) in response to nitrogen sparging, air sparging and reduced convection. The limiting current in absence of stirring, indicating the presence of mass transport limitations. Supporting electrolyte: 50 mM phosphate buffered saline at room temperature.

2.6.2. Cyclic voltammetry

Cyclic voltammetry (CV) involves the change of electrode potential over time in form of a saw tooth function. It is a voltammetric method where the current is recorded in response to the shift in potential resulting in the typical plot which is called cyclic voltammogram. The starting potential (E1) of the working electrode is usually set to a region with negligible current flow, and thus at a potential where the chemical species of interest neither oxidizes nor reduces. The voltage is swept in a linear manner to a second voltage (E2) where the electrode scan then is reversed back to its original value. The scan rate is usually denoted in mV/s and given the small Greek letter Nu ν. The region between E1 and the vertex potential E2 is called potential window and is selected in such a way that the redox processes of interest are likely to occur within [44]. The method is extensively described in fundamental electrochemistry text books e.g. written by Harmann and Vielstich [21], more specific in voltammetry text books written by Compton and Banks [44] and in methodology papers for analysis of electroactive Biofilms [45–47].

Cyclic voltammetry was performed in a three-electrode setup and used

1. to determine the redox activity of a newly developed universal cathode backbone and copper mesh reinforced cathodes,
2. to derive less transient linear sweeps of high capacitive cathode materials to compare their polarization curve,
3. to determine electrode capacity,
4. to assess redox activity of sulfide and sulfide exposed electroactive biofilms during turnover and non-turnover conditions at graphite electrodes,
5. for cathodic stripping of sulfide species (calibration thereof will be described in later sections).

The scan rate was adjusted as required in the experiments as will be denoted in the respective chapters.

2.6.3. Capacity determination

Capacity is defined as the correlation between the amount of charge a material can hold at a certain applied potential and it is measured in Farad (1 F = 1 C/V). In Electrochemistry, capacity refers to the charge of the electrochemical double layer present at the electrode [21]. It depends on the material surface properties and the physiochemical properties of the electrolyte.

Raising the WE-potential results in negatively charged ions migrating to the electrode thereby charging the electrochemical double-layer. This results in anodic capacitive currents. In contrast, when the WE is shifted to a more negative potential, positive charge will migrate to the WE. Then electrons flow in the direction of the WE and result in cathodic currents. If during capacitive charge movement, no other electron transfer reactions are present, the capacity can be determined by cyclic voltammetry.

It is determined by the capacitive charge dQ_C [C] at an incremental change in electrode potential dE [V].

$$C = \frac{dQ_c}{dE}$$

For a linear voltage scan, dQ and dE can be substituted by the scan rate.

$$C = \frac{I_C \cdot dt}{v \cdot dt} = \frac{I_c}{v}$$

Hereby, I_C is the capacitive current and dt the incremental change in time [s]. Usually, the current response I during a linear sweep is the combination of capacitive and faradaic currents.

$$I = I_f + I_c$$

To determine capacity, it is required to choose a potential window in absence of faradaic currents and no chemisorption [21] are present $I_f \rightarrow 0$. For the oxygen reduction at platinum the chemisorption becomes less visible at scan rates below 50 mV/s and faradaic currents become negligible at low oxygen overpotentials. Under these conditions the capacitive currents become predominant:

$$I = I_C = C \cdot v$$

In this case the capacitive currents at a given potential step can be plotted against the scan rate and the slope gives the differential double layer capacitance [21,48]. The capacity was then related to respective material characteristic, such as the mass, the geometric surface area or BET-surface [49].

2.6.4. Electrolyte resistance

Electrolyte resistance was determined during high frequency alternating potential measurements between 100 and 200 kHz at a sine amplitude of 20 mV.

2.7. Analytical Methods

2.7.1. ICP-OES for determination of elemental composition

The elemental composition of samples was analyzed by inductively coupled plasma optical emission spectrometry (ICP-OES) done with the Vista-MPX (Varian, Germany). Each element was detected at five different wavelengths. The device was calibrated by 10 mg/L ICP single standard solutions (Alfa Aeser, Germany). ICP-OES measurements were performed by Ms. Christiane Schmidt at the Technische Universität Braunschweig.

2.7.2. HPLC for lactate and acetate measurements

The concentrations of carbon compounds such as lactate and acetate were estimated by HPLC. Samples were filtered prior to measurement (0.45 µm cellulose acetate syringe filter, Rotilabo) and run in 2.5 mM H_2SO_4 at 25 °C at a volume flow of 0.5 mL/min through a Hyper-REZXP Carbohydrate H+8 mm (S/N:026/H/012-227) column. The analytes were detected by change of the solvent's refraction index (Spectrasystem P4000, Finnigan Surveyor RI Plus Detector, Fisher Scientific, Germany). The Chrome Quest software estimate the peak height,

the calibration curves and calculated the respective concentrations. The retention time of lactate was 16.95 min with standard curve coefficient of 5.9 10^{-6} mmol/peak-area and an r^2 of >0.999. The retention time of acetate was 20.43 min with a standard curve coefficient of 1.3 10^{-5-} mmol/peak-area and an r^2 of >0.998.

2.7.3. Methylene Blue method for sulfide determination

The methylene blue method was used to spectrophotometrically determine hydrogen sulfide in artificial waste water in the range of 3–1200 µM at 670 nm. The method of Cline [50] was adapted by reducing sample size for probing limiting volumes of bioelectrochemical reactors and to cope with the phosphate buffer system of artificial waste water.

The principle of the methylene blue reaction is the dimerization reaction of two N,N-Dimethyl-p-phenylenediamine molecules in a 2:1 stoichiometry. Hereby sulfide splits off ammonia in presence of Iron (III) chloride in acidic media (Figure 9).

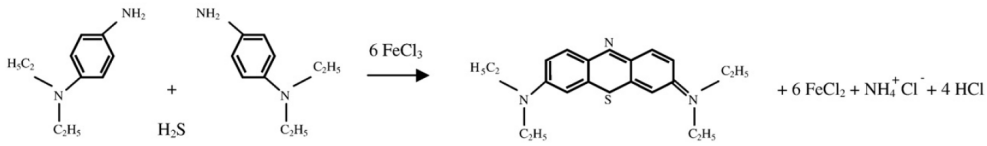

Figure 9: Scheme of Methylene blue formation by Hughes, Centelles and Moore [51].

The π-system of methylene blue has its absorbance maxima at 670 nm. In presence of excess reagents, sulfide will react throughout to methylene blue. This allows spectrophotometrically determination by absorbance measurements.

The method of this study is based on the initial work of Fogo and Popowsky [52] and Cline [50] from the mid-20th century. Fogo and Popowsky entrapped sulfide in a gas washing bottle prior to analysis. The outgassing step allows to investigate any sample matrix but requires extended experimental effort. Still, their principle is used in an adapted form as the German DIN standard (DIN 38405) to estimate sulfides from waste water samples. Cline abdicated the prior outgassing/gas entrapment step and used fresh water samples from anoxic marine basins directly. This method required less experimental expenditure while still being resistant to salt effects.

In this study, the method of Cline was adapted for 5 mL samples of buffered artificial waste water. Small volumes were used to account for the limited size of the bioelectrochemical reactor systems. The method was adapted by changing the stock solutions pH, allowing proper

subsequent sample matrix acidification, a 0.45 µm filtering step to avoid solid particles to interfere with absorption and a general change of the reagent concentration and later dilution steps to respect Beers law for the required sulfide concentration ranges.

A stock of 1 L 1% (m/m) zinc acetate solution ($ZnAc \cdot 2H_2O$, MW = 219.50 g/mol; p.A., 10 g in 1 L distilled water, CAS 970-45-6; Carl Roth) and 100 ml 12% (w/w) sodium hydroxide solution (NaOH, MW = 40.0 g/mol, c.P., 12 g in 100 mL in distilled water) was prepared. The basic zinc acetate solution was made by mixing 250 mL of 1% zinc acetate stock solution and 20 mL of 12% sodium hydroxide stock solution. N,N-Dimethyl-p-phenylenediamine sulfate salt (98%, Sigma Aldrich) and iron (III) chloride ($FeCl_3 \cdot 6H_2O$, MW = 270.33 g/mol, c.P., Carl Roth) were diluted in 6 M HCl. Three different diamine stock solutions (A, B and C) were prepared for three respective sulfide concentration ranges (Table 8).

Table 8: Diamine mix concentrations of stock solution A, B and C.

	Range [µM]	**Diamine [mg/50 mL]**	**$FeCl_3 \cdot 6H_2O$ [mg/50 mL]**
A	3–40	200	300
B	40–250	800	1200
C	250–1000	2000	3000

No special care needs to be taken in the preparation of the reagents. Deviations up to 5% in the concentrations given are allowable [52]. If the diamine used produces a dark colored solution, a fresh supply should be obtained. First mix the solutions, then weight solids then wash solids into Schott bottles. All preparation steps and experiments were performed at room temperature. For storage stock solutions and samples were kept in a dark place at 4 °C.

All work with sulfide was performed with respective safety precautions under the fume hood. Exposure to oxygen was avoided whenever possible. Sulfide stocks were freshly prepared from sodium sulfide ACS 98% ($Na_2S \cdot 9H_2O$, MW = 240.18 g/mol, CAS 1313-84-4, Carl Roth) in anaerobic solvent. Sodium sulfide crystals were washed with deionized water to remove possible oxidation products (indicated by yellow color), dried by tissue paper and grinded to powder prior to use. Anaerobic artificial waste water supplemented with 10 mM DL-lactate was used as solvent for dilution to account for possible matrix effects.

For calibration, the sulfide stock was diluted accordingly. A dilution volume of 5 mL was then mixed with 1 mL basic zinc acetate to precipitate the white milky zinc-sulfide. Afterwards, 400 µL of diamine stock were added and mixed throughout. Then the sample was incubated at room temperature for 20 minutes. Prior to absorbance measurements, samples in range A remained undiluted, samples of concentration range B were diluted 4:5) and samples of

concentration range C were diluted 1:50. After 20 minutes of incubation the absorption was measured at 760 nm (USB200+ with DH-2000 light source, Ocean Optics) to estimate the respective calibration curves (Figure 10).

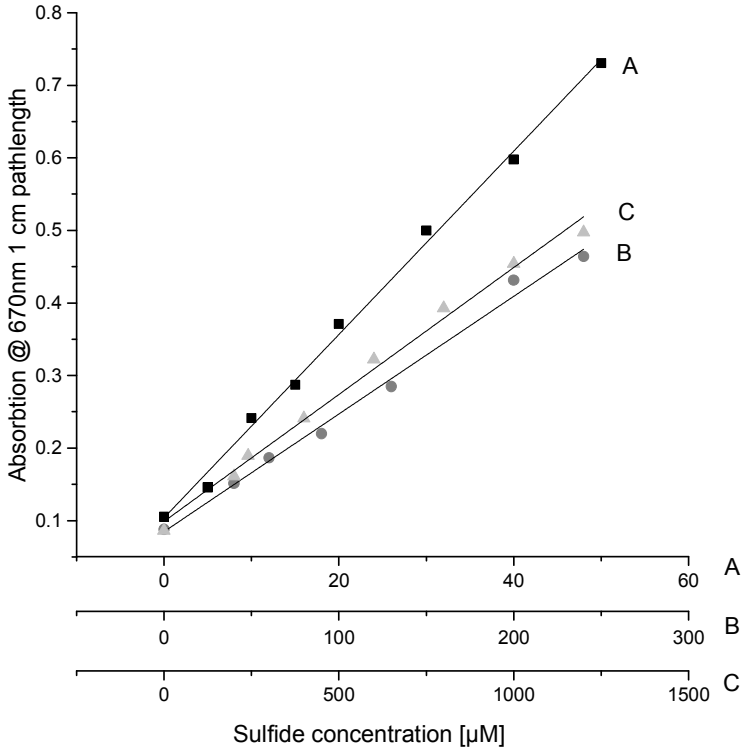

Figure 10: Methylene blue calibration for three different concentration regimes performed with the respective stock solutions: A) 3–40 µM B) 40–240 µM C) 240–1000 µM.

Storage of the precipitated zinc sulfide samples resulted in no significant impact on later concentration determination (Figure 11). The results suggest that the zinc-sulfide precipitate could be stored in the fridge for at least 7 days and probably even longer if frozen.

Accordingly, for sulfide estimation in artificial waste water, 5 mL 0.45 µm filtered samples were mixed with 1 mL basic zinc acetate solution, later processed as the calibration standards and measured at 670 nm. Given a maximum sulfide concentration of ~ 200 µM of AWW 1 at full sulfate conversion range A) and B) were used in most instances. The proper diamine stock for sample preparation was chosen based on the previous result in experiments with linear increasing sulfide concentrations. Concentrations were then calculated based on the calibration curves.

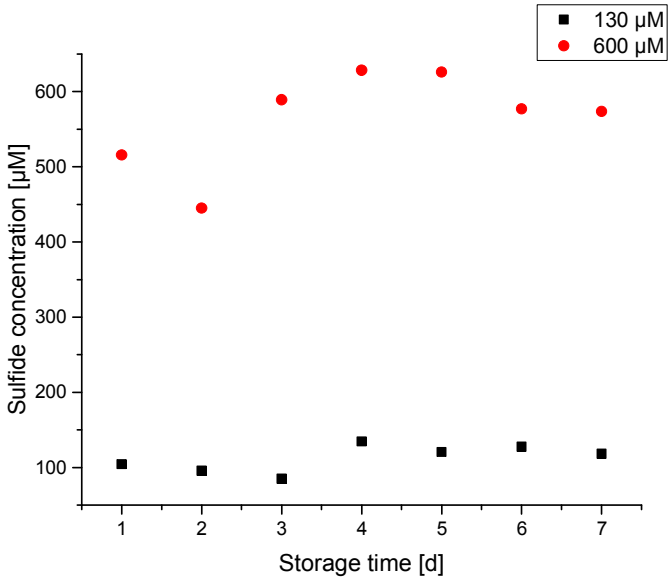

Figure 11: Influence of the storage time of zinc sulfide precipitated samples at 4°C prior to the methylene blue reaction on the respective concentration.

2.7.4. Field measurements

The devices were checked and calibrated if necessary prior to the measurements. Oxygen was determined by the oxygen sensor CellOx 325 (WTW, Germany), conductivity and temperature were measured by the conductivity sensor TetraCon 325 (WTW, Germany), pH was determined by the pH electrode SenTix® 24 equipped with an additional temperature sensor. The electrodes were either attached to the digital multimeter 340i or the 340 (WTW, Germany). The redox potential was determined by the redox electrode GE 105 attached to the GPHR 1400A (Greisinger, Germany). Sampling sites with liquid in motion were sampled by determining the physiochemical parameters of 9 subsequent 10 L samples taken within 10 minutes. Sites with open-air stagnant liquids were sampled at the surface and 10–30 cm underneath the water level in 9 replicates each. Sensors were cleaned after each sampling site by rinsing with deionized water. If the oxygen probing was done in the sediment, the sensor was required to be intruded carefully to prevent damage to its membrane and faulty measurement data.

2.8. Microelectrode fabrication and calibration

The fabrication of gold-amalgam microelectrodes required the gold wire embedding, proper polishing, contacting, mercury plating and a final calibration.

2.8.1. Electrode fabrication and polishing

A 100 µm gold wire was placed in a glass capillary. The capillary was filled with epoxy (Epoxy resin L and hardener GL 2, R&G GmbH) and dried for 2 days at glass transition temperature of 90°C.

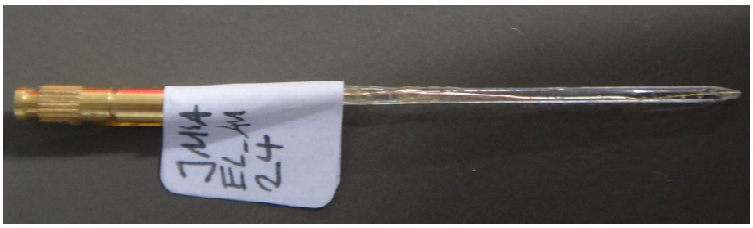

Figure 12: Gold wire within a glass capillary embedded in epoxy and attached to a 2-mm terminal banana jack.

The electrode was then grinded and polished with circular motions for one minute at each step. Sanding paper was used in the following order for coarse grinding: P240 (52 µm), P400 (35 µm) and P600 (25 µm). Micro-mesh polishing cloth was used in the following order for medium coarse grinding and polishing: 1500 (21 µm), 1800 (14 µm), 2400 (11 µm), 3200 (8.4 µm), 4000 (6.35 µm), 6000 (4.23 µm), 8000 (3.18 µm) and 12000 (2.12 µm). The polishing was continued with 1 µm monocrystalline diamond particles (MetaDi II, Buehler) on hard polishing cloth (TexMet C, Buehler) and finished with 0.25 µm monocrystalline diamond particles (MetaDi II, Buehler) on soft polishing cloth (MicroCloth, Buehler). Between steps and after polishing the electrode was cleaned with isopropanol and water and afterwards dried by pressure air to avoid displacement of polishing particles from coarse to fine polishing. At the end of the polishing process the polishing cloths were cleaned with water and dried with pressure air. The electrode was then soldered to a shielded coaxial cable or a 2-mm banana jack.

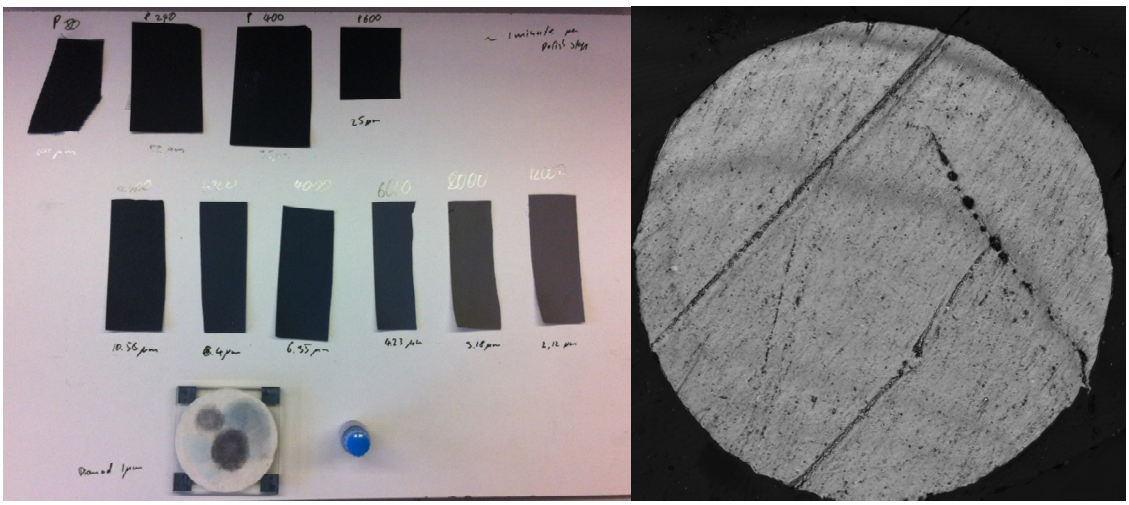

Figure 13: Placement of micro-meshes and cloth on a wooden board for manual polishing of electrode surfaces (left). Polishing result of a 100 µm gold electrode imaged by confocal laser scanning microscopy (right).

2.8.2. Mercury plating

Polished gold electrodes were plated with mercury for 4 minutes at a potential of –100 mV vs. Ag/AgCl in slightly acidified 0.1 mol/L $Hg(NO_3)_2$. The solution was continuously stirred and sparged with nitrogen to remove oxygen before and during deposition. The potential/current curve was used to determine the charge and the amount of plated mercury per time.

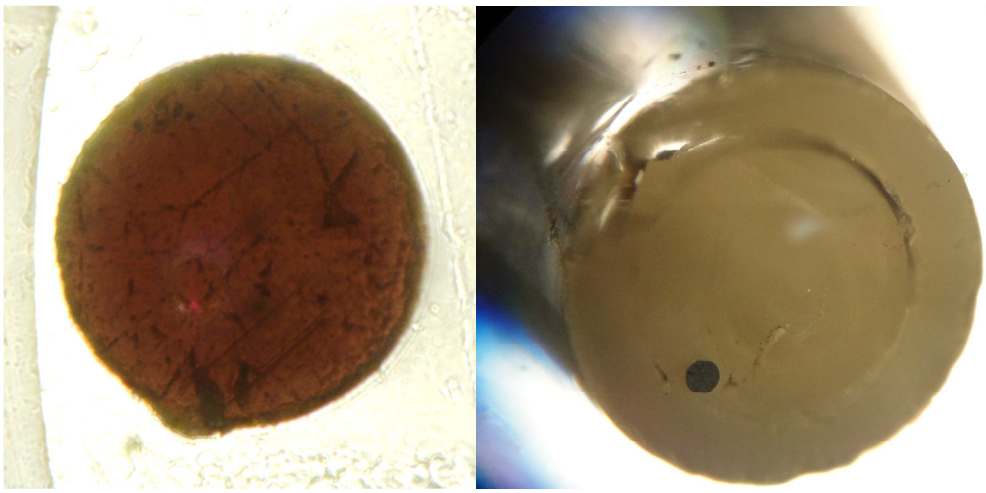

Figure 14: Polished gold electrode surface, Ø 100 µm(left). View on the amalgam electrode after deposition embedded into epoxy resin within a glass capillary (right, black dot).

The deposition height was approximated by calculating the plated mercury volume from the transferred charge assuming a cylindrical volume. Per atom of mercury two electrons are transferred (z = 2). To evaluate the deposition-process, the height of a cylindrical deposition of 1 millicoulomb charge was calculated.

$$Hg^{+2} + 2e^{-} \leftrightharpoons Hg$$

Based on faradays law

$$Q = nFz$$

With the Faraday-constant F = 9.65485 10^4 C/mol the charge of 0.001 C leads to

$$n = \frac{Q_{Hg}}{zF} = \frac{0.001\ C}{2 \cdot\ 9.65\ 10^4 \frac{C}{mol}} = 5.18\ 10^{-9}\ mol$$

deposited mercury. Based on the quantity of moles and the molecular weight of mercury (MW = 0.2006 kg/mol) the mass could be calculated:

$$m = nM =\ 5.18\ 10^{-9}\ mol \cdot 0.2006\ \frac{kg}{mol} = 1.04\ 10^{-9}\ kg$$

Based on a density of (ρ_{Hg} = 13534 kg/m^3) the volume could be calculated:

$$V = \frac{m}{\rho} = \frac{1.04\ 10^{-9}\ kg}{13534\ \frac{kg}{m^3}} = 7.68\ 10^{-14}\ m^3$$

which was used together with the surface area of the 100 µm diameter gold electrode

$$A_{100\mu m} = r^2\pi = (50\ 10^{-6}m)^2\pi =\ 7.85\ 10^{-9}\ m^2$$

to approximate the deposition height as that of a cylinder:

$$h = \frac{V}{A} = \frac{7.68\ 10^{(-14)}m^3}{7.85\ 10^{-9}m^2} = 9.78\ 10^{-6}\ m = 9.78\ \mu m$$

Thus, if mercury equivalent to 1 mC of charge is plated, the deposition height will be at least 9.78 µm. Since the deposition will have a spherical shape, it might be even higher compared to the cylindrical approximation.

2.8.3. Sulfide calibration

Cathodic stripping voltammetry was performed in three steps: Firstly, a 20-s conditioning at −0.9 V vs. Ag/AgCl, secondly, a 2-s deposition step at −0.1 V vs. Ag/AgCl and thirdly, a cathodic sweep at 1 V/s. All experiments were performed in a Faraday cage and with shielded electrodes to avoid inductive interferences disturbing the nanoampere signal.

The baseline corrected sulfide stripping peak current I_P was correlated with concentration (Figure 15). Its height and position was determined using OriginLab's Gaussian quick peak fit function of the "peak analysis tool" gadget. The region of interest (ROI) was set to −0.4 to −0.9 vs. Ag/AgCl. The baseline was set as the lowest reductive current in this range. This approximation allowed to handle large datasets in a short time. If the baseline was subject to tilting during experiments, it was adjusted manually.

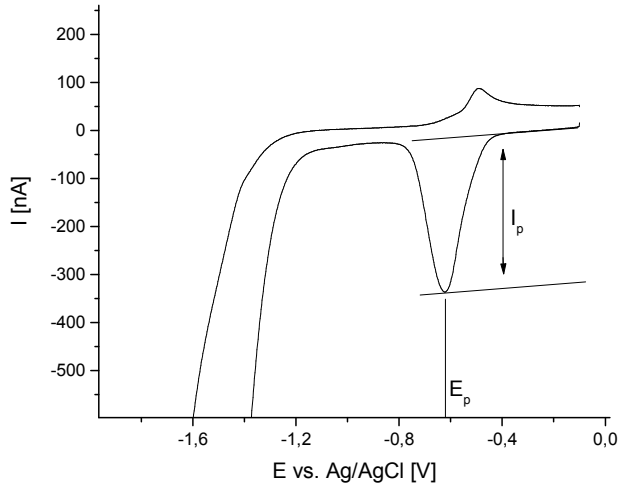

Figure 15: Sulfide peak current (I_P) determination in artificial waste water supplemented with ~200 µM sulfide at room temperature. I_P is the absolute peak current minus the baseline. This and all later microelectrode experiments were performed in a Faraday cage.

2.9. Biological methods

2.9.1. Biological anodes

Within this work electroactive biofilms (EAB) were used for three different applications:

1. to compare sulfide production between electroactive biofilms and sewer slime.
2. to evaluate the resistance of electroactive organisms towards high sulfide concentration.

3. for the application, as biological anodes in Microbial Fuel Cells to compare floating and submersed cathodes.

The EABs were grown in anaerobic AWW 1 on polarized graphite electrodes. The potential was chronoamperometrically controlled by a potentiostat (VMP3 or MPG2, Biologics) using a three-electrode setup. The plain WE consisted of a cylindrical or square shaped graphite slab (CP-Graphite).

For sulfide emission comparison and sulfide shock impact detection, the electrodes were made from cylinders of 1 cm Ø and 3 cm length resulting in a surface area of 22 cm^2 (Figure 16).

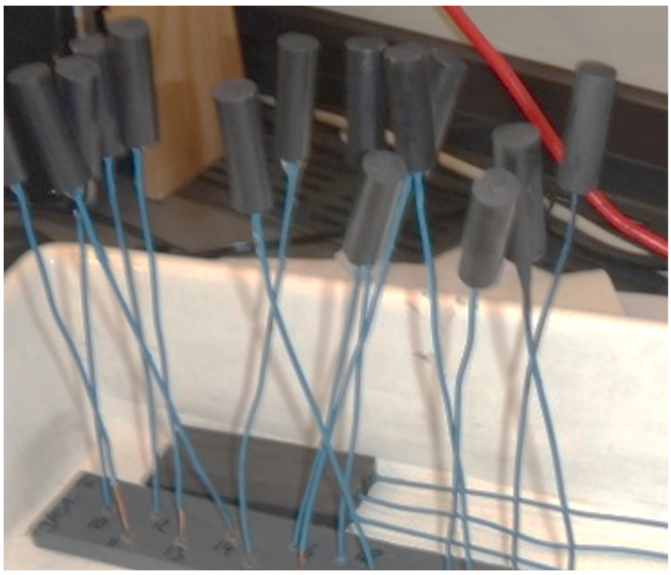

Figure 16: Cylindrical graphite electrodes with a diameter of 1 cm, length of 3 cm attached to a 0.5 mm diameter copper wire insulated with shrinking tube.

The biofilms were cultivated in 300 mL air tight multi-neck round bottom flask (Figure 17) filled with 250 mL anaerobic AWW 1.

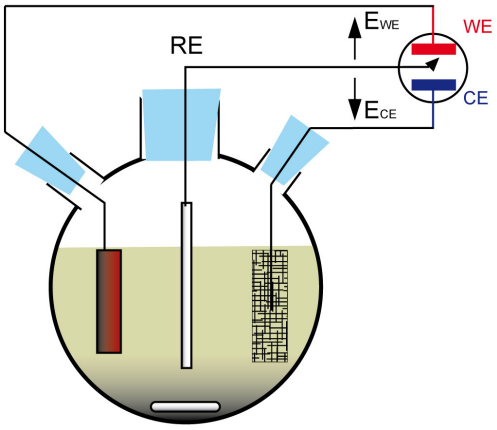

Figure 17: Illustration of anaerobic potentiostatic controlled enrichment of electroactive biofilm. It is grown on a graphite working electrode (WE) within an air tight 300 mL multi neck round bottom flask equipped with a Ag/AgCl reference electrode (RE) and a stainless-steel mesh counter electrode (CE). Magnetic stir bar at the bottom of the flask induces convective mass transport.

In contrast, for the MFC application, a square-shaped graphite blocks of 1 cm × 1 cm × 7 cm were used instead and cultivated in air tight 1 L Schott bottle reactors filled with 500 mL AWW 1.

This study used only secondary biofilms from previously grown EABs as inoculum. For this purpose, the pre-grown electroactive biofilms were detached from their electrode and diluted in phosphate buffer by vortexing. The homogenized solution was then used in varying amounts for the inoculation of the anaerobic waste water in the reactor. The original inoculum originated from real wastewater.

All cultivations took place at 36 °C and under convection induced by magnetic stirring at 250 rpm. The microbial current production was recorded every 10 minutes. It usually had a bell-shaped time-current curve indicating the rate of substrate consumption and its concentration. For acetate, typically a peak current density of 1 mA/cm^2 was observed. Once the current e.g. the carbon concentration dropped to zero, media was replaced with fresh artificial waste water.

2.9.2. Batch MFC operation with submerged and air exposed cathodes

An aquarium filled with waste water was used to perform batch wise MFC experiments simulating anaerobic sewer conditions (Figure 18). Floating cathodes were placed at the air-liquid interphase either exposing the electrode material to air (exposed) or submerging it 1 cm

below the liquid layer (submerged). The top of the bioanodes was kept in 10 cm distance to the cathode bottom.

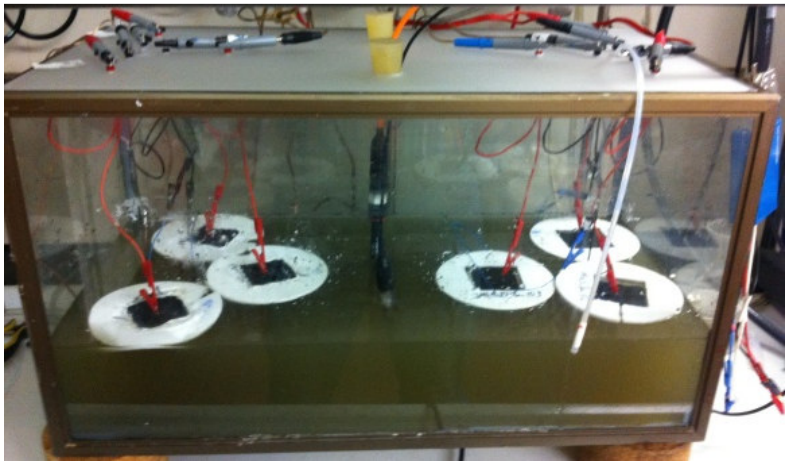

Figure 18: Microbial Fuel Cells with floating cathodes, three submerged (left) and three air-exposed (right), placed in an open aquarium (33 cm × 61 cm × 30 cm) filled with 20 L of waste water. Anode-cathode distance: 10 cm. Oxygen, pH and temperature sensor were placed in the center of the aquarium.

The cathode material was placed in the middle of a piece of Styrofoam (10 cm Ø, thickness ~2 mm) and fixed with silicone (Figure 19). The Styrofoam allows the cathode to float on liquid. The electrode conductivity was increased by using a copper mesh as a current collector in between FM 100 sheets. The copper mesh (5 cm × 5 cm) was placed in between two sheets of activated carbon cloth (5 cm × 5 cm). To further reduce the resistance, the cloth and copper mesh were stitched tightly together by a copper wire (20 cm). This resulted in a mean ohmic resistance below 2 Ohm but also in a high variability of ±60% across the surface. The bioanodes were made as described above (1 cm × 1 cm × 7 cm; 21 cm^2 accessible surface, 0.05 Ω) and connected to a copper wire (0.5 mm Ø).

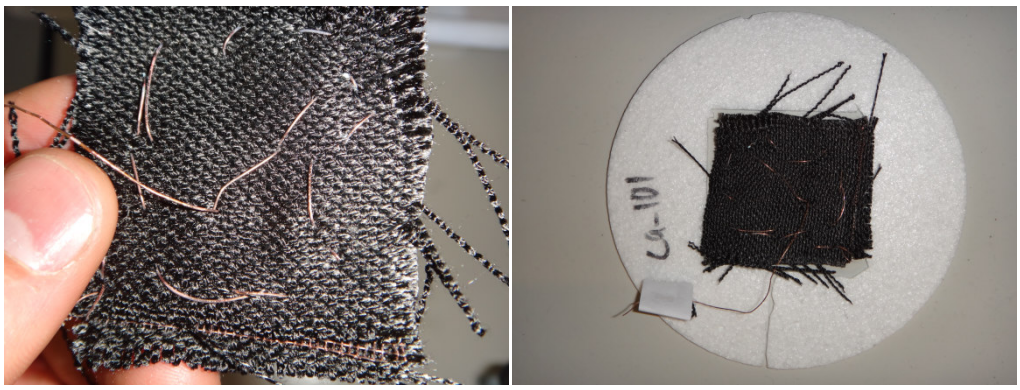

Figure 19: Floating cathode fabrication for batch Microbial Fuel Cell experiment. Activated carbon cloth FM 100 (two layers in total, 5 cm × 5 cm each) was wrapped around a current collector copper mesh and stitched to it.

Anode and cathode were connected via a 100-ohm resistor and cell voltage was measured across by a digital multimeter (DMM, Keithley 2700). Oxygen, pH and temperature were measured continuously. The analog sensor signals were digitalized and recorded by the digital multimeter. The data was stored and handled with the Keithley Excel Plugin EXCELinx every 5 minutes.

After the MFC experiment was performed for two weeks, cathodes were removed from the MFC setup, soaked three hours in 6.25% HCl and neutralized afterwards to remove the black deposits and to restore the copper's metallic shine.

2.9.3. Artificial Sewer Slime reactor

Artificial sewer slime was grown to compare its sulfide emission to that of electroactive biofilms. It was enriched on a graphite cylinder positioned on a steel pin in the center of a tubular flow reactor made of plexiglass (Figure 20). The hole for positioning was also a contacting site to serve as a WE in later potentiostatic controlled experiments.

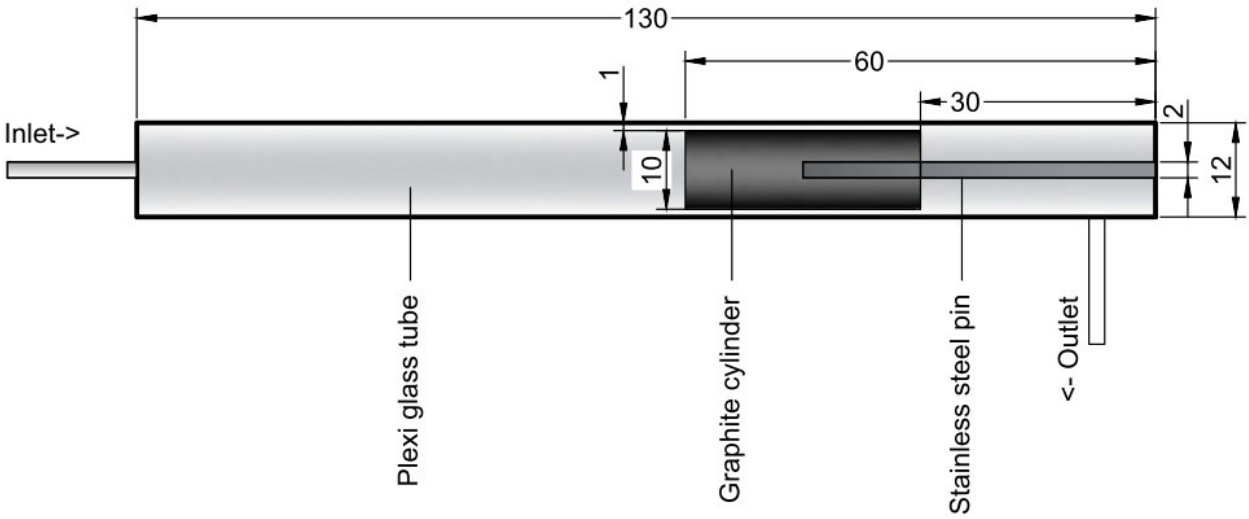

Figure 20: Dimensions of the tubular flow reactor for growth of sulfate reducing sewer slime on a graphite cylinder.

The influx of liquid resulted in a constant flow field surrounding the graphite cylinder and causing a defined shear stress on its lateral side (Figure 21).

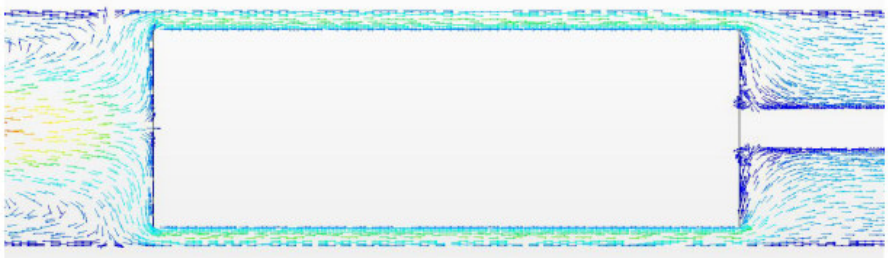

Figure 21: Flow-vector field surrounding the graphite cylinder inside the tubular flow reactor. Computational fluid dynamics calculations courtesy of Bente Thamsen. Colors indicate flow velocity - Red: high velocity; dark-blue: slow velocity.

The liquid flow was adjusted to result in a lateral shear-force of 0.2 N/m^2. It was set below the critical shear force τ_{Cr} = 0.866 N/m^2 recommended for sewer self-cleaning by the American Society of Civil Engineers (ASCE) and the Water Environment Federation (WEF) to account for low velocity sewers more endangered of sulfide corrosion. The required volume velocity of the pump was calculating starting from Newton's law of viscosity. It defines the shear-force by

$$\frac{dv}{dy} \cdot \mu = \tau$$

Here dv is the differential change of flow velocity over the distance dy and μ is the viscosity.

Firstly, the required liquid velocity was determined by rearranging the equation accordingly:

$$dv \cdot = \frac{\tau \cdot dy}{\mu}$$

As a simplification, the differential change in velocity can be expressed as 1/3 of the mean velocity of the laminar liquid flow. In addition, waste water is assumed as a Newtonian fluid with the viscosity of water at 20 °C with $\mu_{H2O} = 10^{-3}$ Ns/m^2. The value of dy can be expressed as the distance between the cylinder wall and the plexiglass tube, $r_{\frac{1}{2}}$. Given these three assumptions the equation turns into:

$$v_{mean} = \frac{\tau_{surf} \cdot r_{\frac{1}{2}}}{3 \cdot \mu_{H_2O}}$$

The electrode cylinder radius is 0.5 cm (r_2) the plexiglass tube inner radius is 0.6 cm (r_1).

$$r_{\frac{1}{2}} = \frac{r_1 - r_2}{2} = 0.05cm$$

Thus, the required mean velocity could be calculated:

$$v_{mean} = \frac{1}{3}\frac{dr_{\frac{1}{2}}\,\tau_{surf}}{\mu_{H2O}} = \frac{1}{3}\frac{0.0005\ m \cdot 0.14\frac{N}{m^2}}{10^{-3}\frac{Ns}{m^2}} = 2.3\frac{cm}{s}$$

Given both, the ring-shaped surface area A_r between the tube and the cylinder

$$A_r = \pi(r_1^2 - r_2^2) = 0.35\ cm^2$$

and the velocity v, the desired mass flow can be calculated:

$$\dot{V} = vA_r = 0.81\frac{cm^3}{s} = 49\frac{ml}{min}$$

AWW 1 without acetate, but 10 mM sodium DL-lactate was used as medium. This was done by adding either 4.42 mL of 85% or 5.73 mL 60% DL-lactate (MW = 90.08 g/mol) per 5 L stock solution.

The media was circulated by a peristaltic pump (MCP Process, Ismatec) equipped with Tygon® LFL tubing with an ID of 2.79 mm at 50 mL/min for several weeks at room temperature. Four one-liter bottles (Schott GL45, Duran) served as reservoir and were connected through a GLS 80 lid (Duran) with PTFE tubes (2 mm ID and 4 mm OD; Bola) to the peristaltic tubing via transition pieces (neoLab) (Figure 22).

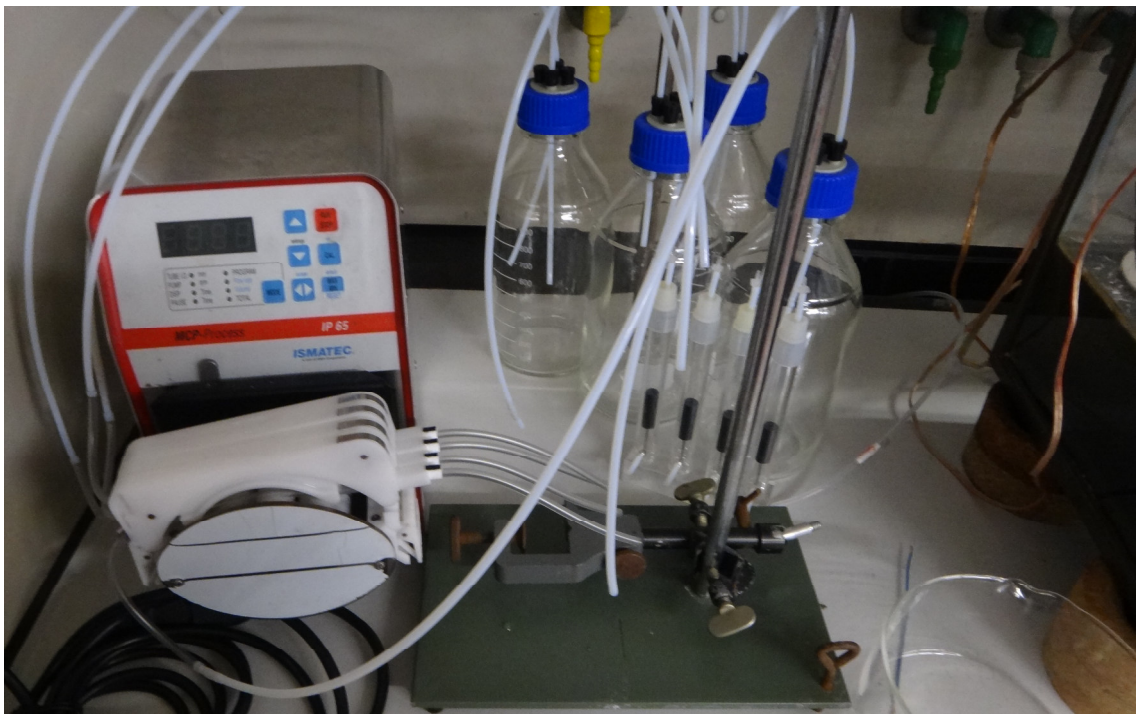

Figure 22: Empty flow-reactor. Illustrates setup of peristaltic pump, tubing, reactor and reservoirs.

The media was replaced times to time with fresh media. The sulfide concentration was estimated by the methylene blue method. Deposition started to appear on the electrodes after three days. After several weeks, a fluffy biofilm had formed and was used for the comparison between secondary electroactive biofilm with respect to their sulfide emission.

2.10. Software, scripts and automatization

Table 9: List of software used

Software	Function	Source
AutoCAD	Reactor design and illustrations	Autodesk
Chrome Quest	HPCL control, data acquisition and analysis	Thermo Fisher Scientific
EC-Lab	Potentiostat control	Biologics
Excel	Calculations	Microsoft
EXCELinx	Multimeter control	Tektronix
Fiji	Image acquisition	[53]
OriginPro	Data analysis and graphic representation	OriginLab
SCA 20	Contact angle determination	DataPhysics

Automated data processing was done with Origin Lab using Lab Talk scripts. All LabTalk-scripts written within the scope of this thesis can be found in the online repository of the author: https://github.com/JonasAndrich/LabTalk.

2.10.1. Micro attenuator controlled electrode positioning

This experimental system allowed investigation of spatial cathode positioning with respect to the air-liquid interphase (Figure 23). The micro attenuator controlled setup allowed a µm-precise movement and a coupled three-electrode setup detected small changes of the electrochemical behavior of a polarized cathode material. In addition, the electrode movements were recorded in time-lapse by a digital microscope to correlate interphase-effects with electrochemical signals. Several porous materials were investigated being attached to the universal cathode backbone while plain graphite and platinum served as flat and smooth controls.

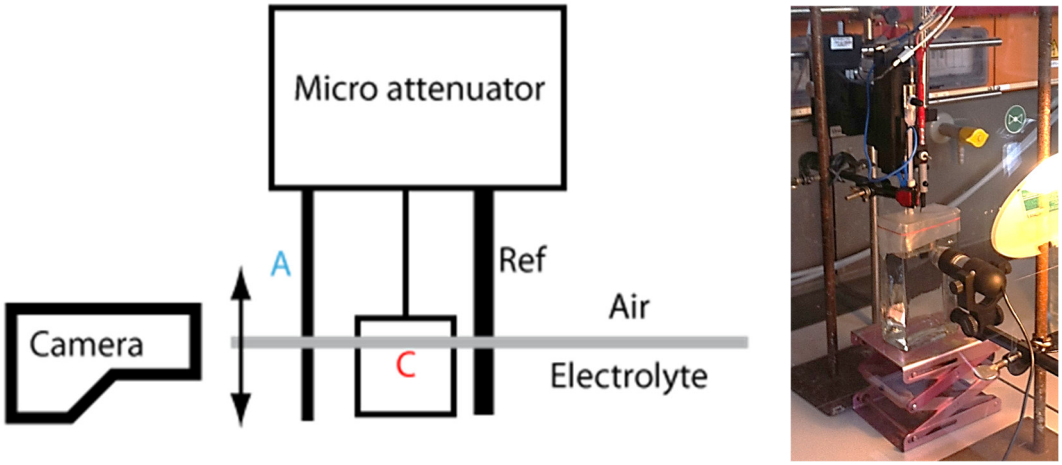

Figure 23: Micro attenuator controlled electrode positioning. Scheme and image of the experimental setup. A – Anode; C – Cathode; Ref – Ag/AgCl reference electrode.

The electrode setup was equilibrated at OCP for up to 12 hours initially. Then, the working electrode was polarized at −200 mV vs. Ag/AgCl (SE 11, Meinsberger) to achieve constant oxygen reduction. A platinum wire served as counter electrode. The current response of the WE were recorded while being slowly moved from 150 % submersion to being fully air exposed (0% submersion). The electrode was moved at 0.5 µm/s (30 µm/min) to obtain a quasi-stationary current at each electrode position except to the experiment in which the electrode speed was altered. At the respective maximum and minimum, the position was held for several hours to observe a potential lag time. The motion sequence was then reversed and repeated over several cycles.

The commands required for the ENCODER MIKE™ motorized actuator controller 18011 were placed in Microsoft® executable text files of the "*.bat"-type (Table 10). The command files were called by the potentiostat software (EC-Lab, Biologic) and send via a RS-232 serial port.

This allowed to use EC-Lab to control the electrochemical experiment and the electrode movement at the same time.

Table 10: Actuator controller commands used in executable batch files (.bat). RS-232 COM5 was used as an example port and accessed by the "echo" command. Complete list of controller commands can be found in the ENCODER MIKE™ manual.*

Command	Action
MODE COM5:4800,N,8,1,P	Setting the com port parameters
echo V000.5<ret> > COM5	Setting movement speed to 0.5 µm/s
echo > > COM5	Pulling electrode out of electrolyte
echo G15000.0 > COM5	Moving 15 mm backward to 150% submersion level

The experimental container was covered with parafilm to prevent electrolyte level changes by evaporation. Phosphate buffer at room temperature served as electrolyte. For some experiments either oil or surfactant were added. Electrodes were cleaned with isopropanol and deionized water prior to experiments.

2.10.2. Image analysis with Fiji

Digital image analysis and processing was performed by Fiji (Fiji is just ImageJ). The geometric electrode surface area was estimated using Fiji's ROI analysis toolbox according to the manual. The software was also used to visualize electrode surfaces calculating the maximum projections of stacked CLSM images. Side views were produced by virtual reslicing. Fiji was also used for making avi-videos from a set of chronological images and labelling.

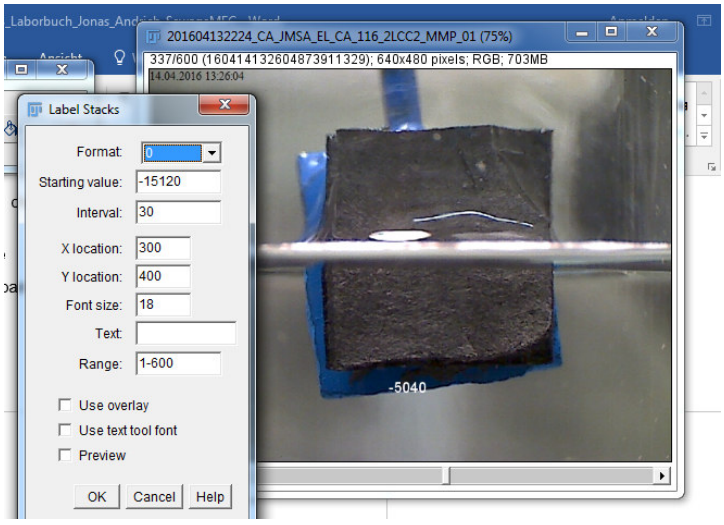

Figure 24: Fiji used for image stack labelling.

3. Evaluating existing infrastructure for Microbial Fuel Cell implementation

What sites along a city's municipal waste water and water infrastructure provide suitable conditions for placement of a Microbial Fuel Cell? The implementation of a Microbial Fuel Cell requires proper operational conditions to convert sewage's organic waste-load into energy. Thus, to answer this question a set of several physicochemical indicators was chosen to evaluate sites: Oxygen concentration, redox potential, as well as temperature, pH and conductivity. These parameters were traced at six different sampling sites over the course of four months. They are important to operate a well-functioning MFC for several reasons:

1) Absence of oxygen is required at the biological anode [54]. In contrast, high oxygen concentration is desired for oxygen reduction at the cathode [55]. Presence of even low amounts of oxygen in the anodic compartment can decrease the cell potential to zero [54] because it is the preferable electron acceptor, even for some electroactive organisms [13]. Thus, if no membrane prevents the oxygen transfer from cathode to anode compartment a distinct oxygen gradient is required.
2) The oxidation-reduction potential (ORP) summarizes the capability of a solution to either release electrons (low redox potential) or to accept electrons (high redox potential). A low redox potential indicates an environment in which organisms are craving for new electron accepting molecules. A generally high redox potential is desired at the cathode which means that it can transfer electrons to the substances within the electrolyte. The ORP even suggests what types of microorganisms could be present in a certain environment and its changes might indicate what stress those are exposed to [56]. It can be used for process observation and regulation e.g. during micro-oxygen injections for sulfide control in anaerobic digesters [57].
3) The pH influences the MFC in three important ways. Firstly, the concentration of protons and hydroxy ions influences the theoretical redox potential of the anodic and cathodic reaction [58] in accordance with the Nernst equation. Low pH increases the redox potential of the oxygen reduction reaction (ORR). Secondly, it may influence the catalytic properties by changing the reaction mechanism e.g. from a four- to a less preferable two-electron transport at alkaline pH [59]. Thirdly, it influences the physiology and growth of the anode respiring bacteria [16] and other organisms present in the electroactive biofilm. Therefore, an acidic cathodic region increases performance and

an alkaline-neutral anodic region is desirable for proton buffering and growth of anodic biofilm.

4) The conductivity of the electrolyte determines the resistance that charge experiences while travelling through it, and thus governs total internal resistance of the MFC. It also effects the microbial community [60–62]. In conclusion, an ideal environment would supply high salinity to reduce internal resistance but still allow microbes to prosper.
5) Temperature increases the catalytic reaction rates in a Van't Hoff manner within certain boundaries. Microorganisms such as the anode respiring bacteria have an mesothermal temperature range in which their physiology and electron transfer work best [15]. Below this temperature, reactions become slow and above their metabolic processes start to fail because of protein degradation. Ideally, an environment provides high temperatures at the cathode and microbe friendly temperatures at the anode.

It is desired to balance the above-mentioned factors to achieve a high potential difference between anode and cathode, high oxygen reduction rates as well as prospering and highly active anode respiring bacteria.

3.1. Results

We examined six different sites in the northern German city Braunschweig (Germany, Lower Saxony) in summer and autumn 2016. They fall into two categories: Either free flowing within the sewer or stagnant exposed to open-air. The order of sampling sites represented the chronological path of sewage in Braunschweig. We followed the sewage starting in the inner city (Bammelsberger Straße), followed it north to the pumping station in Ölper and then 6 km north-west to the waste water treatment plant (WWTP) Steinhof and its surrounding nature oriented postprocessing irrigation field called “Rieselfelder”. The last site was an artificial and slightly eutrophic pond called “Neuer Bleeksteich” which was not part of the waste water treatment system, but a part of an early medieval fishpond system [63].

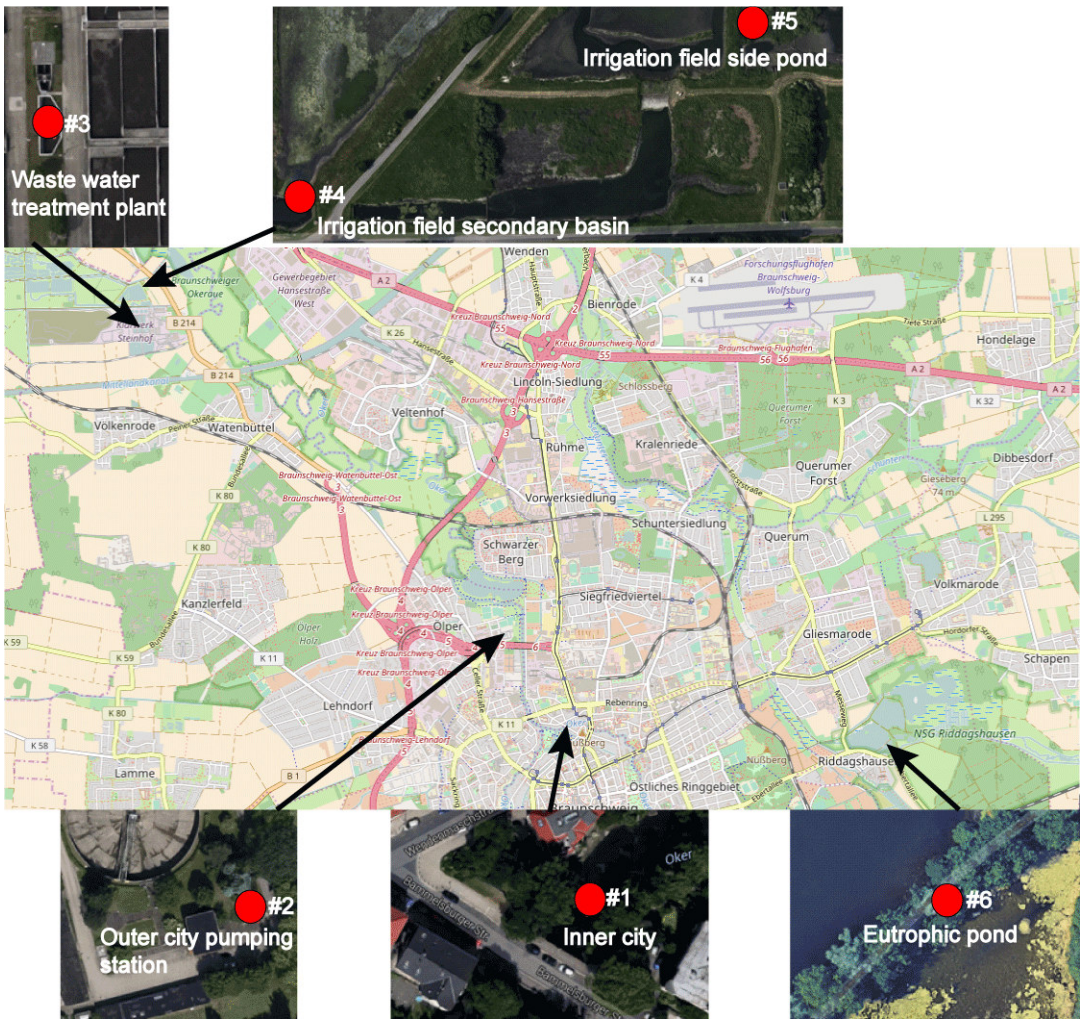

Figure 25: Sampling sites within the city of Braunschweig (Lower Saxony, Germany). Map from Open Street map.

The sampling was performed at the respective sites at the same day of the week and at a similar point in time ±1 h (Table 11).

Table 11: Sampling sites, their coordinates and examination time.

Site	Name	Coordinates	Time
#1	Inner city, Bammelsberger street	52°16'23.2"N 10°31'12.4"E	8:00
#2	Outer city, pumping station Ölper	52°16'57.3"N 10°30'35.3"E	9:00
#3	Main inlet of WWTP Steinhof	52°19'03.0"N 10°26'39.3"E	11:30
#4	Irrigation field side pond	52°19'10.8"N 10°26'29.6"E	12:00
#5	Irrigation field secondary basin	52°19'08.1"N 10°26'18.3"E	13:00
#6	Eutrophic pond “Neuer Bleeksteich”	52°16'16.4"N 10°34'41.0"E	14:00

The sampling sites were firstly, characterized with respect to their general properties, such as the embedding within the city’s infrastructure or their water quality indicators and secondly, with regards to their physiochemical properties.

3.1.1. Characterization of sampling sites

Sampling site #1: Inner city, Bammelsberger street

The sampling site is located within the sewer network north of the city center of Braunschweig. The manhole to the sewer is located at a depth of two meters underneath an open accessible lawn aside the Oker river. The sewer crosses below the Oker via an inverted syphon. The inverted syphon comprises of five curves and a diminution region of 600 mm diameter. The curves and changes in diameter might promote sewage mixing. The waste water load originates from a major part of the city, and thus holds a high population equivalent (PE). A dewatering pump is located upstream and dilutes the sewage in case of heavy rain events. Noteworthy is also a unit for controlled crushing of solids in the sewer 100 m upstream of the sampling site.

Sampling site #2: Outer city, pumping station Ölper

The pumping station is located 3 km north-west of the first sampling site and elevates most of Braunschweig sewage to pass the free-flow pipe in direction of the WWTP Steinhof.

Sampling site #3: Main inlet of WWTP Steinhof

All waste water of Braunschweig enters the treatment plant by the 1500 mm diameter main inlet. The highest waste water flow takes place in the morning.

Sampling site #4: Irrigation field side pond

The irrigation field is intended for the post treatment of the clarified waste water from the WWTP Steinhof. It acts as a reservoir for the storage of excess waste water in case of high rainfall events prior to irrigation of farmland. In average 20 thousand cubic meters are treated daily on 200 ha. Its sediment is a greyish, blackish slurry with sulfurous scent which reminds of the German Wadden Sea and it is rich in similar bird species such as wading birds. A small separate post treatment pond is located north of the main inlet of the irrigation field and close to its major tidal pool. Its water has a black color and its ground is covered with black mud. A barrier to the main irrigation field prevents the carryover of heavy water level changes from the main irrigation field. During sunny days, many red midge larvae, probably *Chironomus thummi,* are visible, which indicates a rather high saprobic index.

Sampling site 5: #Irrigation field secondary basin

The secondary basin is located south west of the main inlet of the irrigation field and it is separated by a barrier from the main basin. Its water was mostly clear during measurements but covered with duckweed throughout summer and autumn. Organisms such as frogs and small fishes were visible and indicated a lower saprobic index compared to the side pond.

Sampling site #6: Eutrophic pond "Neuer Bleeksteich"

The pond "Neuer Bleeksteich" belongs to the nature sanctuary Riddagshausen, which has been a part of a medieval fish pond system constructed by Cistercian monks. Its bottom was covered by foliage and a scent of rotten eggs was noticeable when gas bubbles reached the surface, indicating the presence of sulfide and eutrophic processes. The presence of *Lymnaea stagnalis,* known as the great pond snail indicates medium water quality with a saprobic index of two. The site was directly exposed to sunlight in most parts of the day.

3.1.2. Physiochemical properties at the sampling sites

The first property under investigation was the oxygen concentration and probably the most important. It was measured to determine the degree of anaerobicity required for anodic respiration. Only site three, the WWTP main inlet, appears to be throughout anaerobic (Figure 26). Sites one and four were mostly, but not constantly anaerobic. The first sampling site was closest to the city and exhibited high variability during the nine replicates of a single measurement day. As the waste water proceeds to the WWTP, its anaerobicity becomes more evident and stable. The irrigation field pond was mostly anaerobic except for one day in July. In contrast, the mostly aerobic secondary basin in the irrigation field lacked oxygen the same day. Both observations might be explained. The sampling day in July was performed after morning/overnight rainfall (Table 12). The irrigation field had been without inflow for the past four weeks and the day of sampling was the first day of inflow since then. Sampling site four could have become aerobic because of heavy inflow of water from the field next to it while the inflow did not yet reach the secondary basin at sampling site five, which maintained it anaerobicity acquired during the four weeks of absent inflow. The rainfall event at night caused dilution of the sewage, and thus might have elevated the oxygen concentrations at sampling site one and two.

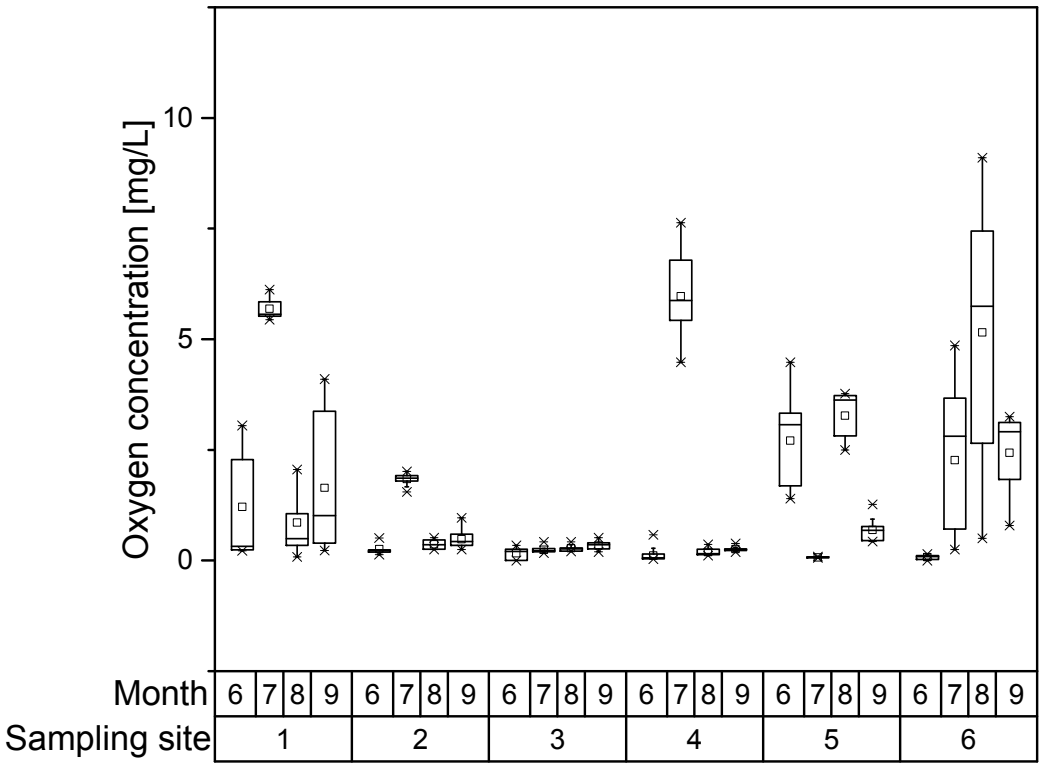

Figure 26: Boxplot of oxygen concentration. Sampling at 4 respective measurement days in June, July, August and September. Sampling site #1: Bammelsberger street; Sampling site #2: pumping station Ölper; Sampling site #3: main inlet WWTP Steinhof; Sampling site #4: irrigation field side pond; Sampling site #5: irrigation field secondary basin; Sampling site #6: eutrophic pond "Neuer Bleeksteich". Boxplot: Box represents 50% of data points; line in box represents median, square represents arithmetic mean, top part of box represents upper quartile, bottom of box represents lower quartile, the whiskers represent the highest and lowest outliers.

In stagnant water, oxygen was determined not only once but in parallel at the top and bottom of the water column. Only slight oxygen gradients were found at sampling site four and five but no clear trend was observed. A more distinct difference was found during measurements directly in the sediment of the fish pond at sampling site six, which was more anaerobic than the water column above.

Table 12: Rainfall, temperature and hours of sunshine at the day of sampling and one day before (Archive data from www.wetteronline.de)

Date	Rainfall [mm]	Temperature [°C]	Hours of sunshine [h]
14.6.	6	20	4
15.6.	11	20	6
26.7.	1	25	7
27.7.	12	25	8
23.8.	0	22	4
24.8.	0	25	13
20.9.	0	17	2
21.9.	0	20	3

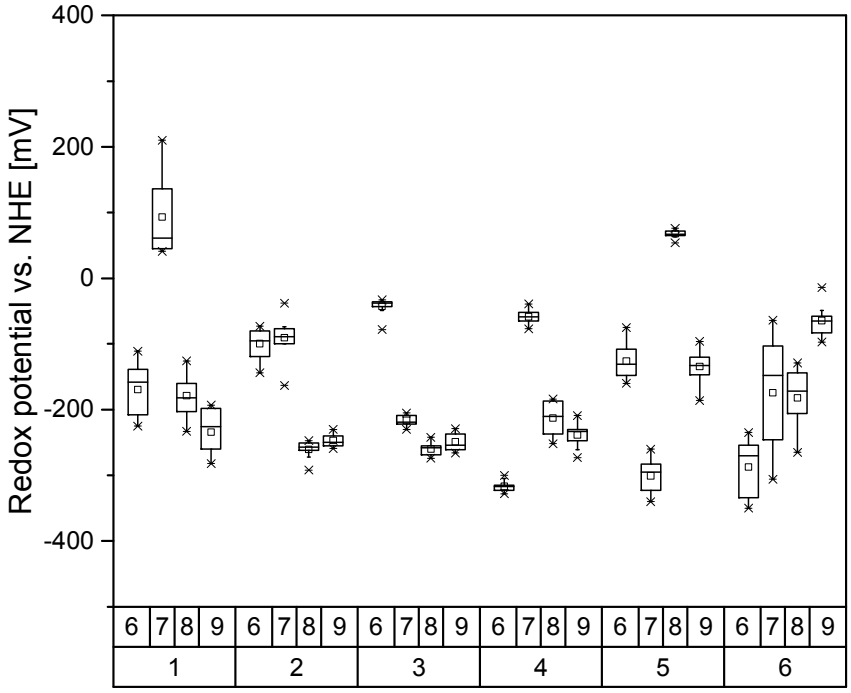

Figure 27: Boxplot of redox potential vs. NHE. Sampling at 4 respective measurement days in June, July, August and September. Sampling site #1: Bammelsberger street; Sampling site #2: pumping station Ölper; Sampling site #3: main inlet WWTP Steinhof; Sampling site #4: irrigation field side pond; Sampling site #5: irrigation field secondary basin; Sampling site #6: eutrophic pond "Neuer Bleeksteich". Boxplot: Box represents 50% of data points; line in box represents median, square represents arithmetic mean, top part of box represents upper quartile, bottom of box represents lower quartile, the whiskers represent the highest and lowest outliers.

The redox potential was mostly negative and therefore beneficial for anode placement (Figure 27). Positive redox potentials occurred only once at site one and site five respectively. Increased

sampling depth correlated with more negative potential at "Neuer Bleeksteich", but was found irrelevant at other sites.

Lower redox potentials were associated with low oxygen concentration as indicated in Figure 28, but no mathematical model described it well. The distribution could be dissected into three regions. Firstly, redox potentials below −200 mV were found only at oxygen concentrations below 1.2 mg/L. Secondly, an ORP between −200 mV and 0 could correlate with a broad concentration range from zero to 4 mg/L O_2. Lastly, an ORP above 0 only correlated with O_2 above 5 mg/L.

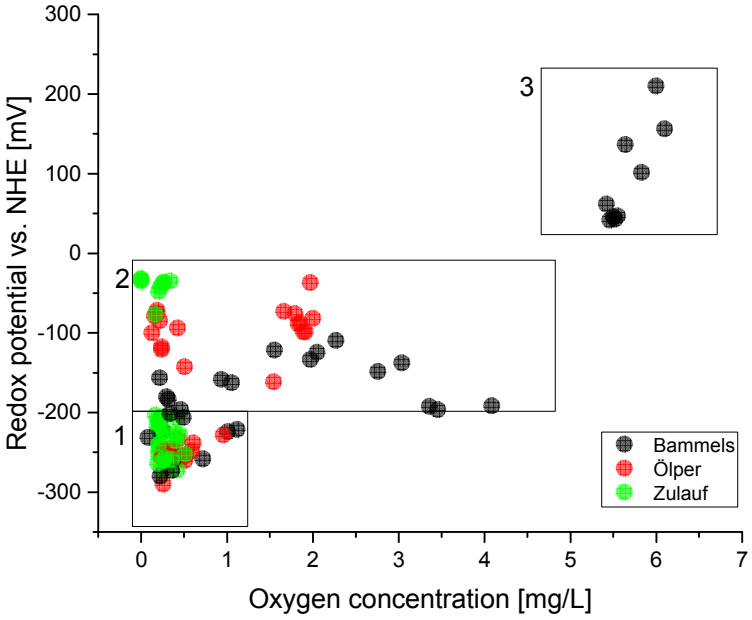

Figure 28: Redox potential and its correlation with oxygen concentration for sampling site 1–3.

The sewage conductivity was in average slightly above 1 mS (Figure 29). This is a much lower value compared to 5.9 ±0.1 mS provided by the 50-mM phosphate buffer at 25 °C, commonly used for laboratory MFCs and also in this study. It decreased heavily in June due to a heavy rainfall event. The conductivity of open-air located sites was slightly lower than 1 mS in average and appeared unaffected by rain. No spatial difference was found between surface and the bottom.

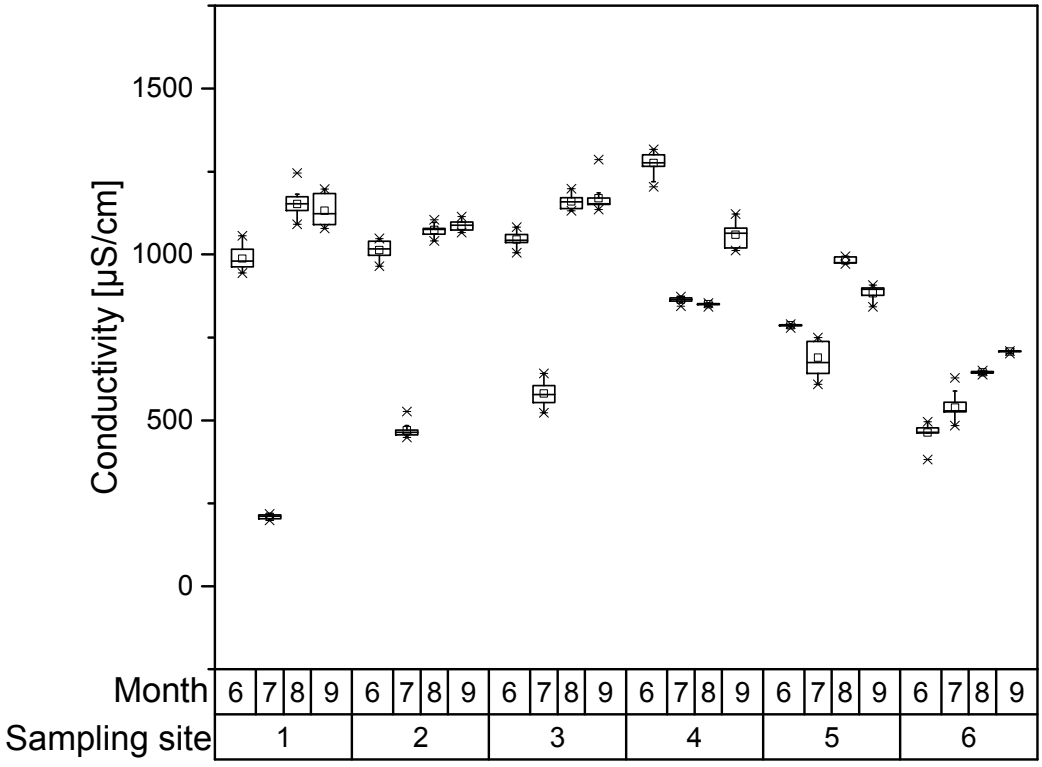

Figure 29: Boxplot of conductivity. Sampling at 4 respective measurement days in June, July, August and September. Sampling site #1: Bammelsberger street; Sampling site #2: pumping station Ölper; Sampling site #3: main inlet WWTP Steinhof; Sampling site #4: irrigation field side pond; Sampling site #5: irrigation field secondary basin; Sampling site #6: eutrophic pond "Neuer Bleeksteich". Boxplot: Box represents 50% of data points; line in box represents median, square represents arithmetic mean, top part of box represents upper quartile, bottom of box represents lower quartile, the whiskers represent the highest and lowest outliers.

The temperature in the sewer is more environmental independent and stable compared to the open-air (Figure 30). This is emphasized in September when open-air sites cooled down to as low as 15 °C by dropping up to 8 °C while the sewage temperature remained stable at ~ 20 °C. This tendency could be possibly more drastic at even colder temperatures. Spatial position played a minor role for temperature. The open air top water column was only 2 °C warmer compared to the bottom (Δd_{max} = 30 cm). Direct sun exposure had only slight effect on the surface temperature.

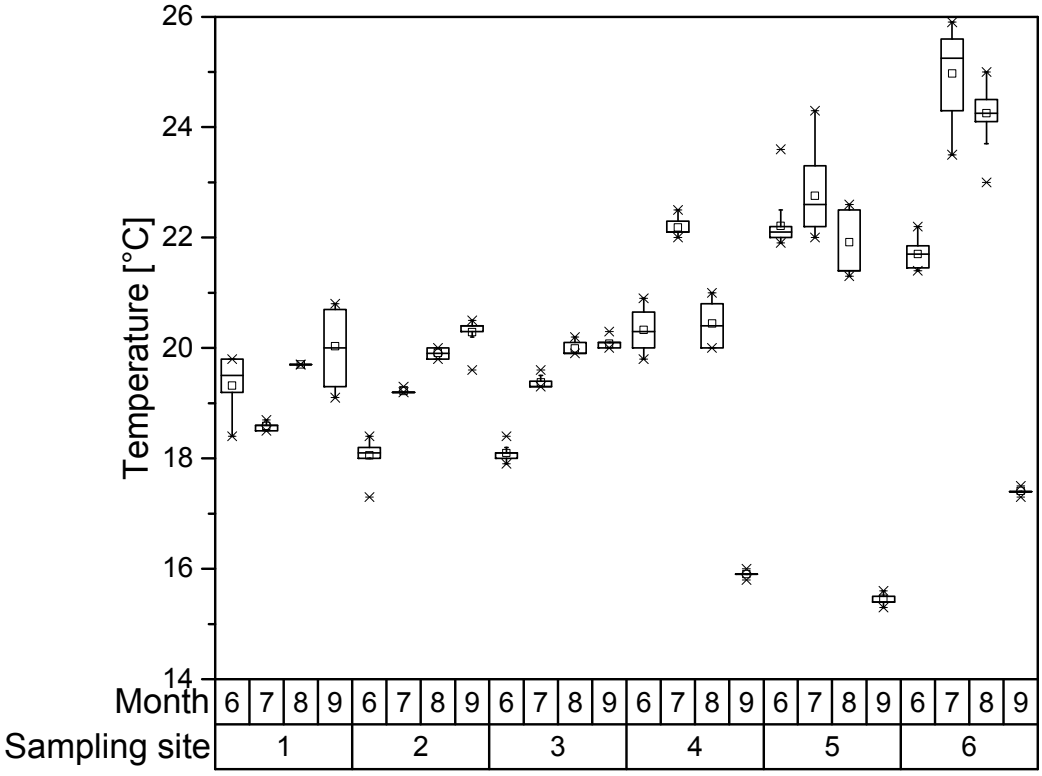

Figure 30: Boxplot of conductivity. Sampling at 4 respective measurement days in June, July, August and September. Sampling site #1: Bammelsberger street; Sampling site #2: pumping station Ölper; Sampling site #3: main inlet WWTP Steinhof; Sampling site #4: irrigation field side pond; Sampling site #5: irrigation field secondary basin; Sampling site #6: eutrophic pond "Neuer Bleeksteich". Boxplot: Box represents 50% of data points; line in box represents median, square represents arithmetic mean, top part of box represents upper quartile, bottom of box represents lower quartile, the whiskers represent the highest and lowest outliers.

The pH was rather alkaline in waste water and slightly more neutral in the open-air (Figure 31). In Ölper the pH reached up to nine. Later, when arriving the WWTP the pH was found less high than in the inner city. A possible reason for this could be the influx of detergents such as shampoo or soap at early dawn before the measurements and a subsequent dilution when approaching the WWTP. The post treatment areas exhibited a more neutral environment. Variability within a measurement was dependent on date and sampling site, but a trend was not determined. The most variable pH in July at "Neuer Bleeksteich" originated from differences between top water and the bottom sediment. In contrast, the two other open-air sampling sites showed no such spatial pH dependence. The at least temporal alkalinity could immediately affect the performance of oxygen reduction, whereas biofilms are considered more robust towards pH variability.

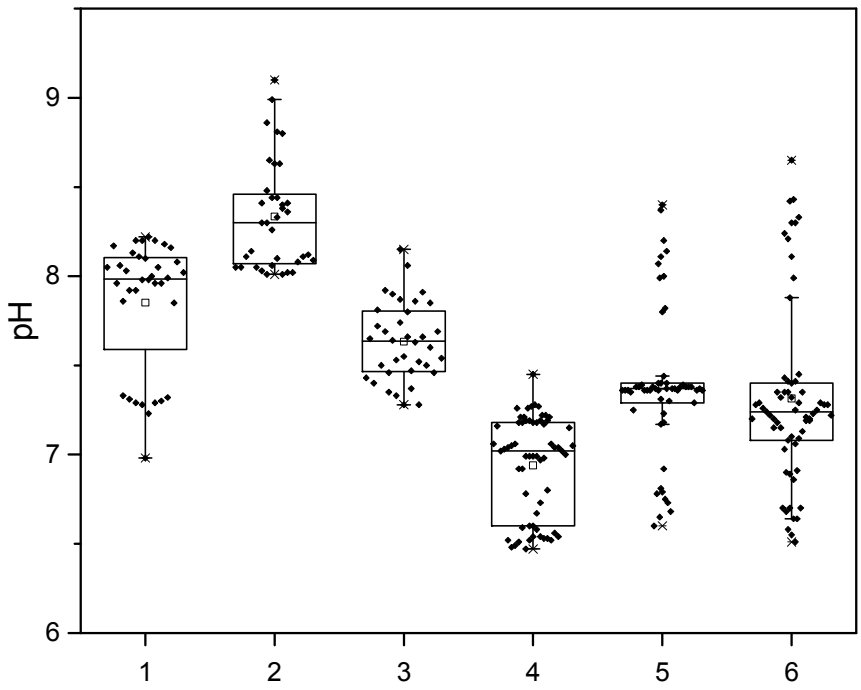

Figure 31: Boxplot of pH. Sampling at 4 respective measurement days in June, July, August and September. Sampling site #1: Bammelsberger street; Sampling site #2: pumping station Ölper; Sampling site #3: main inlet WWTP Steinhof; Sampling site #4: irrigation field side pond; Sampling site #5: irrigation field secondary basin; Sampling site #6: eutrophic pond "Neuer Bleeksteich". Boxplot: Box represents 50% of data points; line in box represents median, square represents arithmetic mean, top part of box represents upper quartile, bottom of box represents lower quartile, the whiskers represent the highest and lowest outliers.

3.2. Summary and discussion

This study presented a procedure to evaluate MFC deployment sites based on physiochemical parameters. The results of this study suggest preferable Microbial Fuel Cell placement between the pumping station and the WWTP and in addition, in the irrigation field side pond. The logical next step would be a continuous measurement over several days to identify the change of sewage properties during the day.

This study investigated a mixed gravity sewer which also conducted rain water. It became evident that rain water influx alters oxygen content and conductivity less useful for MFC applications and this indicated that a separated system for rainwater and sewage might be beneficial.

The results of this study emphasized that the conditions under which MFCs are operated in laboratories only partially represent the environment for application. These experiments are still performed mostly under ideal conditions which therefore suggest higher possible performance than possible. This is because the anodic compartment is kept anoxic and its redox potential low, the conductivity and temperatures are elevated and the pH is buffered. When it comes to the application of Microbial Fuel Cells within the sewer or waste water infrastructure, these parameters will fluctuate and should be considered as non-ideal. As these factors will have a major impact on MFC implementation the next chapters will develop a method for cathodic performance studies which mimic the non-ideal environment of the sewer to provide better estimate of the performance under application conditions in the future.

The systems under investigation showed that surface and bottom water often had similar oxygen concentrations and therefore could only provide slight redox-gradients. This finding implies that new strategies are required for placement of oxygen based cathodes within the anaerobic environment of the sewer. In the later section, the idea of a capillary force enhanced cathode outside the sewage will be investigated and discussed as a possible solution. It might allow to create an aerobic cathode environment outside of an otherwise anaerobic sewage.

Oxygen

It became evident that suitable MFC deployment sites firstly, depend on the sewage source and secondly, on its residence time in the sewer. Both factors strongly determine its oxygen concentration [64]. Sampling site three and four appeared most suitable providing a sufficiently anaerobic environment for anodic respiration – therefore electricity production. But this designated area represents only a marginal length of the city's overall sewer system and therefore points out its possible limitations for MFC implementations intended for electricity production.

The irrigation field side pond represented an interesting environment for the placement of so called MET-lands, wetlands whose clarification is supported by microbial electron transfer [65]. For the implementation of MET-lands, the anaerobicity of the sediment required more investigation. In addition, a sediment based MFC might be applied for reduction of eutrophic sediments from the bottom of a pond.

Redox potential

The redox potential was found to be mostly low at all sampling sites. A low redox potential can coincide with the low oxygen concentration. That was not always the case as illustrated above (Figure 28). This suggests that other chemicals must have caused the low redox potential in

presence of relatively high oxygen levels. In conclusion, both factors, oxygen and ORP together, appear to be required to evaluate suitable sites for MFC deployment. Still, if the ORP influencing factors could become further known, it might become suitable as sole MFC performance predictor.

Conductivity

The measurements indicated that conductivity of real sewage was always lower as compared to laboratory setups and strongly affected by dilution trough rainwater. Both aspects negatively affect the possible MFC as they increase the resistance.

Temperature

The temperature in the sewer was in average around 20 °C and mostly constant while the open-air sampling sites depended more strongly on environmental changes. This designates the sewer more suitable for stable MFC operation.

A high difference in top and bottom temperature of open air waters during sunny days was assumed. The experiments indicated that this effect was not as strong as expected. Surface water level temperature increased only slightly if exposed to sunlight. Nevertheless, radiation effects could be harnessed to support cathodic oxygen reduction. Absorption of sunlight at a black catalytic surface would increase its temperature, and thus could cause higher reaction rates. In addition, the placement of cathodes on the surface of ponds could prevent growth of algae, and therefore decrease eutrophication of the water system. The balance between oxygen solubility, temperature increase and reduction in direct sunlight would be worthwhile to be investigated in the future to determine the application of solar-thermic enhanced floating cathodes.

pH

The pH was mostly alkaline which is beneficial for the anodic oxidation but likely to decrease ORR performance by altering its reduction potential.

4. Comparing cathode materials for sewer integration requires evaluation criteria

This section evaluates materials for the application in a sewer integrated Microbial Fuel Cell. To decide on the suitability of materials, the following eligibility criteria were considered:

- Cheap and renewable
- High inherent reduction rates at highly positive potentials
- Convertibility (Possibility to be modified or loaded to alter catalytic properties)
- Low electrode resistance to allow high MFC power output
- Electrolyte intrusion by capillary forces and high surface area to achieve a large solid-thin liquid-air interphase
- Persistent cathode properties in waste water

The electricity produced by Microbial Fuel Cells is considered a low value product. Accordingly, operation and investment costs are required to be low. The author assumes that MFC-cathodes will rely on cheap and renewable materials instead of expensive precious metals like platinum. To further increase the catalytic properties these materials would be easily modified. To enhance the power output of the MFC, it is required that the electrodes exhibit low internal resistances. The application in the anaerobic sewage stream could need outside cathode placement. Capillary forces are of interest to drag the electrolyte above the water level and allow for facilitated oxygen mass transfer. Lastly, the materials are desired to retain their catalytic properties in the waste water stream despite the harsh and fluctuating environmental conditions. Three cathode materials were investigated with respect to these evaluation criteria. They are introduced with their properties in the next section and the diverse eligibility criteria are investigated thereafter.

The three materials of interest were the following:

- Microporous activated carbon (AC, Zorflex ®) (Figure 32 a & b)
- Macroporous layered corrugated carbon (LCC) made of carbonized cardboard (Figure 32 c & d) [17,66]
- Mesoporous reticulated carbon foam (RCF) electrodes made of carbonized pomelo peel (Figure 32 e & f) [67]

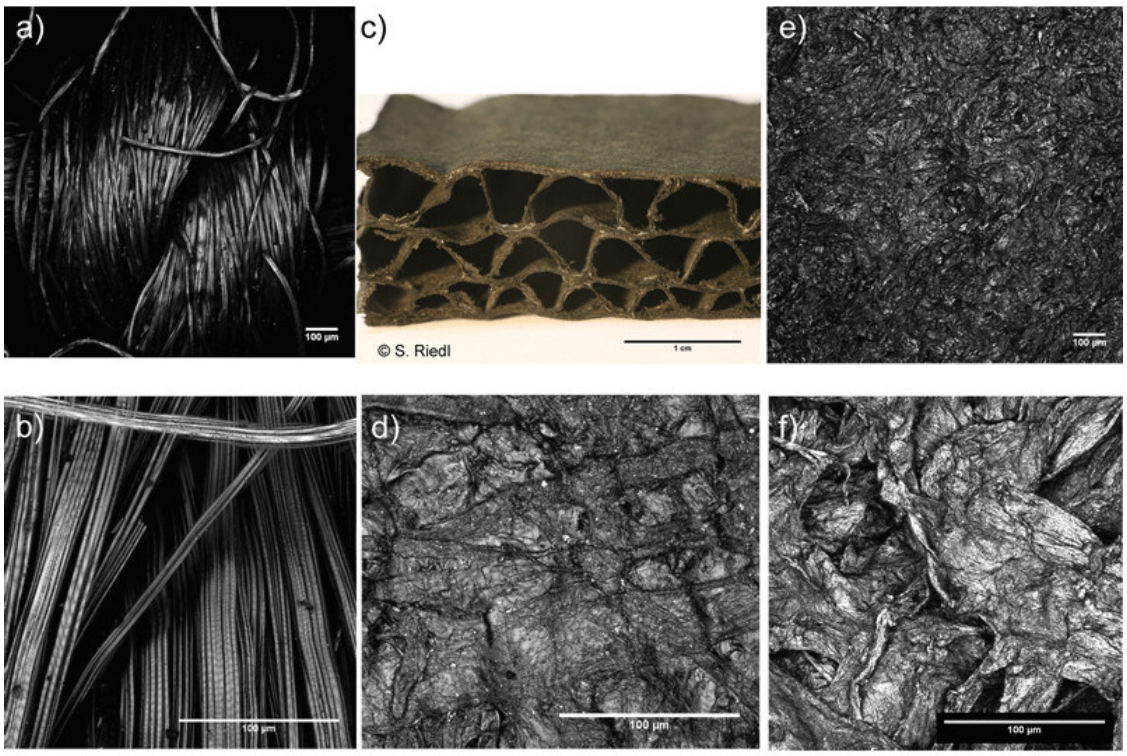

Figure 32: Macroscopic and microscopic material structures of microporous activated carbon (AC, Zorflex ®, a & b), macroporous layered corrugated carbon (LCC, c & d) made of carbonized carboard and mesoporous reticulated carbon foam (RCF, e & f) electrodes made of carbonized pomelo peel. AC, RFC and LCC microscopic images were taken by confocal laser scanning microscopy. LCC photography curtesy of Baudler and Riedl [17,66].

LCC and RCF belong to the group of cheap and renewable electrode materials. Both materials were recently found to be well performing bioanodes with interesting macroscopic and mesoscopic pore structures. Both raw materials required prior carbonization resulting in a conductive electrode structure.

Cardboard is a widely available material with a macroscopic 3-dimensional structure of curvy bended sheets lying between two flat sheets. This structure allows high surface area per volume. Its carbonization results in little mass loss, a solid carbon backbone and adequate conductivity, because of its initially low water and high carbon content. Although this material is fragile, it was used to grow anodic biofilm in a stirred reactor without its macrostructures being clogged [17].

Similarly, pomelo peel is derived from waste materials of renewable sources of the pomelo fruit industry (Pomelo is a crossbred between *Citrus reticulate* and *Citrus maxima*). Its peel has a mesoporous foam like structure whose carbonization results in high hydrophilic surface area

which has been successfully used as a bio-anode for a MFC[67]. It has been suggested as a supercapacitor [68,69], as nitrogen-doped high surface area fuel cell oxygen cathode and for battery applications [70,71]. These factors made LCC and RCF attractive to assess their cathodic properties. LCC was carbonized for two different time periods: 1 hour (LCC1) and 2 hour (LCC2).

Activated carbon has been used in different ways and modifications for water treatment [72,73], as capacitor [74–78] and as electrode material [79] e.g. as oxygen cathode in microbial fuel cells [80–83]. The commercial available activated carbon cloth (AC, Zorflex ®) was used in this study and has been used before once in a MFC [84]. It has a high microporous surface area and was assessed in two textures (FM10 and FM100). Platinum and graphite were used as representative controls for high and low oxygen reduction performance, respectively.

Completing the list of eligibility criteria for the above materials guided the experimental work in the first chapters of this thesis (Table 13).

Table 13: Desired properties and their respective chapter in this thesis.

Property	Chapter
High reduction rates	4.1.3
Low resistance	4.1.4
Convertibility by HNO_3	4.1.5
High surface area	4.1.6
Electrolyte intrusion	6.1.2

4.1. Results

4.1.1. A standardized electrode backbone

Different materials were assessed for their suitability as floating cathodes for the application within a sewer. To study the electrochemical material properties, it was needed to assemble them into electrodes. To guarantee reproducible experimental conditions and simplified handling an electrode backbone for material mounting was designed. The requirements for such a backbone were:

- Stability and negligible reactivity within a potential window of −0.4 to 0.8 V vs. Ag/AgCl at room temperature and neutral pH.
- Capacity to accommodate 1 cm^2 geometric area of electrode material as suggested by previous studies [85].
- Fitting a NS 29 ground glass joint and fitting the pod of a micro attenuator for later capillary force studies.

- Additionally, it should be cheap, easy to build and capable to hold various material types and shapes.

Such a backbone was designed on the basis of previously published work [66,67]. *Figure 33* a) shows the four stages of production. At each stage, it was compared with respect to its potential window using cyclic voltammetry (*Figure 33* b) and particularly its reductive currents at −200 mV vs. Ag/AgCl by chronoamperometry (*Figure 33* c)**.**

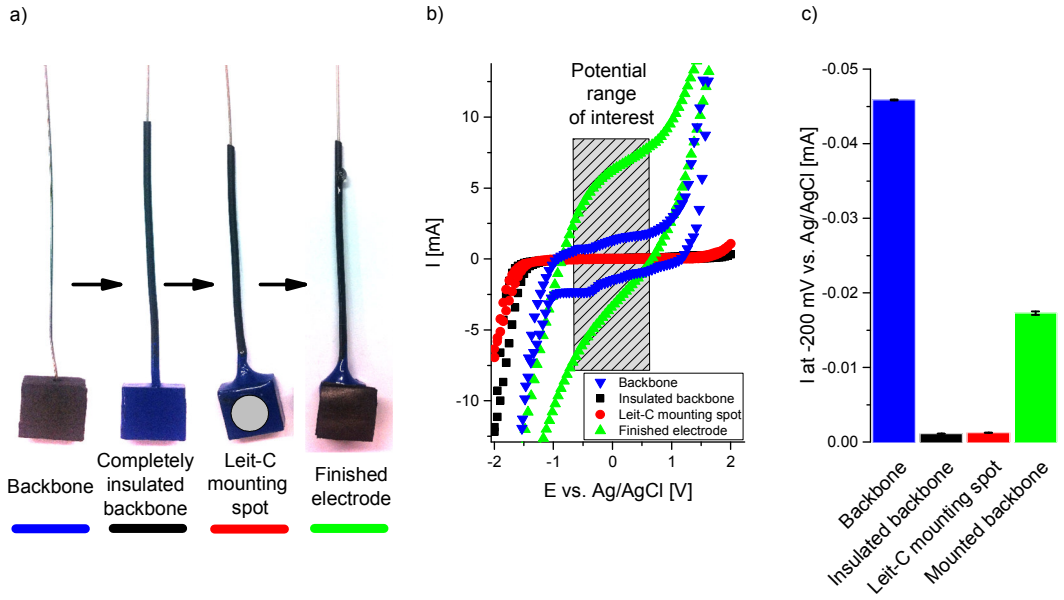

Figure 33: a) Electrode fabrication stages. Backbone: plain polycrystalline graphite; Completely insulated backbone: lacquer covered graphite and insulated current collector; Leit-C-mounting spot: smoothed conductive carbon cement covered region of r = 0.5 cm; Finished electrode: mounted with LCC b) Cyclic voltammograms at each stage of production. c) Reductive currents at each stage of production measured by chronoamperometry at −200 mV vs. Ag/AgCl.

Figure 33 b) indicates the backbones adequate potential window which ranged from over +0.8 to under −0.4 mV vs. Ag/AgCl. Because of high oxygen and hydrogen overpotentials, cathodic processes could be studied. Insulating the electrodes broadened the potential window by reduced anodic and cathodic currents. Adding the mounting spot covered with conductive carbon cement (Leit-C) did not reverse the effect, thus appeared to exhibit little electrochemical activity.

Figure 33 c) shows, the negligible reductive currents of the insulated backbone compared to the bare backbone and to the finished mounted electrode. Resistance of the final electrode backbones was in all cases below 1 ohm. Poising the electrode backbone for extended periods of time at high oxygen or low hydrogen evolution potentials, respectively, did cause the lacquer

to detach from the electrode and therefore, should be avoided. Storage and extended submersion for several weeks in phosphate buffer did not affect the electrode backbones (data not shown).

4.1.2. Copper current collectors are superior over stainless steel current collectors

Later experiments required a lightweight free-floating cathode. For this purpose, flexible copper and stainless steel current collectors were compared and used instead of the static graphite backbone described above. Previous studies found that stainless steel support increased conductivity of MFC-electrodes [86] and also its reduction performance [87]. Since copper is even more conductive it could be a preferable current collector. Nevertheless, it might corrode at cathodic potentials more quickly than stainless steel. Its Pourbaix diagram [88] predicts the onset of corrosion at 0.05 V vs. NHE in pH neutral waste water [89].

The metal- meshes were placed in between two sheets of FM 100 and fortified by stitching using a thin wire of the respective metal. The resulting electrodes were compared with respect to their resistance and reduction performance.

The ohmic resistance of the copper-mesh enforced electrode was 0.1 ±0.1 Ω, and thus two orders of magnitudes lower as compared to the highly variable stainless-steel 45.4 ±64.2 Ω. The variable resistance across the electrode surface might indicate that the metal backbone did not result in homogeneous contacting – especially the less flexible stainless steel. The copper-mesh enforced electrode resulted in an order of magnitude higher reduction performance, although its reductive current declined slightly over time whereas stainless steel's current increased.

In conclusion, the copper-mesh might be beneficial for two reasons: Firstly, it has a higher inherent conductivity compared to stainless steel. Secondly, its higher flexibility could have resulted in a more homogeneous contacting. Therefore, it was used as current collector in the later experiments despite the higher risk of corrosion.

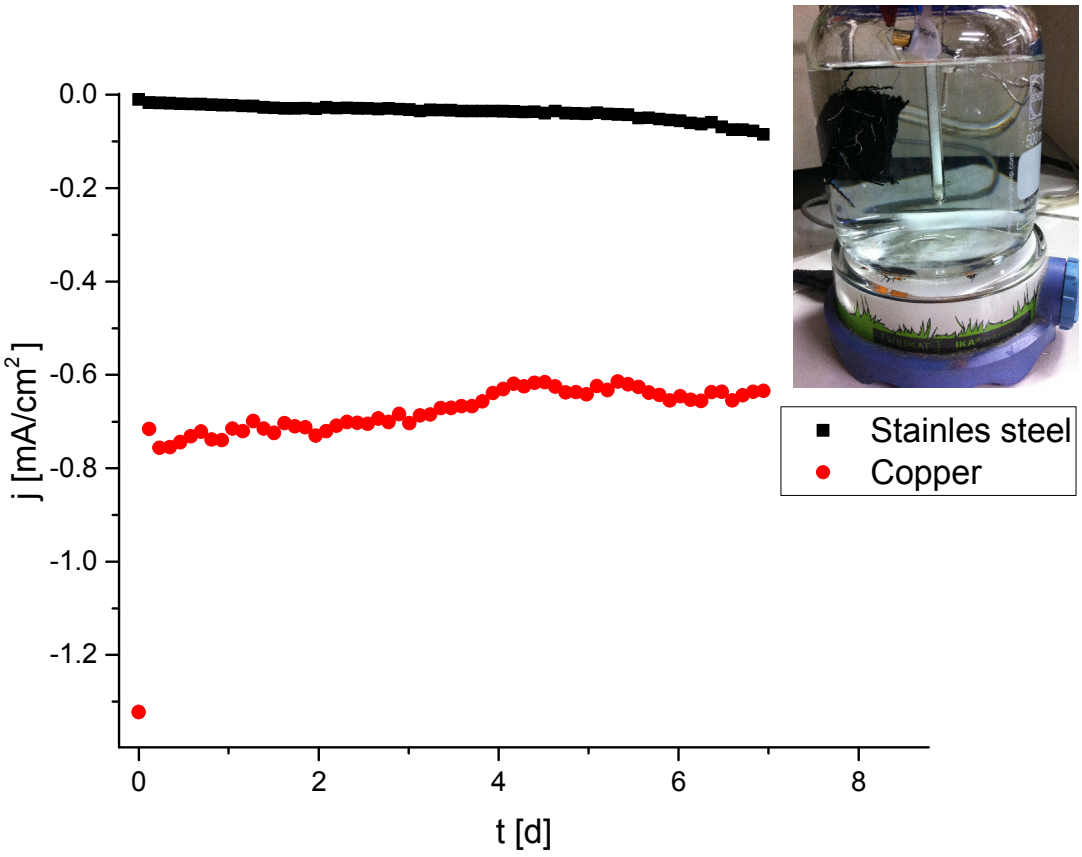

Figure 34: Reductive currents of copper and stainless-steel contacted activated carbon cloth at −200 mV vs. Ag/AgCl in 50 mM phosphate buffered saline at room temperature and stirred at 200 rpm.

4.1.3. RFC and AC perform similarly well

MFC-cathodes require a high current density at low overpotentials. Therefore, the material selection is guided by evaluating these inherent properties. We compared activated carbon (AC), carbonized layered corrugated carbon (LCC) and reticulated carbon foam from pomelo peel (RCF) with regards to their current density at −200 mV and 0 mV vs. Ag/AgCl. Averaged polarization curves were calculated taking the mean of the forward and backward scan at reach respective potential step (Figure 35). Plain polycrystalline graphite and platinum where used as reference materials.

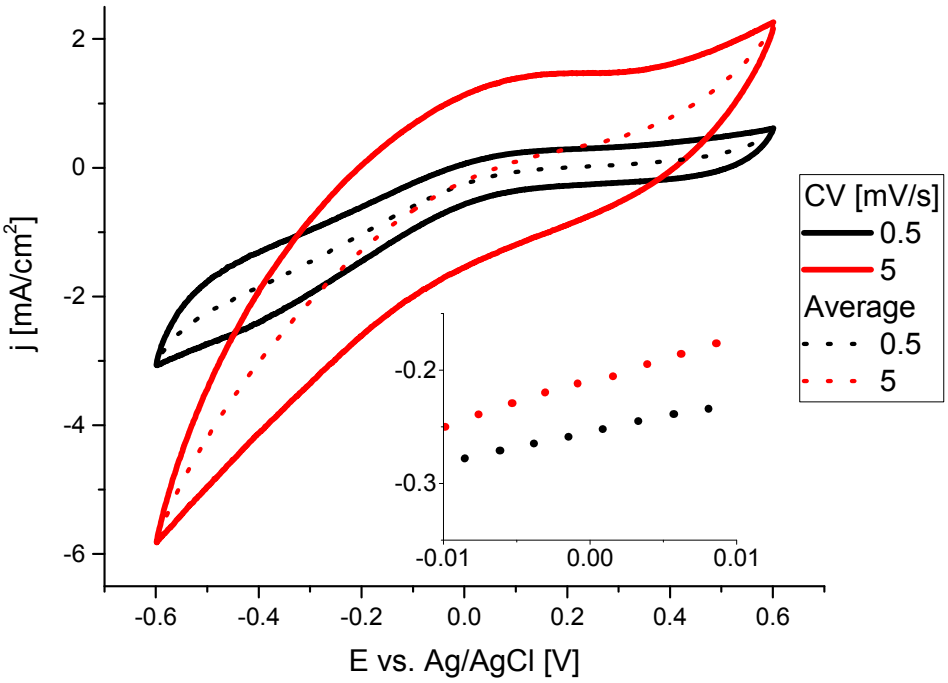

Figure 35: Cyclic voltammograms of activated carbon cloth Zorflex FM 100 at 5 and 0.5 mV/s scan rate. Averaged scans are indicated by dotted line. Inset focuses on the area around 0 mV vs. Ag/AgCl. Electrolyte: Phosphate buffered saline at room temperature.

The reduction performance was first examined by cyclic voltammetry at 5 mV/s (Figure 36 a). Afterwards, the promising candidates were examined more accurately at slower scan rates of 0.5 mV/s (Figure 36 b). A potential of −200 mV vs. Ag/AgCl led to highest reduction rates.

AC FM100 appeared to have the best reductive properties and performed well at high and low overpotential, although its current densities were more variable compared to AC FM10. RCF was found to be second best. In contrast, LCC2 and LCC1, were discarded before the slow scan-rate test, as their least low overpotential performance. LCC2 performed better than LCC1, possibly because a higher carbon content and a resulting higher conductivity due to longer carbonization.

Current densities depended strongly on the scan rate. When set high, RCF and LCC types exhibited slight oxidative instead of reductive currents at 0 mV vs. Ag/AgCl. Also, AC's reduction rate decreased significantly when lowering the scan rate. Reductive currents at 0 mV vs. Ag/AgCl turned out to be higher when being estimated using the slower scan rates (Figure 35, compared to inset). The significant increase of current with scan rate indicated high capacitive currents. The impact of capacitive currents will be discussed in more detail in the later chapter.

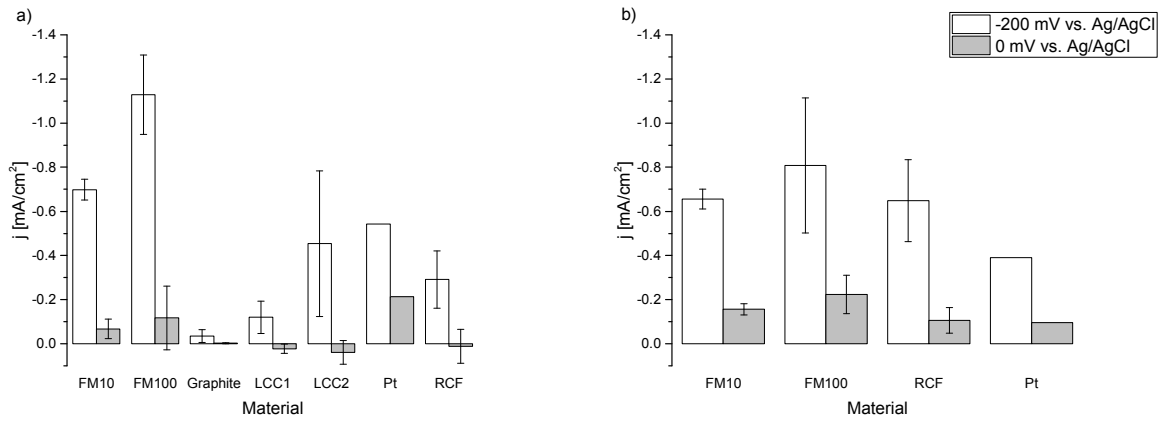

Figure 36: Cathodic current densities of AC, LCC and RFC estimated by averaging cyclic voltammograms with a) 5 mV/s and b) 0.5 mV/s scan rates at −200 and 0 mV vs. Ag/AgCl (n = 3, except for platinum).

4.1.4. Conductivity of RCF outperformed LCC and AC cathodes

Material resistance of the cathode contributes to the internal resistance of MFCs. Therefore, it is desired to be as low as possible to increase the possible maximum power point (MPP) of an MFC.

$$P_{max} = \frac{E_0^2}{R_{ext} + R_{int}}$$

Where E_0 is the open circuit voltage, R_{ext} represent the external load and R_{int} represents the internal resistance, respectively [90]. Electrode resistance of AC, LCC and RCF were assessed by four terminal Kelvin sensing (Figure 37). The resistance probes were attached to the conductive wire of the electrode backbone at one side and at the material mounted onto the backbone at the other side. Therefore, the total electrode resistance was determined, including the material, the contacting and backbone resistance, but without the contact resistance of the probes.

RCF cathodes exhibited the least resistance with ~ 1 Ω. In contrast, AC cathodes had a tenfold higher resistivity. LCC was least conductive, while LCC2 had a lower resistivity than LCC1. This might be partially caused by a higher carbon content due to a longer carbonization period. AC and RCF showed appropriate resistances for the use in MFCs. Including a current collector within LCC could increase their conductivity and render them more suitable for MFC application.

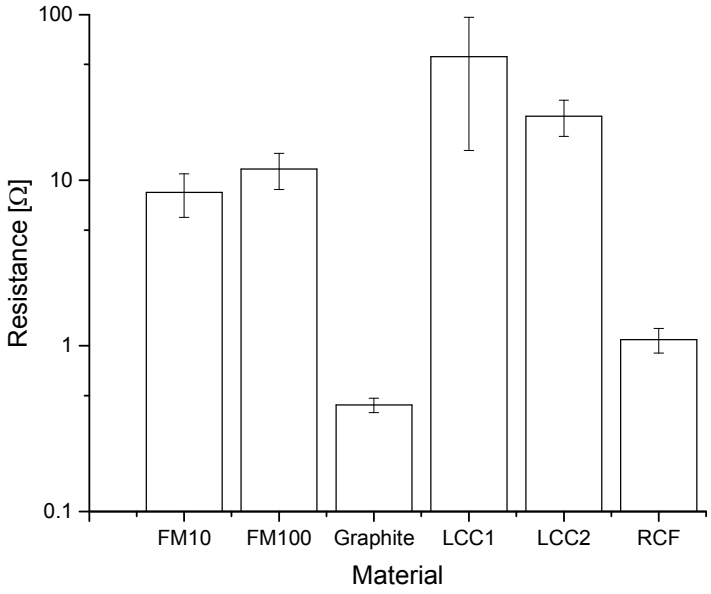

Figure 37: Ohmic resistance of cathode backbones mounted with AC, LCC or RCF (Log-scale). The resistance of the electrode backbone (graphite) served as a control. Ohmic resistance was measured with by four-terminal Kelvin sensing to exclude probe contacting resistance (n = 3).

4.1.5. Nitric acid treatment reduced cathodic performance and increased resistance

Would it be possible to enhance the cathodic properties of AC, RFC and LCC? Chemical treatment of carbonaceous materials can induce reactive groups and might result in more desirable reductive properties. Nitric acid treatment had a positive effect on carbon nanotubes [91] and hence, was investigated in this study. Treated and untreated materials were compared by their cyclic voltammograms, their current densities and resistances. Instead of the expected positive impact, cathode properties became impaired.

Nitric acid treatment significantly changed the electrochemical properties of all materials. Only the graphite control remained unaffected (Figure 38 f). The impact of treatment was most corruptive for AC (Figure 38 a & b) because its current densities became negligible for both textures and its cyclic voltammograms appeared almost as a flat line. LCC and RCF were less affected (Figure 38 c–e). The forward scan appears to be reflected across an axis through the front reversal to the rear reversal point. This shape results in quite linear average polarization curves as indicated by the linear fit (Figure 38 c–e).

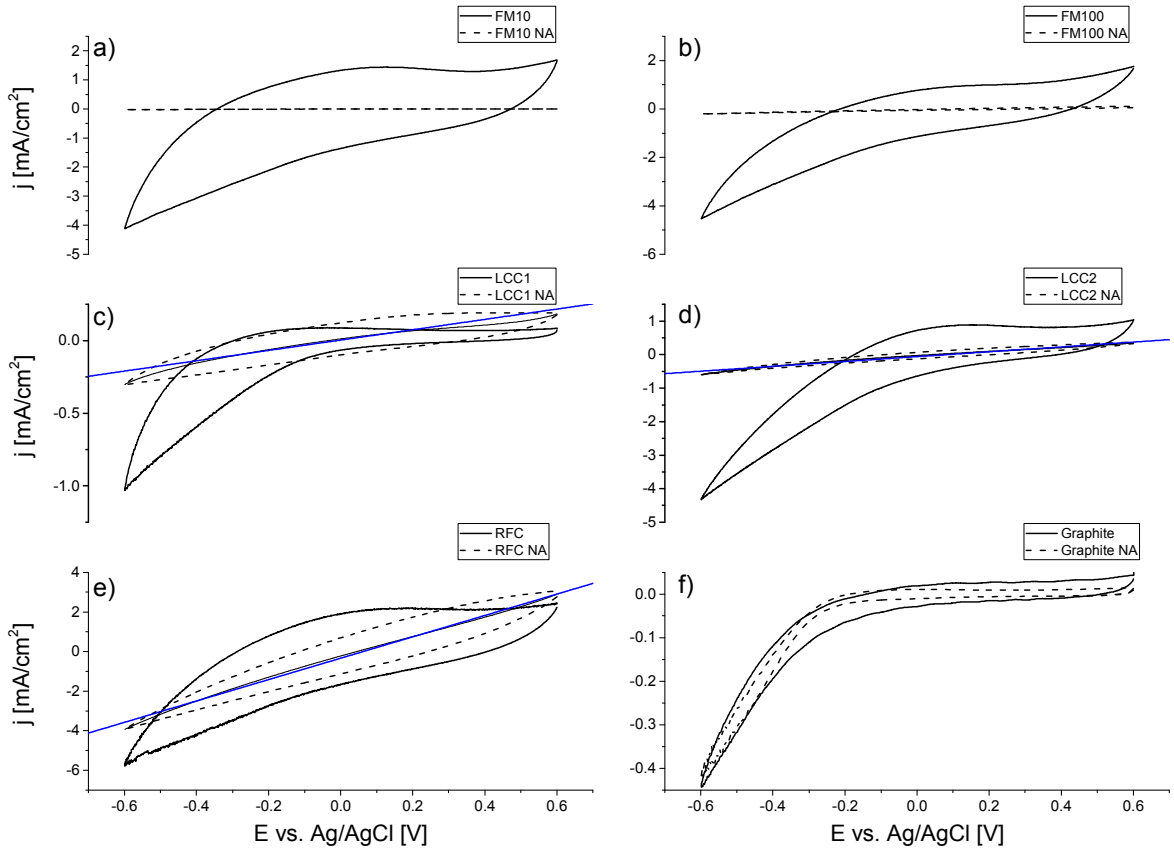

Figure 38: Cyclic voltammograms of nitric acid treated (NA) materials compared to their respective original state. Cyclic voltammograms performed at 5 mV/s in neutral phosphate buffer at RT without convective mass transport.

The current densities of AC and LCC2 decreased upon treatment (Figure 39). In contrast, the current densities of RCF and LCC1 became higher but also more variable.

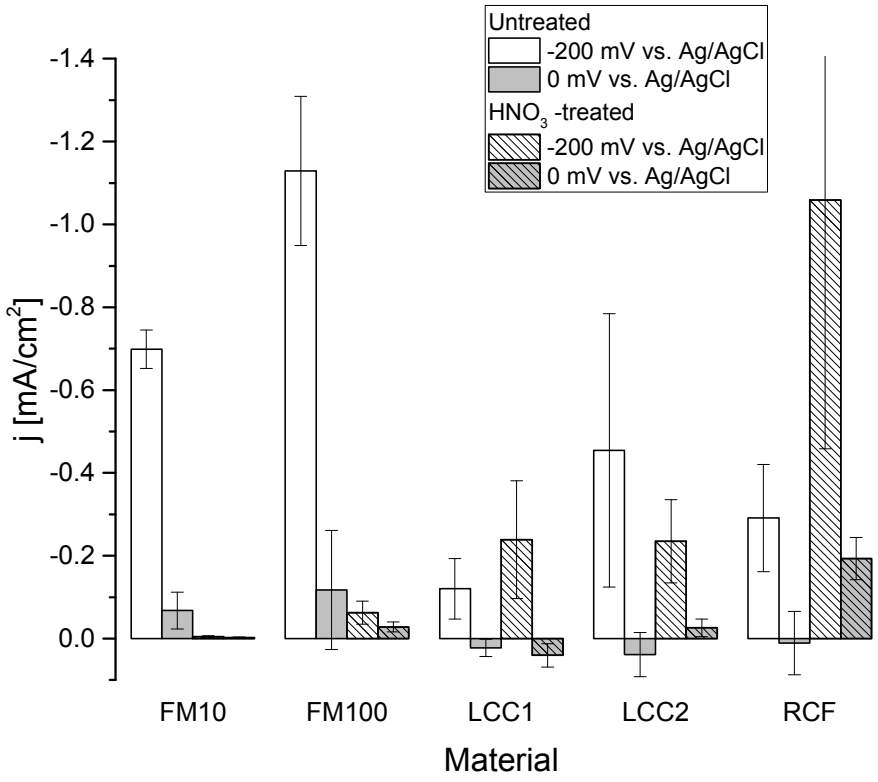

Figure 39: Reductive current densities of nitric acid treated and untreated materials at -200 and 0 mV vs. Ag/AgCl. Current densities were taken from the averaged sweeps of cyclic voltammograms.

Figure 40 shows that nitric acid treatment increased the resistance of all materials at least by six orders of magnitude except for the graphite control.

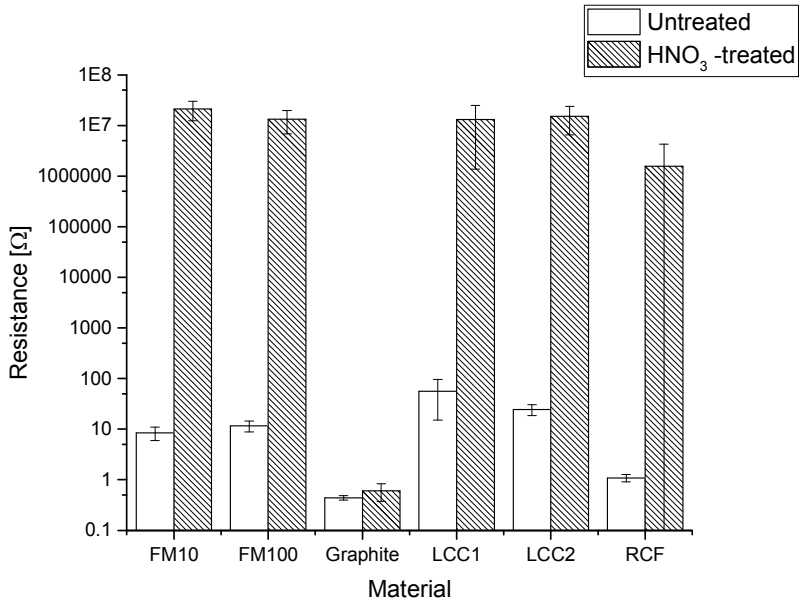

Figure 40: Effect of nitric acid treatment on resistance.

4.1.6. Contact angle Measurement, BET and other aspects

The specific surface area per mass was determined by BET from nitrogen adsorption isotherms. AC provided the largest surface area and RFC the lowest (Table 14).

Table 14: BET surface area.

Material	BET
FM 10	894 ±137
FM 100	845 ±51
LCC	10
RFC	3 ±1

RFC was found to have similar catalytic activity, despite its much lower BET surface area. This indicates that it could be more catalytic active than AC and LCC. The high surface area of AC holds a great potential to enhance its catalytic activity by modifications.

To evaluate the possible inherent capillary forces of the materials, their hydrophobicity was determined by contact angle measurements. The contact angle of a defined water droplet served as an estimate for hydrophobicity. A high angle between the material surface and the drop surface indicated a hydrophilic material.

All three material types were quite hydrophilic and even completely absorbed the water droplet. This indicated, that the carbonized materials must have retained hydrophilic surface groups despite their aliphatic and hydrophobic residues originating from carbonization. In contrast,

graphite was repelling the water exhibiting a contact angle of 45 ±12 ° and therefore more hydrophobic.

The material stability of AC, LCC and RFC was evaluated during electrode fabrication and application within experiments. AC was found robust albeit its fibers might detach from the woven cloth if the material is not tightly glued or tied to a current collector. This loss of fibers will eventually reduce its performance. RFC and LCC were found very fragile. Especially LCC broke apart under slight pressure and after fall from low height. RFC tended to be more resistant to pressure and falling.

4.2. Summary and discussion

Electrode backbone

A cheap and easy to build universal electrode backbone was developed. It allowed to test various material types and shapes in a reproducible and reliable way. It was especially useful to support fragile 3-D electrode structures because of a reduced risk of breakage. The backbone itself did not contribute significant background currents when materials were tested. The backbone was produced in high quantities and kept in stock. The final step allows to finish several electrodes within less than one hour. It required only mounting and drying of the conductive Leit-C carbon cement to manufacture a ready-to-use electrode with various complex materials.

Performance comparison

RCF has been applied as a selenium version for lithium-selenium batteries, but not as MFC-cathode [92]. In contrast, pure LCC has been used previously. It exhibited current densities up to −0.88 mA at −200 mV vs. Ag/AgCl [93] while in this study only values ranging from −0.12 ±0.07 mA for LCC1 up to −0.45 ±0.33 mA for LCC2 were achieved. The reasons of the performance differences are hard to trace as many experimental variables were different: scan speed, stirring rate, air supply, carbonization period, electrolyte (phosphate buffer vs. carbonate buffer) and contacting. One probable reason could be the enhanced contacting with an integrated stainless steel current collector, because this study found a high resistance of sole LCC. In addition, increasing the carbonization period improved both, resistance and catalytic performance, and thus might have played also a major role.

Current densities for AC have been also reported previously, but from a mixture of AC and PTFE on a nickel foam electrode [94]. The reduction performance was ranging between 0.57 and

0.86mA/cm^2 at 0 V vs. Ag/AgCl. This is factor 3 to 4 times higher than in this study. Again, the experimental conditions were different: The previous study tested 30 °C, higher scan rates and an air-cathode setup. All three parameters could have contributed to a higher reduction rate: The elevated temperature might have increased the catalytic activity; the higher scan rate has resulted in additional capacitive currents and the air cathode setup might have facilitated mass transfer.

In another study, AC powder and its modifications were tested on a glassy carbon rotating disc electrode in oxygen super-saturated highly saline solution with a scan rate of 5 mV/s [81]. Watson et al. used different types of AC and evaluated their performance in a similar setup at 2100 rpm with preceding alumina polishing step and 10 mV/s scan rate [95]. The rotational movement will highly increase current densities by forced convection. In contrast, polishing might decrease the surface area, and hence reduces the maximum current density. Higher buffer salinity and oxygen concentration also contribute to higher possible ORR.

In conclusion: Material comparison with the literature was difficult due to the absence of studies or varying experimental conditions. Facing these differences, how should cathode material for a sewer integrated MFC be compared then?

RDE experiments are best suited to compare the pure catalytic properties of materials in absence of mass transfer limitations. These conditions are likely to provide much higher current densities than without convection. An approach desired for sewer-MFC-cathode evaluation would fill the experimental gap between e.g. linear sweep rotating disc electrode experiments and direct application of materials in a MFC. Such an approach will be presented in the following section.

Resistance

Reducing the ohmic resistance is important to lower the total internal resistance of an MFC. This study found RCF most conductive amongst AC and LCC. The conductivity of LCC was highest and should be reduced by including contacting elements as presented by Kretzschmar et al. [93].

Modification

Nitric acid treatment did not improve the cathode materials used in this study. It reduced current densities of all material except for LCC1 and RFC. RFC showed a significant increase but also a much higher deviation thereof. Oxidative treatment increased electrode resistance and made possible power output negligible, thus altered them inappropriately for the use in Microbial

Fuel Cells. Despite nitric acid has been proposed to have a positive effect on carbon nanotubes, it has been proven to be detrimental to AC, RFC and LCC.

Acid treatment of carbon is generally employed to oxidize the porous carbon surface as it increases the acidic property, removes the mineral elements and improves the hydrophilic nature of the surface [72]. Oxidation treatment of AC (Chemviron, F400) by nitric acid reduced surface area and pore volume [96]. Oxidization of carbon nanotubes by ozone increased its ohmic resistance [97]. These findings suggest that the harsh treatment with nitric acid might have reduced the electrochemical active surface area of AC FM10 and AC FM100 and additionally increased its resistance by oxidation.

Nevertheless, this could have affected LCC and RCF in a similar manner, but to a lower extent since their lack of micropores might have made the materials less susceptible for throughout intrusion of nitric acid. The acid might have added an oxide layer onto the surface of RCF and LCC, but it might have left some unoxidized material underneath in the less acid accessible areas, leading only to an increase surface resistance.

Hydrophobicity

All materials in this study were hydrophilic, and thus used in the later section to investigate the use of capillary forces to increase their cathodic performance.

Outlook

The material stability must be considered for the application of sewer integrated cathodes. Fragility might be a downside because it requires replacement of the electrode.

In contrast, a fragile electrode could also renew its own surface by breaking apart and revealing a fresh surface without biofouling and renewed catalytic activity. If the material is cheap and a solution for quick and inexpensive replacement could be found, this would be a desired property to retain catalytic activity. An interesting experiment would be the application of a fragile material in a flow chamber with particle populated waste water and the analysis of surface abrasion possibly impacting the catalytic activity.

Albeit Zhao et al. argued that cathodic potential studies below 0 V vs. Ag/AgCl are not useful because of Microbial Fuel Cell performance reasons [85] it was beneficial to do so in the framework of this study. The high oxygen reduction overpotential region below −200 mV vs. Ag/AgCl was of interest because of its induction of mass transfer limitations, which was a desired condition to tackle by utilization of capillary force in one of the later chapters.

5. Cathode characterization requires to mimic the environment for application

As emphasized in the previous section, the conditions under which materials and their reduction performance were estimated generally differ from their potential field of application. This encouraged the author to investigate an approach to characterize electrode materials under operation conditions. In addition, the materials of interest, especially AC, exhibited high surface area. To generate faradaic polarization curves for such materials usually slow scan rates are required to reduce overlying capacitive currents. Thus, the next section also presents an approach to determine the CV scan rate and an average polarization curve thereof to reduce the capacitive effects.

Studying cathode performance for sewer integration

How to study cathode performance for the application in a sewer integrated Microbial Fuel Cell? Performance is a matter of materials and mass transport. This chapter illustrates the mass transfer conditions under which a sewer integrated MFC will be operated and it highlights the discrepancy to the conditions of common material performance studies of linear sweep rotational disc electrode experiments. Later, practical guidelines are given to mimic more application like conditions and methods to measure them with scan rate adjusted cyclic voltammetry.

Oxygen convection will play a minor role for the sewer integrated cathodes

Figure 41 illustrates the four common ways of cathodic mass transfer in laboratory scale Microbial Fuel Cells: Sparging of air and/or oxygen [90,98–105] (a), air diffusion [106–113] (b), stirring [114,115] (c) and catholyte flow [105,116] (d). The anaerobic environment of the sewage requires the placement of the cathode either directly at the air-sewage interphase (e) or inline of the sewer in contact with the sewage (f). Thus, the sewer integrated cathode is likely to rely on diffusive mass transfer without convective oxygen transport. To properly examine electrode performance these convective conditions, need to be taken in account under experimental conditions.

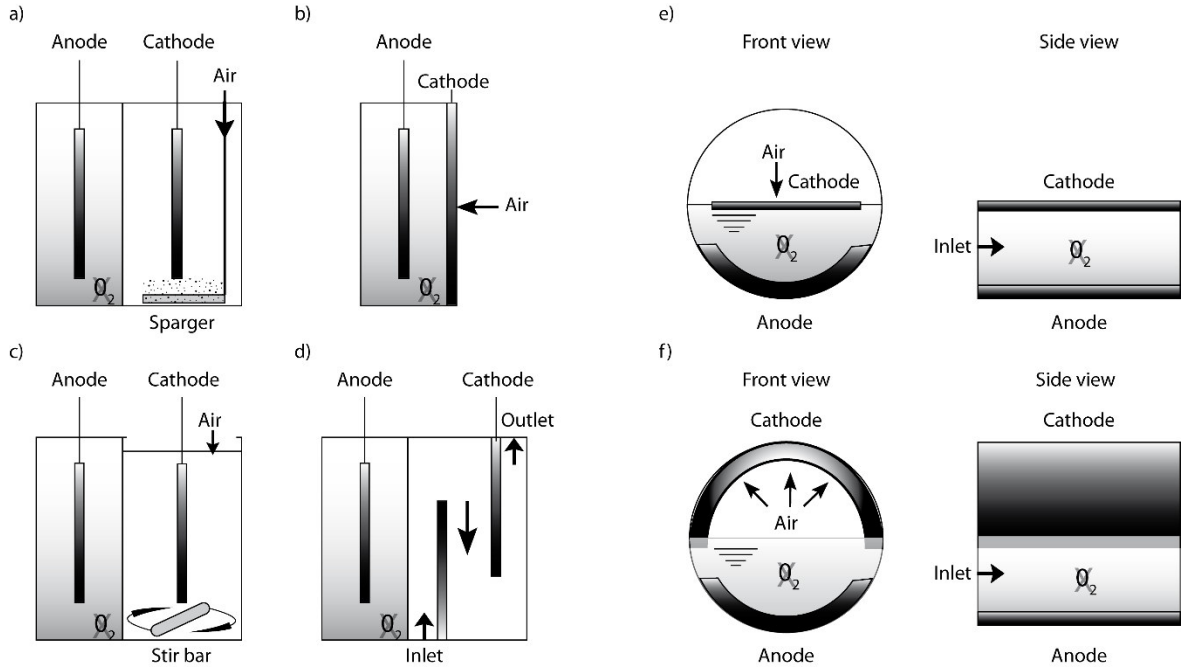

Figure 41: Common types of mass transfer for Microbial Fuel Cells cathodes: a) air sparging, b) air diffusion, c) stirring, d) catholyte circulation. Potential oxygen mass transfer in a sewer integrated Microbial Fuel Cell: e) floating air cathode, f) capillary force cathode.

Common linear sweep experiments do not reflect non-convective conditions

Linear sweep voltammetry relates the current density *j* to the overpotential η. This correlation is commonly measured at a rotating electrode to induce defined convective mass transport (*Figure 42* a). At low overpotentials currents are determined by the reaction rate following the Butler-Vollmer equation. As soon as the surface concentration of oxygen depletes at increased overpotentials, current becomes limited by the rate of mass transport across the Nernstian diffusion layer (Figure 42 c & d):

$$i_{lim} = nFD\frac{c_0}{\delta_N}$$

In this equation, *n* is the total number of electrons involved in the electrochemical reaction, *F* is the value of the Faraday constant (96.485 C/mol), *D* is the diffusion coefficient (m²/s), C_0 is the bulk concentration of oxygen before entering the diffusion layer (mol/L) and δ_N is the diffusion layer thickness (m).

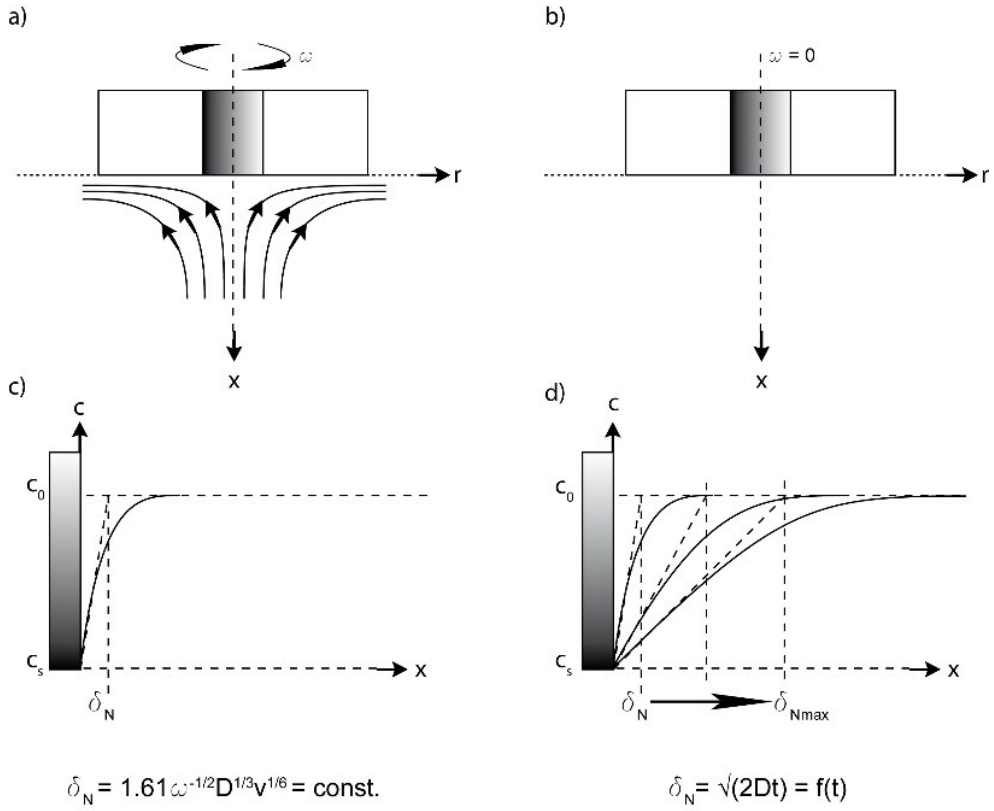

Figure 42: Defined convection creates a steady state Nernstian diffusion layer at a rotating disc electrode (left). Absence of convection creates a transient diffusion layer at a non-rotating planar electrode (right). Transient diffusion layer thickness is limited to $\delta_{N\,max} = 0.5\ mm$ *due to density difference induced micro convection* [21].

Defined convection at a RDE has two major impacts on current densities within the mass transport regime:

1. It results in a time constant diffusion layer δ_N and therefore invariant currents (*Figure 42* c).
2. It reduces diffusion layer thickness δ_N and results in higher limiting currents compared to the non-convective case.

These conditions are ideal to determine and compare the kinetic limitations new two-dimensional MFC cathode catalysts, but these conditions and their resulting current densities must not to be confused with those intended for the application. The RDE determined current densities will be usually much higher. The author suggests, that whenever possible, this discrepancy should be pointed out for materials that are explicitly intended for MFC application, as it improves clarity in its interdisciplinary field of research.

Cathodic mass transfer in laboratory applications is mostly limited to non-ideal convection and even diffusion only (*Figure 41*) – opposite to RDE-Experiments. If convection is absent or low, one must consider two effects disturbing faradaic currents during a linear sweep: Firstly, the time dependent growth of the diffusion layer thickness towards $\delta_{N_{max}}$ (*Figure 42* d) and secondly, the scan rate dependent capacitive current flow.

This highlights the need to estimate the lower end of material performance in absence of convection for application. Similarly, Zhao and colleagues suggested alternative ways to determine the polarization curves of porous cathode materials [85]. They used a slowly stirred system instead of a rotational disc electrode to determine cathodic properties in a low convective system.

The goal of the experimental section was to compare electrode materials under conditions more likely to match the environment they are intended for. This was done by accurately determine non-transient faradaic linear sweep voltammograms for a flat platinum electrode and highly porous activated carbon. Both electrodes were assessed by cyclic voltammetry at varying scan rates in the absence of convection.

5.1. Results

This section covers three aspects: Firstly, how capacitance overlies the faradaic currents during potential scans of platinum and high surface area AC. Secondly, how to determine Faradaic currents despite capacitive charge transfer by an adequately low scan rate. Thirdly, how averaging the forward and backward scan of a cyclic voltammogram could be used as a new method to reduce capacitive noise.

5.1.1. Near-stationary CVs for smooth Pt required scan rates <5 mV/s

Flat rotating platinum electrodes are well studied systems for the characterization of the oxygen reduction reaction [117]. The scan rate during cyclic voltammetry of such an electrode was altered in absence of any convection to estimate a rate at which e.g. $\delta_{N_{max}}$ had fully developed to avoid transient currents. The similarity of the currents at a respective forward and backward step indicate the degree of non-transientness and was measured by the hysteresis (Δj). The absence of a hysteresis indicated that the potential increments are small enough that concentration profiles as well as diffusion layer thickness should be approximately time invariant at each respective potential step.

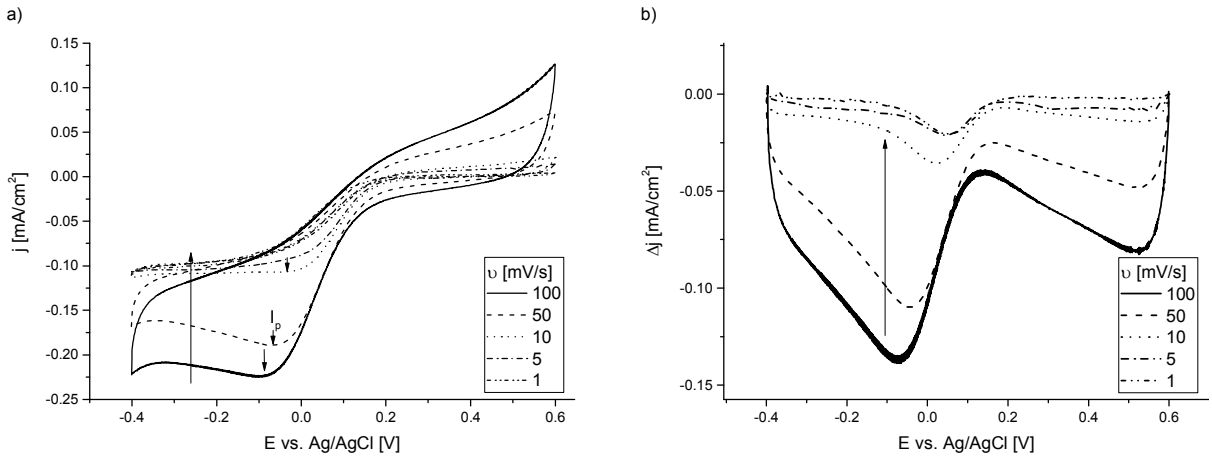

Figure 43: a) Cyclic voltammograms with varying scan rate υ (mV/s) of a platinum disc electrode (1.6 mm Ø). Phosphate buffer, ambient temperature, no convection and $\omega = 0\frac{1}{s}$. *Oxidative currents at low overpotentials are due to a starting potential above the OCP. Small arrows indicate peak currents (I_P). b) Hysteresis of the respective cyclic voltammograms. Long arrow indicates direction of decreasing scan rate.*

At decreasing scan rates, the reductive peak currents I_p decreased in a Randles-Sevcik manner with the square root of the scan rate υ (*Figure 43*; small arrows). By further decreasing υ, the current peaks flattened and started to disappear at below 5 mV/s. The hysteresis between the forward and backward scan became negligible and a sigmoidal shaped current wave was revealed. Within −0.1 and +0.1 V vs. Ag/AgCl currents remained different for the forward and backward scan even at a slow scan rate. Thus, scan rates ≤5 mV/s should be used if time invariant polarization curves for a macroscopic platinum electrode are desired to estimate currents under non-convective conditions.

5.1.2. Near-stationary CVs for high capacity AC required scan rates <1 mV/s

AC is a promising material to serve as a cathode for Microbial Fuel Cells, but also as a good capacitor [78]. A large hysteresis (Δj) of a cyclic voltammogram in absence of distinct current peaks indicate high capacitive currents. Due to low catalytic ORR-activity the underlying faradaic currents are often low and to estimate them the scan rate must be adjusted accordingly to lower capacitive currents. Hence, to reveal the underlying polarization curve for highly capacitive materials with $I_{capacitive} \ll I_{faradaic}$ one requires especially slow scan rates.

AC exhibited a previously liver shaped cyclic voltammogram [118] and high capacitive currents (*Figure 44* a) [119]. The specific differential capacity was 359 ±8 mF/cm^2 (29.9 F/g based on 120 g/m^2 for FM10) at 300 vs. Ag/AgCl for the backward scan ($R^2 = 0.996$). To compare the differential capacitance more accurately, oxygen could be removed by nitrogen sparging to reduce the faradaic impact.

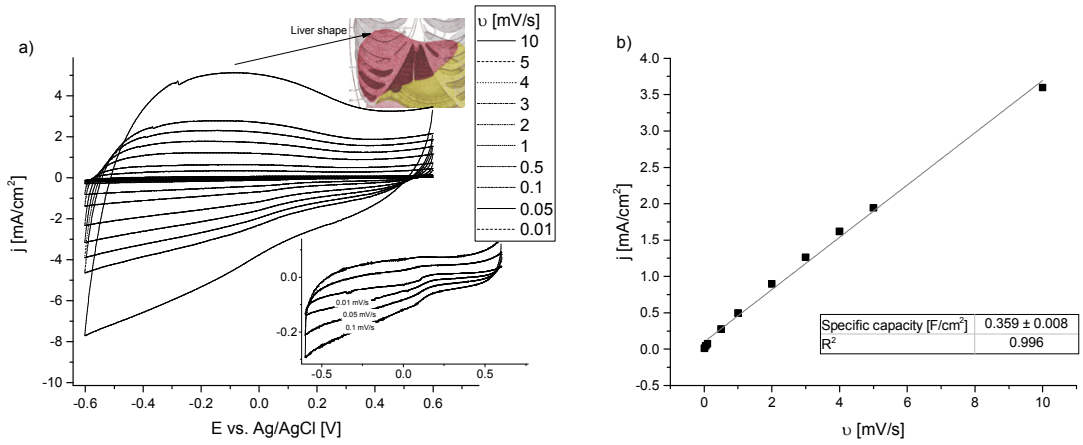

Figure 44: a) Cyclic voltammograms at varying scan rates for activated carbon cloth (Zorflex®; FM 10) and b) the derived capacity of the backward scan @ 300 mV vs. Ag/AgCl. Scan rates ranged from 0.01 mV/s up to 10 mV/s. Electrodes were polarized in phosphate buffer (50 mM; Conductivity: 5.9 ±0.1 mS) at room temperature and pH = 7. No convective mass transport and no air sparging was applied to mimic application conditions. The Buffer was kept in equilibrium with the gas phase to maintain constant oxygen availability amongst all experiments.

Differential capacitance for flat metal surfaces ranges within 5–50 µF/cm^2 dependent on temperature, ionic strength of solution, electrode potential and electrolyte composition [21]. The double layer capacitance of AC in aqueous electrolytes can exceed 150–300 F/g [120] e.g. capacities for nitric acid treated activated carbon fibers has been reported to reach 170 F/g [75] for carbon fibers derived from electrospinning. Therefore, a difference between forward and backward scan remained visible despite reducing the scan rate down to 0.01 mV/s. Hence, determining only the faradaic currents for high capacitive materials remains challenging. Based on the linear dependency of capacitive currents and scan-rate, a way to determine averaged polarization curves is presented in the following section.

5.1.3. Averaged CVs approximate a stationary state more accurate than LSVs

Would there be a way to reduce measurement time of polarization curves of high surface area by reducing the capacitive currents? To answer this question, average polarization curves were derived from cyclic voltammograms at different scan rates and the respective currents were

compared and correlated with the scan rate. The average of a cyclic voltammogram was derived by calculating the mean current of the forward and backward scan at each respective potential step (Figure 35).

Figure 45 indicates that averaged polarization curves of activated carbon were well matching compared to a steady-state, chronoamperometrically determined curve given a broad potential window. Reducing the scan rate from 0.1 to 0.01 mV/s resulted in a better approximation. The measurement for 0.5 mV/s was most time efficient, as it matched well and required only 3 hours in contrast to the steady-state estimation with 13 steps of 6 hours which required three days of experimental time.

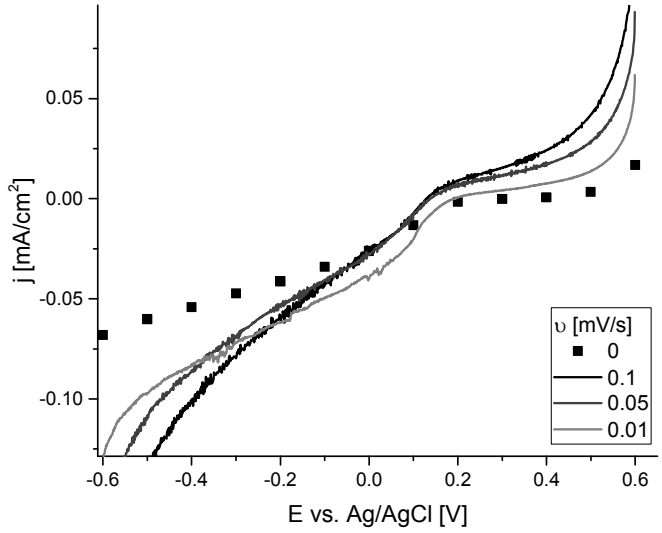

Figure 45: Average polarization curves of activated carbon cloth (Zorflex®; FM 10) compared to chronoamperometric currents (0 mV/s). Scan rates ranged from 0.01 mV/s up to 10 mV/s. Averages were derived from the mean of the forward and backward scan of the second cyclic voltammogram (CV) of a series of CVs. Electrodes were polarized in phosphate buffer (50 mM; conductivity: 5.9 ±0.1 mS/cm) at room temperature and pH 7. No convective mass transport and no air sparging was applied to mimic application conditions. The buffer was kept in equilibrium with the gas phase to maintain constant oxygen availability amongst all experiments.

5.2. Summary and discussion

The analysis of the sewage, the sewer structure and the possible MFC designs showed limited convective conditions. This should be considered in material studies. Therefore, cathode materials intended for sewer integration were compared at non-convective conditions. To do this, flat and porous materials were tested at low scan rates to minimize transient interference currents. Flat and smooth platinum required scan rates below 5 mV/s and porous and capacitive AC required scan rates below 1 mV/s. Otherwise, if MFC high capacity cathodes are characterized at high scan rates heavy transient and capacitive currents will distort the results. In addition, it was shown how that averaging the CV curves can produce less transient polarization cures in less time-consuming experiments.

Two other methods might allow to decrease the effects of capacitive currents: Staircase voltammetry and square wave voltammetry (SWV).

In staircase voltammetry, a staircase shaped potential signal is applied instead of a linear sweep. The current is determined at the end of each potential step which reduces the impact of capacitive double layer charging which decreases exponentially with time. If the number of steps is high, this results in a capacitive free linear sweep voltammogram.

Could square wave voltammetry be another useful method [121]? It has been used previously to characterize AC [122]. Hereby, in addition to the above method, a square wave shaped potential signal is superimposed onto a staircase voltammetry signal. The outcome of the SWV is ΔI, which is the difference between the current response of the first and second half square wave amplitude. SWV provides excellent interference free signals for analytical purposes, but the ΔI allows not to state a polarization curve.

This indicates that rather staircase voltammetry would be preferable, since the faradaic currents at each potential step better reflect the behavior under application than the ΔI from SWV.

Mechanistic studies often require high scan rates to determine the different intermediate steps of a reaction but high capacity materials such as activated carbon prohibit fast cyclic voltammetry. Neither staircase nor square wave voltammetry appear to resolve this problem, since they rely both on an extended measurement time during a held step which interferes with the short lifetime of intermediate steps as well. For mechanistic studies the author suggests avoiding capacitive material structures in the first place or to process a capacitive material to reduce capacitance accordingly.

6. Love is in the air: Cathode improvement by capillary forces

The previous chapter suggested several sites within Braunschweig that provide suitable anaerobic conditions especially for placement of biotic MFC anodes. Now, the question arises how to properly position the oxygen demanding cathode with respect to the anaerobic electrolyte. Since the oxygen concentration within the sewage is low, its mass transfer is likely to be limiting. To face these limitations, this section presents a systematic approach for making use of electrode liquid interphase effects and capillary forces to increase cathode performance. It presents (vertical) air exposed cathodes that benefit from a three-interphase system outside the anaerobic sewage to ultimately increase oxygen transfer. In addition, it shows potentially interfering species such as lipids and surfactants and finally, transforms these findings into real waste water driven MFC application.

The paths to increased oxygen mass transfer are manifold. Air-diffusion cathodes commonly used in laboratory setups provide direct air access to the cathode [123]. The idea behind is derived from Hydrogen Fuel Cell's well known gas diffusion layers (GDL), where cathode performance is increased by balancing a minimized electrolyte contact with maximum air exposure at the catalyst [124,125]. Cathode design for MFC-field application drew much fewer attention to it. Corbella and colleagues argued that the best cathode position in horizontal subsurface flow constructed wetlands would be in proximity of the surface, but they did not investigated the interphase phenomena in detail [126]. Yet, a structured approach for proper cathode positioning within the sewer needs to be undertaken.

How does mass transfer impacts electrochemical reactions? If the concentration of the reactant at the electrode surface is non-zero, the reaction is only governed by the rate constant. When it reaches zero, the mass transfer towards the electrode rules the reaction instead. As described earlier these conditions are determined by the diffusion coefficient and the mass transfer coefficient k (m/s). The constant k is the quotient of bulk concentration c_0 and the Nernstian diffusion layer:

$$k = \frac{c_0}{\delta_N}$$

In industrial electrolysis, the limiting current is raised by either

1) increasing the concentration c_j of the electrochemical active species or
2) decreasing δ_N trough induced convection of the active substance (by stirring, bubbling etc.)

Which of these parameters can be controlled to increase mass transfer in a sewer integrated MFC? Changing the diffusion coefficient is rather not possible as it is likely to be environmentally predetermined e.g. by the temperature and electrolyte composition. Similarly, the oxygen concentration is a result of temperature, oxygen influx and consumption by microbial processes. Stirring to decrease the Nernstian diffusion layer is neither an option, due to its high-energy cost. This leaves only one option for increased mass transfer: The decrease of diffusion layer thickness by proper cathode design. This is done also in in the GDL of conventional Fuel Cells by promoting thin film three interphase areas, where solid, gas and liquid are in intermediate contact with each other [21].

Capillary forces originate from the attraction between a solid and a liquid phase and result in the formation of a meniscus. The top of the meniscus is the visible representative of a thee interphase system. These forces are strong enough to drag an aqueous electrolyte into a hydrophilic electrode material until attractive and gravitational forces reach equilibrium. The result could be a vertical electrode with increased air-liquid interphase with a decreased Nernstian diffusion layer, and thus an increased mass transfer.

At the same time, as adsorptive forces might increase cathode performance, the enrichment of a chemical species at the solid liquid interphase might also lead to aversive effects. If fatty acids are present in the aqueous electrolyte, they could adsorb on a variety materials suggested as oxygen reduction catalyst e.g. activated carbon, carbon black, carbon nanofibers, carbon synthesized from natural precursors (Carboard and pomelo peel) and metal carbon hybrids [19]. They are likely to occur at the interphase since lipids (Oil, grease, fat and fatty acid) generate 30–40% of the total chemical oxygen demand of waste water [127]. Hence, the lipid blocking of accessible surface area would affect the electrode performance. Similarly, surfactants present in waste water might change the liquid and material surface characteristics which might also interfere with the desired interphase effects.

6.1. Results

First the formation of a three-interphase system was investigated during vertical movement of a flat graphite electrode. This knowledge was then applied to the surface of hydrophilic porous electrode materials. Then the effect was tested in long term and in dependency of tidal wetting, simulating the sewage level changes. Afterwards the possible effects of oil and surfactants were examined and finally the principle of air exposed cathodes was applied to a real waste water fed MFC.

6.1.1. The three-interphase system at the meniscus is beneficial for reduction

The meniscus is of interest for heterogenous catalysis because it represents a solid-liquid-air interphase system. A meniscus adhered at the macroscopic electrode might already increase mass transfer. To elucidate a possible positive effect at macroscopic level, a negatively poised graphite cathode was moved repetitively forth and back vertically through an electrolyte layer while recording its currents. The effects at the electrode-liquid interphase were filmed by a microscope camera.

Figure 46 shows the dependency of reductive current on the spatial electrode position. The reductive current increased as the submerged electrode approached the interphase. It suddenly increased more significant, as the electrode started to pass the electrolyte forming a meniscus. As the meniscus is stationary and the electrode proceeds to leave the electrolyte, the reductive currents decrease linearly with air exposure of electrode surface.

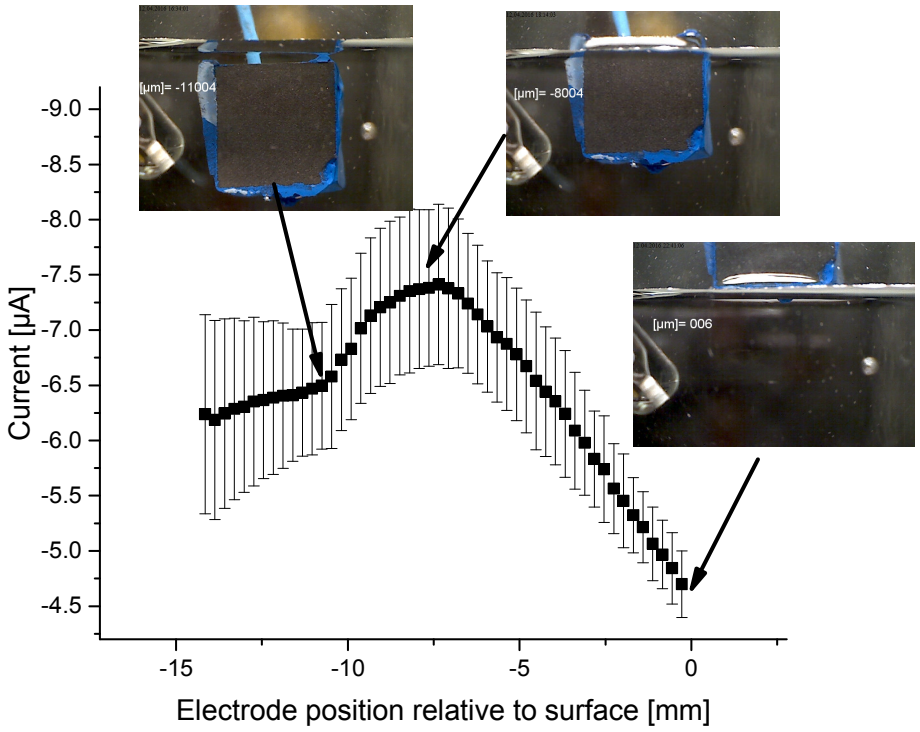

Figure 46: Current response during meniscus formation. A 1 cm² graphite electrode was moved out at 0.5 µm/s of 50 mM phosphate buffer at room temperature. The images illustrate the position of graphite electrode. The electrode was polarized at; −200 mV vs. Ag/AgCl. (Inverted y-axis)

Is there a similar, adverse effect when the three-interphase system is lost? When the electrode is moved back into the electrolyte and below liquid level, the meniscus disappears and a sudden

loss of reductive current is noticed (Figure 47). The loss of 1 µA is equivalent to that gained during the previous meniscus formation (Figure 46).

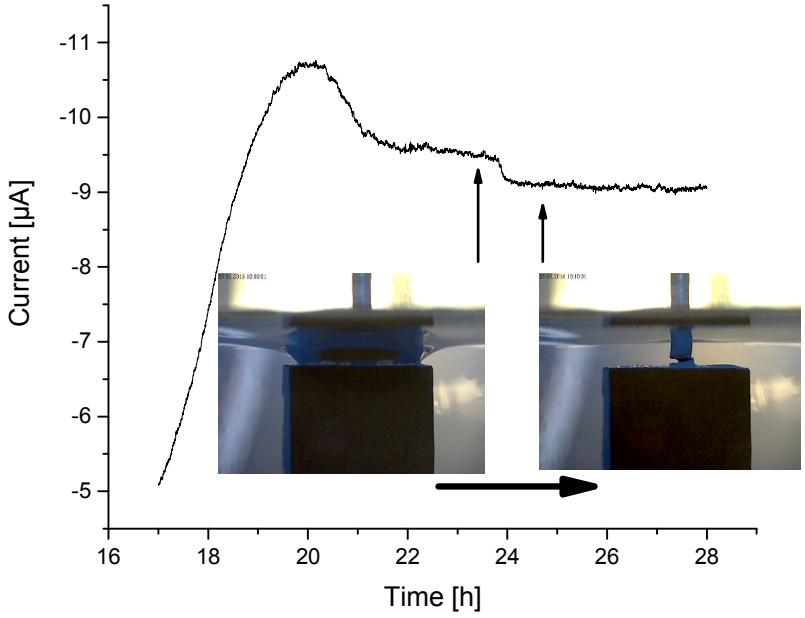

Figure 47: Loss of three interphase system during electrode submersion decreases reduction currents. The picture series illustrates the collapse of the liquid surface above the electrode. Graphite electrode of 1 cm x 1 cm. Supporting electrolyte: 50 mM phosphate buffer at room temperature.

Both experiments indicate that vertical electrode arrangement can promote meniscus formation and therefore lead to a small three-interphase area which ultimately empowers reduction performance. What if the interphase region could be extended further into the vertical by using more attractive electrode materials?

6.1.2. Air exposure almost triples cathodic currents of porous cathodes

Since capillary force derived interphase effects appear to positively influence cathodic currents on flat materials, the previously described porous cathode materials were tested. Activated carbon (AC), layered corrugated carbon (LCC) and reticulated carbon foam (RCF) were more hydrophilic than graphite, and thus expected to benefit even more from air exposure. Different electrode materials were submersed and exposed to air in a cyclic manner and compared with respect to their cathodic currents. Graphite and platinum were used as a control for non-porous flat electrode materials.

All porous materials increased in reduction performance not only to a small extent upon meniscus formation but over the whole range until being fully exposed to air (Figure 48). This effect is most pronounced for activated carbon (FM 100) whose reductive currents almost triples upon air exposure. The other porous materials doubled their current density. In contrast, the flat graphite and platinum electrodes showed their highest reductive not when exposed but when being completely submersed. In conclusion air-exposed porous electrodes resulted in a more than 100% increase of reductive currents – flat and smooth materials did not.

To account for the macroscopic pore orientation of LCC it was compared with its inner macro channels either oriented parallel (=) or perpendicular (||) with respect to the electrolyte surface. The perpendicular oriented macro-pores were found to outperform the horizontal oriented ones.

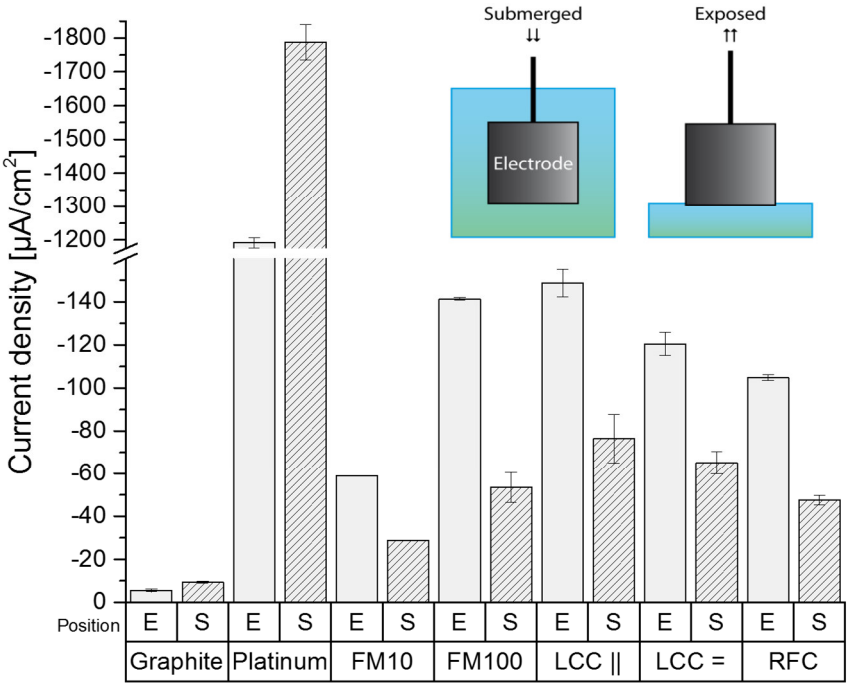

Figure 48: Current density in dependency of relative electrode position. Symbols: E: Electrode exposed; S: Electrode submerged. Chronoamperometric measurement at +200 mV vs. Ag/AgCl. n = 3, except for FM10 (n = 1). Porous electrodes and graphite electrode dimension: 1 cm².

Are these effects due to change in mass transfer resistance? A quick calculation indicates that mass transfer limitations were present and that they derive from the depletion of oxygen within the electrode. As the maximum concentration of 8 mg/L oxygen result in 25 nmol of oxygen within the volume of a 1 mm thick 1 cm² electrode (AC, FM100) and the current of 140 µA results in the consumption of 362 pmol/s all oxygen would be consumed within ~70 s in absence

of oxygen influx. This emphasizes the likeliness of Nernstian diffusion layer formation due to oxygen removal at the electrode surface and interior.

It appears that air-exposed porous and hydrophilic electrode materials attract electrolyte far above the liquid level. In contrast to flat materials, this might have resulted in a three-interphase layer which extended to the complete exposed surface and ultimately decreased mass transfer limitations.

6.1.3. Air exposed cathodes outperform submersed electrodes in long term

Electrodes just moved out of the liquid phase are covered by thin film and soaked with electrolyte. Will the thin layer and its respective positive effect on oxygen mass transfer remain, also when facing evaporation of electrolyte during long term studies? To investigate the benefits of liquid-air interphase placement constantly polarized cathodes were compared for over one week. These electrodes were either submersed or exposed to air.

Figure 49 shows that floating electrodes (red) outperformed the submerged (black) electrode during the whole period. Both electrode types increased slightly in reduction rate and showed only minor variance over the course of time.

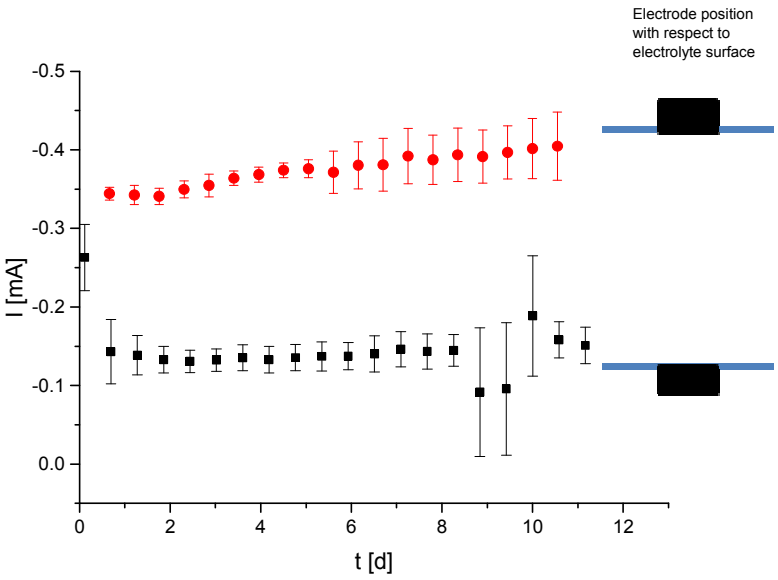

Figure 49: Long term reduction performance of carbon felt either exposed or submerged while being polarized at −200 mV vs. Ag/AgCl. Projected electrode surface area: 4 cm^2. Supporting electrolyte: 50 mM phosphate buffered saline at room temperature.

This indicates that the three-interphase system is not perturbed by evaporation of electrolyte from the electrode. Evaporated electrolyte might be replenished by the constant drag of capillary forces.

6.1.4. Mimic the tidal behavior of the sewer

The intraday transition of sewage levels will induce a periodic wetting of the sewer integrated cathode. The wetting speed will be high upon a heavy rain event, then water level will rise and fall quicker than during the normal man made daytime variations. Beneficial effects of tidal cathode wetting with constant frequency have been seen earlier [128] but they have not been systematically for varying electrode exposure speed. The impact periodicity has guided this experiment. Its effect on current response of a polarized porous cathode was recorded during several cycles.

Current effects of the slow-moving electrode correlated in an immediate manner with electrode position, e.g. current rose instantaneously after the electrode penetrated the liquid surface (Figure 50). In contrast, the faster moving electrode showed a latency in response. Interestingly, it even showed an unexpected drop after being fully exposed. After the fast electrode reached full air exposure its reduction increase until maximum, but first experienced a slight peak. In general, as seen earlier the reductive current increased while the electrode was moved out of the electrolyte. Upon full exposure of the electrode, the reductive current almost quadruples.

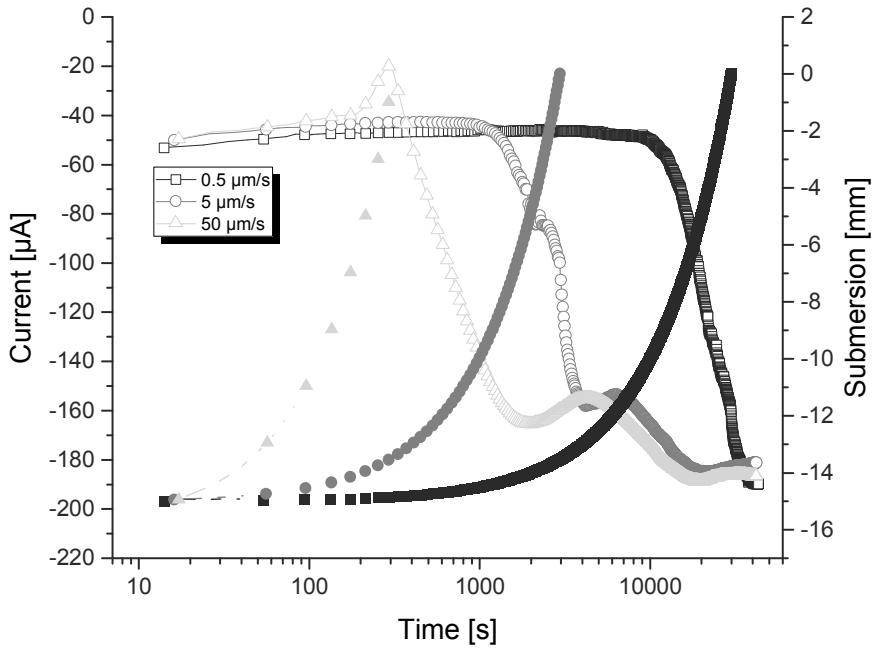

Figure 50: Reductive current dependent on submersion level and on tidal speed during cyclic submersion. Filled symbols: Submersion level. Open symbols: Reductive currents. Material: RFC. Supporting electrolyte: 50 mM phosphate buffer at room temperature. Log scale.

This experiment indicated that the reduction increasing lagged behind the visible interphase effects. A possible explanation would be, that upon electrode exposure the initial thick electrolyte film coverage gradually fades until a minimum film thickness is reached which eventually results in reduced mass transfer resistance.

6.1.5. Reduced electrolyte contact increases electrolyte resistance

The air exposure of electrodes within this study led to higher reductive currents but also to decreased electrolyte contact. Decreasing the electrode-electrolyte contact area will result in a less conductive salt bridge and ultimately increase total internal MFC-resistance. Therefore, the impact of electrode position and electrolyte contact on resistance was estimated. Figure 49 shows how the electrolyte resistance increased upon changing electrode exposure. It almost tripled when the electrode was fully exposed to air (0%) and only in contact to electrolyte at the bottom.

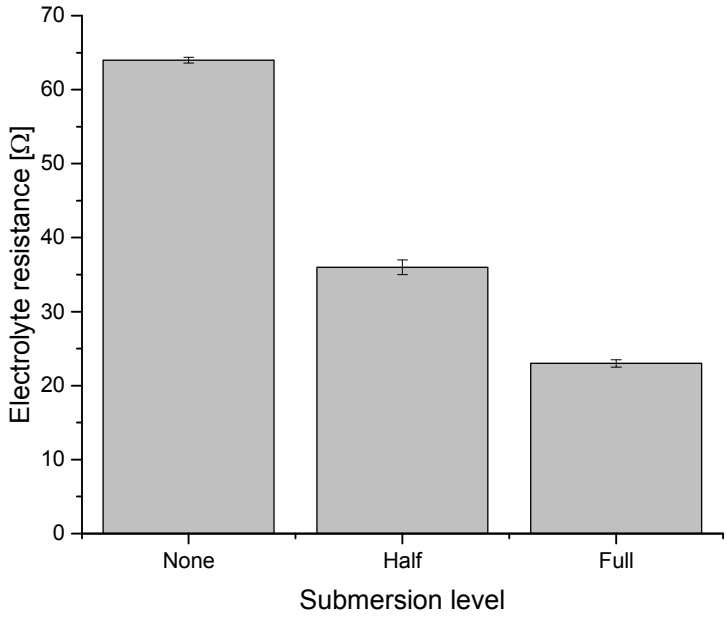

Figure 51: Electrolyte resistance depending on submersion level. Material: RFC. Supporting electrolyte: 50 mM phosphate buffer at room temperature.

This indicates that the loss of electrolyte contact of air exposed electrodes will increase the total internal resistance of a Microbial Fuel Cell and its systematic effect should be estimated before implementation.

6.1.6. Oil blocks the electroactive surface and decreases cathodic currents

Oil, grease and fatty acids are commonly found within sewage [129]. As they might adhere to electroactive surfaces [130] their impact on cathode performance was investigated. For this purpose, a polarized graphite cathode was moved periodically from electrolyte into a covering oil layer to record the respective current response.

Periodic electrode movement in plain buffer resulted in stable cathodic currents which even slightly increased towards high cycle number (Figure 52). In contrast, the same movement in presence of an oil layer gradually decreased the reductive currents with each cycle.

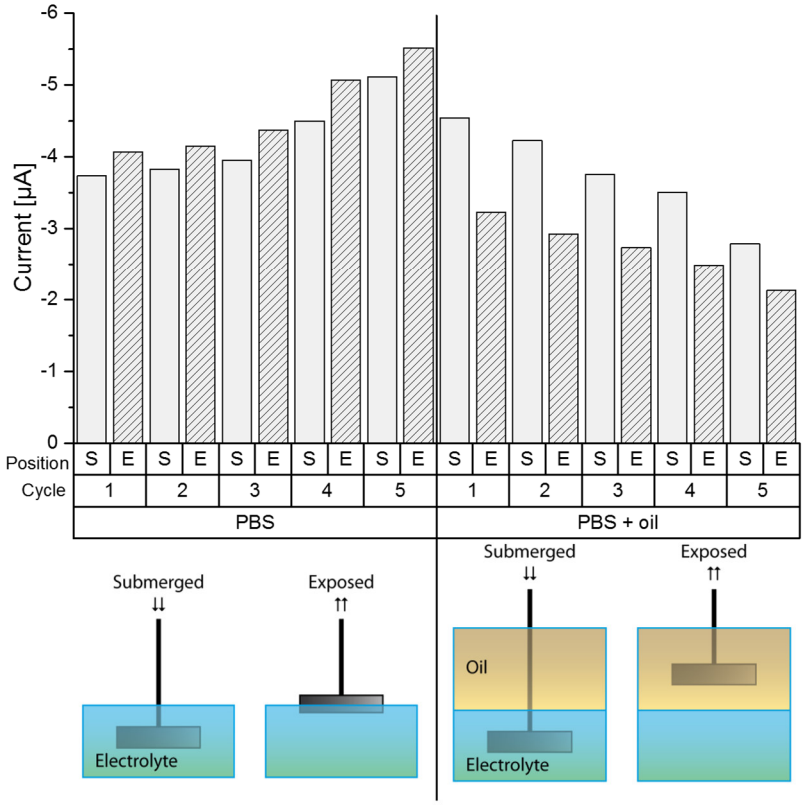

Figure 52: Current response during cyclic exposure of graphite electrode to a canola oil layer (right) compared to a control (left). Supporting electrolyte 50 mM phosphate buffered saline at room temperature. S – Electrode submerged; E – Electrode exposed (with marginal electrolyte contact).

This indicates that lipids such as canola oil might block electrode surface area and negatively impact cathode performance.

6.1.7. Presence of surfactant does not alter current behavior of activated carbon

Like lipids, surfactants are substances found commonly in waste water. To evaluate their impact, potential changes of capillary effects were study in presence of 1 mg/L sodium dodecylbenzenesulfonate (SDBS, typically found in detergents). An activated carbon cloth electrode was observed for several cycles being exposed (E) and submerged (S) in phosphate buffered saline with and without SDBS at room temperature (Figure 52).

No significant difference was found between the current behavior of activated carbon in presence of absence of surfactant. This indicates that SDS at the concentration of 1 mg/L had no significant impact on effects that influence cathode performance.

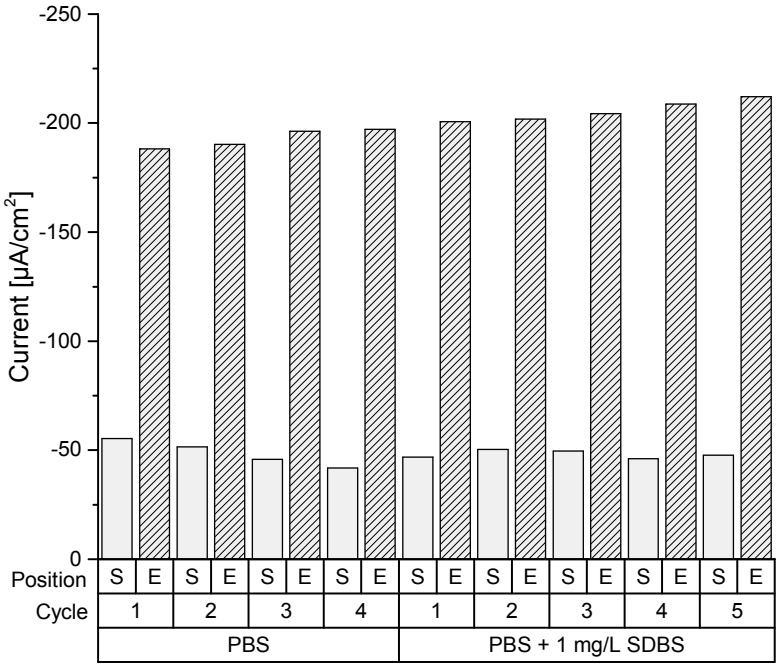

Figure 53: Current densities of activated carbon (FM100) being either exposed (E) or submerged (S) in 1 mg/L sodiumdodecylbenzensulfonat (SDBS) 50 mM phosphate buffered saline.

6.1.8. Floating cathodes increase power output of sewage based MFCs

In the previous sections electrode-performance has been tested in potentiostat controlled and buffered experiments. Negatively poised electrodes are likely to govern performance by mass transport limitations. Under these circumstances exposing electrodes partially to air was beneficial for reduction performance. Will these interphase effects be also beneficial for reduction in a real waste water fed Microbial Fuel Cell without controlled cathode potential where mass transfer might be less limiting?

This was tested in a closed-circuit MFC with 100 Ω external resistance, copper contacted activated carbon cloth cathodes and precultured microbial anodes. Two spatial electrode positions were tested in a batch cell, either submersed or exposed while floating in a waste water tank. The electrodes were compared with respect to their effects on cell performance. The current and was calculated according to Ohms law and related to the geometric surface area.

Floating cathodes performance was throughout higher compared to the submersed electrodes (Figure 54). Their cell potential remained above 50 mV with little decay until day five. After day five their cell potential gradually decreases to almost zero around day ten. In contrast, submersed electrodes cell potential dropped to almost zero within the first two days.

Acetate was added as feed for the bioanodes upon depletion of cell potential. The addition of 10 mM acetate rapidly restores cell potential for both electrode types. But again, floating cathodes performance was higher. Its cell potential remained higher and decayed less quickly compared to the submersed electrodes. This indicates, that the drop of cell potential was caused by the lack of feed for the anode respiring bacteria and not primarily due e.g. cathode aging.

In addition to the cell potential, the temperature and pH were estimated. Acetate addition resulted in a sudden increase of temperature and pH. The temperature change is likely due to heating derived from microbial metabolic activity and pH increase as sodium acetate represents a weak base. Interestingly the addition of a second acetate spike decreased floating cathode cell potential, but showed no comparable effect on submersed cathodes nor on pH nor on Temperature.

The results confirm the previously found beneficial effects of air exposure on activated carbon electrodes became also evident in a real Microbial Fuel Cell setup.

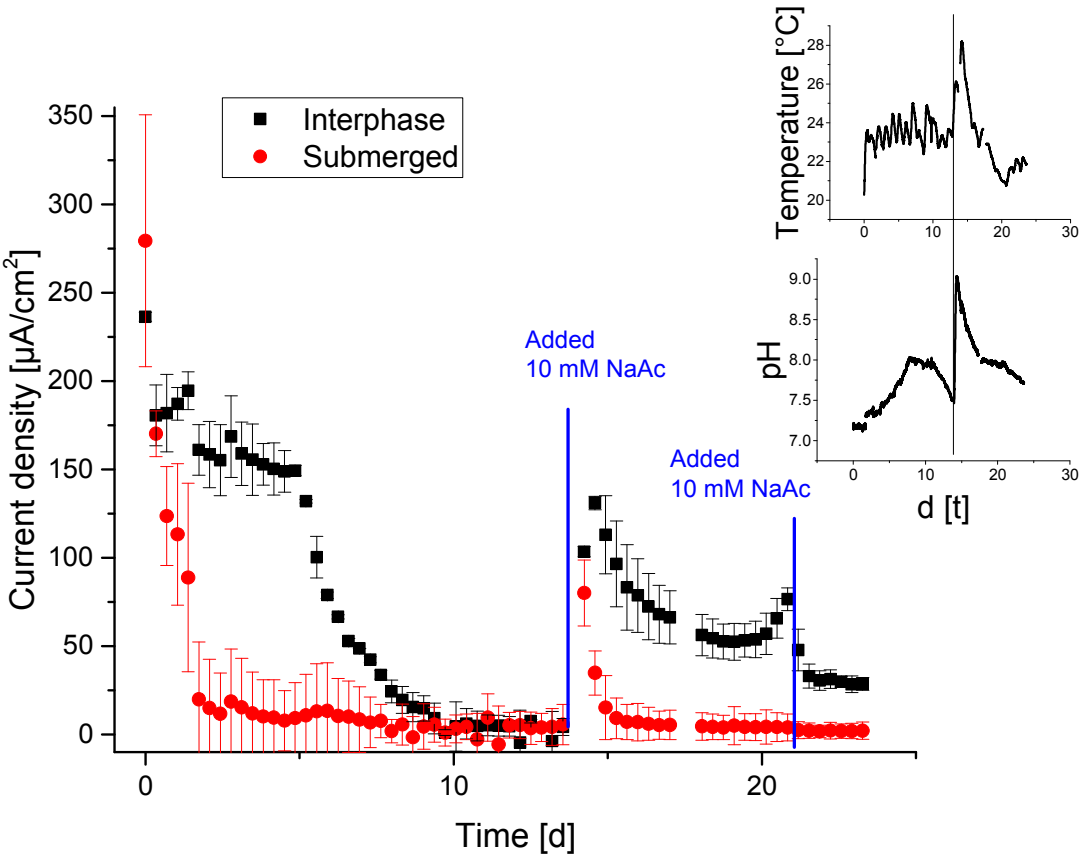

Figure 54: Comparing air exposed and submerged cathodes in a batch Microbial Fuel Cell fed with waste water at room temperature. Secondary anodic biofilm pre-grown in potentiostat controlled experiments. Geometric cathode surface area 25 cm^2. Geometric bio anode area: 21 cm^2. $R_{cathode} < 2.5\ \Omega$; $R_{anode} \sim 0.05\ \Omega$. Electrode distance: 10 cm. Occasional 10 mM acetate (NaAc) feeding indicated by straight lines.

6.1.9. Cathodes and anodes suffer from performance loss after being used in MFC

Replenishment of feedstock partially restored the cell performance, but its initial value was not reached (Figure 54). The reduced cell performance might be partially due to aging of cathode material, corrosion of the current collector or degradation of the biological anodes. Thus, the origin of performance changes was traced by the following investigation.

The floating cathodes have been subject to biomass accumulation during MFC operation (Figure 55). Especially the surface water above the cathodes was covered with a floating biofilm. In contrast, the exposed electrodes were less covered with biomass. The fibers of the electrodes have been partially covered with depositions as could be seen by confocal laser scanning images (Data not shown).

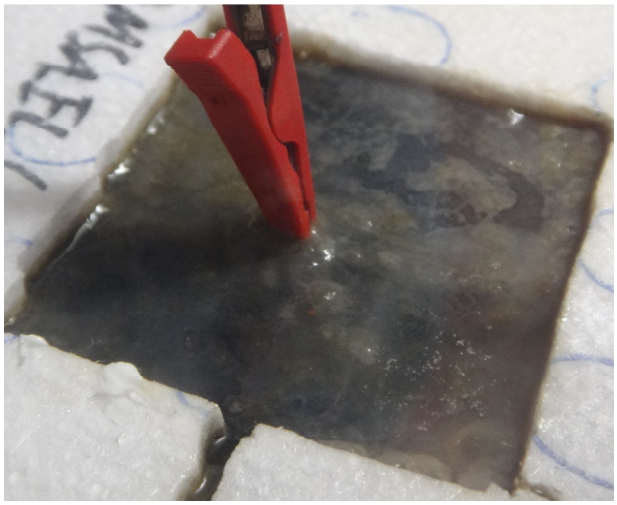

Figure 55: Presence of biomass floating on top of submerged electrode.

The changes in electrochemical behavior were assessed by comparing new, used and HCl cleaned cathodes by linear sweep voltammetry. Figure 56 illustrates that performance did drastically decrease at potentials below −200 mV vs. Ag/AgCl, but not significantly at potentials above. As argued in the previous section, only the potential above −200 mV is of relevance for MFC application. This indicates that electrode characteristics remained suitable.

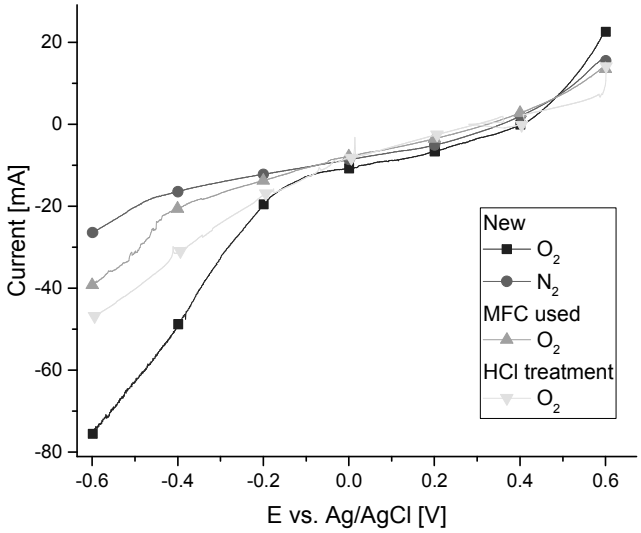

Figure 56:Linear sweep voltammetry of new, used and HCl cleaned electrodes in 50 mM phosphate buffered saline at room temperature. Electrodes were either tested in presence (O_2) or absence (N_2) of oxygen.

A more significant origin of performance losses became evident when comparing resistances. The ohmic resistance of the fresh cathodes increased from 1.8 ±1.3 Ω to 30.0 ±3.9 Ω when they were used at the air-liquid interphase and to only 9.5 ±4.1 Ω when they were submerged. The

increased resistance first indicates the possibility of copper corrosion, which was confirmed by the black oxide layer found on the current collector and secondly, that the increased air exposure of interphase electrodes might have resulted in in higher copper oxidation rate.

Beside the inorganic cathodes, also the biotic anodes where compared before and after MFC application. For this purpose, biotic maximum current generation was traced and averaged over three cycles before and after application. The current density decreased from a typical value of 1.00 ±0.07 mA/cm^2 by 30% to 0.71 ±0.06 mA/cm^2. In addition, the outer appearance of the bio-anodes was observed and found to be subject to changes. The fresh electrodes were initially uniformly covered with a smooth reddish biofilm and after usage left only partially covered with patches of darker biofilm as well as with areas of blackish depositions. The depositions might be due to precipitation of metal sulfides.

It can be concluded that all three major parts of the MFC are subject to aging effects, especially the current collector resistance and the biotic anodes.

6.2. Summary and Discussion

The principle of cathodes that make use of a three-interphase system is not new. Gas diffusion layers are a key element of conventional fuel cells [131]. The novelty of this study is to harness capillary forces to get a three-interphase system at a vertically arranged macroscopic air cathode intended for placement outside of an anaerobic electrolyte. From the authors point of view, such a system would be required to transform the partially filled sewer channels into a Microbial Fuel Cell.

Capillary effects

This study showed that interphase phenomena such as the formation of a meniscus positively effect macroscopic cathodes. Porous cathodes were found to perform even better than flat materials and increased more than double in performance. It would be desired to compare the results to other studies with regards to spatial cathode position, but most MFC cathodes were varied rather in the catalyst than in its position. Some studies note a negative effect of cathodes drowning in either its electrochemically produced water or in water leaking trough the membrane.

Previous studies found a positive influence of air exposure on MFC cathodes [126,132]. They tested the impact of changing water level with respect to a 1 cm high graphite-rod based cathode. They found that the cell voltage collapses when a cathode was submerged too deep into the anoxic

and that direct placement of the electrode at the water-air interphase resulted in highest cell potential. This is in accordance with the finding that cathodes submerged in anaerobic sewage result in negligible overall cell potential found in the application section of this study.

Tidal behavior

Periodical wetting of air cathodes was used to achieve intermittent oxygen supply in a so called tide-type biocathode Microbial Electrochemical System (TBMES) [128]. Gravity was used in a siphon mechanism to achieve tidal wetting. In this study, the speed of electrode exposure was changed which revealed a lag in current response upon fast electrode movement. This finding has a two implication: Firstly, that cathodes require a certain time after wetting to develop their maximum reductive currents and secondly, that the distinct signal patterns found for the fast-changing electrolyte levels might allow to interpret signals from a sewer integrated MFC. This would be a step into the direction of MFC-based sewer monitoring.

Oil and Surfactants

The graphite cathode exposed to canola oil lost nearly 50% of its performance. A comparison of the fouling effects found in this study was not possible since most papers about are only concerned about biomass fouling but not about the blocking with adsorptive chemicals [106,111,133,134].

Canola oil was used because of its similarity to the C18 rich fatty acid composition found in waste water [129,135]. It contains mostly oleic acid (64%; 18:1), linoleic acid (17.7%; 18:2) and *alpha*-linoleic acid (8.6% 18:3) [136,137].

Has canola oil itself undergone electrochemical reactions? It was assumed to not take part in the electrochemically reactions in the experiments of this study. Its unsaturated aliphatic parts and carboxylic groups are unlikely to react in our aqueous electrochemical setup at electrode potentials ranging from −0.2−0.8 V vs. Ag/AgCl. The cathodic reduction of aliphatic compounds is hardly possible under the present experimental conditions due to their low electron affinities [138]. The reduction of double bonds is possible but requires a hydrogen donor, such as formate [139–141] and/or an electrode potential well below −1 V vs. Ag/AgCl. The phosphate buffer present in our experiment neither provides a hydrogen donor nor do we apply cathodic potentials lower than −1 V. A cathodic reduction of aliphatic carboxylic acids is also very unlikely [138].

The anodic platinum counter electrode is poised below +1.5 V vs. Ag/AgCl. Thus, the carboxyl group won't undergo esterification or higher alkane formation by Kolbe electrolysis [138]. Accordingly anodic substitution of CH bonds which require +2.5 V vs. Ag/AgCl [138] is even less

likely. Therefore, we conclude that canola oil will not influence our faradaic currents by participating in electrochemical redox processes but only by adsorptive blocking of the electrode surface.

Application of floating cathodes

A floating type cathode might be useful for the application in waste water streams but it appears even more useful for open air environmental applications e.g. for cleaning eutrophic waters. As they adjust with the water level they are less susceptible to drying which was found problematic in wetland based MFCs [126].

Effects of aging of Anodes and Cathodes in MFC

In this study, the resistance of the current collector did increase between 5 and 15-fold, the bioanodes lost 30% of their performance and the cathodic reduction performance was only to a minor extend in the potential region of interest. Until recently only three papers discussed the problem of cathode fouling and already presented possible solutions [106,111,142]. Many other publications noted the problem of fouling but did not further investigated solutions to it [110,143–148].

6.3. Outlook

What are the possible maximum dimensions of cathods might applied within the sewer? This study was done for 1 cm electrode height – for scaling up, the limitations of drag forces are required to be considered. Nevertheless, the liquid stream from roots to leaves in trees shows that the interplay of evaporation and capillary forces can result in vertical liquid flow above several meters. The electrode dimensions should be varied to investigate the maximum vertical length capillary forces would be capable to increase electrode performance and to determine the best possible cathode thickness and length. In addition, a porous and hydrophilic material with increased catalytic performance should be used to point out the limitations of mass transfer.

To further account for environmental factors, the electrode performance should be determined in a humidity controlled experiment. This would allow to identify the possible range to operate a capillary force based cathode and what degree of dryness would result in fully evaporated electrolyte.

As cathode exposure increases total internal resistance, ways to increase its conductivity and the thickness of its salt bridge should be investigated. Beside the suffering from increased

resistance, air exposed electrodes might also suffer from the decreased ion mobility and a potential pH increase which negatively effects the theoretical oxygen reduction potential and therefore the overall cell performance [149]. It will be required to find a balance between the mass transport of the reacting species and the electrode position.

All the above experiments could benefit from the knowledge about Gas Diffusion Layer electrodes and the galore of equations describing them such as: interphase mass transport, the ohmic resistance within the electrode, the electrode kinetics and the material balances, electroneutrality, normal diffusion, Knudsen diffusion, the species transport within the electrode as well as the solvent transport and evaporation.

Oil negatively affected graphite performance. Its effect on the porous materials used in previous studies should be tested as well. Since oil and fats will negatively affect sewer integrated cathode performance, possible countermeasures should be considered. Additionally, the electrode should be tested more extensively within anaerobic sewage to account for periodic sewage wetting induced aging and biofouling. The single surfactant experiment with 1 mg/L SDBS did not affect cathodic performance of activated carbon. A variation of concentration and surfactant types should be done to identify if the observation follows a trend. Finally, the potential of surfactants to recover oil blocked cathodes should be investigated. Such an effect would show if the presence of surfactants in the sewer might induce a self-cleaning effect.

The problem of anaerobic sewage which is anolyte and catholyte at the same time could be damped by a separate sewerage network, where the rainwater carrying pipe would contain the cathode. At the downside, the function of the cathode would rely on rainwater influx and its internal resistance would be increased by the low conductivity of rain as seen earlier.

7. Anodic potential stimulates sulfide emission of EABs and ASS

Biological sulfide emission in the sewer is not desired. It causes severe damage by sewer corrosion, spreads unpleasant scent and endangers the operators [36,37]. Sulfate reducing microorganisms which are found in the bottom covering sewer slime are responsible for the autogenic sulfide emission in the absence of oxygen. There are several ways to face sulfide emission, such as increasing the redox potential of the sewage by adding oxidation agents, metal complexing agents or antimicrobial agents. The removal prices vary from 1.90 € up to 7.20 € per removed kilogram of sulfur [150]. Unfortunately the addition of chemicals is discontinuous, insufficient, and thus inefficient [151]. A way to target the origin of autogenic sulfide emission directly would be beneficial.

Would it be possible to control sulfide emission by replacing sewer slime with bioelectrochemical systems? Many findings in the literature agree on the decrease of spiked sulfide in the anodic compartment. Electrochemical oxidation [152,153] and even bioelectrochemical systems [154–159] showed good sulfide removal. However, these studies neglect that electrochemically active biofilms (EABs) are also capable of dissimilatory sulfate reduction at the same time [7] and the question arises which process will be predominant: Sulfide oxidation or sulfide emission.

It was tempting to dare the comparison between the natural source of sulfide emission, the sewer slime, with its possible substitute, the electroactive biofilms. The goal of this study was therefore, firstly, to compare the kinetics of autogenic sulfate reduction of electroactive organisms and artificial sewer slime and secondly, to identify if sulfide oxidation outweighs sulfide emission. The intention was to provide evidence if bioelectrochemical systems allow for sulfide emission control and if so to what extent.

For this purpose, first a reactor system was developed to cultivate artificial sewer slime under defined convective conditions and then this slime was compared to EABs with respect to their autogenic sulfide emission. This was done either in presence or absence of applied potential in a membrane less three electrode-setup. The substrate consumption and conversion rate, as well as the current production under potentiostatic control was compared to understand the underlying kinetics.

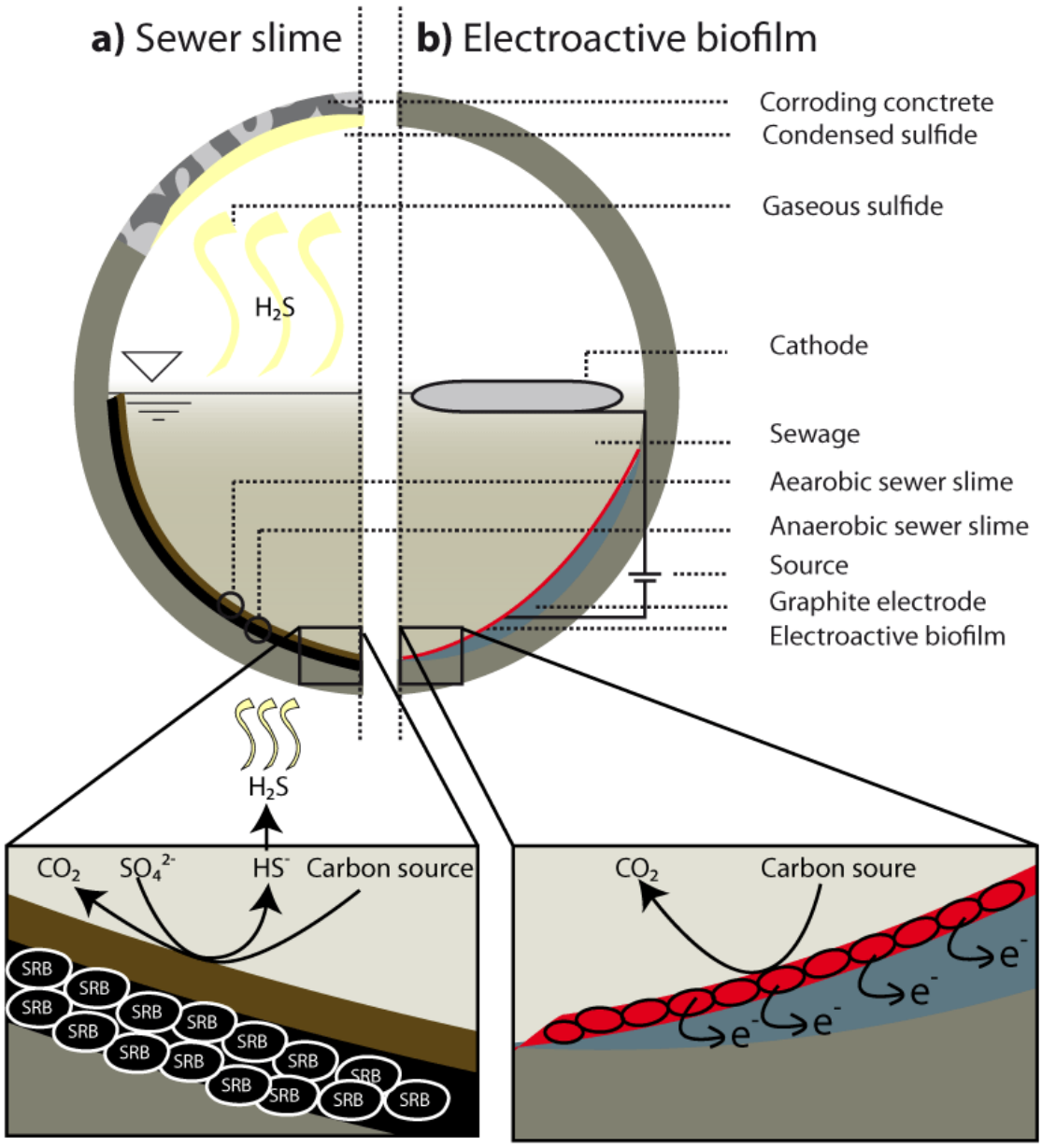

Figure 57: Hypothetical principle of H_2S emission control for a sewer using electroactive biofilms. a) Illustration of origin, fate and impact of sulfide within the sewer in presence of sewer slime and b) hypothetical scenario of reduced sulfide emission in presence of electroactive biofilm.

The following section provides a glance on the environment and composition of the sewer slime. Then the metabolic capabilities of the electroactive biofilms are explained to understand its participation in the sulfur cycle. Finally, sulfur chemistry and metabolic conversion are described to understand the sulfate metabolism of microorganisms.

Biogenic sulfide production in the sewer

Sulfate, the biogenic source of sulfide, is naturally occurring in fresh, ground and surface water which can ultimately end up in the sewer e.g. in form of processed tab water. The monthly tab water analysis report of the city of Braunschweig, Germany, stated its concentration in January 2017 was up to 60.7 mg/L with a pH of 7.8-9.1 [160].

Sulfate is converted to sulfide in the presence of desulfurization bacteria at temperatures favored above 12 °C. Endogenous sulfide is produced within the sewer, whereas exogenous sulfide comes from outside of the sewer. Within the sewage allogenous sulfide is produced by the free floating planktonic organisms, whereas the allogenic sulfide is produced by the sewer slime on the sides of the sewer. Sewer slime forms best on rough surfaces in the presence of reduced shear stress [161]. Natural factors that decrease the activity of sulfide reducing organisms are alternative oxygen donors such as nitrate or the influx of excess oxygen by the rain water. Factors such as mesothermal temperature increase the sulfide emission rate. The pH optimum for sulfide production lies between pH 7 and 8 as in the artificial waste water used in this study.

The composition of sewer slime

The sewer slime represents a complex syntrophic community of different layers and a variety of species. Its behavior depends on the presence of oxygen. Under aerobic conditions the sewer slime is divided in an oxygenic top and an anoxic bottom. Under these conditions the sulfide is first produced by the anaerobic bottom and then oxidized by the overlaying oxygenic top. Thus, sulfide is formed but not emitted. In contrast, under anaerobic conditions, the sewer slime is throughout anoxic and sulfide will be emitted. The anaerobic part of the sewer slime is 300 µm and covered by an aerobic part ranging between 300 and 1000 µm in thickness. A study of particular interest published by J. Sun et al. identified methanogens as the major species in the top and sulfur reducing organisms in the bottom of the sewer slime [162] and hence, revealed its broad metabolic spectrum.

Lactate based dissimilatory sulfate reduction

How is it possible that microorganisms gain energy from alternative electron acceptors other than oxygen? The dissimilatory sulfate reduction

$$SO_4^{2-} + 8e^- + 8H^+ \leftrightharpoons 4H_2O + HS^-$$

has a standard half reaction potential of E' of +0.016 V vs. Ag/AgCl. It is much lower, compared to oxygen reduction potential of around 0.8 V vs. Ag/AgCl at pH 7 but still high enough to represent an electron sink for the oxidation of many carbon sources, especially lactate.

Both biofilms in this study were adapted to lactate carbon source. Lactate is oxidized to provide energy to the cells, but its donated electrons require a final electron acceptor. Sulfate reducing bacteria utilize sulfate and lactate and convert it to sulfide, acetate, carbon dioxide, hydrogen carbonate and water.

$$SO_4^{2-} + 2\,Lactate \leftrightharpoons HS^- + 2\,Acetate + CO_2 + HCO_3^- + H_2O$$

This is an exergonic reaction as the Gibbs free standard enthalpy $\Delta G_0' - 157\ \mathrm{kJ/mol}$.

7.1. Results

7.1.1. Artificial sewer slime and electroactive biofilm production

A direct comparison between sewer slime and electroactive organisms has never been done before but is of distinct importance to evaluate the potential implementation benefits of electroactive organisms within the sewer. The comparison requires the two types of biofilm to be reconstructed in the laboratory: Artificial sewer slime (ASS) and electroactive biofilm (EAB). The cultivation of EABs has been well established during the last decade and biofilms became well characterized [12]. In contrast only few studies have been done on ASSes [162]. Thus, part of this study was dedicated to establishing a biofilm-growing-method to be able to compare EABs and ASSes. The results of biofilm growth are presented in the next section. Later, EAB and ASS will be compared with respect to their sulfide emission and metabolic capacities in absence and presence of an applied potential. The defined mimicking of these biofilms is advantageous over the application of MFC-derived biofilms, which are less defined due to more variations in the anodic potential and electrode chamber conditions [157].

7.1.2. During enrichment of EABs acetate is limited by lactate conversion

Typically, electroactive organisms are fed with acetate as this is the major carbon source of the important electroactive species of *Geobacter sulfurreducens*. However, sulfate reducing bacteria hardly produce sulfide in the presence of acetate as a sole carbon source, but function very well with lactate. Since this study compares sulfide emission of electroactive biofilms and

artificial sewer slime, lactate was chosen as carbon source for both biofilm types. Figure 58 shows the course of current during lactate and acetate batch feedings for three representative cycles. As lactate requires to be converted to acetate by the syntrophic community prior to be available to EABs, its conversion delay and rate represents limitations to anodic respiration. This can be seen from the immediate rise of current after acetate feed compared to the slower and less steeper increase upon lactate feeding.

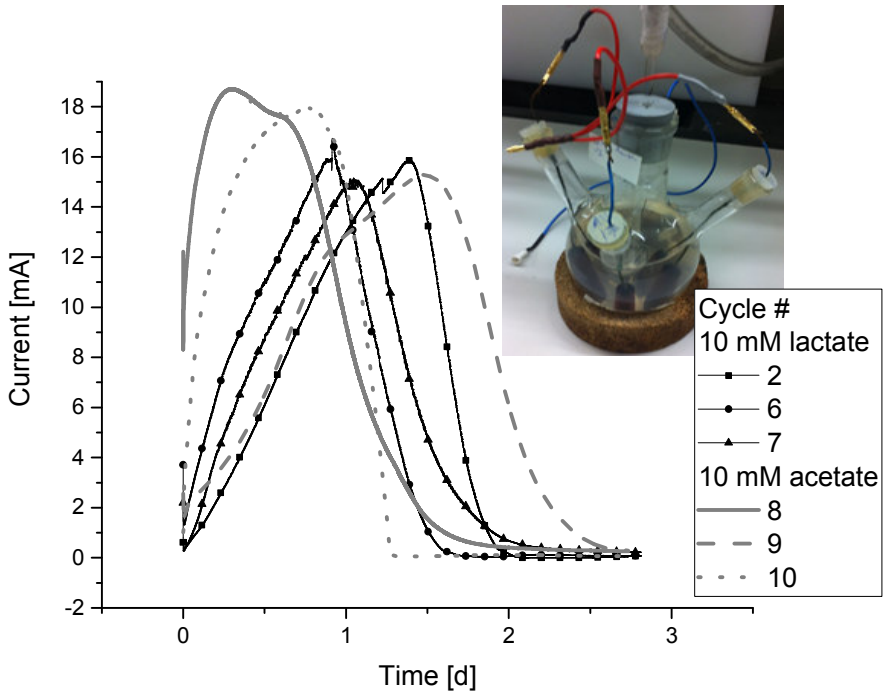

Figure 58: Current over time during enrichment of electroactive biofilms. Biofilms were grown on 3 cylindrical graphite electrodes (Dimensions: 3 cm l x 1 cm Ø; A = ~ 10 cm^2) connected in series (shown on inset image). Electrodes were kept in a multi neck round bottom flask filled with 250 mL AWW and fed with 10 mM lactate or 10 mM acetate. Enrichment potential 200 mV vs. Ag/AgCl. Reactors were incubated at 36 °C and stirred with 250 rpm. Representatives of total 7 lactate feed cycles and 11 acetate feed cycles are shown.

7.1.3. Artificial sewer slime was grown on graphite in a tubular flow reactor

A tubular flow reactor was designed to grow artificial sewer biofilm on smooth graphite electrodes. The reactor requirements were:

- Attachment of sewer slime on graphite electrode.
- Air tightness for an extended period to prevent oxygen entry.
- Defined shear forces for reproducible biofilm formation.
- Removal of electrodes without harming the biofilm.
- Easy to construct and cheap.

The reactor was constructed from plexiglass as described in the method section and run at shear stress of 0.2 N/m^2 with 10 mM lactate in 50 mM phosphate buffered artificial wastewater. Each biofilm was grown at room temperature within a closed loop attached to a 1 L media reservoir. The sulfide concentration was estimated from time to time. Media was replaced 2 times within 3 months.

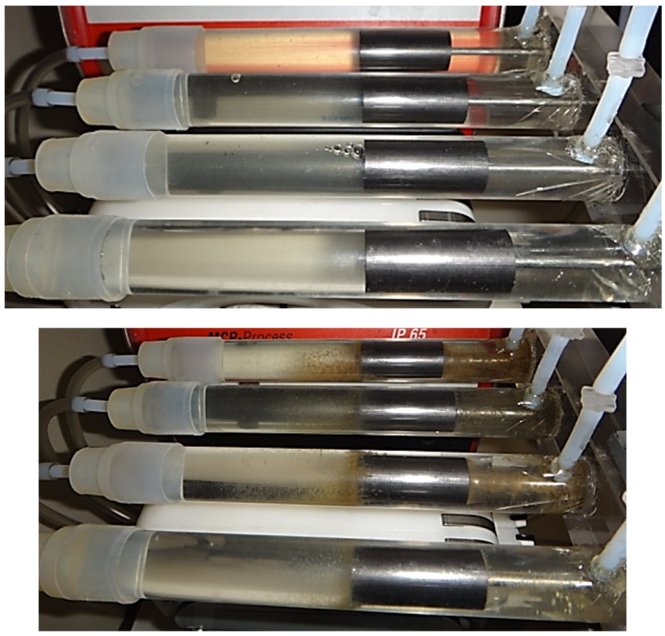

Figure 59: Reactor at the first day of operation (left). Reactor after 3.5 days of operation with visible depositions (right).

Prior to use of the ASS the reactor media contained 143.5 ±21.0 µM (n = 3) of sulfide except for one single reactor with zero µM. Absence of oxygen was proven occasionally by an amperometric dissolved oxygen sensor. Figure 60 shows the electrodes after three months of enrichment with biofilm and prior to its experimental application.

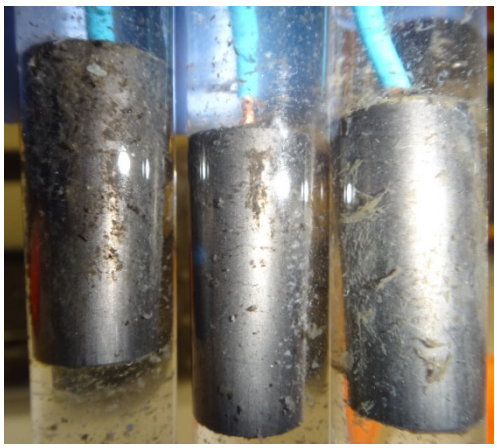

Figure 60: Fuzzy biofilm attached to smooth graphite regarded as artificial sewer slime. Electrode surface A ~10 cm^2. Electrode signatures from left to right: JMSA_Siel_01; JMSA_Siel_02; JMSA_Siel_03.

7.1.4. EAB's and ASS' sulfide emission and substrate conversion rate

It would be beneficial to not only remove sulfide electrochemically by anodic deposition [153], but to avoid sulfide production by means of bioelectrochemistry in the first place. A bioelectric sulfide prevention would be even more desired over a previously observed biogenic back-oxidation [155] in an MFC. The anodic respiring bacteria in this study differ from those anodic compartments of previously used MFCs as they were enriched with electrode respiring bacteria during several cycles. Since the sewer indented for application would lack a membrane, the experiments were performed in a membrane-less three-electrode setup. Electroactive biofilms and artificial sewer slime have been exposed to artificial wastewater with 10 mM lactate to compare their ability to produce sulfide. Their sulfide production was tested in the presence and absence of anodic potential of +200 mV vs. Ag/AgCl. The temperature was kept at room temperature, slightly above those present in the sewer and therefore, well suited for sulfide emission.

7.1.5. Onset of sulfide emission and its rate are stimulated by anodic potential

A direct comparison of sulfide emissions over time by EAB and ASS has never been done before. Could it give information on if and how electroactive biofilms could be applied for sulfide emission control?

The course of emission can be seen below (Figure 61). The experiment showed that sulfide production required a lag phase. It was shortest for EAB and generally less emphasized in presence of applied potential. Interestingly, a lag phase existed, despite microorganisms have

been grown and conditioned under the same conditions previously. An immediate onset instead of a lag would have been expected. In addition, the lag-phase length is most variable ASS. This might indicate not only a lower sulfide emission rate of ASS but also its higher biofilm-heterogeneity as compared to the EAB.

After the lag phase, concentrations increased linearly until reaching a peak and then faded gradually. The rising slope was considered as the apparent sulfide production rate and the falling slope as the apparent sulfide depletion. At a first glance EAB's sulfide emission appeared to be higher.

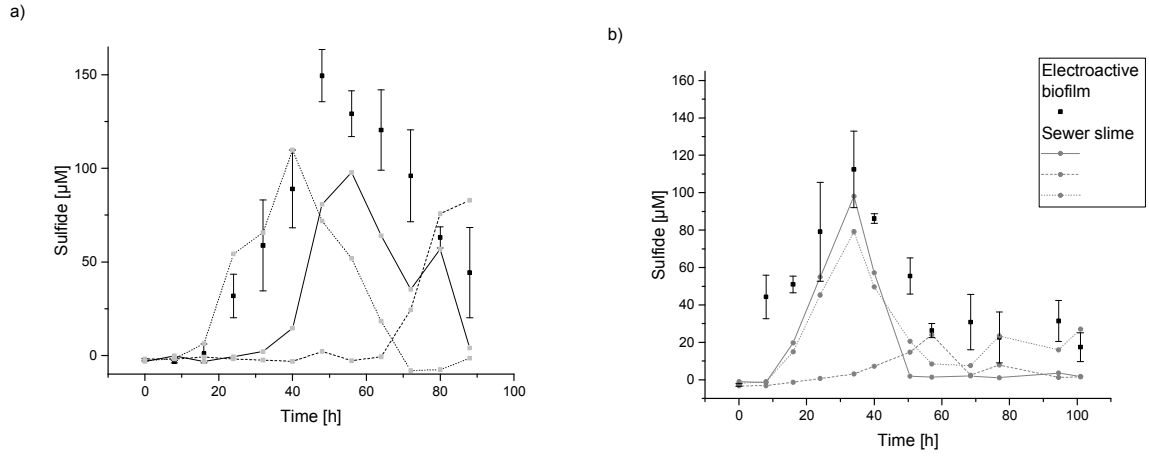

Figure 61: Course of sulfide concentration during a 4-day experiment in presence of electrodes covered either with electroactive biofilm (EAB) or artificial sewer slime (ASS). Electrolyte: AWW 1 with 10 mM lactate instead of acetate. The electrodes were kept at a) open circuit voltage (OCV) or b) +200 mV vs. Ag/AgCl (200). Experiments were performed at room temperature at 200 rpm stirring. No sulfide was produced in the absence of microorganisms (blank, data not shown). Experiments were performed in triplicates. For EABs the mean was calculated – for ASS curves are shown separately due to variability in the lag-phase (See appendix).

Figure 62 illustrates the maximum concentrations as well as the emission and depletion rate of sulfide. EABs provided the highest sulfide concentrations. The application of 200 mV vs. Ag/AgCl reduced maximum concentration for both, EAB and ASS. It also decreased the apparent production rate and increased depletion. The highest sulfide emission rate was achieved by EABs at OCP.

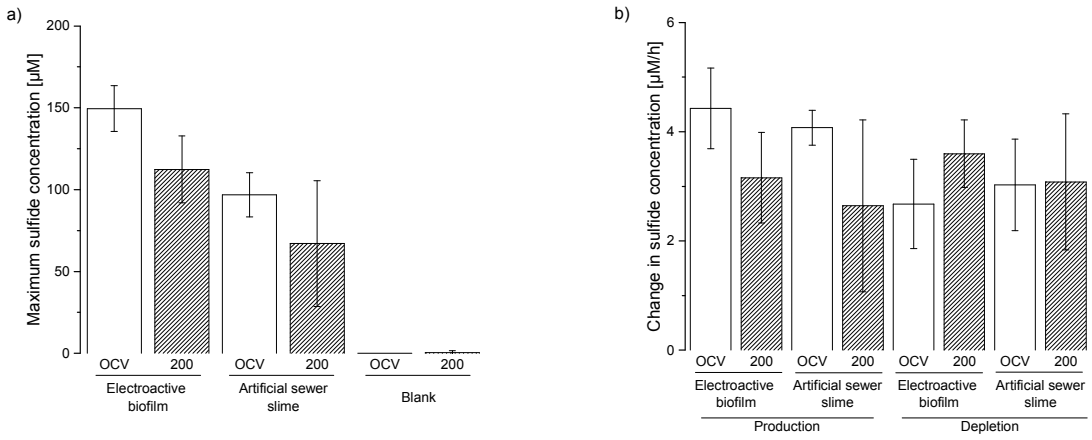

Figure 62: Sulfide production in artificial waste water. a) Maximum sulfide concentrations produced within four days and b) Change in sulfide concentration. Electrodes were covered either with EABs or ASS. Electrolyte: AWW 1 with 10 mM lactate instead of acetate. The electrodes were kept at a) OCV or b) +200 mV vs. Ag/AgCl. Experiments were performed at room temperature at 200 rpm stirring. No sulfide was produced in the absence of microorganisms (blank, appendix). Experiments were performed in triplicates.

Until sulfide concentration peaked, its emission rate ($v_{H_2S_{emit}}$) must have been greater than its re-oxidation rate ($v_{H_2S_{ox}}$):

$$v_{H_2S_{emit}} + v_{H_2S_{ox}} > 0 \rightarrow Net\ sulfide\ emission$$

afterwards, its emission rate must have become lower than its re-oxidation rate:

$$v_{H_2S_{emit}} + v_{H_2S_{ox}} < 0 \rightarrow Net\ Sulfide\ depletion$$

Thus, in the above experiments conditions exist, e.g. given sufficient lactate and sulfate, where the sulfide emission rate is higher than the re-oxidation, which leads to a net increase of concentration. This is most emphasized for EABs. The increased depletion of sulfide in presence anodic potential provides evidence for the electrochemical sulfide oxidation. Its rate will be quantified in the next section.

7.1.6. Sulfide concentrations coincide with oxidative current in presence of ASS

Sulfide has been reported to (re-)oxidize at anodic electrode surfaces [153]. To evaluate the sulfide, decline due to anodic oxidation, its concentration was measured over time while oxidation was traced simultaneously. The amount of possibly oxidized sulfide per charge was calculated according to Faradays law. ASSes were used to avoid interferences from anode respiring EABs. It was assumed that anodic respiration performed by ASSes was negligible.

Figure 63 shows the correlation between oxidative currents and sulfide concentration. The decline of current and concentration coincided well. Both peaks overlapped closely, but the oxidative currents started slightly earlier than the onset of sulfide emission. No oxidation was found in the absence of sulfide. The correlation between current and sulfide is in accordance with previous abiotic studies that used sulfide as the sole electron source [153].

Why were oxidative currents measured before sulfide became visible in bulk? The emissions might have originated from the biofilm close to the electrode and not from planktonic organisms in bulk. In case of planktonic emissions, bulk sulfide concentration and its oxidation rate would have coincided more closely.

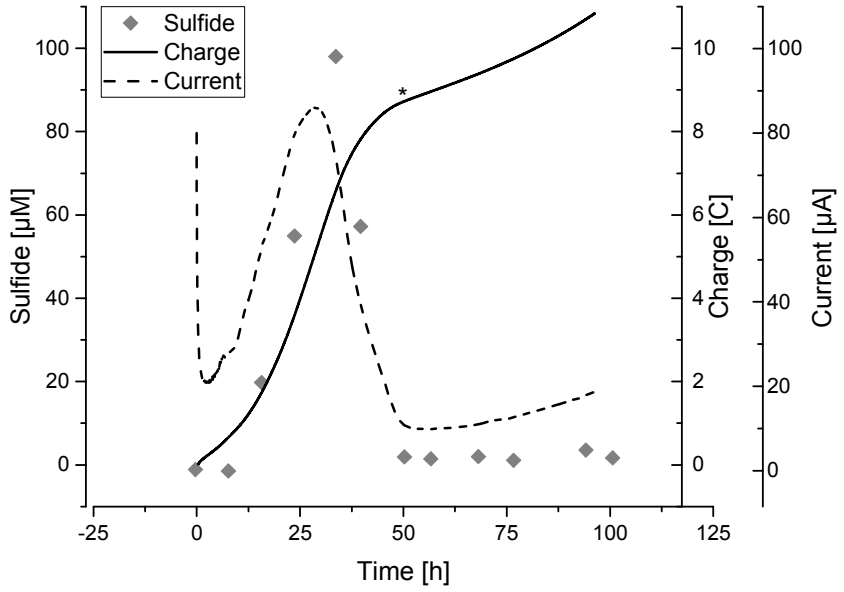

Figure 63: Sulfide concentration, charge and current during potentiostatic control of artificial sewer slime at +200 mV vs. Ag/AgCl. Supporting electrolyte AWW 1 with 10 mM lactate, but no acetate. Experiments were performed at room temperature at 200 rpm stirring. Working electrode: A graphite cylinder (Electrode signature: JMSA_EL_Siel_01; Dimensions: 3 cm length 1 cm diameter). CE: plain graphite cylinder with the same dimensions. The asterisk (*) at 50 h indicates sulfide exhaust at which charge was estimated: 8.7 C.

The results provided evidence for the re-oxidation of sulfide on a graphite electrode despite the presence of ASS-coating. It also showed that its rate depended on sulfide concentration. Replicates were similar, but slightly more variable (see appendix).

The calculations below illustrate, that electrochemically re-oxidation could have accounted for more than 70% of sulfide depletion. The initial sulfate concentration of 212 µM in 300 mL media could yield a maximum of 63.6 µmol sulfide absolute. The absolute charge was determined after current and concentration both depleted and stabilized (Figure 63, *).

It was determined to be 8.7 ±0.2 C (n = 3). A two-electron transfer during sulfide oxidation was assumed:

$$HS^-_{aq} \leftrightharpoons S_s + 2e^- + H^+$$

This allows to calculate the equivalent of moles by Faradays law.

$$Q = znF \rightarrow \frac{Q}{zF} = n$$

It was found to be

$$\frac{8.7 \pm 0.2\ C}{2 \cdot 96485 \frac{C}{mol}} = 45.1 \pm 1.0\ \mu mol.$$

Thus, anodic sulfide oxidation could have been the major cause of depletion for the 63.6 µmol. After sulfide fully depleted, still a slight oxidative current was visible. The low oxidative current might have been due to negligible anodic respiration of ASS. Its associated charge was also too small to have accounted for the difference of depleted and re-oxidized sulfide. There must have been an additional sulfide sink for the non-oxidized 17.5 µmol. These sinks could have been the gas phase, metal sulfide precipitates or biological sulfide oxidation.

7.1.7. From zero to hero: EAB lactate conversion is boosted by anodic potential

Lactate was provided as the feed carbon source for the sulfate reducing bacteria. The EAB and ASS were compared with respect to their ability of lactate conversion. The lactate concentration was traced at open circuit voltage and at 200 mV vs. Ag/AgCl.

Figure 64 shows that lactate conversion and acetate accumulation followed the typical sigmoidal trend of microbial substrate conversion. Anodic potential accelerated the lactate conversion, which was fastest in presence of ASS. Lactate was fully consumed, except in the presence of EABs at OCP. Acetate accumulated at a maximum concentration of 3 mM. For the ASS, the stabilization of acetate concentration coincided with the exhaustion of lactate. In presence of EAB at OCP, this trend is less clear: Acetate concentration reached a plateau while lactate concentration further decreased. Acetate was consumed by EABs in presence of anodic potential as could be seen by the oxidative currents. Interestingly, acetate concentration also stabilized the fastest under these conditions.

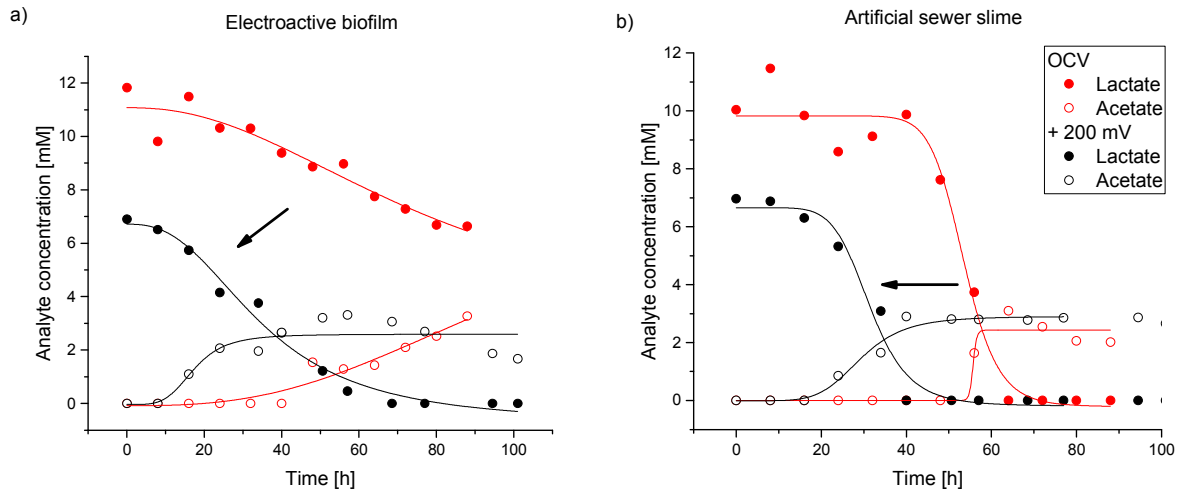

Figure 64: Lactate and acetate concentration over time in the presence of a) electroactive biofilm and b) artificial sewer slime. Supporting electrolyte: AWW 1 with 10 mM lactate instead of acetate. The electrodes were kept at either open circuit voltage (OCV) or poised at +200 mV vs. Ag/AgCl. Experiments were performed at room temperature at 200 rpm stirring. Carbon compounds were traced by HPLC. No acetate was produced in the blank experiment w/o biofilms, despite lactate appeared to be degraded slightly (see appendix). Experiments were performed in triplicates, but since the lag phases were different and the course over time was similar, only representative curves are shown (for other curves see appendix).

The fast conversion of lactate by a mixed electroactive consortia is in accordance with a finding of Gescher and colleagues [163]. There is evidence that lactate is converted fastest in the presence of a mixed culture of *G. sulfurreducens*, *G. metallireducens* and *Shewanella oneidensis* [163] compared to a pure culture of *Geobacter sulfurreducens* [164].

Surprisingly, in potentiostat-controlled experiments lactate concentration was estimated to be less than the initially fed 10 mM. In the blank electrode experiments lactate was found at normal concentrations, therefore, it appeared that a biological absorption process might have accounted for a sink, but only in presence of applied anodic potential. The lactate concentration in the control experiments was found as high as expected, excluding possible errors associated with HPLC samples or media production.

Oxidation of lactate due to oxygen leakage into the reactors is unlikely. Oxygen influx would have also resulted in the observation of discrepancies in sulfide and acetate concentrations, as both would undergo rapid oxidation. This was not the case.

7.2. Discussion of the balance between sulfide emission and oxidation

This study provided insights in the balance between sulfide emission and sulfide re-oxidation of electroactive biofilm and artificial sewer slime. We resolved the process in time and found two concurrent processes: Firstly, the microbial induced sulfide production and secondly, the parallel anodic and biologically catalyzed sulfide re-oxidation. In summary, this study points out that sulfide emission can outweigh sulfide re-oxidation which must be considered, if EAB will be implemented within the sewer system.

This study fostered the evidence for a connection between sulfide formation and re-oxidation. The real sulfide emission rate might be even higher than the apparent sulfide emission rate which was determined from bulk measurement. An example: If the maximum sulfide emission of ASS was 28 nmol/h/cm^2 and its re-oxidization rate was 16 nmol/h/cm^2, the total sulfide formation could would add up to 44 nmol/h/cm^2. EAB's maximum sulfide emission rate could have been even, but this could not be differentiated because its re-oxidation could not have been traced individually as for the ASS.

How is it possible, that most previous studies found fast and complete sulfide removal? Eventually sulfide re-oxidized was so noticeably fast because of a high electrode surface to reactor volume ratio and higher retention times, used e.g. by Rabaey and colleagues. They found an electrode surface to liquid volume of 817 m^2/m^3 able to remove sulfide spikes of 0.1 g/L within a single day [165]. In contrast, the reactor system used within this thesis only had a surface to liquid volume of 5 m^2/m^3 but a similarly high sulfide oxidation performance. In total 0.3 g/L sulfide could be removed within two days, with both biofilm systems, ASS and EAB. It becomes evident that a suitable estimate of the conversion rate per electrode area would allow to optimize the electrode-area-to-volume-ratio for sulfide removal in future MFCs.

Does this mean that the sulfide emission won't be a challenge in terms of a sewer based MFC? Certainly not, because one must keep in mind that for the application in a continuous system like the sewer, the flow and its subsequent retention time will be governed by the sewer influx which is most likely determined by external factors. Therefore, the factors that were beneficial for sulfide remediation and prevention, such as limited sulfate supply for sulfate reducing bacteria, proper electrode-to-volume ratios and low retention times, those factors will probably not be applicable for a sewer integrated MFC. To predict the sulfide outcome of the sewer based MFC it will be necessary to determine the sulfide emission and oxidation rates per electrode surface area in the future under the variable conditions found in the sewer.

Thus, dependent on the way of application of the MFC either the operational parameters will determine its sulfide emission or the desired sulfide emission rate will determine the operational parameters. The key parameters that balance sulfide emission and oxidation will be the biofilm composition, the physiochemical media properties, especially pH and temperature, the anode potential, the carbon source and the available sulfur compounds. Two key operational parameters will be the ratio of electrode-area-to-reactor-volume as well as the retention time. More dead volume results in much more side reactions will impair COD removal [166]. This requires determining sulfide emission and oxidation balance for different substrate concentrations, electrode configuration and operational conditions to be to able predict Microbial Fuel Cell behavior in the future.

What effect will sulfide re-oxidation have on the electrode performance? The author agrees with Dutta and colleagues on the conclusion that precipitated sulfur might interfere with long term experiments [153], for instance, because it was found to increase electrode resistance [167]. In contrast, experiments in our institute performed by Baudler and Riedl have shown that bioanodes deliver constant current over an extended period of time without visible sulfur passivation [17]. Two reasons for non-passivation could be possible. On the one hand sulfate might have been dosed too low, resulting in limited amounts of sulfide and subsequent negligible sulfide oxidation. On the other hand, microbial back-oxidation might have kept the electrodes clean. Thus, it would be of interest if and how sulfur passivation of the electrode is (microbially) prevented. The increase of electrode resistance could be studied by impedance spectroscopy and the extend and composition of surface deposition could be investigated by surface analyzing methods such as Raman spectroscopy. A long-term goal could be even the development of a microbial detoxification strategy of sulfide poisoned precious catalysts.

Could sulfide emission be useful? The possible induction of sulfide emissions could become handy if the precipitation of metal ions would be desired. The short stimulation by an applied anodic potential stimulating could increase the sulfide emission. A quick switch to OCP would prevent further oxidation. In contrast to this possibly beneficial application, the higher sulfide emissions must be taken in account for the placement of the cathode. Studies have shown that the deposition of oxidized sulfide in the pores of activated carbon [168] decreased its catalytic activity. The cathode must be prevented from sulfide poisoning.

How can sulfide re-oxidation be prevented or its effect be reduced? If sulfur deposition should be prevented in an MFC, the electrode is required to be kept below the sulfide oxidation potential, which was found to start at 0 V vs. Ag/AgCl [165]. The potential which represents a

balance between sulfur accumulation and anodic respiration rate could be determined by performing experiments with varying anodic potential. Unfortunately, this would also decrease the power output of a Microbial Fuel Cell. An elegant solution for sulfur removal from the anode would be cyclic switching of anode and cathode introduced first by Dutta and colleagues [169]. The concerted release of sulfide and polysulfides was beneficial for recovery and could make chemical countermeasures more efficient. Another way to prevent sulfur accumulation would be a material or electrode coating that allows for high anodic potentials but prevents sulfur deposition. To this point a sulfur retracting and conductive material is not known.

Could the sulfur deposition be useful for the electrode performance? Sulfur is regarded as a possible electron shuttle for EABs. Previous studies found that sulfur was an electron acceptor for acetate oxidizing bacteria [170] and it was found to be reduced to sulfide independent of the electrode potential [171]. This might initiate a cycling process between sulfur reduction and anodic sulfide oxidation. During this study, the accumulation of sulfide was observed, most strikingly for anodic respiring EAB. The presence of sulfide and potential sulfur at the electrode would provide all parts required for the respective shuttle system, but our study provided no evidence.

In contrast, the detected oxidative charge transfer allowed to explain the re-oxidation of sulfide to sulfur, but it was not sufficiently high to allow for further charge transfer due to shuttling processes. If sulfur would have acted as an electron shuttle or mediator, a charge flow exceeding its sulfide equivalent would have been expected. Thus, it is assumed that sulfide was not a mediator in the presence of artificial sewer slime and a positively poised anode.

How could lactate have been converted by means other than dissimilatory sulfate reduction? An imbalance was found between lactate conversion and sulfate consumption – more lactate was consumed than assumed in this study. Could a different conversion route have resulted in the consumption of lactate? At least the accumulation of an analyte other than acetate was detected during this study (Not pyruvate, data not shown). A possible explanation could be the propionate production based on lactate and amino acid conversion [163]. It appears likely that this analyte could account for the lactate sink. Additionally, methanogenic activity might contribute to lactate conversion. Hydrogen based methanogenesis would have been possible since the counter electrode releases hydrogen. To confirm these hypothesis, the unknown accumulated analytes would need to be identified by applying a method such as HPLC-MS-MS and carbon dioxide and methane emissions would need to be traced online e.g. by GC-FAIMS.

In contrast, anodic deposited sulfur might have not served as an electron acceptor for further lactate oxidation, because it was not found to participate in cyclic electron shuttling between the electrode and the biofilm. Furthermore even if sulfur was present, sulfur reducing organisms were found to be actually incapable to use lactate as a carbon source [170].

How does the presence of a poised electrode influence the regulation of microbial metabolism? This study found a significantly higher lactate conversion rate in presence of anodic potential and noticeably, an absent lag phase in case of EABs sulfide emission. This finding could be in accordance with a study by Ishii and colleagues that identified an upregulation of dissimilatory sulfate reduction in presence of anodic potential [7]. Their study provided valuable information on the regulation of metabolic networks within Microbial Fuel Cell biofilms. Given this information one could assume that anodically induced dissimilatory sulfate reduction pathways might have increased sulfate conversion and lactate consumption rate.

7.3. Discussion of reactor design and sewer slime growth and morphology

To create laminar flow to induce defined shear stress for biofilm growth two methods were considered: Either the shear stress comes from the hyperbolic shaped velocity profile that arises within a liquid overflowing the surface (Figure 65, b) or from the mostly linear velocity gradient between two proximal plates which are moving with respect to each other (Figure 65, a). The former way was used in this study the latter way was used moving cylinder reactors made by Sun and colleagues [162] and Norsker and colleagues [172]. Both systems have their advantages and disadvantages when applied for biofilm-reactor design. The flow reactor used in this study is ready to build and functions without moving parts and motors, but the flow velocity was limited by the capability of the pumping system resulting in limited shear forces. The shear-force of a moving-plate reactor is easier to calculate and adjust, because of the linear relationship between the liquid velocity and the distance to the moving element. Additionally, higher shear forces can be easily obtained due to higher capabilities of motors compared to pumps. On the downside, a reactor system with moving plates and joints will be more sophisticated to maintain anaerobic.

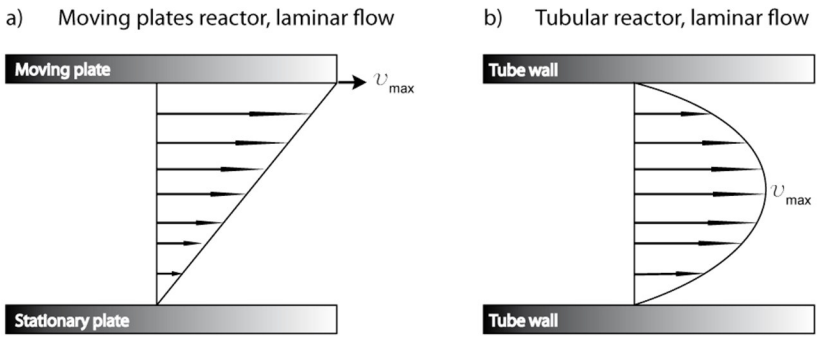

Figure 65: Laminar flow velocity profiles inducing shear stress for sewer slime formation a) in between two moving plates used by Sun et al. [162] as well as Norsker et al. [172] and b) in a tubular flow chamber used in this study.

0.2 N/m^2 of shear force were applied to the electrode surface in the flow reactor of this study. This was factor 10 less compared to the 2.1 N/m^2 of the rotating cylinder reactor setup by Sun and colleagues [162] and much lower compared an earlier biofilm study by Norsker colleagues which used 10 N/m^2 [172]. Sun and colleagues obtained a 700 µm thick and dense biofilms within 10 months where in contrast this study resulted in a thin and fuzzy biofilm of inhomogeneous thickness. This is in accordance with the variable lag time found in our experiments. Similarly, Norsker et al. obtained thin and dense biofilms. Biofilms tend to grow more dense and thinner if a higher shear force is applied [173]. Dense and homogeneous biofilms were of great use for the vertical profiling by micro sensors and dissection for Sun et al. or the characterization of Norsker et al., but to reconstruct the conditions of a slow flowing sewer in danger of sulfide emission a smaller shear stress was preferred in this study. Creating a denser biofilm by applying higher shear forces for a longer period might have resulted in higher amounts of homogeneous biofilm on the electrodes. In this study, the adhered sewer slime biomass was most likely lower than the thick anode respiring *Geobacter sulfurreducens* dominated secondary biofilms grown in a three-electrode setup.

The higher rate of sulfide emissions by *Geobacter sulfurreducens* dominated secondary biofilms might be partially due to mere higher amount of biomass, and thus potentially higher percental presence of sulfate reducing bacteria in this complex consortium. For better comparability in future experiments, it is suggested to grow both biofilms, sewer slime and secondary electroactive biofilm, to a similar thickness and absolute mass (or better, similar amount of biocatalyst). This would allow to correlate the sulfide emission to the amount of biofilm present, rather to the electrode surface area. An artificial sewer slime of higher density might be achieved by rougher electrode surfaces, higher shear forces and longer incubation

time. Additionally, the use of defined amounts of sewer slime sampled directly from various sewers with sulfide emission problems would allow to better compare the sulfide emission performance of both systems and being at the same time closer to the real application conditions. Such sampling strategies have been recently developed by Birgit Fiebig at the waste water treatment plant Steinhof in Braunschweig, Germany (Figure 66).

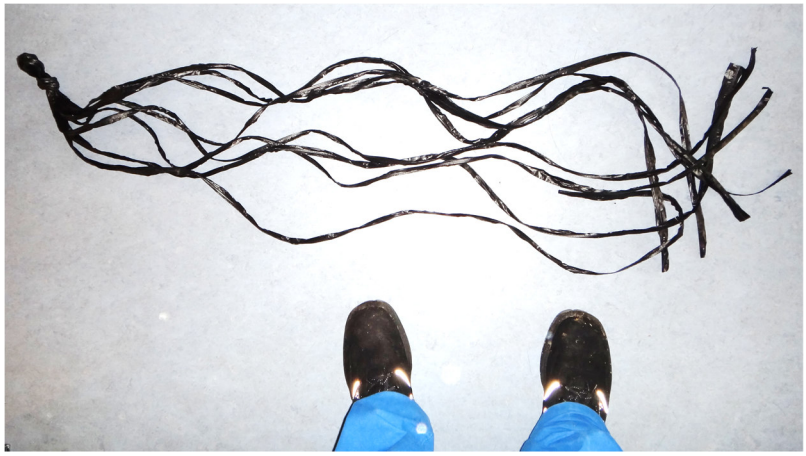

Figure 66: Plastic sisal fibers for accumulation of sewer slime samples within the sewer for cadmium determination developed by Frau Dipl. Ing. Birgit Fiebig at the wastewater treatment plant Steinhof in Germany. Author's feet for scale.

Lastly the composition of the biofilm consortia would be of interest to compare the ASS inhabiting microorganisms with those present in real sewer slime to further validate its use for laboratory experiments. The biofilm found in the previous studies contained a mixture of methanogenic and sulfate reducing bacteria which well reflected the typical composition of sewer slime [162].

8. Breathless and slow: Sulfide shocks impair anodic respiration

Extremely high sulfide concentrations are unlikely to occur in municipal waste water, but might be present in industrial waste waters such as in the highly alkaline tannery effluent used for unhairing of hide (above 1 g/L) [174]. Only few studies investigated the resistance of microorganisms towards high sulfide concentrations [175]. Sulfide toxicity originates its negative effects on the respirational chain due to the interaction with the iron clusters of heme-containing proteins. The toxicity effects and possible antidotes have been pointed out in studied of animal cells [30,32], but are less known in the kingdom of microorganisms. Some studies reported its impact and the pH dependency on the growth rate [176] or the general effect on sulfate reducing bacteria [175]. Thus, the presence of sulfide might interfere especially with the heme-centers of the cytochromes involved in direct electron transfer of *G. sulfurreducens*. Other elements of the mediated or nanowire based electron transport might be impaired as well, but this has not been investigated yet. Moreover, the resistance of electroactive biofilms towards high sulfide concentrations is less known but of even more interest if these are intended for application in sulfide rich environments. To evaluate its effect, EABs were exposed to sulfide shocks.

8.1. Results

8.1.1. Potential window of sulfide oxidation

Sulfide was found to oxidize at graphite anodes in previous studies [167]. Thus, firstly its potential window was estimated under the anaerobic experimental conditions intended for later experiments.

Figure 67 shows a reversible electrochemical process. The rate constant of the reduction appears to be higher than the rate of the oxidation. This indicates that sulfide oxidation starts above -200 mV vs. Ag/AgCl and sulfur reduction onsets is slightly below -700 mV vs. Ag/AgCl which is lower than the onset of −400 mV vs. Ag/AgCl reported by Dutta et al. [177].

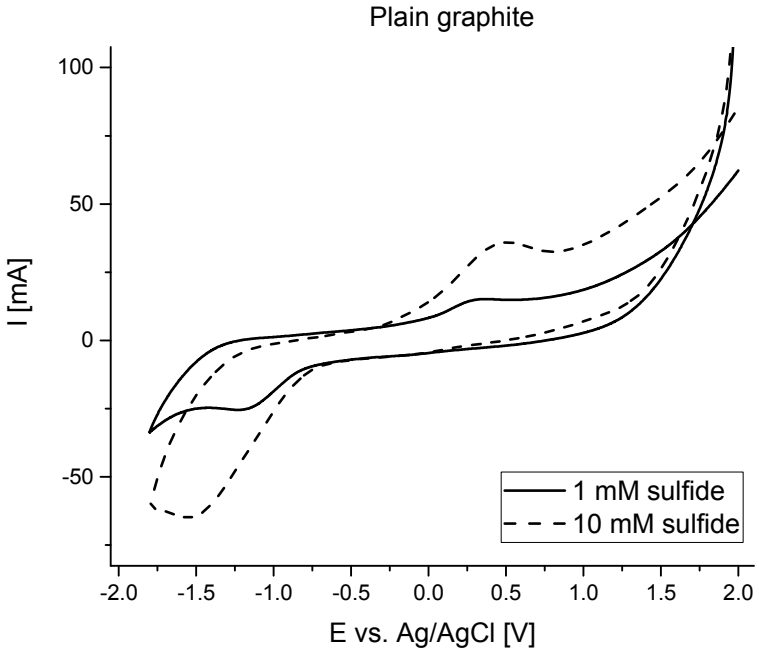

Figure 67: Potential window for sulfide oxidation and sulfur reduction on a plain graphite electrode in 50 mM phosphate buffer saline provided with 10 mM acetate at 36 °C and 200 rpm stirring in a 250-mL round bottom flask.

8.1.2. Anodic current production is impaired after sulfide shocks

Next, previously cultivated EABs were exposed to 10 mM sodium sulfide shocks in AWW 1. Afterwards, the biofilm was recovered in sulfide free AWW 1. The EABs were provided with +200 mV vs. Ag/AgCl while the current was recorded. The oxidative performance of sulfide shocked anodic biofilm dropped to only 10% of its maximum current in absence of sulfide. As the abiotic experiment showed, most part of that oxidative current is due to anodic sulfide oxidation. This is evidence that microbial respiration is highly impaired in presence of high sulfide concentration (Figure 68 a). After 48 h exposure, the biofilms color turned from maroon into a grey-brown, which might have indicated the modification of biofilm's hem centers or sulfur depositions.

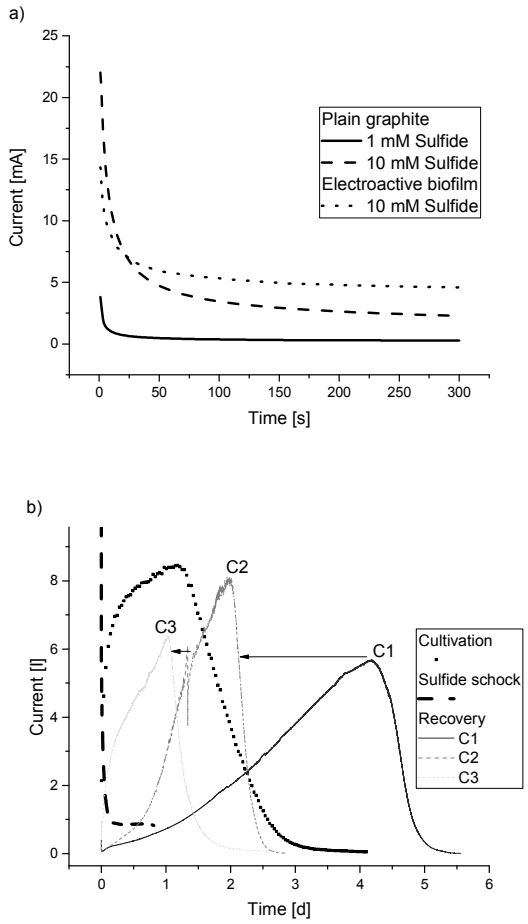

Figure 68: a) Sulfide oxidation current in presence and absence of electroactive biofilm. b) Current response during cultivation, sulfide shock and recovery of electroactive biofilms. EABs were grown on cylindrical graphite electrodes (Dimensions: 3 cm length x 1 cm Ø) and kept at +200 mV vs. Ag/AgCl in a multi neck round bottom flask filled with 200 mL artificial waste water and fed with 10 mM lactate. Reactors were incubated at 36 °C and stirred with 250 rpm. Experiments were performed in triplicates.

Figure 68 b) shows that the first recovery cycle after exposure was distinctively longer than the previous cycles. As more recovery cycles were performed, the cycle length decreased, but not constantly, as it doubled again after the third recovery cycle. Additionally, the peak currents during the recovery cycles remained below their initial maximum. Both findings indicate that the electroactive organisms were subject to irreversible damage.

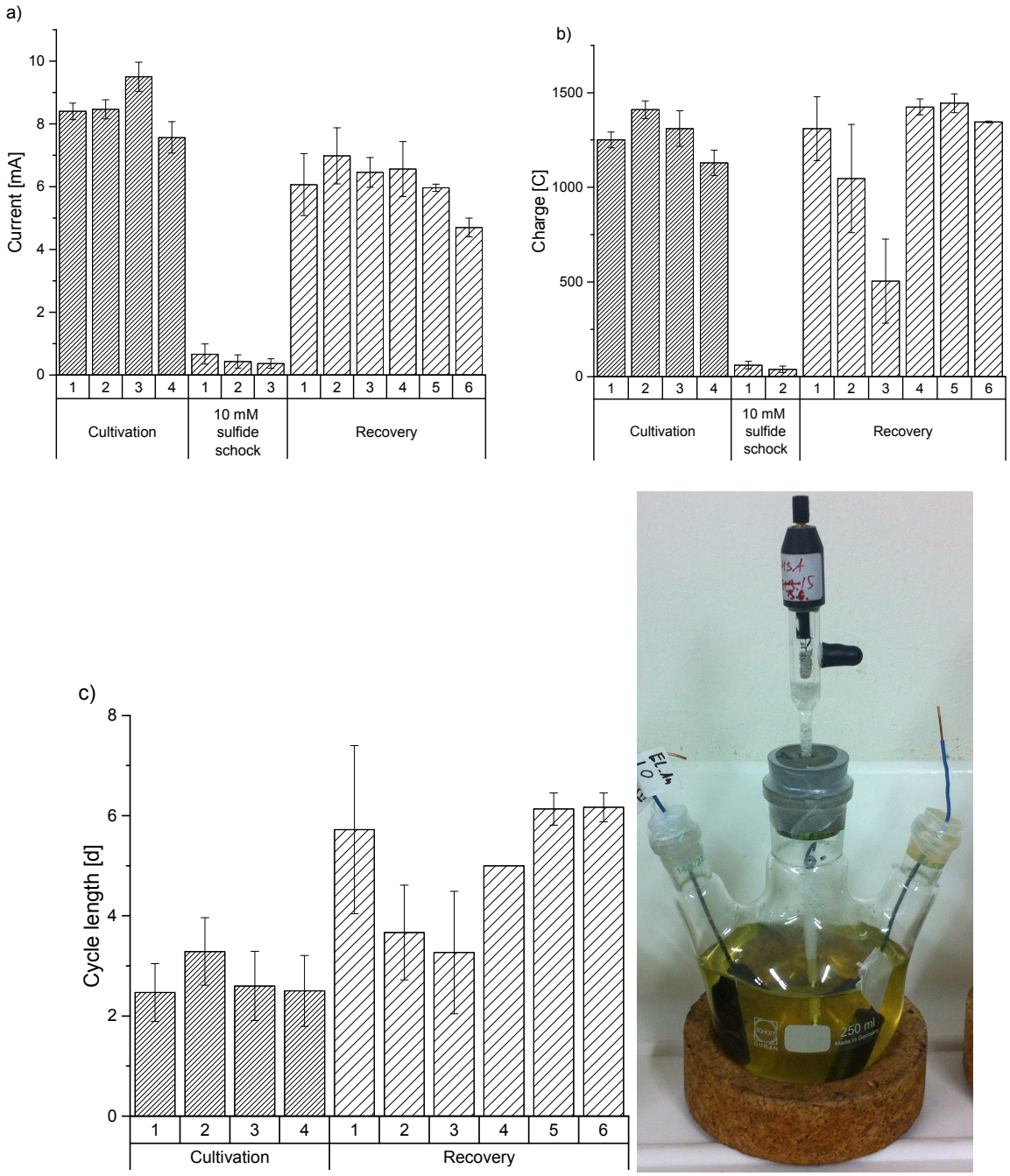

Figure 69: a) Peak currents, b) charge transfer and c) cycle duration during cultivation, sulfide shock and recovery. Biofilms were grown on cylindrical graphite electrodes (Dimensions: 3 cm length; 1 cm diameter) and kept at +200 mV vs. Ag/AgCl in a multi neck round bottom flask filled with 200 mL artificial waste water fed with 10 mM lactate. Reactors were incubated at 36 °C and stirred with 250 rpm (n = 3). During sulfide shock experiments charge was only determined twice.

8.1.3. Turnover and non-turnover cyclic voltammograms

Electrode respiring organism require redox molecules on their surface to donate their metabolic electrons to the accepting electrodes. The participating redox centers can be revealed by cyclic

voltammetry [12,46,178]. In this study, the voltammograms of EABs were compared while and after being exposed to 10 mM sulfide shocks. The potential sweep started in the cathodic region to reduce possibly accumulated sulfur and then continued into the anodic. Voltammetry in absence of sulfide shocks was performed firstly, at turnover conditions, thus while actively performing anode respiration and secondly, after the substrate has been consumed, so called non-turnover conditions, to evaluate the participating redox species centers of the biofilm.

Figure 70 shows that in presence of sulfide, the oxidative currents were significantly lower, but not as low as under non-turnover conditions. This indicates, that presence of sulfide inhibited electrode respiration and/or acetate metabolism. This is consistent with the chronoamperometric findings above. Two oxidative peaks which are present in the recovery non-turnover CV are only barely visible in the sulfide-shock CV. As the sweep progresses in the anodic area the current increases in a similar manner as in the turnover CV but to a much lower extent as compared to the recovery turnover CV.

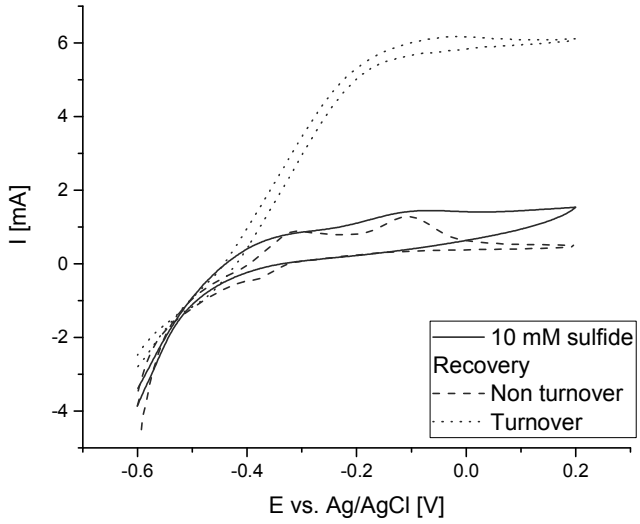

Figure 70: Cyclic voltammetry of electroactive biofilms in presence of 10 mM sulfide shocks and during recovery at non-turnover and turnover conditions. Supporting electrolyte: Artificial waste water made of 50 mM phosphate buffer with 10 mM acetate. Sweeps at 1 mV/s starting in the negative potential region.

8.2. Summary and conclusion

The study showed that 10 mM sulfide shocks had a severe impact on EABs. Its outer appearance has changed and its current generation drastically decreased. The electroactive biofilms of this study appear more susceptible to sulfide as those sulfate reducing organisms whose metabolism was inhibited above 16.1 mM [175]. The complete consumption of acetate within this setup

potentially produces 1543 C of charge, however the coulombic efficiency reaches only 80% during cultivation. Interestingly the coulombic efficiency did increase slightly in the long term.

The reasons of increasing cycle duration were not clear. I could possibly due to sulfur depositions resulting in reduced accessible surface area for direct and indirect electron transfer. Such an effect could account for both, lower maximum currents and a subsequently longer duration required for substrate consumption.

Interestingly, similar observations were made during long term experiments when EABs were grown in sulfide rich AWW 2 (Personal communication, Sebastian Riedl). The oxidative performance of EABs in this media did decrease gradually at high cycle numbers whereas the performance in AWW 1 with low possible sulfide concentrations did not show a decrease in performance. The long-term impact of sulfide on EAB performance should be studied in more depth. A suitable range for further long-term studies should range between a sulfide concentration of 1 and 10 mM. Abiotic studies might investigate the change of isolated cytochrome's redox properties in presence and absence of sulfide.

9. Sense or no-sense – Sulfide detection by Au-amalgam microelectrodes in AWW

Online sulfide detection in waste water is important for several reasons: Operator safety, sewer corrosion precautions and water quality assessment. Cathodic stripping voltammetry at solid state gold amalgam microelectrodes has been proven to be a versatile method for sulfide detection and analysis of a variety of further ions in sea and freshwater [179–182]. Despite of its analyte spectrum, its simple fabrication and straightforward instrumentation, this method has not been adapted for waste water. Certainly, water analytics are challenging due to the complex sample matrix containing a manifold of interfering species and varying physiochemical properties such as temperature or salinity. Therefore, the scope of this study was the adaption of the solid-state gold amalgam microelectrode electrode to a complex but defined artificial waste water environment to trace microbial sulfide production.

During the study, it has been successfully calibrated for up to 2 mM (40 mg/l) of sulfide in different types of artificial waste water despite interfering signals. This represents the medium range of sulfide concentrations commonly found within the sewer. Consequently, the electrodes were used to monitor microbial sulfide production in two types of artificial waste water (AWW): Firstly, in AWW 1 with low sulfide concentration derived from sulfate during acetate consumption. Secondly, in AWW 2 with high sulfide concentration derived from cysteine and sulfate during conversion of fermentable carbon sources.

Reliable analytics require constant sensor quality and a stable reproducible signal. Yet, both factors were initially not granted for the gold amalgam solid state microelectrode. First, the mercury deposition and the amalgamation process were regarded as sources of uncertainty, the sensor quality could not be held constant. Thus, a previous method for mercury deposition was carefully reconsidered and found to hold the potential for improvements. Second, the amalgam surface itself is subject to aging which reasons and proceedings are not fully clear. Hence, the magnitude and proceeding of amalgam crystallization and aging were visualized and found to result in significant surface disruption. Despite the possibility of disruptions, the sensor conditioning currents remained stable during microbial sulfide production but cyclic voltammetry shapes did change profoundly. It remained unclear which production parameters, e.g. mercury deposition and amalgam shapes will be most beneficial for long term measurement.

In the following section the reader is exposed to the theory of

1. sulfide sensing,
2. gold-amalgam formation,
3. cathodic stripping,
4. sulfide stripping,
5. its potential sources of interferences in AWW.

Theory

Sulfide can be measured by many different analytical methods [183,184] as for example with chromatography such as fluorescence labelling HPLC [185], with colorimetric assays like the methylene blue method [50,52] and also by electrochemical means [186]. Electroanalytical techniques allow to correlate a current response to the quantity of an accumulated analyte [21]. This can be done amperometrically [187] or by the sensitive inverse polarography or stripping analysis.

Cathodic stripping voltammetry at solid state gold amalgam microelectrodes has been proven useful for online sulfide detection in the µM-range. This electrode detects sulfide and other analytes of interest in parallel under different aquatic conditions such as in the extreme environment of hot deep sea vents [179] and also concentration profiles in marine pore waters [188] and freshwater sediments [189]. Besides its analytic capability the sensor is easy to fabricate and only requires a potentiostat detecting currents in the nano-ampere range. Thus, such a sensor can be established comfortably without additional instrumentation in a typical electrochemistry laboratory.

In cathodic stripping the analyte is enriched by oxidative deposition at the positively poised working electrode and analyzed in a cathodic sweep which reduces the analyte back to the solution. The potential sweep results in a cathodic current whose reductive peak heights I_p are proportional to the dissolved species concentration (if the enrichment conditions are held constant). Accordingly, the unknown species of interest can be determined by comparison to a calibration curve based on known concentrations.

Micro electrodes provide an improved signal to noise ratio compared to planar macroelectrodes for two reasons [44]. Firstly, their non-planar diffusion allows faster mass transfer which increases faradaic currents per area. This effect is further increased in case of a hemispherical electrode. Secondly, at the same time their double layer capacitance only scales linearly with surface. Thus, its contribution to current density remains constant. This allows to raise the scan rate to increase analyte sensitivity but only to a certain extend as the quotient of capacitive currents I_C and Faradaic current I_F scales with its square root of speed v.

$$\frac{I_C}{I_F} \propto \sqrt{v}$$

The gold amalgam provides a broad potential window for the detection of analytes. This is because, its hydrogen evolution overpotential is high and its onset potential below −1 V vs. AgCl [188]. Thus, most potential analyte signals won't be swamped by the reduction current of hydrogen evolution.

Mercury deposition and amalgam formation

Gold-amalgam formation requires the mercury to meet gold. To do this in a defined manner, Hg^{2+} can be electrochemically deposited on a polished gold surface from nitric acid solution:

$$Hg^{2+} + 2e^- \leftrightharpoons Hg$$

The complex deposition process itself became focus of science in the late 70s [190]. A monoatomic mercury layer [191,192] is formed first. Then, once a certain amount has been deposited, the amalgam formation starts [192]. The deposition of mercury itself was found to proceed fast in contrast to the diffusion of mercury into gold. This was observed during plasmonic monitoring of Au-Hg nanoparticle formation [193].

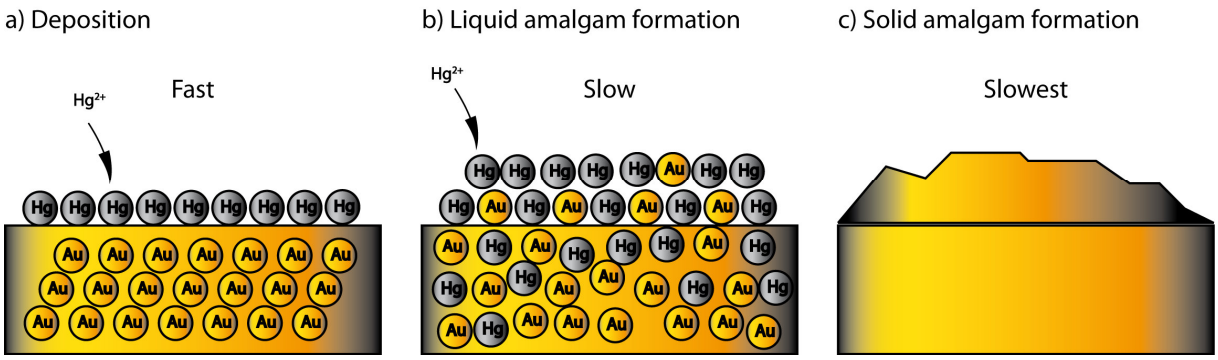

Figure 71: Model of solid state gold amalgam microelectrode formation by electrodeposition of mercury on gold. a) Mercury deposition onto the plain gold (Au) surface. b) The diffusion of gold into the excess mercury on the surface forming liquid amalgam and parallel diffusion of mercury into the gold surface and the c) solid gold amalgam formation.

Finally, it was found that diffusion of silver into mercury happened on a faster scale than the subsequent slow conversion of liquid amalgam into solid amalgam [194]. Once the solid gold amalgam electrode surface has formed the electrode is ready for cathodic stripping voltammetry.

Steps and experimental parameters of cathodic stripping voltammetry

Cathodic stripping voltammetry is performed in a three-step process (Figure 72). Firstly, a negative conditioning potential E_{cond} is applied to maintain the electrode free of oxidation products. Secondly, an accumulation potential E_{acc} is set. It determines the oxidation products for later stripping and its application period t_{acc} determines the amount of deposited material. Finally, a cathodic sweep is performed and analytes are stripped away in the order of their decreasing redox potential.

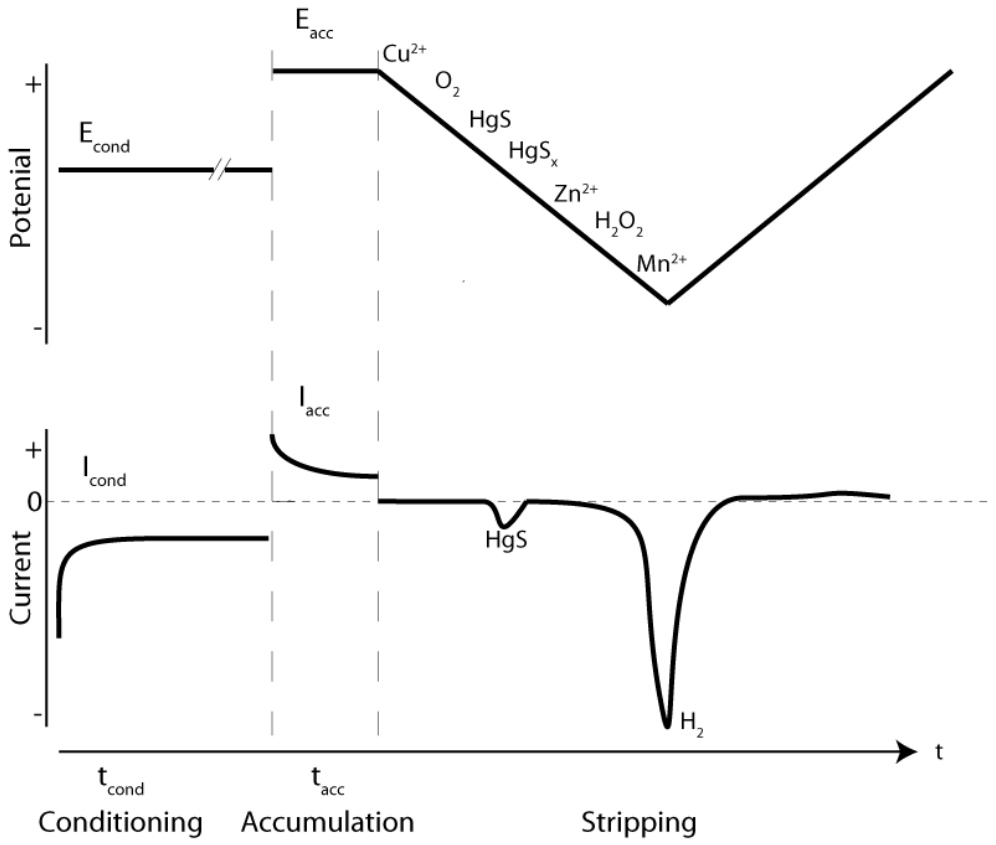

Figure 72: Illustration of cathodic stripping voltammetry potential/current dependency over time during sulfide detection. Conditioning potential E_{cond} is applied for t_{cond}. The accumulation potential E_{acc} is applied for t_{acc}. Species of interest are marked along scanning potential in order of their qualitative peak occurrence base on the publication of Luther et al. [189]. A HgS stripping peak is qualitatively marked is illustrated.

The conditioning potential E_{cond} is set low enough to remove all previously enriched analytes to maintain a clean electrode surface. At the same time, it should not be set too low, to prevent blocking of the electrode surface by hydrogen gas. A low stationary conditioning current I_{cond} is an indicator for good electrode-surface quality. In contrast, a high reductive conditioning current points out possible exposure of gold or electrode surface modifications which both might increase hydrogen evolution.

The accumulation potential E_{acc} determines which analytes enrich at the at the electrode surface. It is required to be set positive enough to collect the analytes of interest but not higher as + 0.3V vs. Ag/AgCl [192] to prevent amalgam oxidation. Continuous oxidation and reduction of mercury is not desired because it would change the surface structure and increase surface roughness of the electrode. The accumulation time t_{acc} determines the sensitivity of the electrode. A long accumulation time might enrich sufficient analyte even if its concentration in bulk is low.

Accordingly, the first vertex potential of the cathodic sweep should be below the dissolution potential of the amalgam but high enough to detect the analyte of interest with the highest redox potential. The scan rate and the analyte concentration of the cathodic sweep determine the peak height I_p:

$$i_p \sim n^{\frac{2}{3}} D^{\frac{1}{2}} v^{\frac{1}{2}} c^0$$

Where D is the diffusion coefficient of the species (m^2/s), n is the number of electrons transferred and c^0 (mol/L) is the concentration of the analyte.

The accumulation and stripping of sulfur species on gold amalgam

Cathodic stripping voltammetry allows to distinguish between different sulfide species. These species' absorption and stripping processes can be described by the following two sets of equations. The sulfide stripping proceeds as follows:

1a)	$HS^- + Hg \leftrightharpoons HgS + H^+ + 2e^-$	Adsorption
1b)	$HgS + H^+ + 2e^- \leftrightharpoons HS^- + Hg$	Stripping

It shows that the oxidation state of sulfide is not changed – a disproportionation reaction – but the mercury is oxidized during absorption and reduced during stripping [195]. Ultimately, this leads to one visible peak in the voltammogram of sulfide stripping. In contrast, polysulfide stripping proceeds in two electrochemical steps and results in two distinct reductive peaks during stripping:

3a)	$Hg + S_x^{2-} \leftrightharpoons HgS_x + 2e^-$	Adsorption
3b)	$HgS_x + 2e^- \leftrightharpoons Hg + S_x^{2-}$	Stripping
3c)	$S_x^{2-} + xH^+ + (2x-2)e^- \leftrightharpoons xHS^-$	Reduction

Increasing the scan rate will result in peak separation of the reaction 3b) and 3c) since reduction of S_x^{2-} to xHS^- is an electrochemically irreversible process [196]. This difference can be used to electrochemically distinguish sulfide from polysulfide stripping.

Two factors influence the sulfide availability at the electrode surface and should be considered. The first is temperature, which changes the diffusion coefficient of sulfide, and thus the diffusion rates during adsorption and stripping. The second is pH, which does impact the equilibrium between HS^- and H_2S and therefore the availability of HS^-. Lastly, the sulfide peak potential is shifted slightly by salinity [188] and rising concentrations.

Sources of interference for cathodic stripping in artificial waste water

Artificial waste water provides nutrients for the growth of electroactive organism. Its contains analytes and substances which might result in interferences to the sulfide signal (Table 15).

Table 15: Compounds of artificial waste water 1 with concentrations higher than 1 µmol/L

Chemical	Concentration [µmol/L]
Nitrilotriacetic acid	98
$MgSO_4 \cdot 7\ H_2O$	152
$MnSO_4 \cdot 2\ H_2O$	33
NaCl	214
$FeSO_4 \cdot 7H_2O$	4
$CoCl_2$	10
$CaCl_2 \cdot 2\ H_2O$	9
$ZnSO4 \cdot 7\ H_2O$	8
$CuSO_4$	5
$AlK(SO4)_2$	5
H_3BO_3	20
$Na_2MoO_4 \cdot 2H_2O$	5
Sodium acetate	9996
$NaH_2PO_4 \cdot 1\ H_2O$	19494
Na_2HPO_4	30502
NH_4Cl	5795
KCl	1744

Copper (Cu) stripping was reported at −0.18 V vs. Ag/AgCl with a detection limit >100 nM, oxygen reduction at −0.3 V with a detection limit of 3 µM, zinc stripping at −1.02 V with a detection limit of >100 nM, peroxide reduction at −1.23 V with a detection limit of 3 µM, iron (II) stripping at −1.43 V with a detection limit of >10 µM and manganese stripping at −1.55 V with a detection limit of 5 µM [179].

What about the other substances? The standard reduction potentials of magnesium, calcium and sodium are lower than the overpotential for hydrogen evolution at amalgam, and thus represent no interference at all. The standard potential of aluminum (Al^{3+}) is −1.4 V vs. Ag/AgCl and could be visible in the lower potential range. Sulfate is neither a source of interference as E_{acc} and the starting potential of the cathodic sweep are set above sulfates reduction potential [197]. Ammonia has been reported to undergo chemical reactions with mercury [198]. Cobalt and Manganese have not been reported yet to interact with amalgam. Besides AWW 1 also AWW

2 was tested which had additional 3.3 mM glycine, 0.5 mM D-ribose, 2 mM cysteine and 0.4 mM glucose. Given a reported electrochemical glucose reduction at -1.55 V vs. NHE [199] little interference during sulfide detection is expected. Lastly the methylation of mercury by microorganisms in the presence of cysteine and other sulfur compounds needs to be considered [200–203] as it might alter the amalgam surface structure.

The list and description of possible reactions above will increase the experimenter's awareness of the potentially visible interferences during stripping and it will allow to narrow down their sources.

Sulfide might precipitate trace metals in artificial waste water

The presence of sulfide and metal ions is likely to result in the formation of metal sulfides because of their low solubility products. The solubility product of metal sulfides is low for manganese and very low for iron, copper, cobalt and zinc. The precipitation would have several effects. Firstly, it would reduce the trace element availability for the bioelectrochemical systems and artificial sewer slime. Secondly, precipitation would alter them inaccessible for analytical determination.

This also leads to the question if the high sulfide environment of artificial waste water or real waste water does allow for detection of traces of metals, or if the precipitation will withdraw the elements from analytical assessment.

A metal sulfide precipitation occurs if the product of concentrations of the dissociated species is greater than the solubility product, e.g. if:

$$K_L < [Me^{2+}][S^{2-}]$$

The equilibrium of sulfide gas and its ion can estimated by the first and second equilibrium constants of H_2S dissociation [204]:

$$H_2S + H_2O \overset{K_{S1}}{\leftrightharpoons} HS^- + H_3O^+$$

where $K_{S1} = 10^{-7}$ mol/L

$$HS^- \overset{K_{S2}}{\leftrightharpoons} S^{2-} + H_3O^+$$

where $K_{S2} = 10^{-17.4}$ mol/L

$$H_2S + H_2O \overset{K_{S3}}{\leftrightharpoons} S^{2-} + 2H_3O^+$$

Therefore, $K_{S1}K_{S2} = K_{S3} = 10^{-24.4}$ mol^2/L^2 and the concentration of [S^{2-}] can be calculated by

$$[S^{2-}] = \frac{10^{-24.4}[H_2S]}{[H_3O^+]^2}$$

If the pH is 7 and $[H_3O^+]^2 = 10^{-14}$ and the total sum of sulfide species is 212 µM, the maximum possible concentration of [S^{2-}] would be 8.44×10^{-15} mol/l. For 10 µM total sulfide the maximum possible S^{2-} concentration would be 3.98×10^{-16} mol/l.

Based on the trace metals in artificial waste water the required S^{2-} concentration for precipitation can be estimated (Table 16).

Table 16: Sulfides, their solubility product K_L at 25°C, their corresponding metal concentration in artificial waste water and the required S^{2-} concentration for precipitation [205].

Sulfide	K_L at 25°C	Me^{2+} in artificial waste water [mol/L]	Least S^{2-} required for precipitation [mol/L]
CoS	5×10^{-22}	9.6×10^{-6}	5.2×10^{-17}
CuS	1×10^{-37}	5×10^{-6}	5×10^{-31}
FeS	1×10^{-19}	4.5×10^{-6}	4.5×10^{-13}
MnS	1×10^{-15}	33.4×10^{-6}	3.34×10^{-8}
ZnS	1×10^{-22}	7.7×10^{-6}	7.7×10^{-16}

This means that during the calibration at low sulfide concentrations, metal precipitates of zinc, copper and cobalt might form and could reduce the sulfide concentration by over 20 µM.

As the system gets more alkaline, the S^{2-} concentration increases and more metals would start to precipitate. Iron sulfide will form eventually, e.g. when pH 8 increases the S^{2-} concentration by two decades. This could result in more than 4.5×10^{-13} mol/L of sulfide to precipitate iron in cysteine-rich AWW 2. Despite the high S^{2-}-concentration, manganese precipitation seems still unlikely. In marine pore water metal sulfides were reported to precipitate already below the critical sulfide concentration and they confirmed that sulfide becomes unavailable due to precipitation [182].

If the precipitation does affect the cathodic stripping voltammetry, this should be visible in a reduced charge transfer during accumulation and a higher detection level. Figure 73 illustrates that the detection of sulfide requires a concentration above the precipitation level. With respect to artificial waste water it is likely that the calibration curve requires sulfide concentrations above 20 µM.

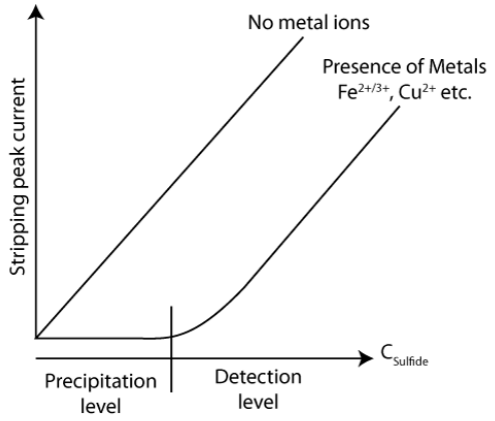

Figure 73: Illustration of the current peak behavior in presence and absence of metal ions.

9.1. Results

This section first reassesses the deposition process, reveals uncertainties in the reproducibility of electrode fabrication and points out possibilities for improvement. The latter section characterizes the electrode in artificial waste water and the visibility of sources of interference. In the subsequent section the calibration is performed to measure biological sulfide production. Lastly the crystallization and aging of the electrodes is examined in more depth.

9.1.1. Previous method induces excess mercury plating and surface variability

A chronoamperometric electroplating procedure was recommended by Luther et. al [179]. According to their manual, a constant potential of −1 V vs. Ag/AgCl was applied for 4 minutes to plate mercury from an anaerobic and stirred acidic solution. A deposition height ranging from 10–20 µm was recommended. This would require less than an equivalent of 2 mC charge for a 100 µm Ø electrode. The current-time behavior of mercury deposition was recorded for quality control purposes to calculate the equivalent of plated mercury.

In this study, the total charge of plating ranged from a few mC up to 200 mC (Figure 74 a). This indicates that in many cases, the depositions must have exceeded the recommended 10–20 µm layer height.

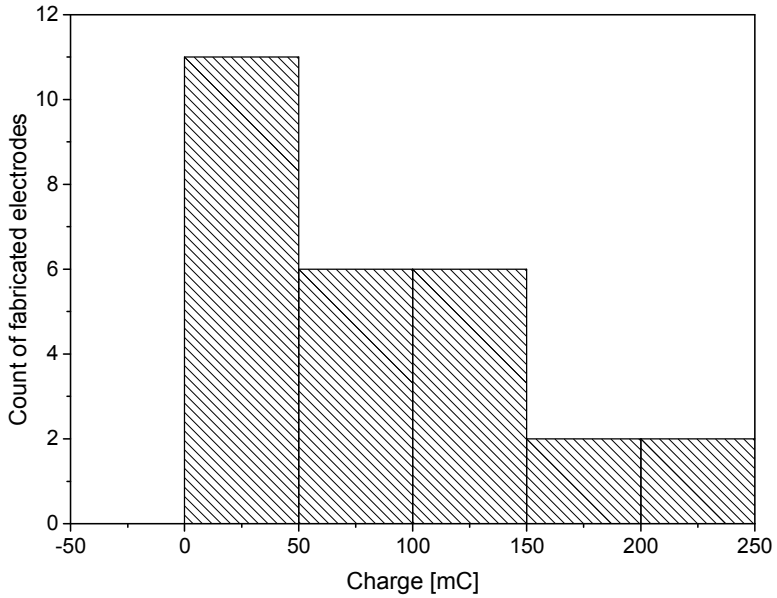

Figure 74: Histogram of charge transfer during 4-minute mercury deposition at −0.1 V vs. Ag/AgCl on 100 µm diameter gold surfaces. Total electrode count: n = 27. 3.4 g $Hg(NO_3)_2$ in 100 mL pH 1.5 nitric acid solution. The stirred electrolyte was kept anaerobic by nitrogen sparging at room temperature.

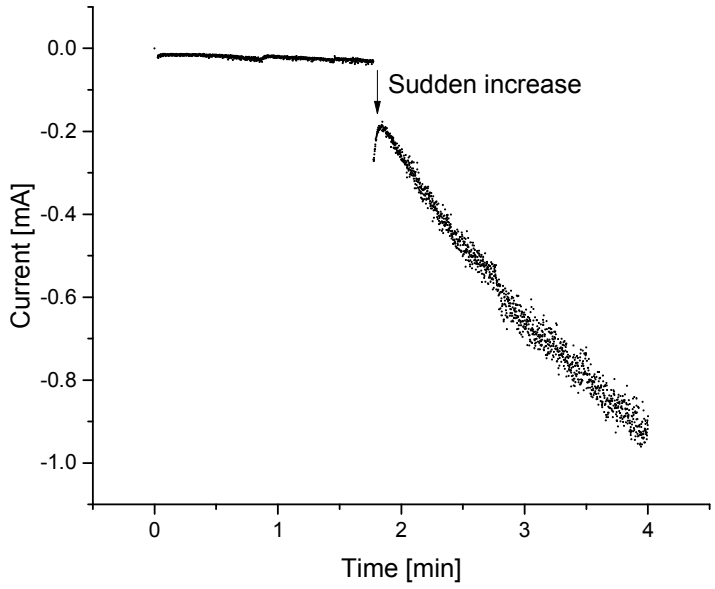

Figure 75: Current-time behavior during mercury deposition on a 100 µm Ø gold electrode. Supporting electrolyte: 3.4 g $Hg(NO_3)_2$ in 100 mL pH 1.5 nitric acid solution. Deposition for 4-minute at −0.1 V vs. Ag/AgCl. The stirred electrolyte was kept anaerobic by nitrogen sparging at room temperature.

The electroplating procedure could be divided into two subsequent velocity phases (Figure 75): Firstly, a slow charge transfer with varying duration and secondly, a faster charge transfer. The transition from the first to the second phase was marked by a sudden steep increase in current. In most cases, the first phase would have been sufficient for a mercury layer several micrometers in thickness. The second phase would have led to tremendous excess of mercury. The effects that lead to the step wise increase of current behavior and to the variation in time of phase one are not clear.

Despite the high charge transfer, laser scanning images showed that spherical shaped depositions were limited to a maximum of 50–80 µm in height which theoretically do not require more than a charge of 4–8 mC (Figure 76). Moreover, the electrodes b) and e) with the highest charge transfer resulted in the smallest depositions, whereas electrodes a) and d) with the least charge transfer correlate most closely with the observed deposition height.

A possible explanation for this unexpected behavior could be a mercury droplet formation upon excess deposition. This putative droplet would continuously grow and remain stable just until the electrode is removed from the solution as illustrated (Figure 77). The loss of excess mercury during handling would leave varying amounts of remaining mercury, and thus an uncertain microelectrode surface.

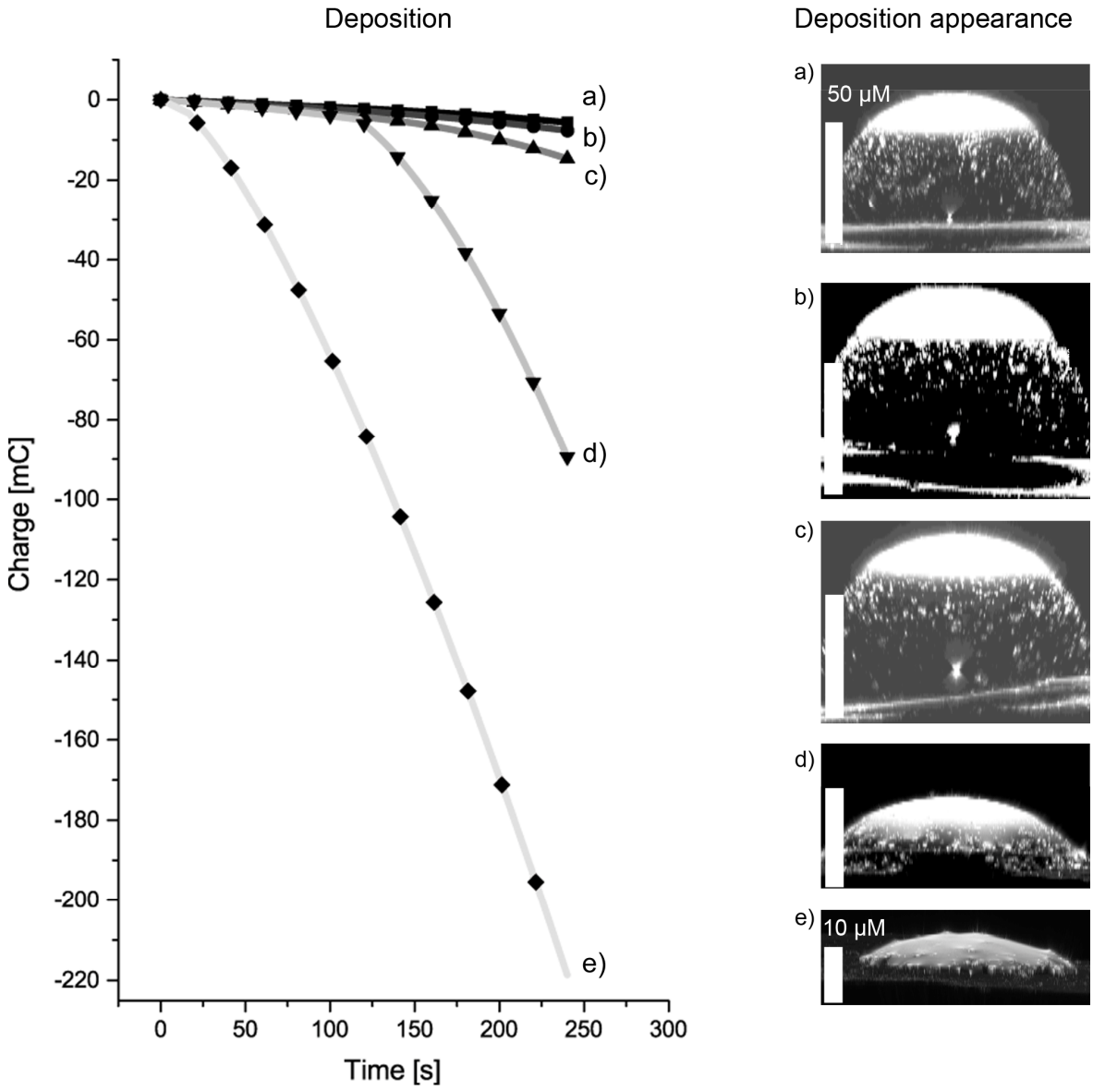

Figure 76: Correlation between charge transfer Q and mercury deposition height for 5 electrodes a) – e). Gold electrode diameter: 100 µm Ø. White bar in graphics indicates 50 µm unless otherwise specified. Supporting electrolyte: 3.4 g $Hg(NO_3)_2$ in 100 mL pH 1.5 nitric acid solution. Mercury deposition for 4-minute at −0.1 V vs. Ag/AgCl. The stirred electrolyte was kept anaerobic by nitrogen sparging at room temperature. Confocal laser scanning microscopy was done within several minutes after deposition. Raw Leica image files were processed by FIJI, resliced and visualized as max intensity z-stack-projection. Electrode signatures and total deposition: JMSA_AuHg_17, 5.6 mC; JMSA_AuHg_18, 89.5 mC; JMSA_AuHg_19, 14.6 mC; JMSA_AuHg_20, 7.6 mC; JMSA_AuHg_21, 218.6 mC.

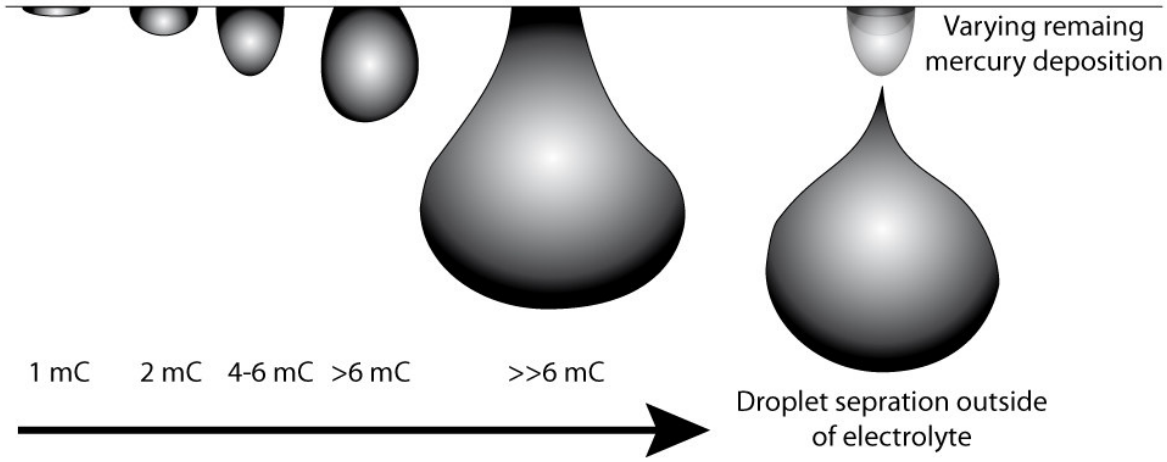

Figure 77: Hypothetical mercury droplet formation after excess deposition. The surface area increases non-linear and accordingly the current increases. The change in current over time is dependent on the change in surface area, which depends on the current itself and could therefore be described by a differential equation.

The incautious handling of the electrode might result in a further decrease of plated mercury as indicated below (Figure 78).

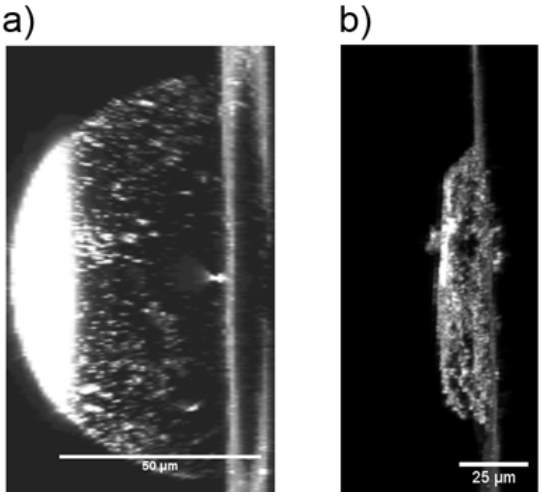

Figure 78:Loss of mercury due to incautious handling. a) Mercury droplet after deposition and b) surface after amalgam formation and partial loss of mercury. Electrode signature JMSA_EL_AuHg_17.

Extremely high deposition charge ~ 1 C possibly points out deficient electrode fabrication. Such a tremendous amount of plated mercury has been observed for a flawed electrode with clearance between the gold wire and the epoxy coating. Other mercury sinks are unlikely. It does not adhere to glass or epoxy resin, and thus would not accumulate at the epoxy-glass embedment of the gold wire. Additionally, the diffusion of mercury into gold is slow ($D = 1.24\ 10^{-11}\ cm^2/s$) [206] and its according currents would be in the range of pico- to nanoamperes. This is out of proportion compared to the milliamperes measured.

Surface roughness was considered to influence the first phase of mercury deposition and the subsequent excess accumulation. A high roughness would increase the accessible surface area for monolayer formation and it would influence the initial deposition time. Ultimately, a higher roughness might reduce the electrode quality which could be estimated by a high conditioning current. Figure 79 shows that both hypotheses could not be proven. Firstly, the surface roughness did not affect the amount of total plated mercury, nor was it found to affect the initial fast mercury deposition phase (Figure 79 a)). Secondly, no correlation was found between deposition and conditioning current. The conditioning current varied in three orders of magnitudes. Electrodes with conditioning currents below 10 nA were preferred for further studies.

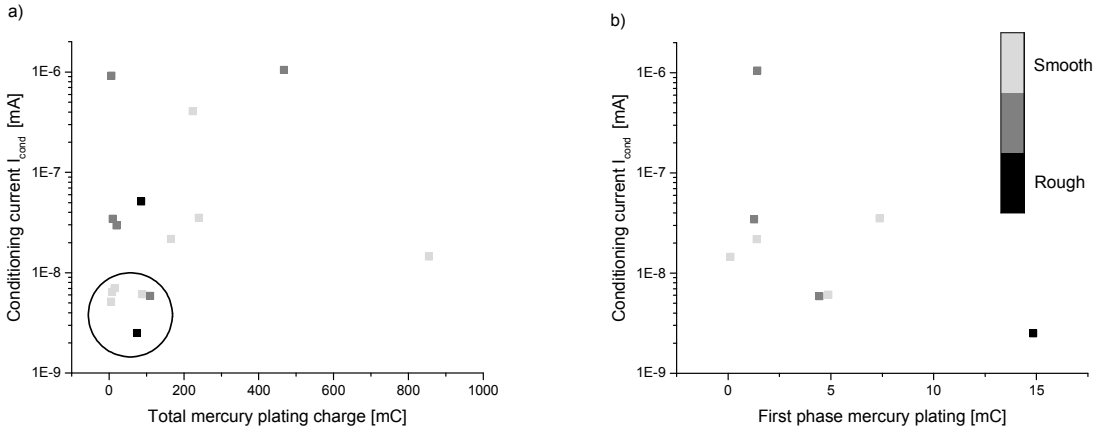

Figure 79: a) Total mercury and b) first phase mercury plating charge correlated with conditioning current I_{cond}. Electrode diameter: 100 µm. I_{cond} at E_{cond} of −0.9 V vs. Ag/AgCl. 50 mM phosphate buffer at room temperature. Colormap indicates roughness: Grey and black represent smooth and rough surfaces respectively.

The above experiments indicate that electrode surface varied heavily due to irregular deposition under the given conditions and that under these circumstances charge is not a sufficient criterion to evaluate electrode quality. It appears that the electrode roughness plays a minor role compared to the plating itself. Therefore, together with the results from the previous section it is concluded that a fixed mercury deposition below 6 mC (100 µm Ø, Au) would be preferred over a constant deposition time to result in more reproducible electrode surface. In addition, electrodes should be handled with care after deposition to not perturb the mercury droplet prior to amalgam formation.

9.1.2. Electrode characterization in AWW – a prerequisite for sulfide stripping

The electrodes were characterized in artificial waste water to identify possible interferences with the potential region of sulfide detection indicated below (Figure 80) and to evaluate the best settings for cathodic stripping. For 200 µM sulfide, its stripping peak was found at below -0.5 mV.

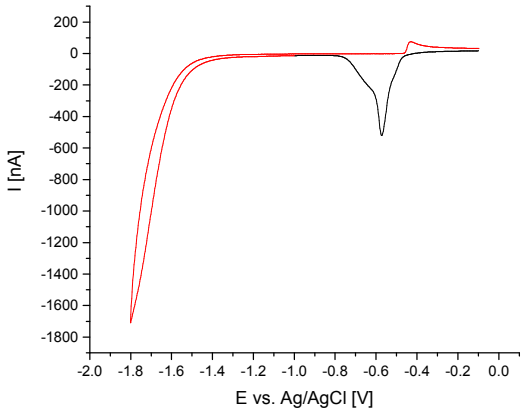

Figure 80: Location of the sulfide stripping peak (black) in artificial waste water spiked with 200 µM sulfide.

9.1.3. E_{cond} below 1 V vs. Ag/AgCl and t_{acc} at 2 s minimize interferences

The complex sample matrix of waste water might interfere with gold amalgam sensor system. Artificial waste water is less variable than real waste water but still rich in a broad range of possible interacting analytes. For this reason, the sensor was characterized in AWW 1 with 10 mM acetate and compared to plain phosphate buffer.

The onset potential and the hydrogen evolution rate are higher in artificial waste water when compared to the plain 50 mM phosphate buffer (Figure 81). A reversible redox species with a formal potential of around −0.65 V vs. Ag/AgCl and a peak current of ~15 nA is visible. Other present analytes such as copper, zinc or manganese peaks appear not to be visible. The unknown redox species might due to organic molecules from the vitamin solution.

The best signal response was determined by changing conditioning, accumulation and stripping parameters. The least interference was visible at a conditioning potential of −1 V vs. Ag/AgCl (Figure 82). Potential changes into either the positive or negative induced undesired redox peaks. Altering the conditioning potential more positive resulted in highest obstructions which indicated that the unknown redox species required an accumulation potential more anodic than

−1 V vs. Ag/AgCl. The reasons for the obstructions at lower conditioning potential are not clear.

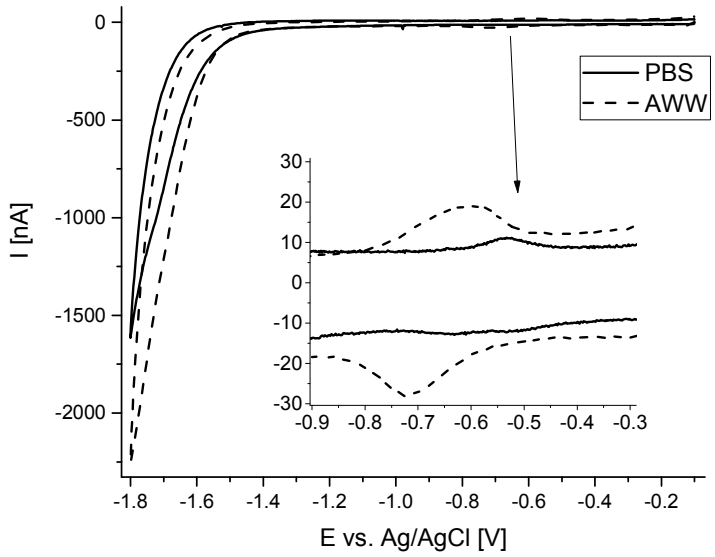

Figure 81: Cathodic sweep of a gold amalgam microelectrode (100 µm Ø). Inset: Zoom in on potential window for sulfide stripping. Comparison between artificial waste water and 50 mM phosphate buffer.

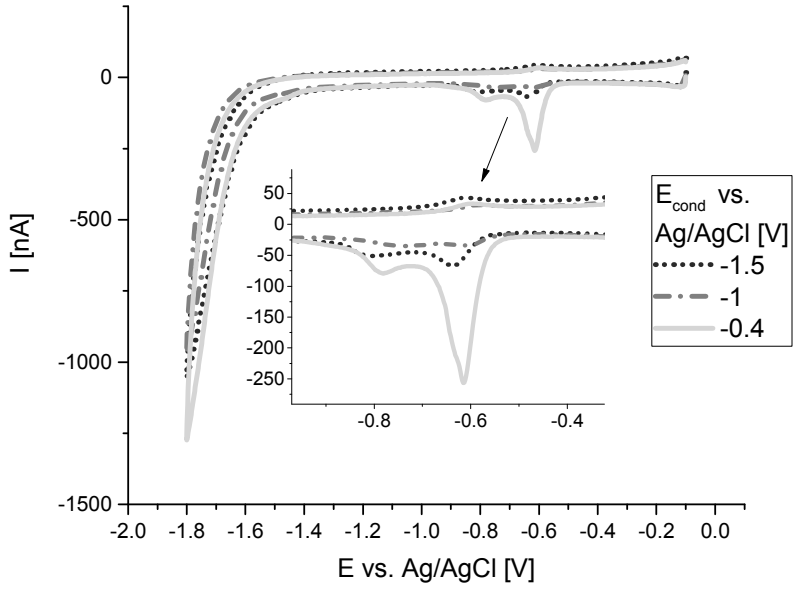

Figure 82: Variation of conditioning potential E_{cond} AgCl and its impact on the cathodic sweep in artificial waste water with 50 mM phosphate buffer and 10 mM sodium acetate. Inset: zoom in the region of sulfide detection. Electrode signature: JMSA_EL_AuHg_24.2.

The stripping peak of the unknown species increased by raising the deposition time t_{acc} (Figure 83). If it would be identified and of interest, it could be detected in AWW in absence of sulfide.

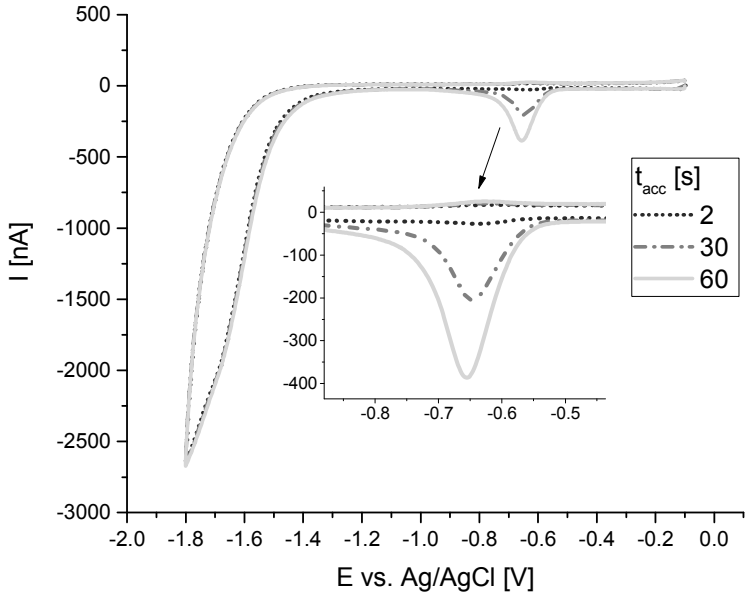

Figure 83: Variation of accumulation time t_{acc} at E_{acc} of −0.1 vs. Ag/AgCl and its impact on the cathodic sweep in artificial waste water with 50 mM phosphate buffer and 10 mM sodium acetate. Inset: zoom in the region of sulfide detection. Electrode signature: JMSA_EL_AuHg_24.2.

As expected, increasing the scan rate lead to higher capacitive currents as well as elevated hydrogen production. In addition, it revealed a new oxidation peak (Figure 84). On the other side, no other analyte was visible in the cathodic/negative current spectra when raising the sweep rate.

Shifting the start and vertex potential of the sweep from −0.1 to 0 V vs. Ag/AgCl increased both, the initial reduction currents and the later oxidative currents (Figure 85). Thus, the upper oxidation limit was set to −0.1 V vs. Ag/AgCl in all later experiments, because increasing above revealed no new redox peaks (e.g. copper) and to avoid the related risk of mercury decay in the anodic region.

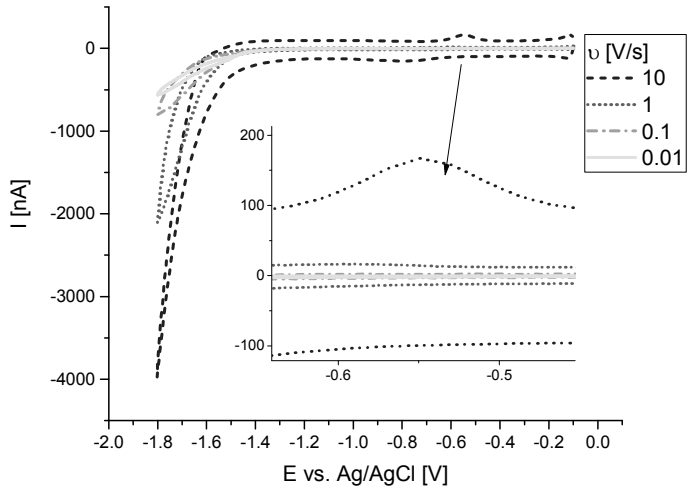

Figure 84: Variation of scan rate υ and its impact on the cathodic sweep in artificial waste water. Supporting electrolyte was 50 mM phosphate buffer and 10 mM sodium acetate. Inset: zoom in the region of sulfide detection. Electrode signature: JMSA_EL_AuHg_24.2.

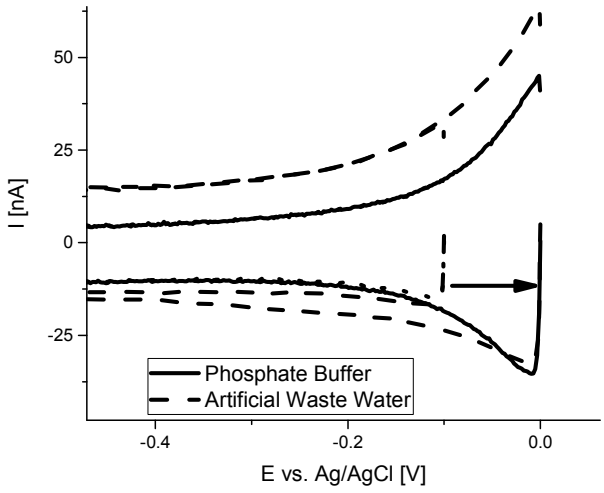

Figure 85: Increased anodic potential limit of the cathodic stripping voltammetry Gold amalgam microelectrode. Deposition, start and vertex potential were changed from −0.1 V to 0 V vs. Ag/AgCl. The electrolyte was waste water with 50 mM phosphate buffer and 10 mM sodium acetate. Electrode signature: JMSA_EL_AuHg_24.2.

9.1.4. Manganese detection limit is too high in artificial waste water

The manganese concentration was raised to 2 mM to locate potential stripping peaks and to evaluate if cathodic stripping is sensitive enough to detect its depletion in the context of

artificial waste water. Its addition did not result in distinct peak formation. Only a slightly apparent earlier onset potential of hydrogen evolution was found. Since artificial waste water contains manganese concentrations well below 2 mM, cathodic stripping would not allow detection. Noteworthy, this is different to previous studies where manganese could be detected in the micro molar range [189]. A change in accumulation time and scan rate might improve discriminatory power.

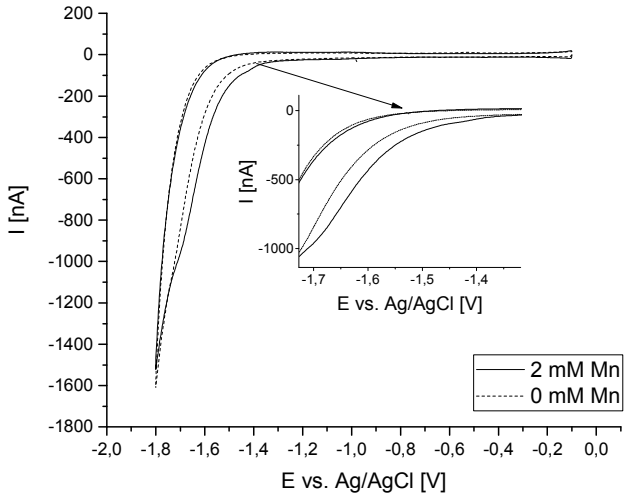

Figure 86: Cathodic stripping voltammetry of manganese at gold amalgam microelectrode (100 µM diameter) in 50 mM phosphate buffer at room temperature.

9.1.5. Double layer capacitance of the gold-amalgam electrode is marginal

The capacitive double layer was determined in the absence of faradaic currents at −0.4 V vs. Ag/AgCl. The gold amalgam electrode shows a linear current-scan rate relationship in phosphate buffer and artificial waste water. When increasing ion concentration of phosphate buffer by adding sodium acetate, vitamin and mineral solution the double layer capacitance increased from 6.95 nF ±0.08 nF to 8.62 ±0.08 nF. Reduction of the sodium ion content in artificial waste water without acetate, but with 10 mM glucose and 2 mM $MnSO_4$ resulted in 8.03 ±0.07 nF of double layer capacitance. The marginal capacitive currents allow a good signal to noise ratio. Adding further ions will increase the capacitive currents, and thus decrease the signal to noise ratio of the cathodic sweep.

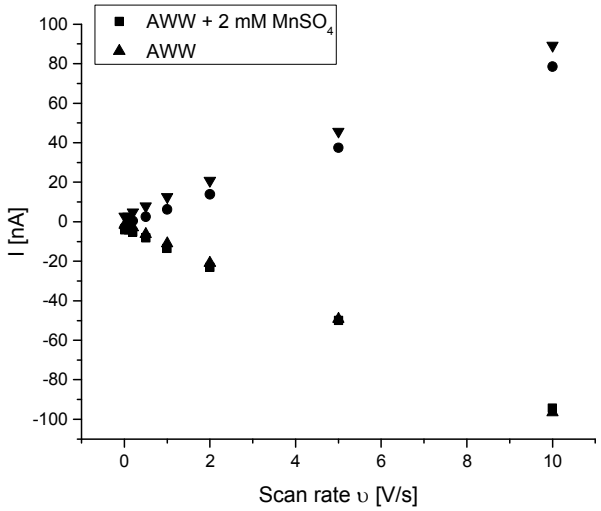

Figure 87: Currents vs. scan rate during voltammetry scans at −0.4 V vs. Ag/AgCl. Currents of the forward and backward scan at varying scan rates for capacity determination in artificial waste water and artificial waste water plus extra carbon and sulfate source. The reverse scan was used to determine the double layer capacity.

The standard parameters for cathodic stripping suggested by Luther et. al appear to be suitable for the adaption of the gold amalgam micro sensor for artificial waste water [189]. Setting the scan rate to 1 V/s, the deposition potential to −0.1 V vs. Ag/AgCl for 2 s and the conditioning potential to −1 V vs. Ag/AgCl for 20 s will allow sulfide detection with little interference. The presented cyclic voltammograms provide a point of reference to the experimenter as when performing the stripping experiments.

Other species of interest, such as copper, manganese, iron or zinc, were concentrated low enough not to interfere with the sulfide signal. Raising the conditioning potential and deposition time might lead to accumulation of some of the cations possibly obstructing the sulfide signal.

9.1.6. Calibration allows to detect up to 2 mM sulfide

The previous experiments suggested the setting parameters for cathodic stripping voltammetry in artificial waste water. Next, the stripping response of sulfide at varying temperatures and accumulation time t_{acc} is determined. Calibrations were performed for two magnitudes of sulfide concentrations ~2 mM and ~200 µM.

9.1.7. Linear signal-temperature correlation: 10 °C quadruples the sulfide signal

Temperature influences several parameters of the cathodic stripping procedure such as diffusion and reaction rates. Therefore, higher temperature causes increased accumulation, and thus increases stripping peaks. The correlation of the sulfide peak height and temperature was done to evaluate if calibration results might be interpolated linearly to a different temperature regime. In a linear correlation, the change of the peak current I_P would depend on temperature (T), a correlation factor a_{corr}.and a baseline (b) in a simple manner:

$$I_p(T) = T * a_{corr} + b$$

The temperature was changed from 25 to 36°C to determine the impact on peak height during cathodic stripping at 25 µM sulfide. The peak height was found to increase linearly with a_{corr} of -32.3 nA/°C. Thus, an increase of 10 °C quadrupled the sulfide peaks and increases the sensitivity drastically. This rate of change indicated that the stripping is very temperature sensitive and temperature should be kept constant during experiments.

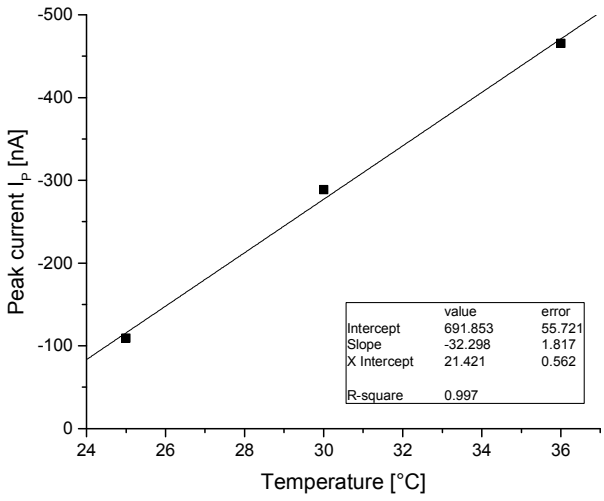

Figure 88: Cathodic stripping peak current I_p at 25 µM sulfide in dependency of temperature changes. Supporting electrolyte was artificial waste water with 50 mM phosphate buffer and 10 mM sodium lactate. Measured in a faraday cage without stirring. E_{cond} = −1 V vs. Ag/AgCl.; t_{acc} = 2 s; E_{acc} = −0.1 V vs. Ag/AgCl; t_{cond} = 20 s; υ_{sweep} = 1 V/s.; Electrode signature JMSA_EL_AuHg_17.

9.1.8. Accumulation time up to 20 s proportionally increases stripping peaks

A key step in cathodic stripping is the time for analyte accumulation at the Au-Hg electrode. Therefore, next it was determined how its duration influenced the sensitivity.

The sulfide stripping peak height correlated linearly with accumulation time until 20 seconds (Figure 89). Afterwards a flattening, therefore non-linear behavior became evident. This might have indicated saturation effects which could be well fitted by a quadratic function ($R^2 = 1$).

As the detection of other species might require a deposition time with a non-linear response for sulfide stripping, the wish for additional analyte detection was discarded and the deposition time for sulfide was kept as short as two seconds in later experiments. It is noteworthy, that a tenfold increase of accumulation time only doubles the signal the. As seen from the previous section, temperature impacts the signal more significantly.

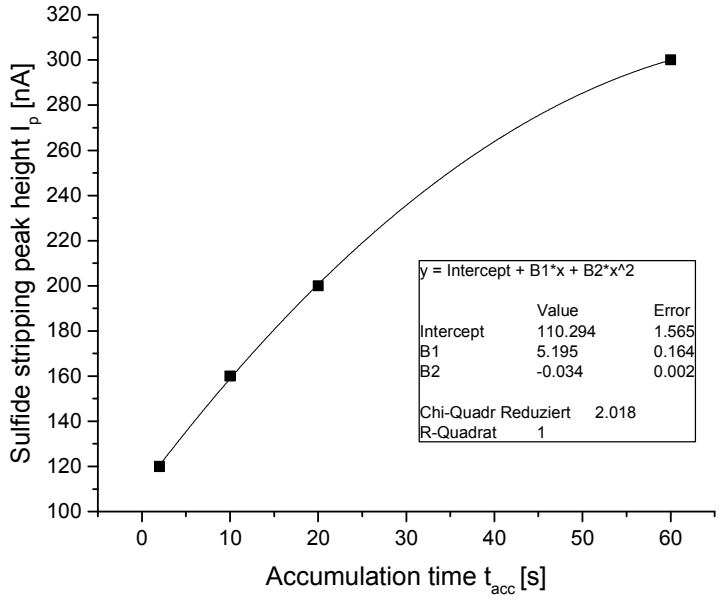

Figure 89: Sensitivity for sulfide increased with accumulation time. Non-linear fit of sulfide stripping peak height with t_{acc} at −0.1 V vs. Ag/AgCl.

9.1.9. Sulfide calibration for up to 200 µM in AWW 1

Sulfide calibration was performed first in AWW 1, which is most commonly used for electroactive biofilm growth. It was calibrated up to its inherent maximum sulfide concentration of 200 µM.

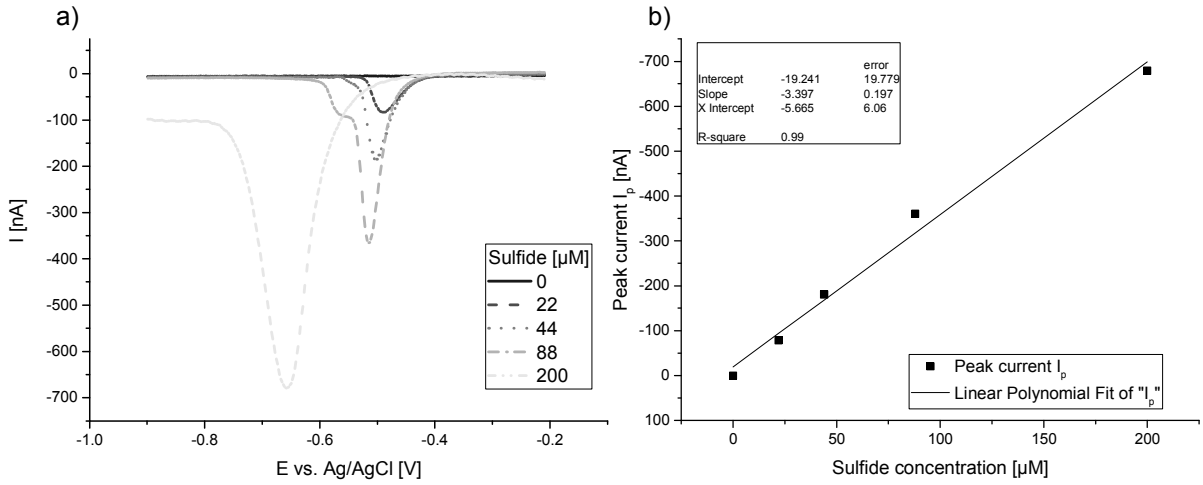

Figure 90: Sulfide calibration in artificial waste water. a) sulfide peaks during cathodic stripping b) respective calibration curve. Supporting electrolyte artificial waste water with 10 mM sodium acetate at room temperature in a faraday cage without stirring. t_{acc} = 2 s; E_{acc} = −0.1 V vs. Ag/AgCl; t_{cond} = 20 s; E_{cond} = −1 V vs. Ag/AgCl.; υ_{sweep} = 1 V/s.; Electrode signature JMSA_EL_AuHg_17

The calibration curve exhibited a slightly more promising R^2 as compared to a newly developed spectrophotometric detection system for waste water [207].

9.1.10. Sulfide calibration for up to 2 mM in AWW 2

An alternative waste water (AWW 2) composition is currently under development by Riedl et al to better represent the carbon composition and buffer capacity of real waste water. Sulfide calibration for AWW 2 has been done in the range of 0–2000 µM. This represented the maximum possible sulfide concentration due to sulfate and cysteine conversation in this media. The peak height increases similarly as in the previous experiment but as the sulfide concentration increased above 415 µM a second stripping peak became visible. According to the literature this might be due to the presence of polysulfide anions [181].

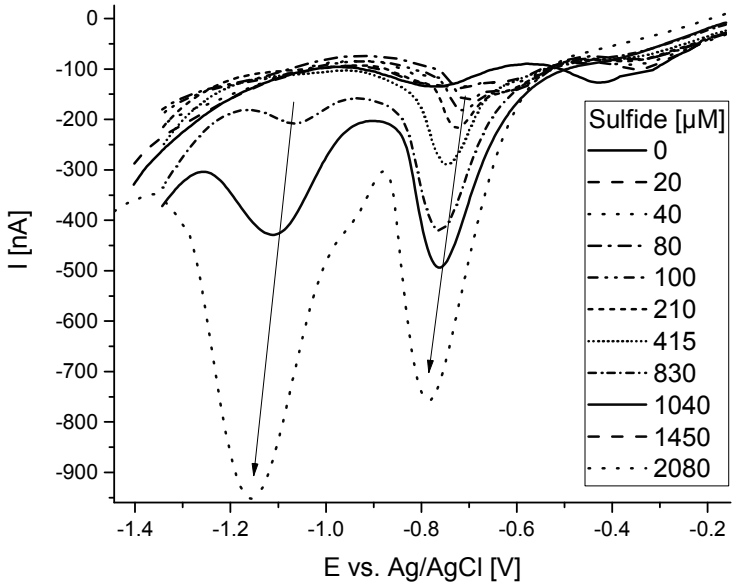

Figure 91: Cathodic stripping of sulfide for calibration for up to 2080 µM. Supporting electrolyte: Artificial waste water 2 with carbonate buffer containing 2.5 mM sodium acetate, 3.3 mM glycine, 0.5 mM D-ribose, 2 mM cysteine, 0.4 mM glucose 10 mM sodium acetate at room temperature in a faraday cage without stirring. t_{acc} *= 2 s;* E_{acc} *= −0.1 V vs. Ag/AgCl;* t_{cond} *= 20 s;* E_{cond} *= −1 V vs. Ag/AgCl.;* υ_{sweep} *= 1 V/s.; Electrode signature JMSA_EL_AuHg_08.*

In contrast to the previous experiment, stripping peaks became only visible if sulfide exceeded ~ 50 µM (Figure 92, inset). This is in accordance with the theory of a precipitation level dependent stripping illustrated above (Figure 73). Interestingly, this indicated a less suitable limit of detection, compared to AWW 1. A possible reason could be an increased sulfide precipitation in the presence of a more alkaline carbonate buffer. This would require exceeding a certain sulfide threshold to precipitate all free metal ions prior to visible sulfide stripping peaks. On the other end of the calibration scale, the current response starts to flatten at high sulfide concentrations. This indicated a saturation response whose degree varied for the three electrodes tested. Linearity appeared to be given in between 50–1500 µM.

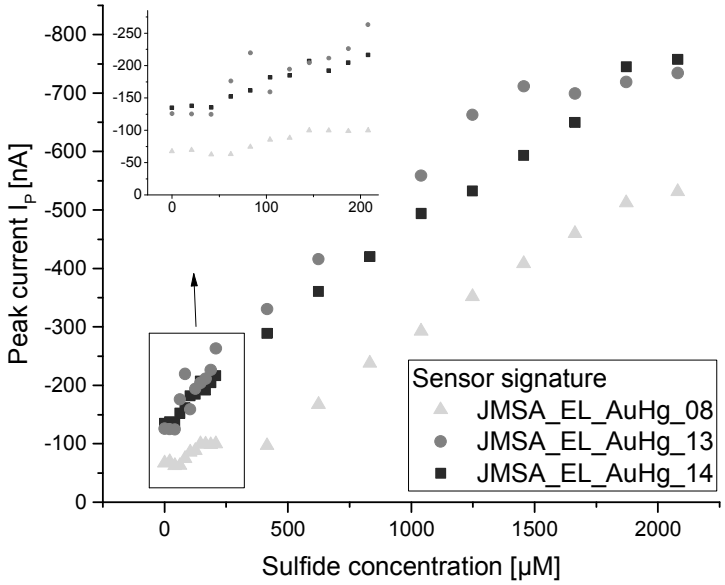

Figure 92: Sulfide calibration in AWW 2 up to 2080 µM. AWW 2 with carbonate buffer containing 2.5 mM sodium acetate, 3.3 mM glycine, 0.5 mM D-ribose, 2 mM cysteine, 0.4 mM glucose 10 mM sodium acetate. Measurements at room temperature in a faraday cage without stirring. t_{acc} = 2 s; E_{acc} = −0.1 V vs. Ag/AgCl; t_{cond} = 20 s; E_{cond} = −1 V vs. Ag/AgCl.; υ_{sweep} = 1 V/s.; Electrode signature JMSA_EL_AuHg_08.

9.1.11. Little difference of semispherical and flat amalgam microelectrodes

The varying mercury deposition presented in the previous section resulted in either semi-spherical or flat amalgam micro-electrodes. Semispherical electrodes exhibit spherical diffusion which increases mass transport and the signal to noise ratio. Thus, it was considered to have an influence on the sensor sensitivity of the gold amalgam electrodes. A semispherical and a flat amalgam microelectrode were compared with respect to their cyclic voltammograms, capacity and calibration curve.

The onset potential for hydrogen evolution and its reduction rate were slightly higher for the flat amalgam electrode (Figure 93). A possible explanation could be a slightly higher presence of unamalgamated gold e.g. at rim of the flat electrode.

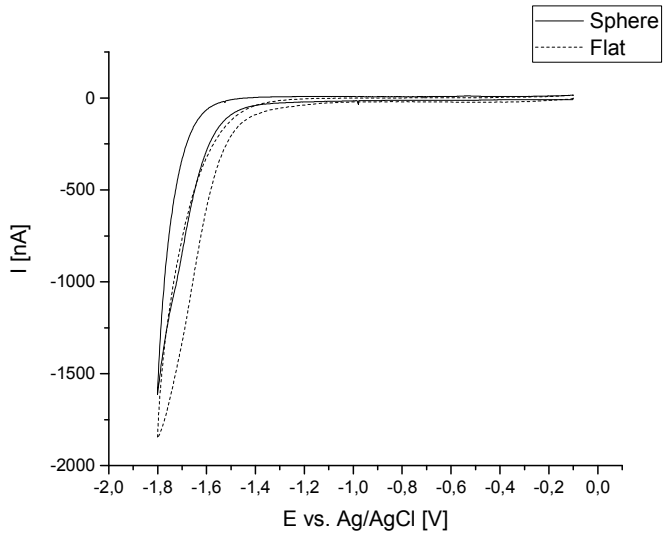

Figure 93: Cyclic voltammograms of spherical and flat gold amalgam electrodes in 50 mM phosphate buffered saline at room temperature without convection. Scan rate 1 V/s.

The double layer capacitance of 6.95 ±0.1 nF for the semi-spherical electrode was slightly higher compared to 4.9 ±0.3 nF of the flat micro electrode. This is in accordance with the theory that capacity scales linearly with electrode surface area.

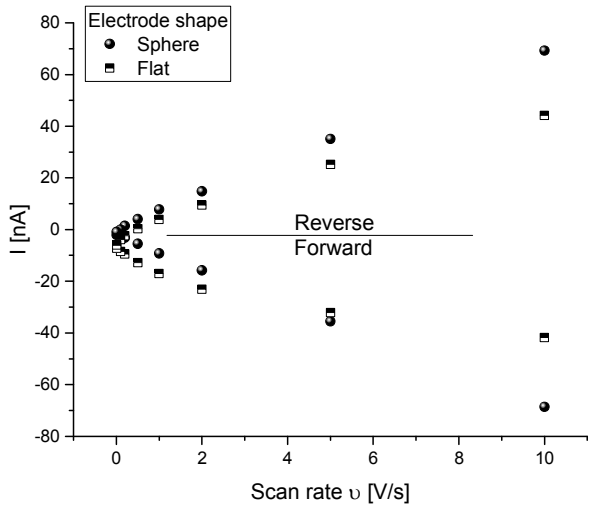

Figure 94: Currents of the forward and backward scan of cyclic voltammograms at 0.4 V vs. Ag/AgCl with varying scan rates for capacity determination. Double layer capacity was determined from the reverse scan.

The sulfide detection window around −0.6 mV vs. Ag/AgCl appeared similar for both electrodes. The stripping peaks were higher for the flat amalgam electrode compared to the semispherical micro electrode (Figure 95), thus more material must have been accumulated at the flat electrode. This was not in accordance with the expected increase in mass transfer due

to spherical diffusion. A possible explanation could be the presence of an inhomogeneous and rough surface of the flat electrodes whose effects on later stripping might have outweighed the diffusive effects.

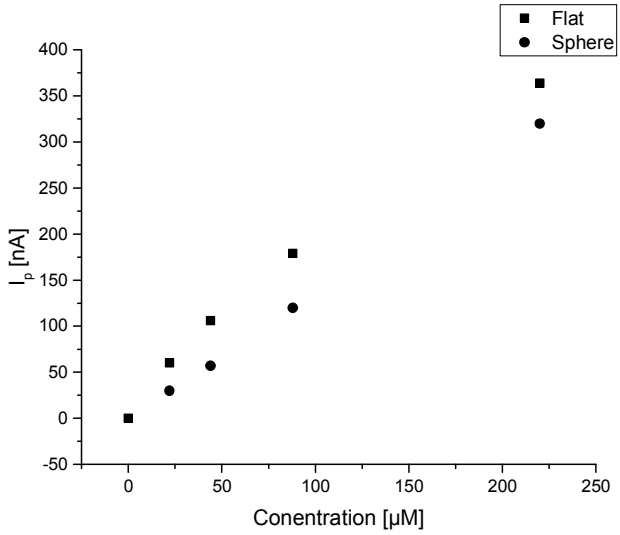

Figure 95: Sulfide calibration curve by cathodic stripping voltammetry in artificial waste water 1. Peak currents (I_P) are correlated to sulfide concentrations varying from 0 to over ~200 µM. I_P is the absolute peak current minus the baseline. Cathodic stripping voltammetry was performed with a 20-s conditioning at −1 V vs. Ag/AgCl followed by a 2-s deposition step at −0.1 V vs. Ag/AgCl and a cathodic sweep at 1 V/s.

In conclusion, the electrochemical difference of semi-spherical and flat 100 µm gold amalgam electrodes appeared to be marginal. Whereas the difference in surface area agrees well with the small change in double layer capacitance, its effect on deposition and stripping is less obvious. This could point out a reduced difference between spherical and planar diffusion at microscale electrodes.

9.1.12. Tracing microbial sulfide production in AWW

Ultimately the gold amalgam microelectrodes were intended for the online determination of microbial induced sulfide emissions in two different types of AWW. AWW 1 with low total sulfur species content (~ 200 µM) and AWW 2 with 10 times increased total sulfur species content. The low total sulfur media was supplied by acetate and the high total sulfur media was supplied with further fermentable carbon sources.

9.1.13. Sulfide emission in AWW 1 – partial conversion

The gold amalgam microelectrode was intended for the online measurement of biogenic sulfide emission in artificial waste water. For this purpose, a calibrated microelectrode was inserted into a reactor with AWW 1 inoculated with ASS. Cathodic stripping was performed every half hour over the course of four days. The AWW 1 contained 10 mM lactate instead of acetate and 212 µM of sulfate as feedstock for sulfate reducing bacteria.

The qualitative assessment of the sulfide peak development suggested a lag phase of 10–15 hours until significant sulfide production takes place (Figure 96). This is in accordance with the previous experiments where ASSes exhibited a similar lag phase at OCP (Figure 61). After reaching maximum peak height, oscillations became visible. Their magnitude could be explained by incubator temperature changes impacting peak height (see Figure 88: 32.3 nA/°C).

The previous calibration was used to determine the sulfide concentration (Figure 97). Sulfide was not detectable until 20 h. Then, a steep increase to 60–70 µM sulfide was observed until 42 h and followed by a continuous decrease. Only >79 µM sulfide concentration was reached and not the maximum possible 212 µM. The maximum sulfide concentration was also lower as compared to the EABs and ASSes found in the previous chapter (Figure 62). In accordance to the qualitative analysis, the calculated concentrations showed oscillations of around 20 µM.

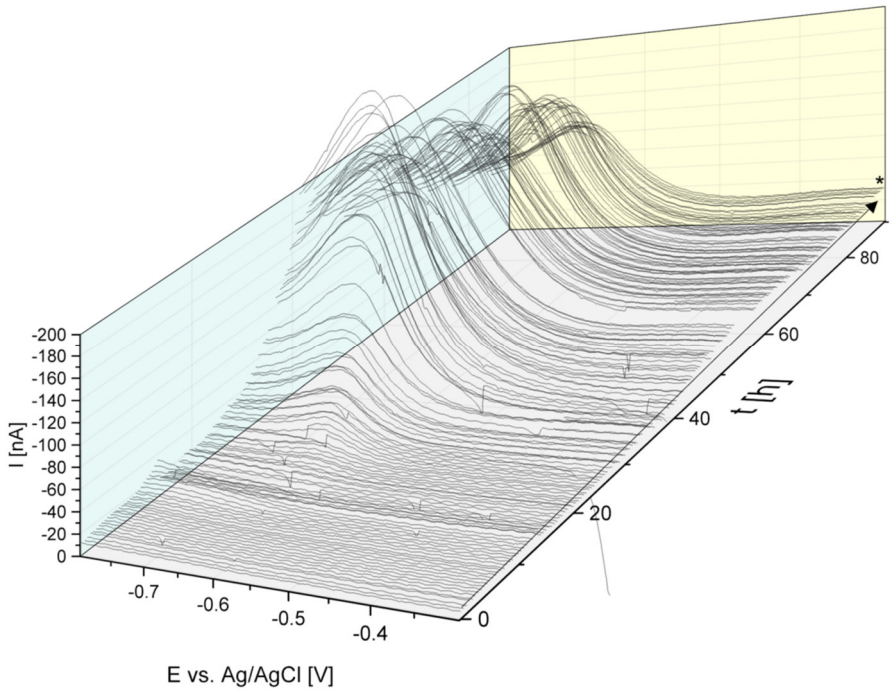

Figure 96: Cathodic stripping peaks during sulfide formation in artificial waste water. AWW with 10 mM lactate instead of acetate. Room temperature. No convection. E_{cond} of −1 V vs. Ag/AgCl for t_{cond} of 20 s. Accumulation of sulfide at E_{acc} at −0.1 V vs. Ag/AgCl for t_{acc} of 2 s. Cathodic sweep starting at −0.1 V vs. Ag/AgCl. Star indicates the temporal increase of the baseline. Experiment performed in Faraday cage at RT.

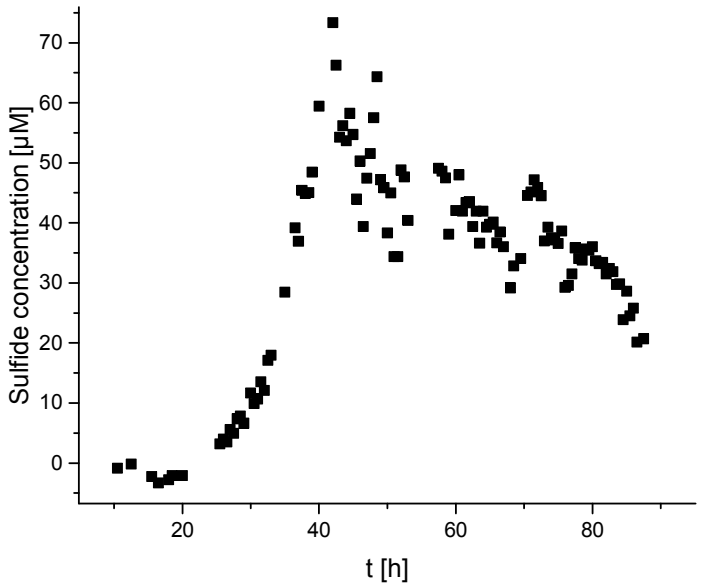

Figure 97: Sulfide concentration over time in AWW 1. Sulfide stripping peaks were determined by Gaussian curve fitting with Origin Pro Gaussian Peak quick fit. The concentration was determined based on a previous calibration curve.

9.1.14. Sulfide emission in AWW 2 – full conversion

Waste waters might contain more than 200 µM sulfide. AWW 2 might account more accurately for a sulfide rich waste water providing a maximum possible concentration of 2152 µM. Therefore, the Au-Hg electrode was also used to trace sulfide emissions in this type of AWW during 48 h.

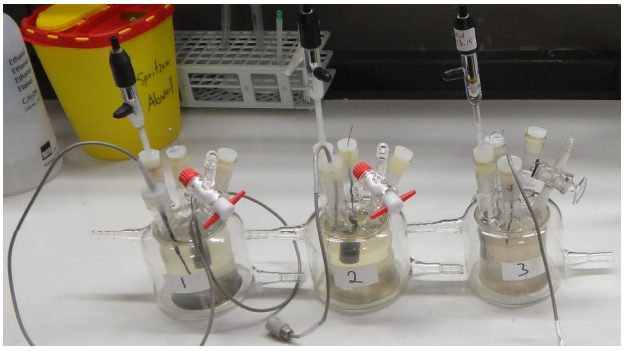

Figure 98: Reactor setup for cathodic stripping analysis of biogenic sulfide emission in artificial waste water.

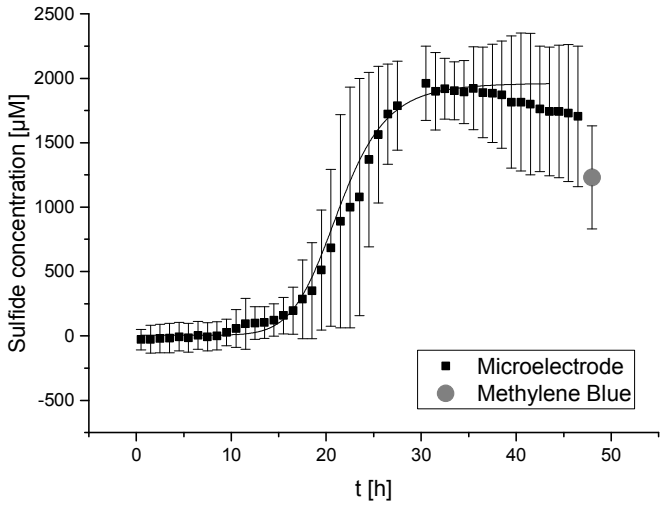

Figure 99: Sulfide concentration over time in AWW 2 measured by cathodic stripping voltammetry. The maximum sulfide content is limited by cysteine and sulfate to a maximum of 2212 µM. Inoculation at 0 h with 1 mL waste water from primary effluent of WWTP Steinhof, Braunschweig, Germany. Scan rate 2 V/s; E_{cond}= −0.9 V vs. Ag/AgCl.; t_{cond} = 5 s; E_{acc}= −0.1 V; t_{acc} = 2 s. Signatures of used electrodes: JMSA_EL_AU_07, JMSA_EL_AU_08, JMSA_EL_AU_08.3, JMSA_EL_AU_09, JMSA_EL_AU_13, JMSA_EL_AU_14. Sulfide concentration at end of run was additionally determined by the methylene blue method (n = 6). Experiment performed in Faraday-cage at 36 °C.

The sulfide production exhibited a sigmoidal course (straight line, Figure 99) with a 10 h lag time and the exponential increase between 15 h and 25 h, a subsequent plateau and a final decrease after 30 h. The lag phase was shorter compared to experiments in AWW 1, which might be explained by the high temperature and more diverse nutrient content. The apparent sulfide emission was found to be ~170 µM/h during growth. The results of cathodic stripping and methylene blue at 28 h varied by 200 µM. The causes of systematic error were not clear. It was found that both methods showed also a significant random error. This might firstly, originate from the varying composition of the waste water inoculum and secondly, from a variable temperature.

In contrast to the previous experiment, sulfide concentration nearly reached its maximum which indicated that sulfate and cysteine must have been both converted nearly throughout. This could be explained by the presence the carbon sources aside of lactate. Facing more diverse carbon sources the microorganisms might have required more electron accepting sulfur compounds and thereby emitted more sulfide.

The lag time might be induced by switching the metabolic capabilities towards dissimilative sulfate reduction and partially by proliferation of sulfate reducing bacteria. The decrease could be partially explained by fermentation coupled to back oxidation of sulfide to sulfate. At day 6, the decay of sulfide was further investigated and found to be varying between 0 and 400 µM by the Methylene Blue method. Such sulfide back oxidation has been be observed earlier e.g. in interspecies relationship where *Thiobacillus denitrificans* prevented the sulfide accumulation of *Desulfovibrio desulfuricans* [208]. Sulfur did not gas out as it was still found in media by ICP-OES.

9.1.15. Sulfide might precipitate zinc, cobalt and copper

Varying amounts of precipitates were found on the bottom of the reactors ranging from bright to dark color. The pH was found to increase slightly, despite being buffered. This observation suggested to investigate the change in trace elements in the media of the previous experiment by ICP-OES.

Copper was below detection limits in all samples (Table 17). Similarly, the concentration of all metals dropped significantly as well. Interestingly, they did not precipitate throughout as concentrations of cobalt, iron and zinc remained present, but reduced. This is surprising, as high

sulfide concentrations have been present. As expected from the solubility product of manganese sulfide, the concentration of manganese only reduces slightly.

Table 17: Selected elements initially present in artificial waste water and determined by ICP-OES after seven days of incubation with sulfate reducing bacteria. n = 6 denoted by 1–6.

Element	Initial	1	2	3	4	5	6	Mean	Dev.	Dev.
	Concentration [µM]									[%]
Ca	107	20	21	24	35	34	34	28	6	23
Co	10	1	4	4	3	3	4	3	1	29
Cu	5	–	–	–	–	–	–	–	–	–
Fe	4	–	3	–	2	2	2	2	1	28
K	3011	*	7026	7949	5308	5359	6359	6400	1007	16
Mg	152	91	56	116	125	120	147	109	29	26
Mn	33	20	19	29	30	29	32	27	5	19
Na	14016	13304	17522	16261	15739	15696	15957	15746	1253	8
P	1293	1013	1532	1545	1455	1469	1516	1422	186	13
S	2212	1857	2896	563	974	226	558	1179	924	78
Zn	8	–	11	2	3	1	3	4	3	86

This experiment emphasized that presence of sulfide and its potential impact of trace element precipitation must be considered when using this composition for the growth of electroactive organisms. E.g. calcium limitations are expected to reduce the electroactive biofilms' current production [209]. The visible decrease to 1/3 of the initial calcium should be considered in future long-term experiments. High amounts of potassium have been found despite not being added to the media. This effect must originate the leakage of potassium from reference electrode saturated KCl electrolyte into the media. We recommend using leak-proof reference electrodes to avoid such interferences in the future.

9.1.16. The conditioning currents as quality indicator – stability in PBS and AWW

The signal drift over time determines the need for occasional recalibration and the date of expiration at which the electrode cannot be used any more. Amalgam electrodes were noticed to have limited shelf life, but time scales and reasons for deterioration appear to be less known, especially not in the new application field of artificial waste water. To estimate a possible drift, cathodic stripping voltammetry was performed for several days in firstly, phosphate buffer and secondly, in AWW 2 during biological sulfide emission to note the drift in conditioning I_{cond} and accumulation currents I_{acc}.

The conditioning current in plain phosphate buffer deviated only a few nanoamperes and converged to less than −5 nA towards the end (Figure 100 a). The variations in conditioning currents response were more diverse during microbial sulfide production (b).

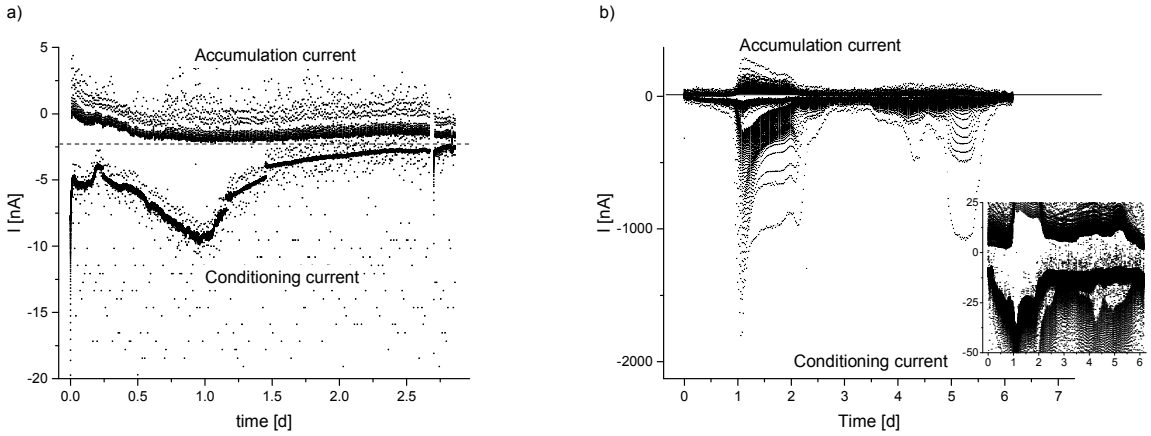

Figure 100: The change of conditioning and accumulation current a) in 50 mM phosphate buffer and b) during microbial induced sulfide production in AWW 2. A 100 µm gold amalgam electrode was used at 25 °C. E_{cond} = −1 V vs. Ag/AgCl, t_{cond} 15; E_{acc} = −0.1 V vs. Ag/AgCl, t_{acc} = 2 s.

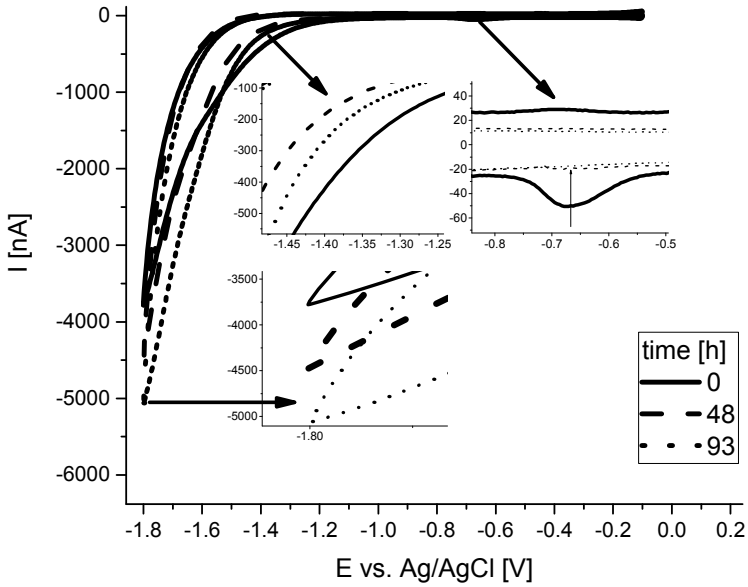

Figure 101: Change of cyclic voltammograms over the course of 93 h at a gold amalgam electrode in 50 mM phosphate buffer at room temperature.

Hydrogen evolution currents increased over time by 1000 nA at −1,8 V vs. Ag/AgCl (Figure 101). Accordingly, its onset overpotential decreased over time. The baseline current within the potential window for sulfide detection stabilized at −20 nA. An initial reduction peak

disappeared. Thus, the electrode appeared only to age slightly during four-day cathodic stripping. Despite the marginal signal changes, the surface structure changed more significantly as will be seen in the next chapters.

9.1.17. The vibrant life of gold amalgam: crystallization and aging

Albeit a defined electrode surface area is essential for the electro-analytical chemistry, little is known about the micro electrode surface formation during mercury deposition and subsequent gold amalgam formation. Moreover, despite being known for its limited shelf-life, time dependent recrystallization of amalgam has not been correlated to the aging process of the electrodes yet. Thus, during the curse of this study the amalgam surface formation and its aging process was its surface formation and aging was more closely investigated.

This study revealed recrystallization processes of the amalgam as one origin for aging. It was found that the major changes during recrystallization occur during the first 24 hours. The later changes affect the smooth crystal structures, resulting in rougher surface and even loss of amalgam.

9.1.18. CLSM studies reveal the temporal gold amalgam crystallization

The deposited mercury will form an amalgam, moreover the deposition of liquid mercury will initiate the amalgam crystallization process. The initial plated mercury serves as the solvent for the solid gold underneath. Crystallization requires supersaturation of a solvent with solute. Gold supersaturation will start at 0.13% (w_{Au}/w_{Hg}) [210] and it will initiate the subsequent crystallization of gold amalgam.

The crystallization process of amalgam was followed by confocal laser scanning microscopy (Figure 102). It was found that a thin mercury coating gives rise to several crystallization nuclei (Figure 102 c)) whereas large spherical depositions results in a single more monolithic crystal (Figure 102 g). Crystal growth ends, once all smooth and glossy excess mercury has precipitated (Figure 102 d). The crystal shapes are diverse and do not match with the ideal cubic, rhombic and icosahedra geometries observed in previous experiments [211] and in the field [212].

Changing surface properties of the electrode should influence the analytic response during cathodic stripping. Thus, prior to use a waiting period of one to two days to complete amalgam crystallization is recommend. Natural amalgams usually have higher gold concentration than required for supersaturation and crystal formation. Therefore, after initial crystallization a change in material composition over time could be still possible but would proceed slower due

to the lower diffusion coefficients within solid amalgam. It has to be noted that the diffusion rate of gold [213] and other metals [214] within mercury is much higher than metal diffusion within solid gold [206]. This is important to understand that the initial crystallization must happen at a faster time scale then the ongoing crystallization.

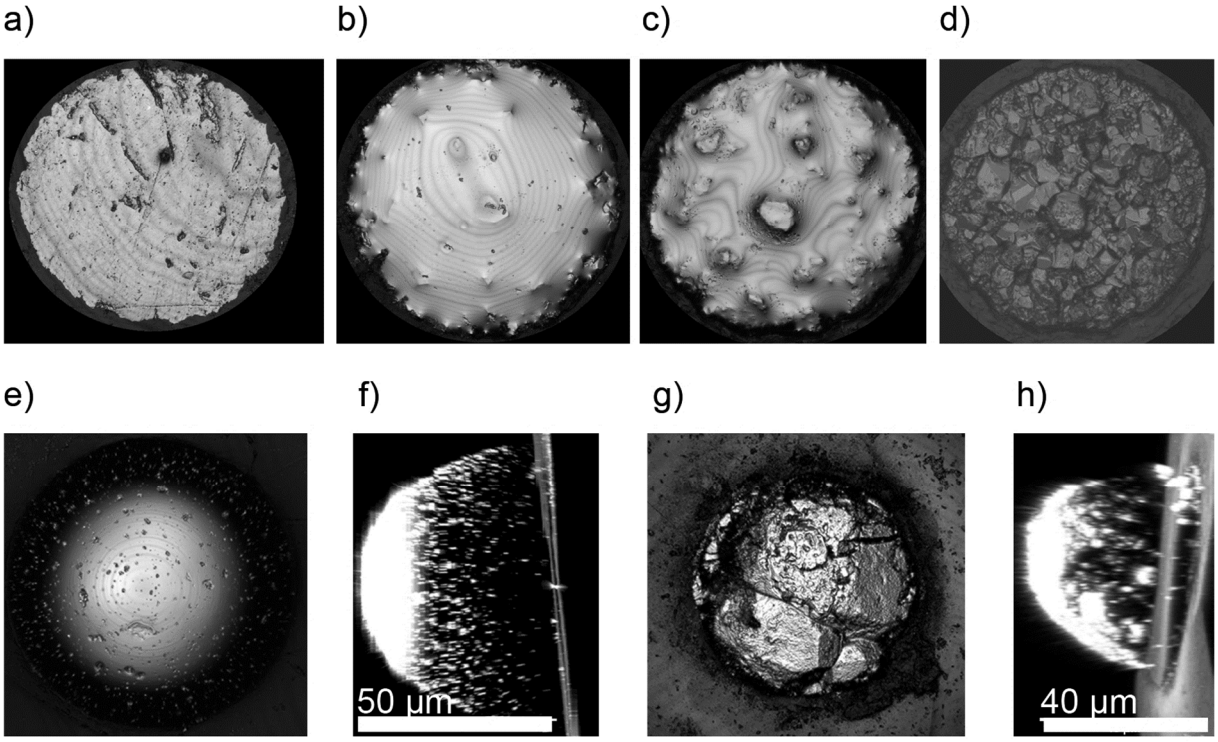

Figure 102: Microscopic view on electrode fabrication, mercury deposition and amalgam crystallization process. a) Polished 100 µm diameter gold wire; b) thin layer of electrodeposited mercury with visible crystallization nuclei; c) ongoing crystallization; d) crystallization state at 5 h; Conical shaped mercury deposition just after deposition: top e) and side f); Crystallized deposition: g) top and h) side.

9.1.19. Aging: Ongoing crystallization, deposition and roughening

Amalgam electrode shelve-life- limitations might be associated with surface changes. Therefore, the extent of aging was observed before and after heavy usage by confocal laser scanning microscopy.

Liquid mercury remained present during crystallization, indicated by flat and smooth regions (Figure 103). It disappeared gradually as the crystallization continued comparing a) and b). After calibration and several hundred stripping cycles, the previously smooth crystalized surface c) started to roughen d) c) and d).

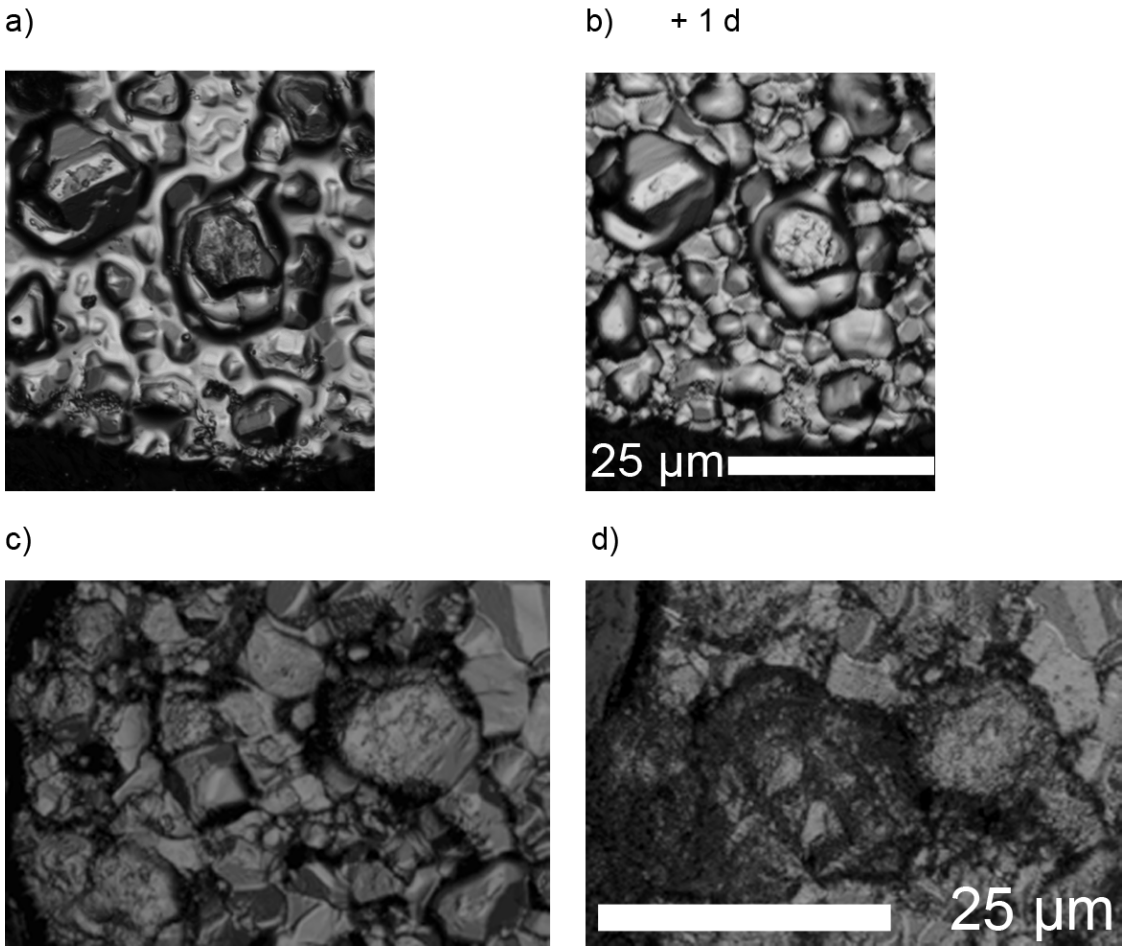

Figure 103:Gold amalgam electrode aging traced by confocal laser scanning microscopy. a) The day of plating; b) 1 d after deposition; c) Prior before use; d) After calibration and several hundred cathodic stripping cycles. Scale bars of b) and d) refer also to the respective image on the left.

This emphasizes the need for regular calibration to ensure proper sensitivity and to measure the drift associated with electrode aging. More attention needs to be paid to the treatment of the electrodes after deposition and how the electrode surface changes during experiments.

9.1.20. Remaining sulfide residues and the gold-mercury-ratio identified by XPS

It was not sure how and if the gold amalgam surface composition changed over time. To detect changes in the top surface composition X-ray photoelectron spectroscopy (XPS) was performed. The XPS spectra were used to estimate the gold-mercury ratio within the top nanometers of the amalgam and to detect possibly absorbed analytes after the electrode has been in use. A 100 µm X-ray spot was targeted to measure the electrode composition and another spot represented the surrounding epoxy resin background noise. It must be considered that the XPS-spectra only gave information on the first few nanometers of the outer amalgam

layer and the amalgamation process is likely to proceed from the bottom to the top of the electrode. The spectra are referred to in the appendix. It was found that the surface amalgam consisted to a higher extend of mercury than gold. In contrast, natural gold amalgams have been reported to consist to a higher extend of gold and only 30%–50% of mercury [215]. This indicates that the amalgam formation might continue and therefore changes the surface composition as well as the surface structure until the final mercury-gold equilibrium is reached.

Additionally, it was found that sulfur species remained at those electrodes which had been subject to sulfide exposure. The accumulation of sulfur species will cause the electrode surface to change. It is not known in which state the sulfide species are present at the electrode. High background noise came from carbon, oxygen and nitrogen, major components of the epoxy resin and as well as from silica the major compound of the surrounding glass.

The XPS data suggests two reasons for the temporal change of the gold amalgam signal. Firstly, the gold amalgam formation could be incomplete until the final equilibria is reached. Secondly, the electrode surface might be subject to sulfur poisoning. The latter one cannot be avoided when sulfide is the intended analyte, but the first aspect might be countered by waiting until the amalgam has reached its final gold-mercury composition.

9.2. Summary and discussion

The gold amalgam microelectrode for cathodic stripping voltammetry was successfully adapted to detect sulfide in artificial waste water. The working range of the analytical method matched well with the environmental conditions in the sewer and the sulfide concentrations possible in artificial waste water. Linearity of the signal was found in between 0 and 200 µM for AWW 1 and ranging from 50–1500 µM AWW 2.

Sulfide could be detected well within the complex sample matrix of artificial waste water with negligible interference of additional compounds. The concentrations of copper, iron, manganese and zinc were below detection limits. Speaking in terms of an analytical chemist, the specificity for sulfide detection was high during the cathodic sweep.

The robustness is an estimate of how the surrounding environment (parameters, personal, equipment, laboratory) influences an analytical method. As aforementioned, the temperature and accumulation time strongly influenced the experiments and thus should be kept constant during the calibration and the measurement. The same holds true for the potential boundaries, because they influenced the specificity. In summary, the best settings for sulfide detection were similar to those suggested by Luther et al [179]. The novice in electrochemistry needs to be very

considerate to maintain constant experimental conditions and he or she needs to be very mindful when deviating from the above experimental parameters. A change in settings could be desired if the method was required for stripping of other compounds.

The analytical method was applied for online detection of biological sulfide emission in artificial waste water. In AWW 2 cysteine and sulfate were found almost completely dissimilated to sulfide within 30 hours whereas in AWW 1, sulfate was dissimilated only partially which took up to 45 hours. The conversion rate appeared to be higher in presence of cysteine and additional carbon sources. The course of sulfide emissions of ASS in AWW 1 with 10 mM lactate matched well with the previous methylene blue based study, but the maximum sulfide concentration was slightly lower.

A proper electrode production is the key element for the robustness of the analytical method. This study considered the mercury deposition process and the electrode aging. It suggests to rather limit the amount of mercury than the deposition time. A 100 µm gold electrode appeared unlikely to hold deposition higher than 3–6 mC of Hg^{2+} and loss of excess mercury might have resulted in non-defined mercury depositions, and thus varying signals. The method should be adjusted accordingly by limiting the plating charge.

By observing the crystallization process, it could be concluded, that the transport rate of gold into mercury is sufficient for crzstallisation of even large mercury depositions. Amalgam electrodes were suggested to mature at least 12 hours prior to measurement [216]. This is in accordance with the findings of an ongoing crystallization process. In addition, XPS studies suggested that reaching the final gold-amalgam equilibrium will require a long period of time. This is most likely due to a reduced diffusion rate of gold once the amalgam has solidified. Also, careful handling of the amalgam forming electrodes during and after deposition is suggested to prevent unintended loss of mercury which could lead to less defined surface area.

This study found that resulting flat and spherical amalgam surfaces both had similar capacitance and sulfide calibration results. A transition from a spherical to flat Nernstian diffusion could not be observed. This indicates that surface geometry plays a minor role on cathodic stripping with micro-scale electrodes.

9.3. Outlook

More data was recorded than required for sulfide peak detection. The amount of data could be reduced in further sulfide studies. Firstly, by performing cathodic linear sweeps instead of cyclic voltammograms and secondly, by reducing the amounts of repeats per measurement. During sampling the cathodic stripping was performed 1–4 times after another to determine the reproducibility of a measurement. In most cases, the cyclic voltammograms were closely matching, few measurements showed divergence. The first voltammogram deviated the most from the subsequent voltammograms. It was found sufficiently reproducible to use the second sweep for analysis. Thus, not more than two stripping-sweeps are required per point in time. Both measures would decrease the amount of data and required measurement time.

Together with the solution resistance Rs the double layer capacitance C could be used to calculate the time constant CRs which is an estimate for the maximum possible sweep speed with suitable signal to noise ratio at a certain sulfide concentration.

The final step to proceed would be the adaption to the environment of real waste water.

10. Summary and conclusion

The goal of this thesis was to investigate aspects of a potential MFC implementation into the waste water infrastructure. For this purpose, three aspects were focused on:

1. Deployment sites within the municipal sewer infrastructure were identified and evaluated.
2. MFC's major bottleneck is the cathode. It was targeted by comparing renewable carbonaceous materials, by improving the required analytics and by a spatial positioning strategy to reduce mass transfer.
3. Sulfide emission-control trough electroactive biofilms was examined to tackle sewer corrosion. In addition, a method for electroanalytical online sulfide determination was adapted.

Evaluating existing waste water infrastructure and eutrophic environments for Microbial Fuel Cell implementation

Studies on MFC implementation strategies are rare. In the first chapter of this thesis, a procedure was presented to characterize and evaluate MFC deployment sites based on their physiochemical parameters. Oxygen content was considered the most important factor, due to its influence on the performance of electroactive microorganism. Day-to-day measurements in the city of Braunschweig suggested that an electricity generating Microbial Fuel Cell would be most feasible between the pumping station Ölper and the waste water treatment plant Steinhof or even in one the irrigation field side ponds. These sites provided high anaerobicity which correlated with the sewage's residence time. Other sites were less suitable regarding the oxygen content, but could be still of interest for signal generation if the MFC is intended as a sewer state information system. Two possible events whose detection might be of interest are firstly, heavy rain events or secondly, the influx of contaminated sewage. The logical next step would be a continuous measurement of the intra-day-changes to a) evaluate its possible impact on current production, b) give insights in its potential as signal output and c) derive conclusions for the cathode design.

This study investigated a mixed gravity sewer which also conducted rain water. The influx of rain water increased oxygen content and reduced conductivity. In case of rain, it therefore provided less useful conditions for MFC energy recovery. Constructing more separated sewer systems in the future, separating rainwater and sewage, might change that by providing higher nutrient density and more anaerobicity in the future [217].

In summary, the sewer system appears not to be evenly suitable for electricity generation. Deployment sites appear to improve while getting closer to the waste water treatment plant. Less suitable sites within the sewer might be still of interest for signaling purposes.

Cathode characterization requires to mimic the environment intended for application

The aforementioned results together with an analysis of recent literature emphasized that cathode performance studies often only partially account for future operational conditions. Polarization curves taken from rotating disc electrodes are well suited for comparing catalytic performance but they won't reflect the behavior during MFC operation. Therefore, an improved method for mimicking the non-ideal sewer environment was provided. This included low scan rate voltammetry in absence of convective forces using high porous and smooth materials. Otherwise, if MFC cathodes weren't characterized at relatively low scan rates, transient and capacitive currents would have contributed to a significant current increase resulting in misleading performance assumption. In addition, a simple averaging method was suggested to determine less transient polarization curves for materials with high capacitive currents in reduced time. In contrast, if not a polarization curve, but the current of single polarization voltage step is of interest, chronoamperometric current determination at discrete potentials is recommended.

Materials comparison

Three different hydrophilic, carbonaceous materials for MFC cathodes were compared: Microporous activated carbon cloth (AC), mesoporous reticulated carbon foam (RCF) and macroporous carbonized layered corrugated carbon (LCC). To perform experiments with these fragile materials, a cheap and easy to build multi-purpose-electrode backbone was developed to hold and test them in a reproducible and reliable way.It was found, that all investigated electrode materials exhibited only limited cathode performance, especially when poised above 0 V vs. Ag/AgCl which was unfortunate as high cathode potentials are desired.

Nitric acid treatment did improve cathode perfomance of carbon nanotubes in earlier studies on [91], but it did not improve the materials used in this study. It reduced all materials' current densities except that for RCF, whose significant increase also came along with a much higher variability. In all cases the nitric acid treatment significantly increased electrode resistance, which made them inappropriate for the use in MFCs due to its negative impact on power output.

With respect to resistance, mesoporous RCF turned out to be most suitable, whereas LCC turned out to be worst. The conductivity of AC appeared to be variable depending on the contacting pressure. However, conductivity of AC might be improved by implementing copper mesh

current collectors, a similar approach as presented by Kretzschmar et al. [93]. Thus, despite exhibiting naturally high resistance, a current collector can be used to improve the internal resistance if the material has desired cathode properties.

In summary, although it is tempting to use renewable noble-metal- free catalysts for MFC applications, the plain materials are often still low in performance and require proper ways to improve catalytic activity. It was shown, that for activated carbon cloth, reticulated carbon foam and carbonized layered corrugated carbon another method than nitric acid treatment will be required. To compare cathode performance, they should be tested at low scan rates and under similar conditions as in the future MFC: In absence of convection.

Love is in the air: Cathode improvement by capillary forces

The initial evaluation of possible deployment sites often revealed a homogeneous oxygen concentration. Since MFCs rely on the potential difference between anodic and cathodic compartment, e.g. provided due to oxygen gradients, this is a major caveat for MFC implementation. Therefore, a new strategy was required to place oxygen based cathodes within the anaerobic environment of the sewer. This study provides such an approach by placing porous cathode materials outside the electrolyte. This allowed to harness the capillary forces to obtain a three-interphase system improving performance of vertically arranged macroscopic air cathodes.

Reduction performance increased in all porous cm-scaled materials until being until being fully exposed to air. This effect was most clearly seen for AC whose currents almost tripled upon full air exposure. In contrast, the flat graphite and platinum control electrodes performed best when being completely submersed. This knowledge was used to design free floating air-interphase cathodes which resulted in higher MFC performance compared to submerged electrodes. At the downside, exposure did also increase the total internal resistance and resulted in higher corrosion of the current collector backbone.

Two experiments were performed to account for the effects of oil and surfactants on electrodes placed at the interphase. Activated carbon cloth showed no significant difference in presence of surfactant. In contrast, the graphite cathode exposed to canola oil lost nearly 50 % of its performance.

In conclusion air-exposed porous electrodes resulted in a more than 100 % increase of reductive currents, in contrast to flat and smooth material, but the disadvantages are an increased resistance and the danger of fats and oils blocking electroactive surface area as well as a higher rate of corrosion. However, even with those drawbacks, a system with air-exposed porous

electrodes represents a crucial step to transform the variable filled sewer system into an electricity producing Microbial Fuel Cell.

The winner is reduction – anodic potential stimulates sulfide emission of electroactive biofilms and artificial sewer slime

Laboratory grown sewer slime and electroactive organisms have been compared with respect to their sulfide emission and the possibility to get control thereof. This study provides insights in the balance between sulfide emission and sulfide oxidation. It became evident that the microbial induced sulfide production as well as the anodic and biologically catalyzed sulfide oxidation take place simultaneously. Under certain conditions the sulfide emission can outweigh sulfide oxidation. This needs to be considered during the scale up of MFC systems to account for its corrosive and toxic effects. One reason for increased sulfide emission can be a high reactor volume/electrode surface ratio or a high dead reactor volume. In addition, this study found a significantly higher lactate conversion rate in the presence of anodic potential. This might be due to induced dissimilatory sulfate reduction pathways or the hydrogenic methanogenesis facilitated by counter electrode derived hydrogen.

In conclusion, biofilm presence and electric potential influenced the course of sulfide production, but a strategy to decrease sulfide emissions will require further research. The initial hypothesis, that electroactive organisms could result in reduced sulfide emissions could not be proven. However, this also comprises the potential for sulfide induced heavy metal precipitation. Further experiments using different potentials and biofilm composition will improve the understanding of potential controlled sulfide emission in the future.

Breathless and slow: Sulfide shocks impair anodic respiration and affect maximum current and cycle duration permanently

The study showed that 10 mM sulfide shocked EABs altered in their outer appearance and long lastingly lost potential to produce current. A broader sulfide concentration range from 1 to 10 mM should be tested to state helpful guide-lines for MFC operation. If the exact impact of sulfide on the biofilms' redox centers is of interest, abiotic cyclic voltammetry studies should consider the change of cytochrome's redox properties in presence and absence of sulfide.

Making sense or no-sense – the application of gold amalgam solid state microelectrodes for the determination of sulfide in artificial waste water

The gold amalgam microelectrode for cathodic stripping voltammetry was successfully adapted to detect sulfide in artificial waste water. Sulfide could be detected well within its complex sample matrix with negligible interference of additional compounds. Linearity of the signal was

found in between 0 and 200 µM for artificial waste water type 1 with 10 mM acetate in phosphate buffer and ranging from 50 – 2000 µM in carbonate buffered artificial waste water type 2 with additional carbon sources in carbonate buffer. The working range matches well with the environmental conditions in the potential field of application and the possible sulfide concentrations in artificial waste water.

The analytical method was found robust, as temperature and accumulation time influenced the signal response in a linear and predictable manner. The best settings for sulfide detection were similar to those suggested by Luther et al [179]. Since almost all parameters of the experiment were found to have a key influence on the signal, constant experimental conditions must be maintained and adjusted carefully.

A proper electrode production is a key element leading to robustness of an electroanalytical method. Therefore, parts of this thesis were dedicated to the mercury plating process and the subsequent amalgam aging.

In contrast to previous studies it suggests limiting the amount of plated mercury rather by charge than by time. This conclusion was drawn from the finding that a 100 µm gold electrode appeared unlikely to hold more than a spherical mercury blob of 3-6 mC and over-deposition might result in loss of excess mercury leaving an undesired, non-defined electrode surface. In addition, careful handling just after the mercury deposition is suggested to avoid unintended material loss.

The observation of the amalgam crystallization revealed that the change in surface structure is an ongoing process during the life of an amalgam electrode. This finding matches well with an previously proposed electrode maturation period prior to use [216].

The analytical method was applied to trace dissimilatory cysteine and sulfate conversion in two types of artificial waste water. In presence of cysteine and sulfate almost complete sulfide conversion was observed within 30 hours whereas in presence of only sulfate, only partial conversion took place and required more time.

Next, it would be of interest for the analytical researcher to point out the detailed merits and downsides of cathodic stripping based sulfide detection compared to other methods. This would require an extensive comparison od techniques such as amperometric sensors, the methylene blue method or chromatography. The long-term objective is online measurement of sulfide in real waste water which required insights in the response to its even more variable and complex sample matrix.

11. References

1. Rabaey, K. & Rozendal, R. a. Microbial electrosynthesis - revisiting the electrical route for microbial production. *Nat. Rev. Microbiol.* **8,** 706–16 (2010).

2. Logan, B. E. *et al.* Microbial fuel cells: Methodology and technology. *Environmental Science and Technology* **40,** 5181–5192 (2006).

3. Harnisch, F., Wirth, S. & Schröder, U. Effects of substrate and metabolite crossover on the cathodic oxygen reduction reaction in microbial fuel cells: Platinum vs. iron(II) phthalocyanine based electrodes. *Electrochem. commun.* **11,** 2253–2256 (2009).

4. Verstraete, W. *et al.* Microbial fuel cells: methodology and technology. *Environ. Sci. Technol.* **40,** 5181–92 (2006).

5. Kouzuma, A. *et al.* Comparative metagenomics of anode-associated microbiomes developed in rice paddy-field microbial fuel cells. *PLoS One* **8,** e77443 (2013).

6. Yamamuro, A., Kouzuma, A., Abe, T. & Watanabe, K. Metagenomic analyses reveal the involvement of syntrophic consortia in methanol/electricity conversion in microbial fuel cells. *PLoS One* **9,** e98425 (2014).

7. Ishii, S. *et al.* Microbial metabolic networks in a complex electrogenic biofilm recovered from a stimulus-induced metatranscriptomics approach. *Sci. Rep.* **5,** 14840 (2015).

8. Zhang, H., Chen, X., Braithwaite, D. & He, Z. Phylogenetic and Metagenomic Analyses of Substrate-Dependent Bacterial Temporal Dynamics in Microbial Fuel Cells. **9,** (2014).

9. Reguera, G. *et al.* Extracellular electron transfer via microbial nanowires. *Nature* **435,** 1098–1101 (2005).

10. Shi, L. *et al.* Extracellular electron transfer mechanisms between microorganisms and minerals. *Nat Rev Microbiol* **14,** 651–662 (2016).

11. Bond, D. R. & Lovley, D. R. Electricity Production by Geobacter sulfurreducens Attached to Electrodes. **69,** (2003).

12. Gimkiewicz, C. & Harnisch, F. Waste water derived electroactive microbial biofilms: growth, maintenance, and basic characterization. *J. Vis. Exp.* 50800 (2013). doi:10.3791/50800

13. Lin, W. C., Coppi, M. V & Lovley, D. R. Geobacter sulfurreducens Can Grow with Oxygen as a Terminal Electron Acceptor. *Appl. Environ. Microbiol.* **70,** 2525–2528

(2004).

14. Harnisch, F. & Freguia, S. A basic tutorial on cyclic voltammetry for the investigation of electroactive microbial biofilms. *Chem. - An Asian J.* **7,** 466–475 (2012).

15. Patil, S. A., Harnisch, F., Kapadnis, B. & Schröder, U. Electroactive mixed culture biofilms in microbial bioelectrochemical systems: the role of temperature for biofilm formation and performance. *Biosens. Bioelectron.* **26,** 803–8 (2010).

16. Patil, S. *et al.* Electroactive mixed culture derived biofilms in microbial bioelectrochemical systems: the role of pH on biofilm formation, performance and composition. *Bioresour. Technol.* **102,** 9683–90 (2011).

17. Baudler, A., Riedl, S. & Schröder, U. Long-Term Performance of Primary and Secondary Electroactive Biofilms Using Layered Corrugated Carbon Electrodes. *Front. Energy Res.* **2,** 1–6 (2014).

18. Perry, S. C. *et al.* The oxygen reduction reaction (ORR) on reduced metals: evidence for a unique relationship between the coverage of adsorbed oxygen species and adsorption energy. *Phys. Chem. Chem. Phys.* **18,** 10218–10223 (2016).

19. Yuan, H., Hou, Y., Abu-Reesh, I. M., Chen, J. & He, Z. Oxygen reduction reaction catalysts used in microbial fuel cells for energy-efficient wastewater treatment: a review. *Mater. Horiz.* **3,** 382–401 (2016).

20. Nørskov, J. K. *et al.* Origin of the Overpotential for Oxygen Reduction at a Fuel-Cell Cathode. 17886–17892 (2004).

21. Hamann, C. H. & Vielstich, W. *Elektrochemie*. (Wiley-VCH, 2005).

22. Popat, S. C., Ki, D., Rittmann, B. E. & Torres, C. I. Importance of OH- transport from cathodes in microbial fuel cells. *ChemSusChem* **5,** 1071–1079 (2012).

23. Liu, H., Cheng, S., Huang, L. & Logan, B. E. Scale-up of membrane-free single-chamber microbial fuel cells. *J. Power Sources* **179,** 274–279 (2008).

24. Logan, B. E. Scaling up microbial fuel cells and other bioelectrochemical systems. *Appl. Microbiol. Biotechnol.* **85,** 1665–71 (2010).

25. Cusick, R. D. *et al.* Performance of a pilot-scale continuous flow microbial electrolysis cell fed winery wastewater. *Appl. Microbiol. Biotechnol.* **89,** 2053–63 (2011).

26. Hosang, W. & Bischof, W. *Abwassertechnik*. (Teubner Verlag, 1998).

27. *Bau und Betrieb der Kanalisation*. (Ernst & Sohn, 1995).

28. Ellis, T. G. in *ENVIRONMENTAL AND ECOLOGICAL CHEMISTRY – Vol. II – Chemistry of Wastewater* **II,** (1983).

29. Tchobanoglous, G., Burton, F. L. (Franklin L. & Metcalf & Eddy. *Wastewater engineering : treatment, disposal, and reuse*. (McGraw-Hill, 1991).

30. Jiang, J. *et al.* Hydrogen Sulfide—Mechanisms of Toxicity and Development of an Antidote. *Sci. Rep.* **6,** 20831 (2016).

31. Millero, F. J., Plese, T. & Fernandez, M. The dissociation of hydrogen sulfide in seawater. *Limnol. Oceanogr.* **33,** 269–274 (1988).

32. Beauchamp, R. O., Bus, J. S., Popp, J. A., Boreiko, C. J. & Andjelkovich, D. A. A critical review of the literature on hydrogen sulfide toxicity. *Crit. Rev. Toxicol.* **13,** 25–97 (1984).

33. Morse, J., Millero, F., Cornwell, J. & Rickard, D. The chemistry of the hydrogen sulfide and iron sulfide systems in natural waters. *Earth-Science Rev.* **24,** 1–42 (1987).

34. Rabus, R., Hansen, T. A. & Widdel, F. *Dissimilatory sulfate- and sulfur-reducing prokaryotes*. *The Prokaryotes: Prokaryotic Physiology and Biochemistry* (2013). doi:10.1007/978-3-642-30141-4_70

35. Bowker, R. P. G., Audibert, G. A. & Donovan, E. *Hydrogen Sulfide Corrosion: Its Consequence, Detection and Control*. (1991).

36. Nielson, A. R. H., Vollertsen, J. & Hvitved-Jacobsen, T. *Sewer Processes: Microbial and Chemical Process Engineering of Sewer Networks*. (Crc Pr Inc, 2013).

37. Jensen, H. S. Hydrogen sulfide induced concrete corrosion of sewer networks. (Aalborg University, 2009).

38. Balch, W. E., Fox, G. E., Magrum, L. J., Woese, C. R. & Wolfe, R. S. Methanogens: reevaluation of a unique biological group. *Microbiol. Rev.* **43,** 260–96 (1979).

39. Brunauer, S., Emmett, P. H. & Teller, E. Adsorption of Gases in Multimolecular Layers. *J. Am. Chem. Soc.* **60,** 309–319 (1938).

40. Thommes, M. *et al.* Physisorption of gases, with special reference to the evaluation of surface area and pore size distribution (IUPAC Technical Report). *Pure Appl. Chem.* **87,** 1051–1069 (2015).

41. Attia, A. A., Rashwan, W. E. & Khedr, S. A. Capacity of activated carbon in the removal of acid dyes subsequent to its thermal treatment. *Dye. Pigment.* **69,** 128–136 (2006).

42. Namane, A., Mekarzia, A., Benrachedi, K., Belhaneche-Bensemra, N. & Hellal, A. Determination of the adsorption capacity of activated carbon made from coffee grounds by chemical activation with ZnCl2 and H 3PO4. *J. Hazard. Mater.* **119,** 189–194 (2005).

43. Hirschberg, J., Loewenthal, L., Krupp, A., Emmert, S. & Viöl, W. Plasma Induced Changes in Human Lipid Composition as Revealed through XPS-Analysis. *Nat. Sci.* **8,** 125–137 (2016).

44. Richard G Compton. *Understanding Voltammetry*. (2010).

45. Labelle, E. & Bond, D. R. Cyclic voltammetry for the study of microbial electron transfer at electrodes. (2005).

46. Harnisch, F. & Freguia, S. A basic tutorial on cyclic voltammetry for the investigation of electroactive microbial biofilms. *Chem. Asian J.* **7,** 466–75 (2012).

47. Fricke, K., Harnisch, F. & Schröder, U. On the use of cyclic voltammetry for the study of anodic electron transfer in microbial fuel cells. *Energy Environ. Sci.* **1,** 144 (2008).

48. Herrmann, I. Entwicklung und Optimierung neuer Präparationsverfahren für Übergangsmetall-basierte Elektrokatalysatoren für die Sauerstoffreduktion. (FU Berlin, 2006). at <http://www.diss.fu-berlin.de/diss/receive/FUDISS_thesis_000000002133>

49. Shi, H. Activated carbons and double layer capacitance. *Electrochim. Acta* **41,** 1633–1639 (1996).

50. Cline, J. Spectrophotometric determination of hydrogen sulfide in natural waters. *Limnol. Oceanogr.* 454–458 (1969). doi:10.4319/lo.1969.14.3.0454

51. Hughes, M. N., Centelles, M. N. & Moore, K. P. Making and working with hydrogen sulfide. The chemistry and generation of hydrogen sulfide in vitro and its measurement in vivo: A review. *Free Radical Biology and Medicine* **47,** 1346–1353 (2009).

52. Fogo, J. K. & Popowsky, M. Spectrophotometric Determination of Hydrogen Sulfide. *Anal. Chem.* (1948).

53. Schindelin, J. *et al.* Fiji: an open-source platform for biological-image analysis. *Nat. Methods* **9,** 676–682 (2012).

54. Oh, S. E., Kim, J. R., Joo, J. H. & Logan, B. E. Effects of applied voltages and dissolved oxygen on sustained power generation by microbial fuel cells. *Water Sci. Technol.* **60,** 1311–1317 (2009).

55. Juang, D. F., Lee, C. H., Hsueh, S. C. & Chou, H. Y. Power generation capabilities of

microbial fuel cells with different oxygen supplies in the cathodic chamber. *Appl. Biochem. Biotechnol.* **167,** 714–731 (2012).

56. Oktyabrskii, O. N. & Smirnova, G. V. Redox potential changes in bacterial cultures under stress conditions. *Microbiology* **81,** 131–142 (2012).

57. Nghiem, L. D., Manassa, P., Dawson, M. & Fitzgerald, S. K. Oxidation reduction potential as a parameter to regulate micro-oxygen injection into anaerobic digester for reducing hydrogen sulphide concentration in biogas. *Bioresour. Technol.* **173,** 443–447 (2014).

58. Erable, B., Féron, D. & Bergel, A. Microbial catalysis of the oxygen reduction reaction for microbial fuel cells: a review. *ChemSusChem* **5,** 975–87 (2012).

59. Song, C. & Zhang, J. Electrocatalytic Oxygen Reduction Reaction. *PEM Fuel Cell Electrocatal. Catal. Layers* 89–134 (2008). doi:10.1007/978-1-84800-936-3_2

60. Yong, L. *et al.* Salinity Effect on the Microbial Fuel Cell Performance. *Appl. Mech. Mater.* **651–653,** 1365–1369 (2014).

61. Miyahara, M., Kouzuma, A. & Watanabe, K. Effects of NaCl concentration on anode microbes in microbial fuel cells. *AMB Express* **5,** 123 (2015).

62. Miyahara, M., Kouzuma, A. & Watanabe, K. Sodium chloride concentration determines exoelectrogens in anode biofilms occurring from mangrove-grown brackish sediment. *Bioresour. Technol.* **218,** 674–679 (2016).

63. Camerer, L., Garzmann, M. R. W., Pingel, N.-M. & Schuegraf, W.-D. *Braunschweiger Stadtlexikon*. (Joh. Heinr. Meyer Verlag Braunschweig, 1992).

64. *Advances in Water Pollution Research: Proceedings of the Second International Conference Held in Tokyo, August 1964*. (Elsevier, 2013). at <https://books.google.com/books?id=N_sbBQAAQBAJ&pgis=1>

65. Doherty, L. *et al.* A review of a recently emerged technology: Constructed wetland – microbial fuel cells. *Water Res.* **85,** 38–45 (2015).

66. Chen, S. *et al.* Layered corrugated electrode macrostructures boost microbial bioelectrocatalysis. *Energy Environ. Sci.* **5,** 9769 (2012).

67. Chen, S. *et al.* Reticulated carbon foam derived from a sponge-like natural product as a high-performance anode in microbial fuel cells. *J. Mater. Chem.* **22,** 18609 (2012).

68. Qu, G. *et al.* Asymmetric Supercapacitor Based on Porous N-doped Carbon Derived

from Pomelo Peel and NiO Arrays. *ACS Appl. Mater. Interfaces* **8,** 20822–20830 (2016).

69. Peng, C., Lang, J., Xu, S. & Wang, X. Oxygen-enriched activated carbons from pomelo peel in high energy density supercapacitors. *RSC Adv.* **4,** 54662–54667 (2014).

70. Yuan, W.-J. *et al.* Nitrogen-doped nanoporous carbon derived from waste pomelo peel as a metal-free electrocatalyst for the oxygen reduction reaction. *Nanoscale* **8,** 8704–8711 (2016).

71. Lu, S. *et al.* A Sheet-like Carbon Matrix Hosted Sulfur as Cathode for High-performance Lithium-Sulfur Batteries. *Sci. Rep.* **6,** 20445 (2016).

72. Bhatnagar, A., Hogland, W., Marques, M. & Sillanpää, M. An overview of the modification methods of activated carbon for its water treatment applications. *Chem. Eng. J.* **219,** 499–511 (2013).

73. Yin, C. Y., Aroua, M. K. & Daud, W. M. A. W. Review of modifications of activated carbon for enhancing contaminant uptakes from aqueous solutions. *Sep. Purif. Technol.* **52,** 403–415 (2007).

74. Abbas, Q. *et al.* Strategies to Improve the Performance of Carbon/Carbon Capacitors in Salt Aqueous Electrolytes. *J. Electrochem. Soc.* **162,** A5148–A5157 (2015).

75. Nian, Y.-R. & Teng, H. Nitric Acid Modification of Activated Carbon Electrodes for Improvement of Electrochemical Capacitance. *J. Electrochem. Soc.* **149,** A1008 (2002).

76. Hsieh, C. T. & Teng, H. Influence of oxygen treatment on electric double-layer capacitance of activated carbon fabrics. *Carbon N. Y.* **40,** 667–674 (2002).

77. Aslan, M. *et al.* Improved capacitive deionization performance of mixed hydrophobic / hydrophilic activated carbon electrodes. *J. Phys. Condens. Matter* **28,** 114003 (2016).

78. Biesheuvel, P. M., Fu, Y. & Bazant, M. Z. Electrochemistry and capacitive charging of porous electrodes in asymmetric multicomponent electrolytes. *Russ. J. Electrochem.* **48,** 580–592 (2012).

79. Yan, X. *et al.* Activated carbon becomes active for oxygen reduction and hydrogen evolution reactions. *Chem. Commun.* **52,** 8156–8159 (2016).

80. Santoro, C. *et al.* Parameters characterization and optimization of activated carbon (AC) cathodes for microbial fuel cell application. *Bioresour. Technol.* **163C,** 54–63 (2014).

81. Zhang, B. *et al.* Synthesizing Nitrogen-Doped Activated Carbon and Probing its Active Sites for Oxygen Reduction Reaction in Microbial Fuel Cells. *ACS Appl. Mater.*

Interfaces (2014). doi:10.1021/am5008547

82. Yang, W., Kim, K. Y. & Logan, B. E. Development of carbon free diffusion layer for activated carbon air cathode of microbial fuel cells. *Bioresour. Technol.* **197,** 318–322 (2015).

83. Zhang, X., Xia, X., Ivanov, I., Huang, X. & Logan, B. E. Enhanced Activated Carbon Cathode Performance for Microbial Fuel Cell by Blending Carbon Black. *Environ. Sci. Technol.* (2014). doi:10.1021/es405029y

84. Aelterman, P., Versichele, M., Genettello, E., Verbeken, K. & Verstraete, W. Microbial fuel cells operated with iron-chelated air cathodes. **54,** 5754–5760 (2009).

85. Zhao, F. *et al.* Challenges and constraints of using oxygen cathodes in microbial fuel cells. *Environ. Sci. Technol.* **40,** 5193–5199 (2006).

86. Merino-Jimenez, I. *et al.* Carbon-Based Air-Breathing Cathodes for Microbial Fuel Cells. *Catalysts* **6,** 127 (2016).

87. Zhang, F. *et al.* Mesh optimization for microbial fuel cell cathodes constructed around stainless steel mesh current collectors. *J. Power Sources* **196,** 1097–1102 (2011).

88. Beverskog, B. & Puigdomenech, I. Revised Pourbaix Diagrams for Copper at 25 to 300°C. *J. Electrochem. Soc.* **144,** 3476 (1997).

89. Baudler, A., Schmidt, I., Langner, M., Greiner, A. & Schröder, U. Does it have to be carbon? Metal anodes in microbial fuel cells and related bioelectrochemical systems. *Energy Environ. Sci.* **8,** 2048–2055 (2015).

90. Zhao, F. *et al.* Challenges and constraints of using oxygen cathodes in microbial fuel cells. *Environ. Sci. Technol.* **40,** 5193–9 (2006).

91. Santoro, C. *et al.* Activated carbon nanofibers (ACNF) as cathode for single chamber microbial fuel cells (SCMFCs). *J. Power Sources* **243,** 499–507 (2013).

92. Sun, K., Zhao, H., Zhang, S., Yao, J. & Xu, J. Selenium/pomelo peel-derived carbon nanocomposite as advanced cathode for lithium-selenium batteries. *Ionics (Kiel).* **21,** 2477–2484 (2015).

93. Kretzschmar, J., Riedl, S., Brown, R. K., Schröder, U. & Harnisch, F. eLatrine: Lessons Learned from the Development of a Low-Tech MFC Based on Cardboard Electrodes for the Treatment of Human Feces. *J. Electrochem. Soc.* **164,** H3065–H3072 (2017).

94. Cheng, S. & Wu, J. Air-cathode preparation with activated carbon as catalyst, PTFE as

binder and nickel foam as current collector for microbial fuel cells. *Bioelectrochemistry* **92,** 22–6 (2013).

95. Watson, V. J., Nieto Delgado, C. & Logan, B. E. Influence of chemical and physical properties of activated carbon powders on oxygen reduction and microbial fuel cell performance. *Environ. Sci. Technol.* **47,** 6704–10 (2013).

96. Strelko, V. & Malik, D. J. Characterization and metal sorptive properties of oxidized active carbon. *J. Colloid Interface Sci.* **250,** 213–220 (2002).

97. Simmons, J. M. *et al.* Effect of Ozone Oxidation on Single-Walled Carbon Nanotubes. 7113–7118 (2006).

98. Freguia, S., Rabaey, K., Yuan, Z. & Keller, J. Sequential anode-cathode configuration improves cathodic oxygen reduction and effluent quality of microbial fuel cells. *Water Res.* **42,** 1387–1396 (2008).

99. Oh, S. & Min, B. Cathode Performance as a Factor in Electricity imp Generation in Microbial Fuel Cells - Environmental Science & Technology (ACS Publications). **38,** 4900–4904 (2004).

100. Ter Heijne, A., Strik, D. P. B. T. B., Hamelers, H. V. M. & Buisman, C. J. N. Cathode potential and mass transfer determine performance of oxygen reducing biocathodes in microbial fuel cells. *Environ. Sci. Technol.* **44,** 7151–6 (2010).

101. Borole, A. P., Hamilton, C. Y., Aaron, D. S. & Tsouris, C. Investigating microbial fuel cell bioanode performance under different cathode conditions. *Biotechnol. Prog.* **25,** NA-NA (2009).

102. Liu, Y., Liu, H., Wang, C., Hou, S. X. & Yang, N. Sustainable energy recovery in wastewater treatment by microbial fuel cells: Stable power generation with nitrogen-doped graphene cathode. *Environ. Sci. Technol.* **47,** 13889–13895 (2013).

103. Wang, H., Jiang, S. C., Wang, Y. & Xiao, B. Substrate removal and electricity generation in a membrane-less microbial fuel cell for biological treatment of wastewater. *Bioresour. Technol.* **138,** 109–116 (2013).

104. Ghangrekar, M. M., Shinde, V. B. & Duteanu, N. M. Effect of Wastewater Characteristics and Biomass Growth in Cathode Compartment on Performance of Membrane-less Microbial Fuel Cell. (2010).

105. Nandy, A. *et al.* Performance evaluation of microbial fuel cells: effect of varying electrode configuration and presence of a membrane electrode assembly. *N. Biotechnol.*

32, 272–281 (2015).

106. Oliot, M., Etcheverry, L. & Bergel, A. Removable air-cathode to overcome cathode biofouling in microbial fuel cells. *Bioresour. Technol.* **221,** 691–696 (2016).

107. Khilari, S., Pandit, S., Das, D. & Pradhan, D. Manganese cobaltite/polypyrrole nanocomposite-based air-cathode for sustainable power generation in the single-chambered microbial fuel cells. *Biosens. Bioelectron.* **54,** 534–40 (2014).

108. Logan, B., Cheng, S., Watson, V. & Estadt, G. Graphite fiber brush anodes for increased power production in air-cathode microbial fuel cells. *Environ. Sci. Technol.* **41,** 3341–6 (2007).

109. Zhang, F. *et al.* Mesh optimization for microbial fuel cell cathodes constructed around stainless steel mesh current collectors. *J. Power Sources* **196,** 1097–1102 (2011).

110. Zuo, K. *et al.* Carbon filtration cathode in microbial fuel cell to enhance wastewater treatment. *Bioresour. Technol.* (2015). doi:10.1016/j.biortech.2015.02.108

111. Pasternak, G., Greenman, J. & Ieropoulos, I. Regeneration of the power performance of cathodes affected by biofouling. *Appl. Energy* **173,** 431–437 (2016).

112. Liu, H. & Logan, B. E. Electricity generation using an air-cathode single chamber microbial fuel cell in the presence and absence of a proton exchange membrane. *Environ. Sci. Technol.* **38,** 4040–6 (2004).

113. Bourdakos, N. A defined co□culture of Geobacter sulfurreducens and Escherichia coli in a membrane□less microbial fuel cell. *Biotechnol. …* **111,** 709–718 (2014).

114. Liang, P., Yuan, L., Wu, W., Yang, X. & Huang, X. Enhanced performance of bio-cathode microbial fuel cells with the applying of transient-state operation modes. *Bioresour. Technol.* **147,** 228–33 (2013).

115. Kakarla, R. & Min, B. Evaluation of microbial fuel cell operation using algae as an oxygen supplier: carbon paper cathode vs. carbon brush cathode. *Bioprocess Biosyst. Eng.* (2014). doi:10.1007/s00449-014-1223-4

116. Ter Heijne, A., Hamelers, H. V. M., De Wilde, V., Rozendal, R. a & Buisman, C. J. N. A bipolar membrane combined with ferric iron reduction as an efficient cathode system in microbial fuel cells. *Environ. Sci. Technol.* **40,** 5200–5 (2006).

117. Shinozaki, K., Zack, J. W., Richards, R. M., Pivovar, B. S. & Kocha, S. S. Oxygen Reduction Reaction Measurements on Platinum Electrocatalysts Utilizing Rotating Disk

Electrode Technique: I. Impact of Impurities, Measurement Protocols and Applied Corrections. *J. Electrochem. Soc.* **162,** F1144–F1158 (2015).

118. Wang, G. *et al.* Activated carbon nanofiber webs made by electrospinning for capacitive deionization. *Electrochim. Acta* **69,** 65–70 (2012).

119. Engelhardt, S. & Menche, N. *Biologie, Anatomie, Physiologie : kompaktes Lehrbuch für Pflegeberufe*. (Elsevier, Urban & Fischer, 2012).

120. Simon, P. & Gogotsi, Y. Materials for electrochemical capacitors. *Nat. Mater.* **7,** 845–854 (2008).

121. Ramaley, L. & Krause, M. S. Theory of Square Wave Voltammetry. *Anal. Chem.* **41,** 1361–1365 (1969).

122. Kaplan, J. D., Marsh, J. H. & Orchard, S. W. Voltammetric Characterization of Activated Carbons in Modified Carbon Paste Electrodes. *Electroanalysis* **5,** 509–516 (1993).

123. Liu, H. & Logan, B. E. Electricity generation using an air-cathode single chamber microbial fuel cell in the presence and absence of a proton exchange membrane. *Environ. Sci. Technol.* **38,** 4040–6 (2004).

124. Jordan, L. . *et al.* Diffusion layer parameters influencing optimal fuel cell performance. *J. Power Sources* **86,** 250–254 (2000).

125. Gupta, G. *et al.* Direct bio-electrocatalysis by multi-copper oxidases: Gas-diffusion laccase-catalyzed cathodes for biofuel cells. *Electrochim. Acta* **56,** 10767–10771 (2011).

126. Corbella, C., Garfí, M. & Puigagut, J. Long-term assessment of best cathode position to maximise microbial fuel cell performance in horizontal subsurface flow constructed wetlands. *Sci. Total Environ.* **563–564,** 448–455 (2016).

127. Chipasa, K. B. & Mędrzycka, K. Behavior of lipids in biological wastewater treatment processes. *J. Ind. Microbiol. Biotechnol.* **33,** 635–645 (2006).

128. Wang, H. *et al.* Enhanced power generation of oxygen-reducing biocathode with an alternating hydrophobic and hydrophilic surface. *ACS Appl. Mater. Interfaces* acsami.6b10876 (2016). doi:10.1021/acsami.6b10876

129. Pastore, C., Pagano, M., Lopez, A., Mininni, G. & Mascolo, G. Fat, oil and grease waste from municipal wastewater: Characterization, activation and sustainable conversion into biofuel. *Water Sci. Technol.* **71,** 1151–1157 (2015).

130. Wood, M. H. *et al.* Comparative Adsorption of Saturated and Unsaturated Fatty Acids at

the Iron Oxide/Oil Interface. *Langmuir* **32,** 534–540 (2016).

131. Park, S., Lee, J.-W. & Popov, B. N. A review of gas diffusion layer in PEM fuel cells: Materials and designs. *Int. J. Hydrogen Energy* **37,** 5850–5865 (2012).

132. An, J. *et al.* Floating-type microbial fuel cell (FT-MFC) for treating organic-contaminated water. *Environ. Sci. Technol.* **43,** 1642–7 (2009).

133. Kim, K.-Y. *et al.* Polydopamine coating effects on ultrafiltration membrane to enhance power density and mitigate biofouling of ultrafiltration microbial fuel cells (UF-MFCs). *Water Res.* **54,** 62–8 (2014).

134. Noori, M. T., Jain, S. C., Ghangrekar, M. M. & Mukherjee, C. K. Biofouling inhibition and enhancing performance of microbial fuel cell using silver nano-particles as fungicide and cathode catalyst. *Bioresour. Technol.* (2016). doi:10.1016/j.biortech.2016.08.061

135. Quéméneur, M. & Marty, Y. Fatty acids and sterols in domestic wastewaters. *Water Res.* **28,** 1217–1226 (1994).

136. Ghazani, S. M. & Marangoni, A. G. Minor components in canola oil and effects of refining on these constituents: A review. *JAOCS, J. Am. Oil Chem. Soc.* **90,** 923–932 (2013).

137. Otowa, T., Nojima, Y. & Miyazaki, T. Development of KOH activated high surface area carbon and its application to drinking water purification. *Carbon N. Y.* **35,** 1315–1319 (1997).

138. Bard, A. J., Stratmann, M. & Wilson, G. S. *Encyclopedia of Electrochemistry*. *Encyclopedia of Electrochemistry* **8,** (Wiley-VCH Verlag GmbH & Co. KGaA, 2007).

139. Xiao, H., Kim, H. J., Min, D. B. & Lalvani, S. B. High oleic and low trans fatty acid formation by an electrochemical process. *JAOCS, J. Am. Oil Chem. Soc.* **87,** 9–17 (2010).

140. Mondal, K. & Lalvani, S. B. Mediator-assisted electrochemical hydrogenation of soybean oil. *Chem. Eng. Sci.* **58,** 2643–2656 (2003).

141. Mondal, K. & Lalvani, S. Low temperature soybean oil hydrogenation by an electrochemical process. *J. Food Eng.* **84,** 526–533 (2008).

142. Chatterjee, P. & Ghangrekar, M. M. Preparation of a fouling-resistant sustainable cathode for a single-chambered microbial fuel cell. *Water Sci. Technol.* **69,** 634–639 (2014).

143. Chatterjee, P. & Ghangrekar, M. M. Design of clayware separator-electrode assembly

for treatment of wastewater in microbial fuel cells. *Appl. Biochem. Biotechnol.* **173,** 378–390 (2014).

144. Tang, X., Li, H., Du, Z. & Yong, H. Bioresource Technology Spontaneous modification of graphite anode by anthraquinone-2-sulfonic acid for microbial fuel cells. *Bioresour. Technol.* **164,** 184–188 (2014).

145. Huang, Y. *et al.* Electricity generation from a floating microbial fuel cell. *Bioresour. Technol.* **114,** 308–13 (2012).

146. Ketep, S. F. *et al.* Forming microbial anodes with acetate addition decreases their capability to treat raw paper mill effluent. *Bioresour. Technol.* **164C,** 285–291 (2014).

147. Jiang, D. *et al.* A pilot-scale study on utilizing multi-anode/cathode microbial fuel cells (MAC MFCs) to enhance the power production in wastewater treatment. *Int. J. Hydrogen Energy* **36,** 876–884 (2011).

148. Ghadge, A. N. & Ghangrekar, M. M. Bioresource Technology Performance of low cost scalable air – cathode microbial fuel cell made from clayware separator using multiple electrodes. *Bioresour. Technol.* 1–5 (2015). doi:10.1016/j.biortech.2015.01.115

149. Popat, S. C., Ki, D., Rittmann, B. E. & Torres, C. I. Importance of OH(-) transport from cathodes in microbial fuel cells. *ChemSusChem* **5,** 1071–9 (2012).

150. Zhang, L. *et al.* Chemical and biological technologies for hydrogen sulfide emission control in sewer systems: a review. *Water Res.* **42,** 1–12 (2008).

151. Ganigue, R., Gutierrez, O., Rootsey, R. & Yuan, Z. Chemical dosing for sulfide control in Australia: An industry survey. *Water Res.* **45,** 6564–74 (2011).

152. Pikaar, I., Rozendal, R. a, Yuan, Z., Keller, J. & Rabaey, K. Electrochemical sulfide oxidation from domestic wastewater using mixed metal-coated titanium electrodes. *Water Res.* **45,** 5381–8 (2011).

153. Dutta, P. K., Rabaey, K., Yuan, Z. & Keller, J. Spontaneous electrochemical removal of aqueous sulfide. *Water Res.* **42,** 4965–75 (2008).

154. Rabaey, K. *et al.* Microbial fuel cells for sulfide removal. *Environ. Sci. Technol.* **40,** 5218–5224 (2006).

155. Sun, M. *et al.* Microbial communities involved in electricity generation from sulfide oxidation in a microbial fuel cell. *Biosens. Bioelectron.* **26,** 470–6 (2010).

156. Cai, J. *et al.* Simultaneous anaerobic sulfide and nitrate removal coupled with electricity

generation in Microbial Fuel Cell. *Bioresour. Technol.* **129,** 224–8 (2013).

157. Eaktasang, N., Min, H.-S., Kang, C. & Kim, H. S. Control of malodorous hydrogen sulfide compounds using microbial fuel cell. *Bioprocess Biosyst. Eng.* (2013). doi:10.1007/s00449-012-0881-3

158. Cooney, M. J., Roschi, E., Marison, I. W., Comninellis, C. & von Stockar, U. Physiologic studies with the sulfate-reducing bacterium Desulfovibrio desulfuricans: evaluation for use in a biofuel cell. *Enzyme Microb. Technol.* **18,** 358–65 (1996).

159. Ieropoulos, I., Gálvez, A. & Greenman, J. Effects of sulphate addition and sulphide inhibition on microbial fuel cells. *Enzyme Microb. Technol.* **52,** 32–7 (2013).

160. Braunschweig - Untersuchung Stadtwasser. at <https://www.bs-energy.de/fileadmin/BS_ENERGY/privatkunden/produkte/wasser/Stadtwasser_20170217.pdf>

161. Conradin, F., Hahn, H. H. & Lengyel, W. *Handbuch Wasserversorgungs- und Abwassertechnik*. **Band 1: Ro,** (Vulkan-Verl, 1999).

162. Sun, J., Hu, S., Sharma, K. R., Ni, B.-J. & Yuan, Z. Stratified Microbial Structure and Activity in Sulfide- and Methane-Producing Anaerobic Sewer Biofilms. *Appl. Environ. Microbiol.* **80,** 7042–7052 (2014).

163. Prokhorova, A., Sturm-Richter, K., Doetsch, A. & Gescher, J. Resilience, dynamics and interactions within a multi-species exoelectrogenic model biofilm. *Am. Environ. Microbiol.* (2017). doi:10.1128/AEM.03033-16

164. Speers, A. M. & Reguera, G. Electron donors supporting growth and electroactivity of geobacter sulfurreducens anode biofilms. *Appl. Environ. Microbiol.* **78,** 437–444 (2012).

165. Rabaey, K. & Sompel, K. Van de. Microbial fuel cells for sulfide removal. ... *Sci. Technol.* **40,** 5218–5224 (2006).

166. Brown, R. K. *et al.* Evaluating the effects of scaling up on the performance of bioelectrochemical systems using a technical scale microbial electrolysis cell. *Bioresour. Technol.* **163,** 206–213 (2014).

167. Ateya, B. Anodic oxidation of sulfide ions from chloride brines. *Electrochem. commun.* **4,** 231–238 (2002).

168. Donner, J. *Aufbereitung schwefelwasserstoffhaltiger Wässer durch katalytische Oxidation an porphyrinmodifizierten kohlenstoffhaltigen Materialien*. (Fakultät Forst-,

Geo- und Hydrowissenschaften Institut für Wasserchemie, 2009).

169. Dutta, P. K., Rabaey, K., Yuan, Z., Rozendal, R. a & Keller, J. Electrochemical sulfide removal and recovery from paper mill anaerobic treatment effluent. *Water Res.* **44,** 2563–71 (2010).

170. Pfennig, N. & Biebl, H. Desulfuromonas acetoxidans gen. nov. and sp. nov., a new anaerobic, sulfur-reducing, acetate-oxidizing bacterium. *Arch. Microbiol.* **110,** 3–12 (1976).

171. Dutta, P. K., Keller, J., Yuan, Z., Rozendal, R. A. & Rabaey, K. Role of sulfur during acetate oxidation in biological anodes. *Environ. Sci. Technol.* **43,** 3839–45 (2009).

172. Norsker, N. H., Nielsen, P. H. & Hvitved-Jacobsen, T. Influence of oxygen on biofilm growth and potential sulfate reduction in gravity sewer biofilm. *Water Sci. Technol.* **31,** 159–167 (1995).

173. Liu, Y. & Tay, J. H. The essential role of hydrodynamic shear force in the formation of biofilm and granular sludge. *Water Res.* **36,** 1653–1665 (2002).

174. Sayers, R. H. & Langlais, R. J. Removal and Recovery of Sulfide from Tannery Wastewater. 143 (1977).

175. Reis, M. a, Almeida, J. S., Lemos, P. C. & Carrondo, M. J. Effect of hydrogen sulfide on growth of sulfate reducing bacteria. *Biotechnol. Bioeng.* **40,** 593–600 (1992).

176. O'Flaherty, V., Mahony, T., O'Kennedy, R. & Colleran, E. Effect of pH on growth kinetics and sulphide toxicity thresholds of a range of methanogenic, syntrophic and sulphate-reducing bacteria. *Process Biochem.* **33,** 555–569 (1998).

177. Dutta, P. K., Keller, J., Yuan, Z., Rozendal, R. A. & Rabaey, K. Role of sulfur during acetate oxidation in biological anodes. *Environ. Sci. Technol.* **43,** 3839–45 (2009).

178. Marsili, E., Rollefson, J. B., Baron, D. B., Hozalski, R. M. & Bond, D. R. Microbial biofilm voltammetry: direct electrochemical characterization of catalytic electrode-attached biofilms. *Appl. Environ. Microbiol.* **74,** 7329–37 (2008).

179. Luther, G. W. *et al.* Use of voltammetric solid-state (micro)electrodes for studying biogeochemical processes: Laboratory measurements to real time measurements with an in situ electrochemical analyzer (ISEA). *Mar. Chem.* **108,** 221–235 (2008).

180. Luther, G. W. *et al.* Thermodynamics and kinetics of sulfide oxidation by oxygen: A look at inorganically controlled reactions and biologically mediated processes in the

environment. *Front. Microbiol.* **2,** 1–9 (2011).

181. Luther, III, G. W. *et al.* Sulfur speciation monitored in situ with solid state gold amalgam voltammetric microelectrodes: polysulfides as a special case in sediments, microbial mats and hydrothermal vent waters. *J. Environ. Monit.* **3,** 61–66 (2001).

182. Luther, G. W. & Ferdelman, T. G. Voltammetric Characterization of Iron(Ii) Sulfide Complexes in Laboratory Solutions and in Marine Waters and Porewaters. *Environ. Sci. Technol.* **27,** 1154–1163 (1993).

183. Pandey, S. K., Kim, K.-H. & Tang, K.-T. A review of sensor-based methods for monitoring hydrogen sulfide. *TrAC Trends Anal. Chem.* **32,** 87–99 (2012).

184. Lawrence, N. S., Davis, J. & Compton, R. G. Analytical strategies for the detection of sulfide: A review. *Talanta* **52,** 771–784 (2000).

185. Rethmeier, J., Rabenstein, A., Langer, M. & Fischer, U. Detection of traces of oxidized and reduced sulfur compounds in small samples by combination of different high-performance liquid chromatography methods. *J. Chromatogr. A* **760,** 295–302 (1997).

186. Kroll, a. V., Smorchkov, V. . & Nazarenko, a. Y. Electrochemical sensors for hydrogen and hydrogen sulfide determination. *Sensors Actuators B Chem.* **21,** 97–100 (1994).

187. Jeroschewski, P., Haase, K., Trommer, a & Grundler, P. Galvanic sensor for determination of hydrogen sulfide. *Electroanalysis* **6,** 769–772 (1994).

188. Brendel, P. J. & Luther, G. W. Development of a gold amalgam voltammetric microelectrode for the determination of dissolved Fe, Mn, O2, and S(-II) in porewaters of marine and freshwater sediments. *Environ. Sci. Technol.* **29,** 751–761 (1995).

189. Ma, S. *et al.* Solid-State Au/Hg Microelectrode for the Investigation of Fe and Mn Cycling in a Freshwater Wetland: Implications for Methane Production. *Electroanalysis* **20,** 233–239 (2008).

190. Sherwood, W. G. A Rotating Ring-Disk Electrode Study of the Underpotential Deposition of Mercury on Gold. *J. Electrochem. Soc.* **125,** 1098 (1978).

191. Herrero, E. & Abruna, H. D. Underpotential deposition of mercury on Au(111): Electrochemical studies and comparison with structural investigations. *Langmuir* **13,** 4446–4453 (1997).

192. Schadewald, L. A., Lindstrom, T. R., Hussein, W., Evenson, E. E. & Johnson, D. C. Deposition and Stripping of Mercury At Gold Electrodes in Acidic Media. I.

Voltammetric Studies. *J. Electrochem. Soc.* **131,** 1583–1587 (1984).

193. Wang, J. G., Fossey, J. S., Li, M., Xie, T. & Long, Y. T. Real-Time Plasmonic Monitoring of Single Gold Amalgam Nanoalloy Electrochemical Formation and Stripping. *ACS Appl. Mater. Interfaces* **8,** 8305–8314 (2016).

194. Stojek, Z. & Kublik, Z. Silver based mercury film electrode Part I. *J. Electroanal. Chem. Interfacial Electrochem.* **60,** 349–358 (1975).

195. Luther, G. W. *et al.* Sulfur speciation monitored in situ with solid state gold amalgam voltammetric microelectrodes: polysulfides as a special case in sediments, microbial mats and hydrothermal vent waters. *J. Environ. Monit.* **3,** 61–66 (2001).

196. Bond, A. M. *Modern polarographic Methods in Analytical Chemistry*. *Ed. Marcel Dekker Inc.Nueva York.* (M. Dekker, 1980).

197. Glazer, B. T., Cary, S. C., Hohmann, L. & Luther, G. W. In situ sulfure speciation using Au/Hg microelectroes as an aid to microbial characterization of an intertidal salt marsh microbial mat. *Environ. Electrochem. Anal. trace Elem. Biogeochem.* 283–304 (2002). doi:doi:10.1021/bk-2002-0811.ch015 10.1021/bk-2002-0811.ch015

198. Arora, S. D., Lipscomb, W. N. & Sneed, M. C. Some Aspects of Reactions between Ammonia and Mercury(I) Compounds. *J. Am. Chem. Soc.* **73,** 1015–1018 (1951).

199. Creighton, H. J. The Electrochemical Reduction of Sugars. *Trans. Electrochem. Soc.* **75,** 289 (1939).

200. Schaefer, J. K. & Morel, F. M. M. High methylation rates of mercury bound to cysteine by Geobacter sulfurreducens. *Nat. Geosci.* **2,** 123–126 (2009).

201. Lin, H., Lu, X., Liang, L. & Gu, B. Cysteine Inhibits Mercury Methylation by *Geobacter sulfurreducens* PCA Mutant Δ *omcBESTZ*. *Environ. Sci. Technol. Lett.* **2,** 144–148 (2015).

202. Si, Y., Zou, Y., Liu, X., Si, X. & Mao, J. Chemosphere Mercury methylation coupled to iron reduction by dissimilatory iron-reducing bacteria. *Chemosphere* **122,** 206–212 (2015).

203. Lu, X. *et al.* Anaerobic Mercury Methylation and Demethylation by Geobacter bemidjiensis Bem. *Environ. Sci. Technol.* acs.est.6b00401 (2016). doi:10.1021/acs.est.6b00401

204. Lewis, A. E. Review of metal sulphide precipitation. *Hydrometallurgy* **104,** 222–234

(2010).

205. Riedel, E. *Allgemeine und Anorganische Chemie : Lehrbuch für Studenten mit Nebenfach Chemie*. (De Gruyter, 2004).

206. Mortlock, A. J. & Rowe, A. H. Atomic diffusion of mercury in gold. *Philos. Mag.* **11,** 1157–1164 (1965).

207. Sutherland-Stacey, L. *et al.* Continuous measurement of dissolved sulfide in sewer systems. *Water Sci. Technol.* **57,** 375–381 (2008).

208. Montgomery, A. D., Mclnerney, M. J. & Sublette, K. L. Microbial control of the production of hydrogen sulfide by sulfate-reducing bacteria. *Biotechnol. Bioeng.* **35,** 533–539 (2008).

209. Liu, T. *et al.* Calcium-dependent electroactive biofilm structure and electricity generation in bioelectrochemical systems. *J. Power Sources* **294,** 516–521 (2015).

210. Wilkinson, M. The Surface Properties of mercury. *Chem. Rev.* **72,** 575–625 (1972).

211. Somerville, H. & Metallurgist, G. Notes on gold amalgam. (1956).

212. Wu, F. & Qi, S. Global View of Engineering Geology and the Environment - Proceedings of the International Symposium and 9th Asian Regional Conference of IAEG BT - International Symposium and 9th Asian Regional Conference of IAEG "Global View of Engineering Geology and t. in International Association for Engineering; Geology (2013).

213. Guminski, C. & Galus, Z. Determination of diffusion coefficient and concentration of gold in mercury based on the pre-peak formation in the reduction of zinc(II) at hanging gold amalgam drop electrodes. *J. Electroanal. Chem. Interfacial Electrochem.* **83,** 139–150 (1977).

214. Baranski, A., Fitak, S. & Galus, Z. Diffusion coefficients of metals in mercury. *J. Electroanal. Chem.* **60,** 175–181 (1975).

215. Huang, S. & Li, S. Mineralogical Characteristics and its Prospecting Significance of Gold-Mercury Minerals in Davao Gold Placer in Mindanao Islands , Philippines. **5,** 810–817 (2011).

216. O'Shea, T. J. & Lunte, S. M. Selective detection of free thiols by capillary electrophoresis-electrochemistry using a gold/mercury amalgam microelectrode. *Anal. Chem.* **65,** 247–250 (1993).

217. Schönbäck, W., Oppolzer, G., Kraemer, A. & Hansen, W. Internationaler Vergleich der Siedlungswasserwirtschaft. (2003). at <http://media.arbeiterkammer.at/wien/Informationen_zur_Umweltpolitik_153.pdf>

12. Appendix

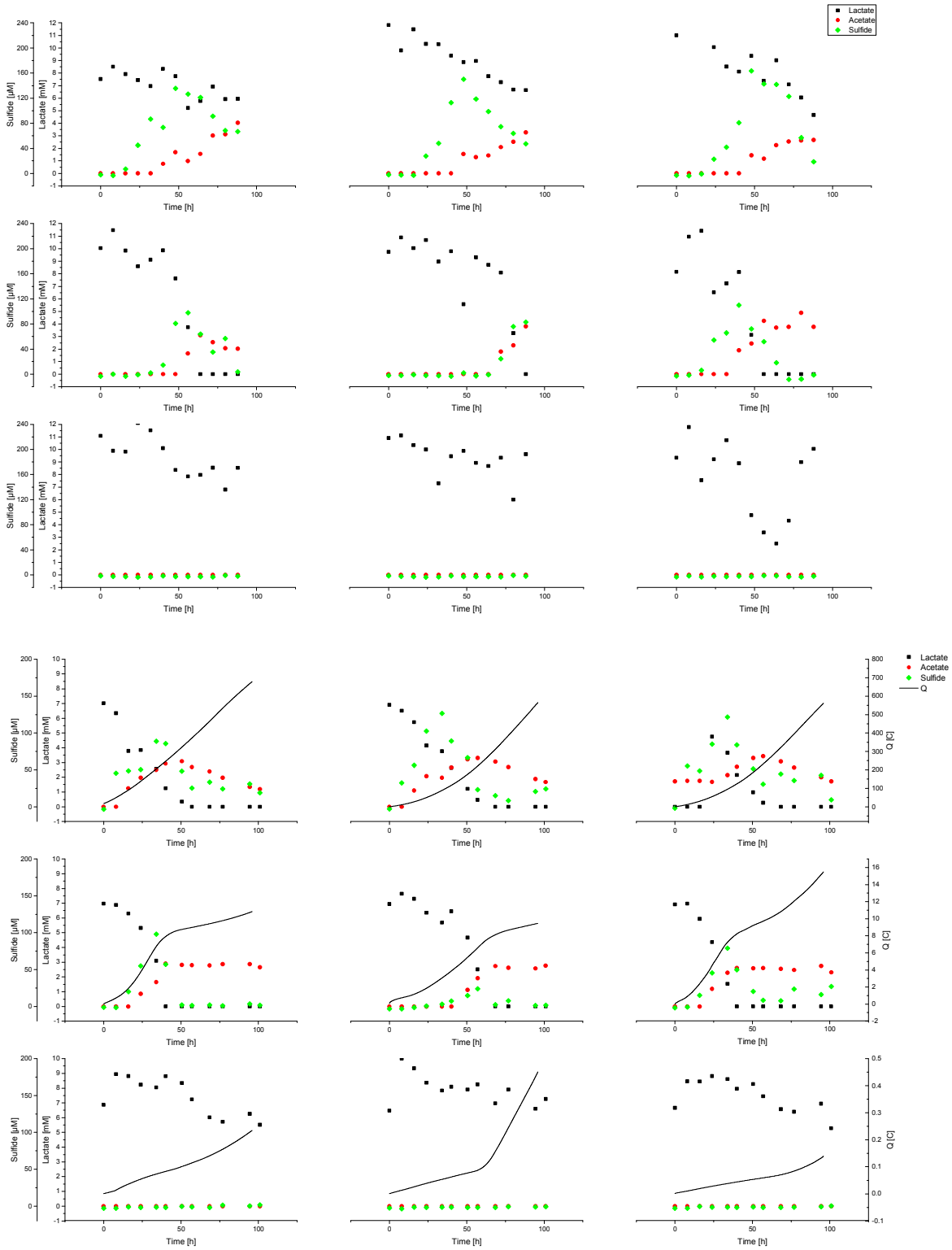

Figure 104: Sulfide (◆), lactate (■), acetate (●) and charge transferred (Q, line) over time. Top block: OCV, bottom block: +200 mV vs. Ag/AgCl. 1. row electroactive biofilm; 2. row artificial sewer slime; 3. row blank. A row represents three triplicates.

XPS measurement 23.02.2016

Alt 1 Mitte (9-1) und Alt 1 Epoxy (9-2):

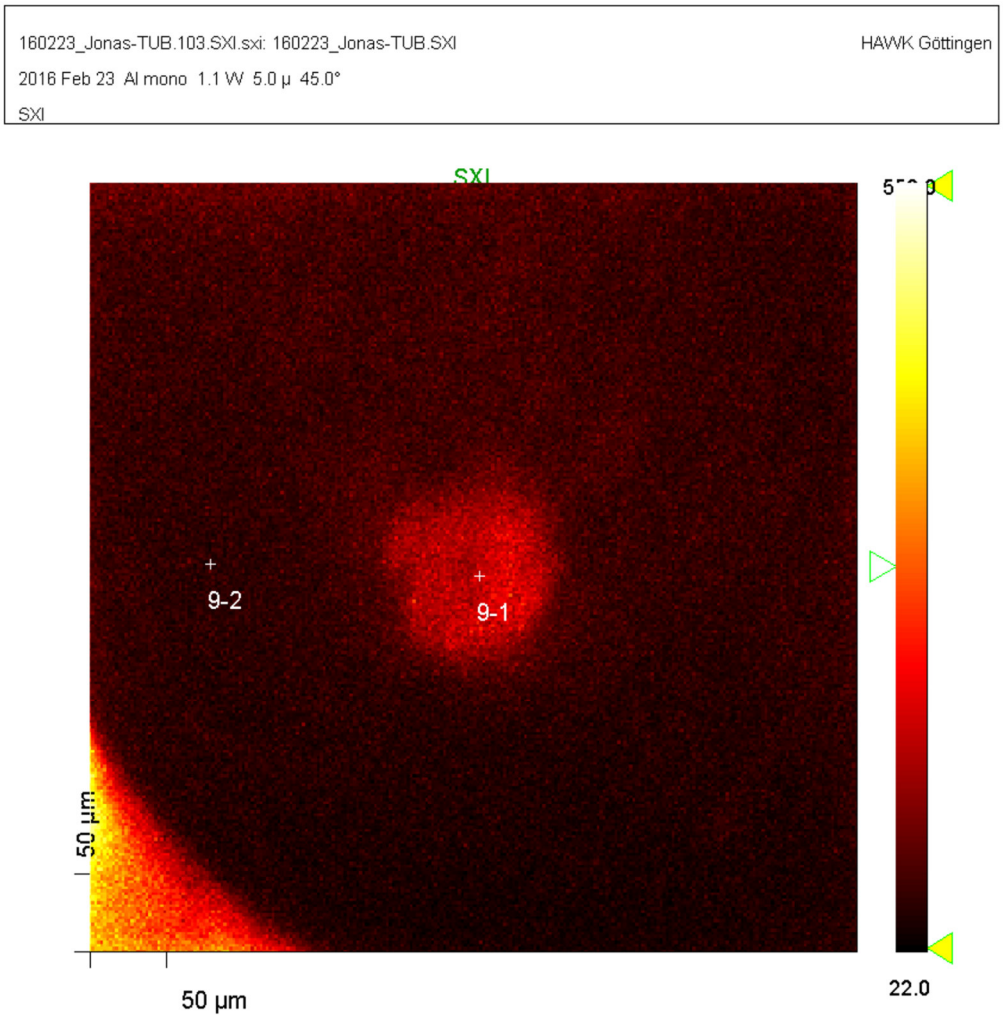

160223_Jonas-TUB.119.Alt 1.spe: 160223_Jonas-TUB.Alt 1 HAWK Göttingen

2016 Feb 24 Al mono 25.1 W 100.0 µ 45.0° 187.85 eV 3.1837e+004 max 35.01 min

Su1s/9-1: Alt 1 Mitte/1

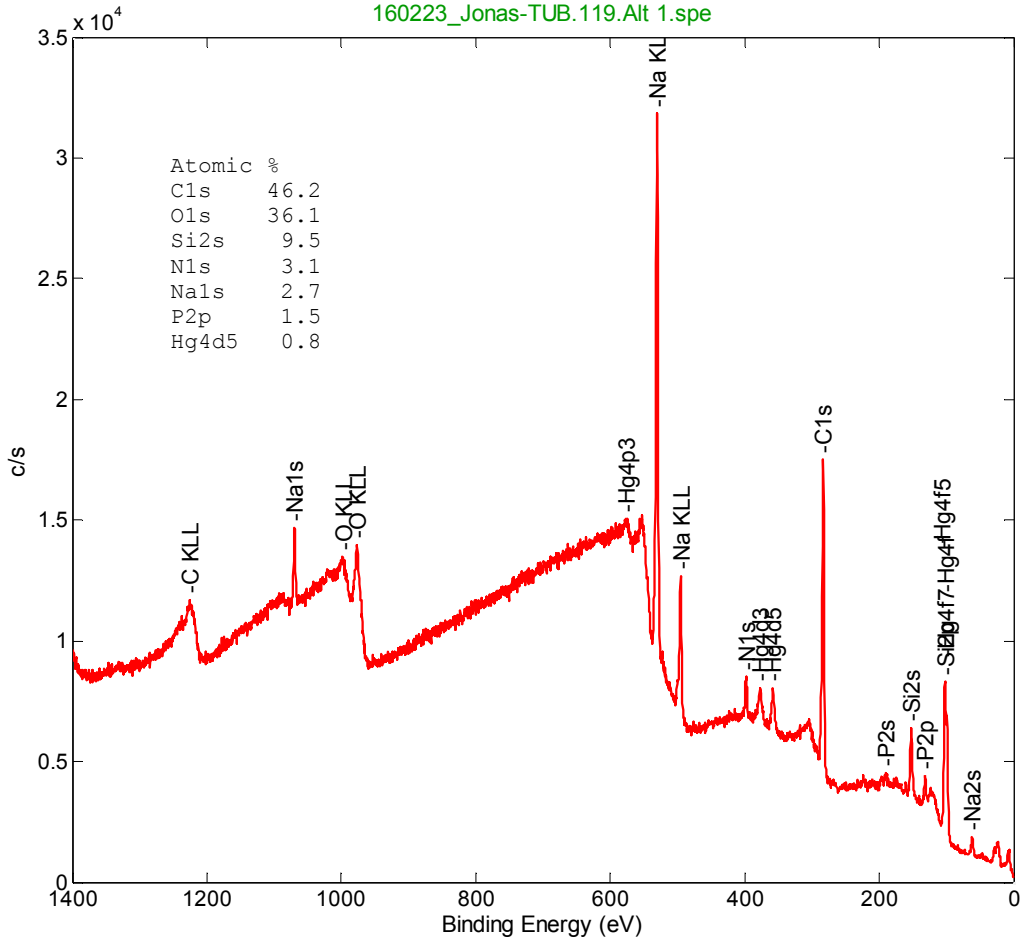

160223_Jonas-TUB.119.Alt 1.spe: 160223_Jonas-TUB.Alt 1 HAWK Göttingen

2016 Feb 24 Al mono 25.1 W 100.0 µ 45.0° 187.85 eV 4.1487e+004 max 35.01 min

Su1s/9-2: Alt 1 Epoxy/2

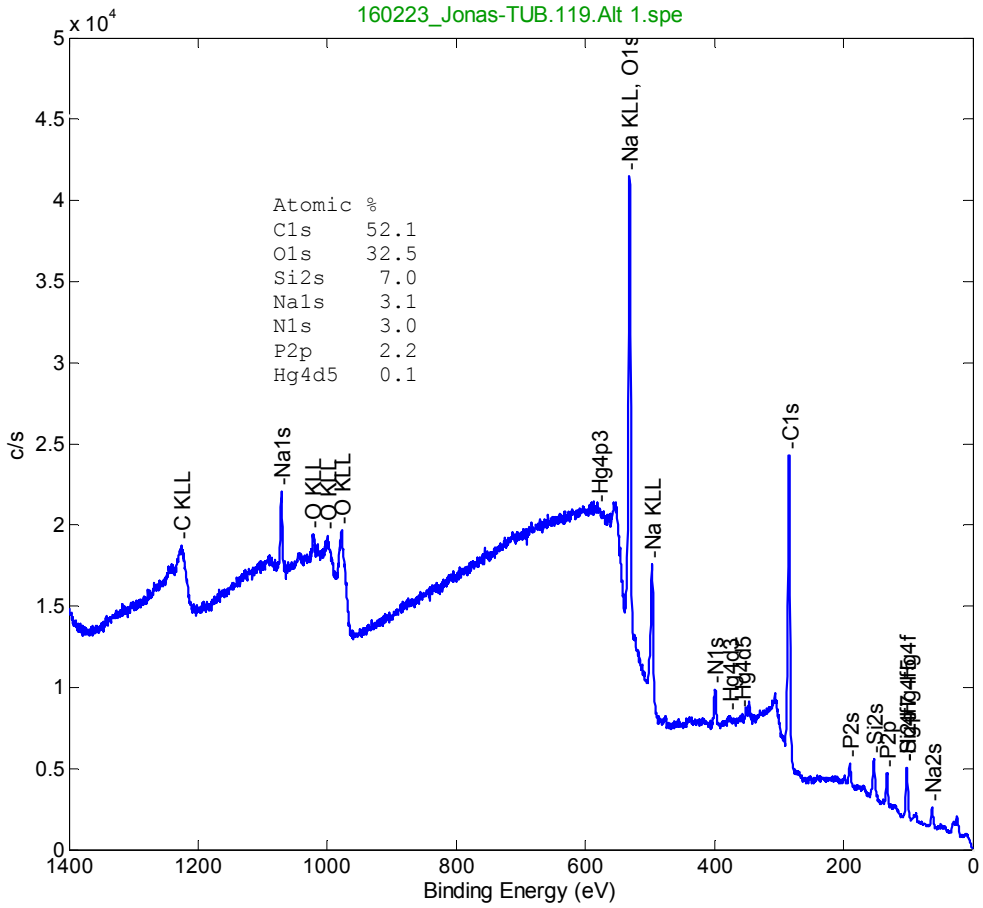

El Au 17 Mitte und Rand:

160223_Jonas-TUB.105.SXI.sxi: 160223_Jonas-TUB.SXI HAWK Göttingen
2016 Feb 23 Al mono 1.1 W 5.0 µ 45.0°
SXI

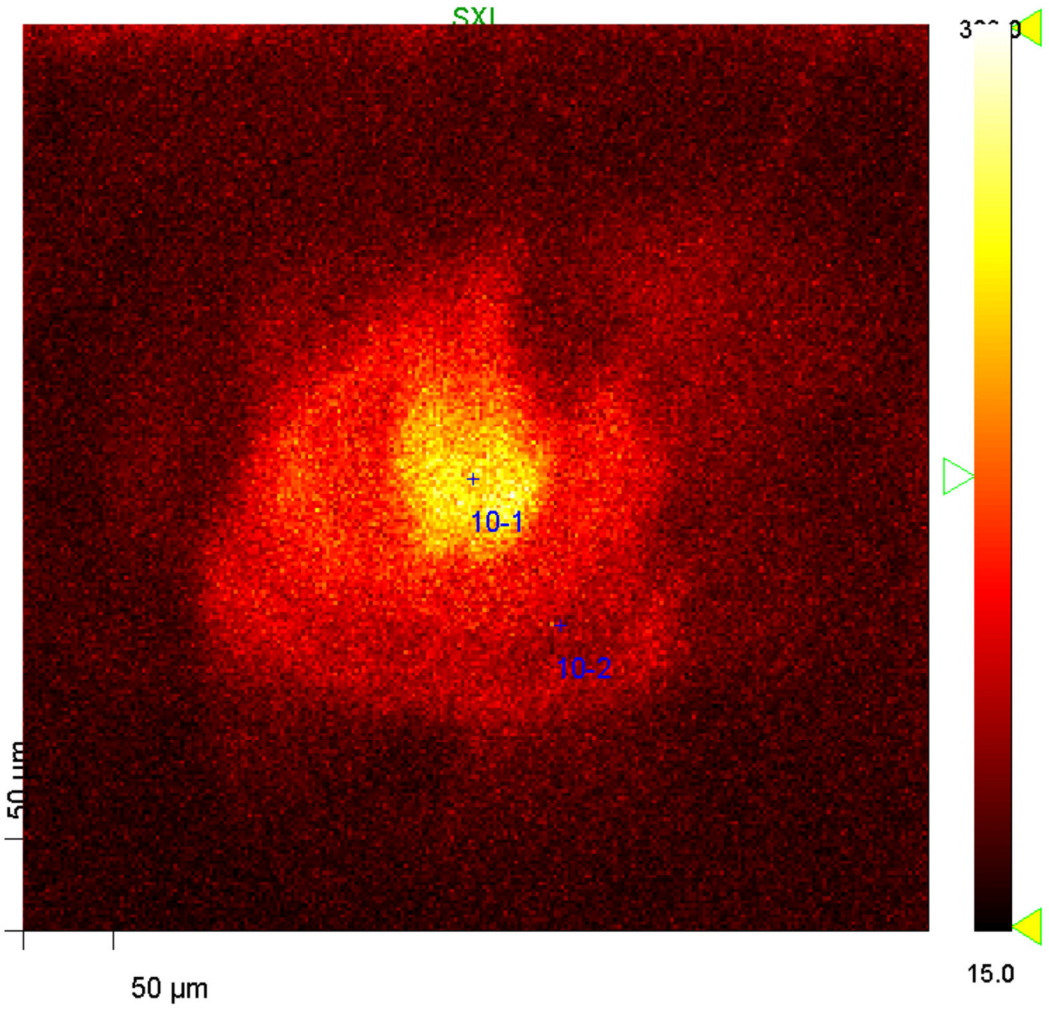

160223_Jonas-TUB.120.spe: 160223_Jonas-TUB HAWK Göttingen

2016 Feb 24 Al mono 25.1 W 100.0 µ 45.0° 187.85 eV 4.3848e+004 max 35.01 min

Su1s/10-1: El Au 17 Mitte/1

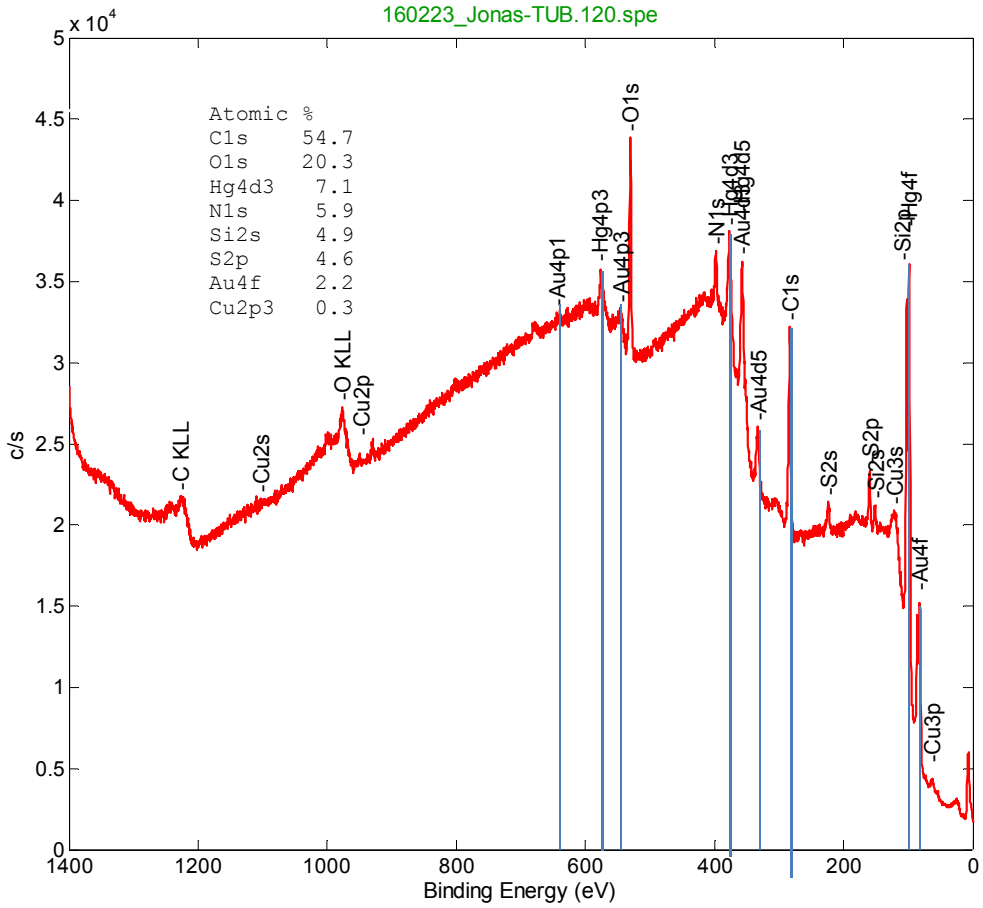

160223_Jonas-TUB.120.spe: 160223_Jonas-TUB HAWK Göttingen

2016 Feb 24 Al mono 25.1 W 100.0 µ 45.0° 187.85 eV 3.2658e+004 max 35.01 min

Su1s/10-2: El Au 17 Rand/2

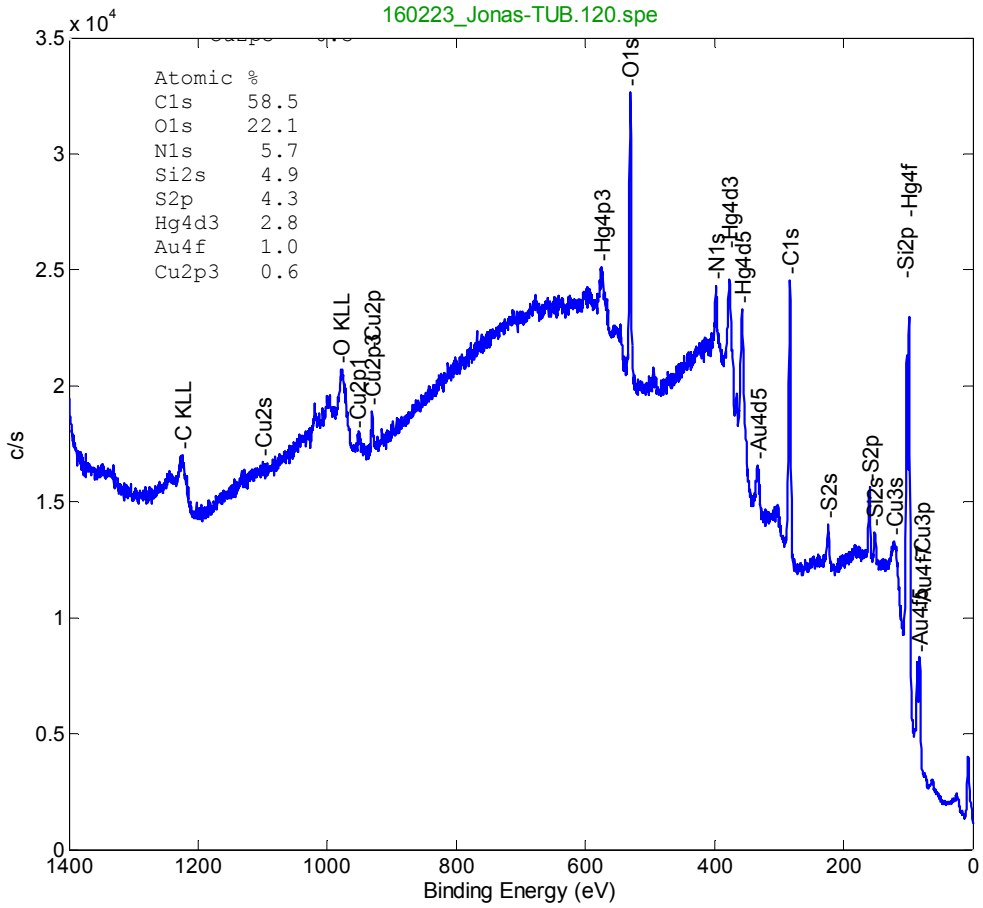

El Au 16 Mitte und Epoxy:

160223_Jonas-TUB.107.SXI.sxi: 160223_Jonas-TUB.SXI HAWK Göttingen
2016 Feb 23 Al mono 1.1 W 5.0 µ 45.0°
SXI

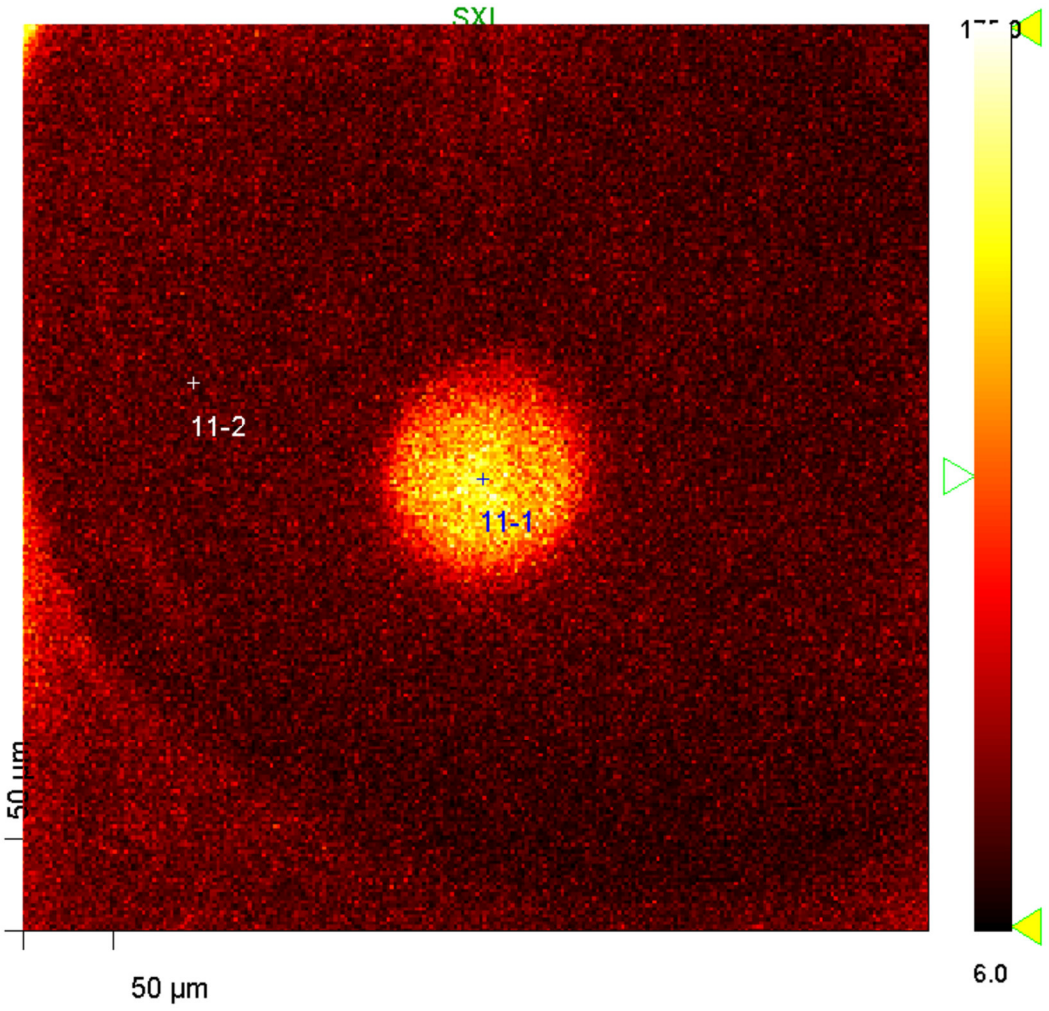

160223_Jonas-TUB.121.spe: 160223_Jonas-TUB HAWK Göttingen

2016 Feb 24 Al mono 25.1 W 100.0 µ 45.0° 187.85 eV 2.0292e+004 max 35.01 min

Su1s/11-1: El Au 16 (fresh)/1 (Shft)

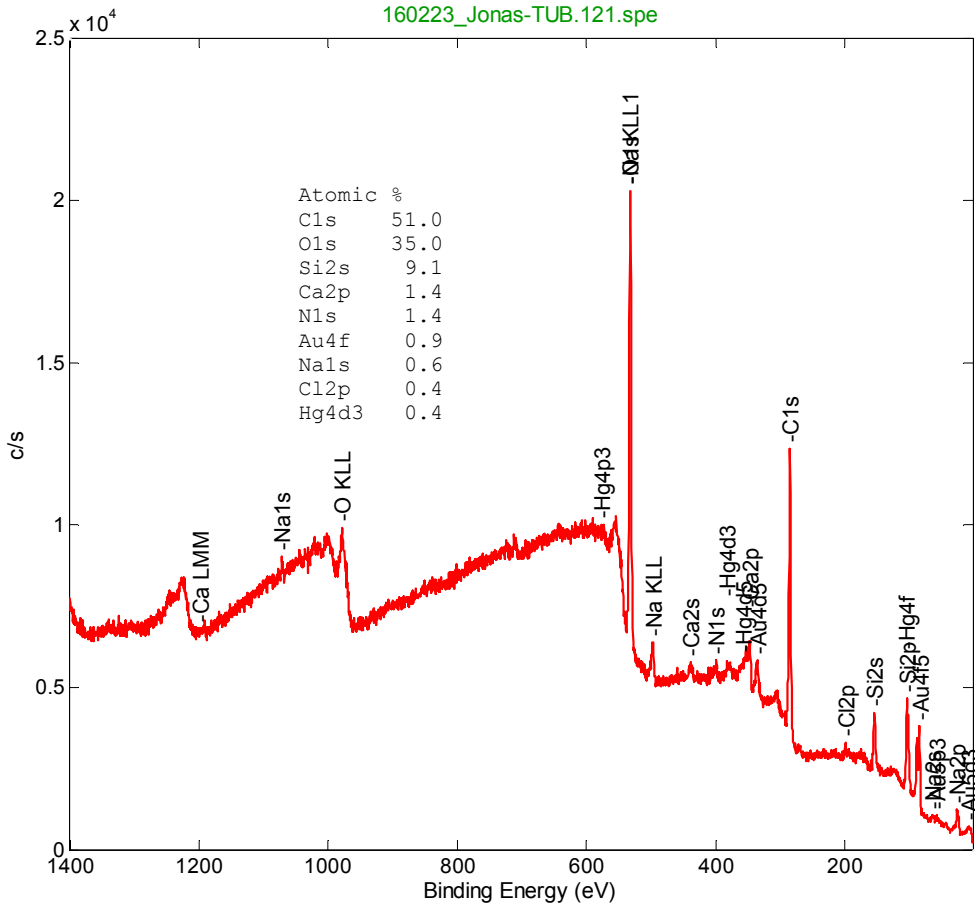

160223_Jonas-TUB.121.spe: 160223_Jonas-TUB HAWK Göttingen

2016 Feb 24 Al mono 25.1 W 100.0 µ 45.0° 187.85 eV 2.7017e+004 max 35.01 min

Su1s/11-2: El Au 16 (fresh) Epoxy/2

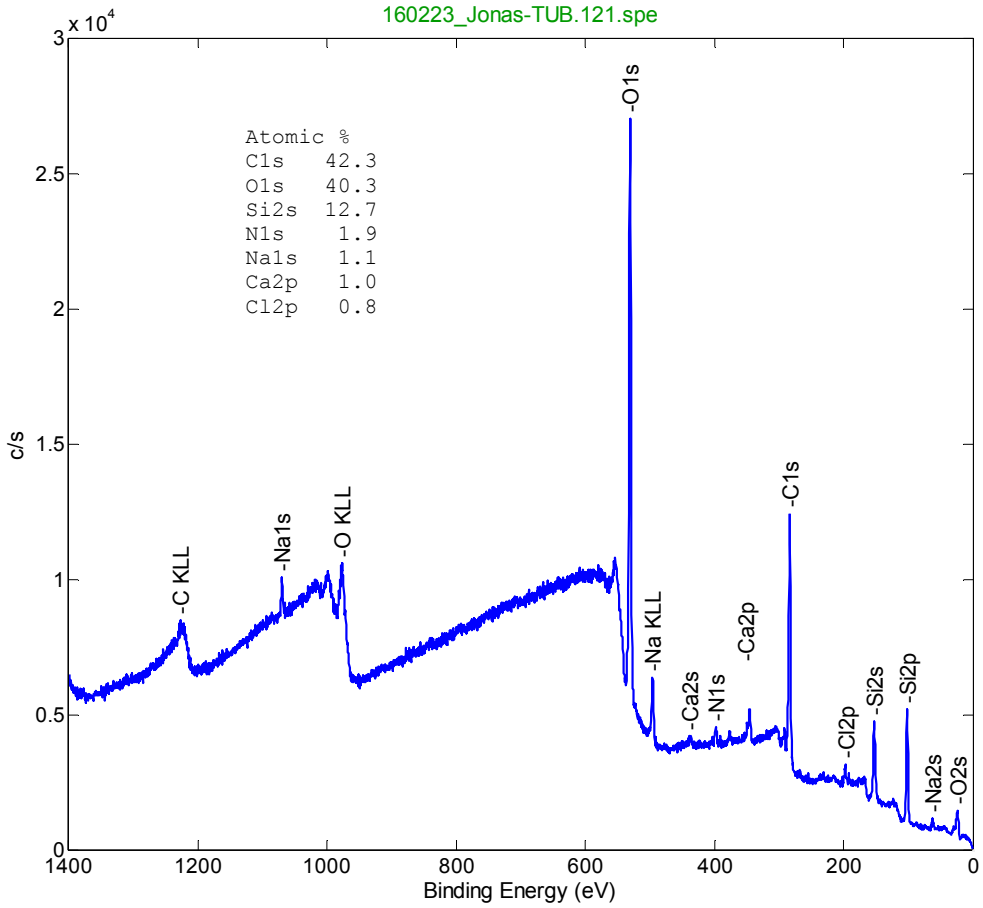

EL AU 24.2. Mitte und Epoxy:

160223_Jonas-TUB.109.SXI.sxi: 160223_Jonas-TUB.SXI HAWK Göttingen
2016 Feb 23 Al mono 1.1 W 5.0 µ 45.0°
SXI

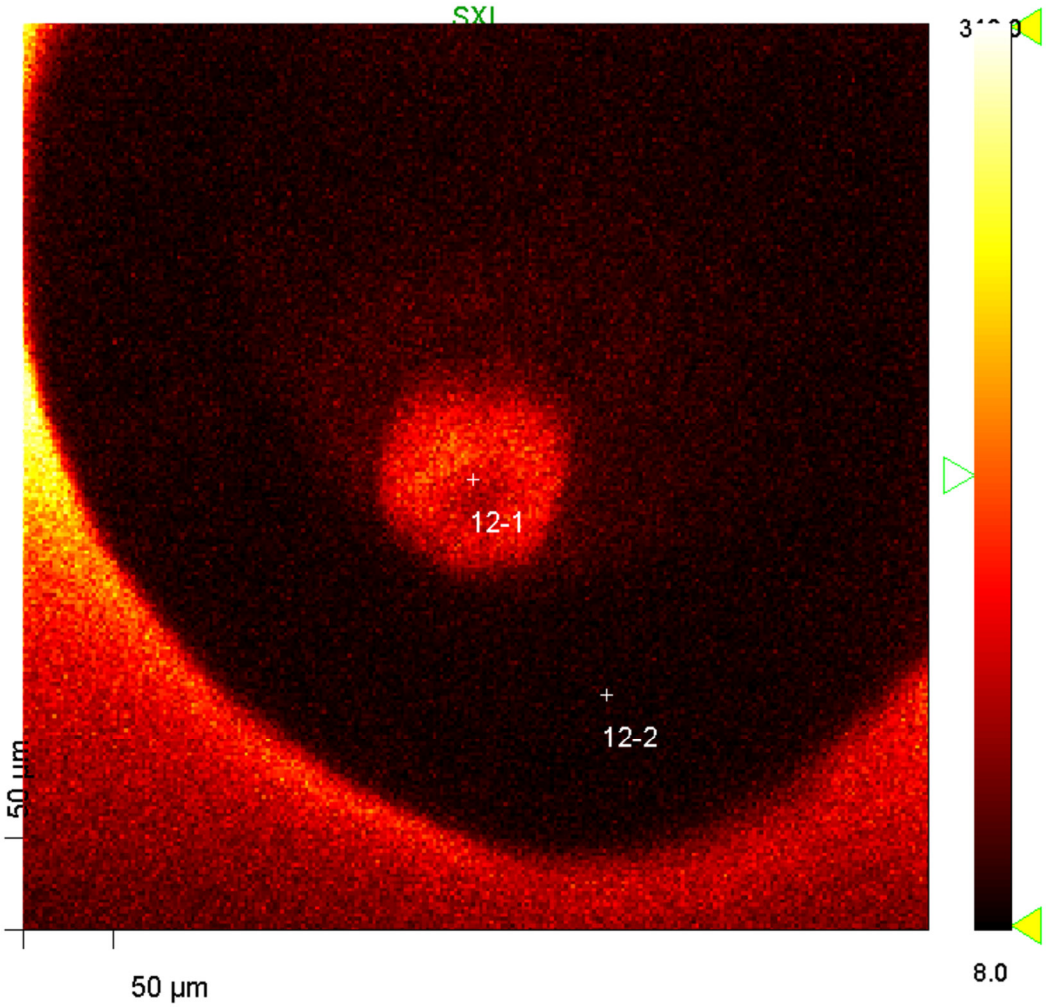

160223_Jonas-TUB.122.spe: 160223_Jonas-TUB HAWK Göttingen

2016 Feb 24 Al mono 25.1 W 100.0 µ 45.0° 187.85 eV 3.3970e+004 max 35.01 min

Su1s/12-1: El Au 24 Mitte/1

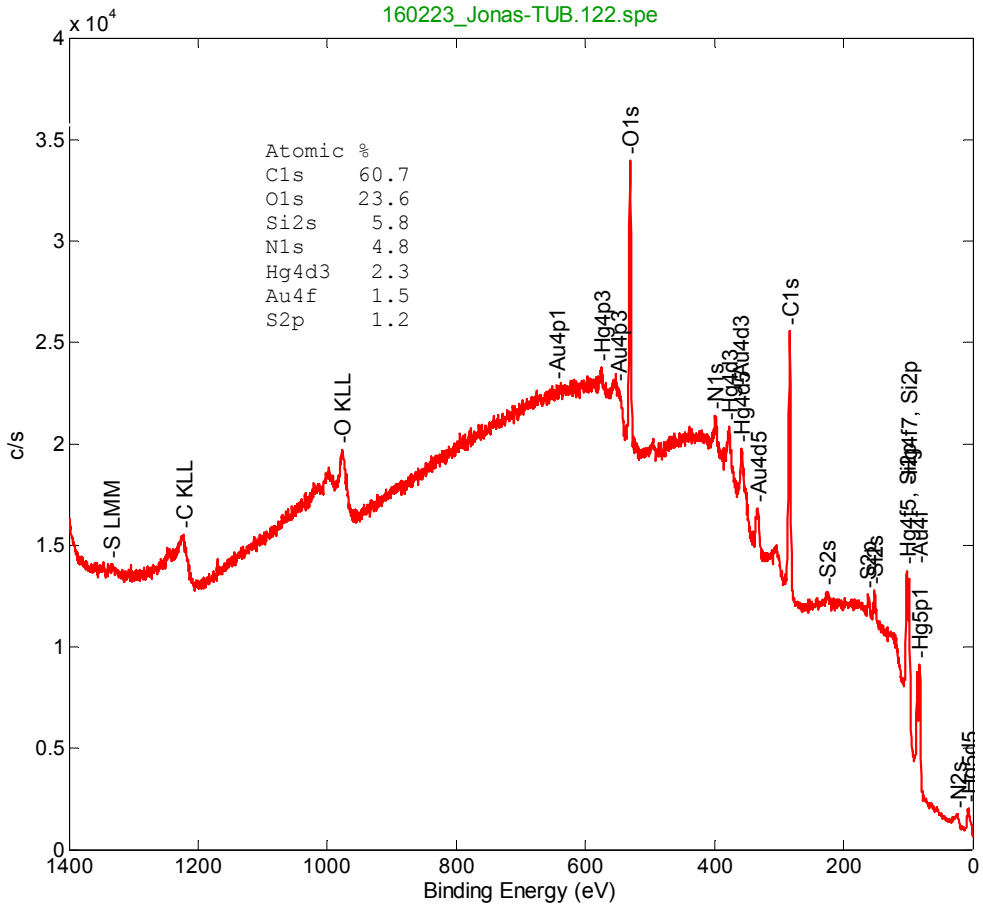

160223_Jonas-TUB.122.spe: 160223_Jonas-TUB HAWK Göttingen

2016 Feb 24 Al mono 25.1 W 100.0 µ 45.0° 187.85 eV 3.1193e+004 max 35.01 min

Su1s/12-2: El Au 24 Epoxy/2